DEPOSITION AND CHARACTERIZATION OF THIN FILM MULTILAYER STRUCTURE FOR APPLICATION AS NEUTRON AND X-RAY MIRROR

By

Arup Biswas

PHYS012008024

Bhabha Atomic Research Centre

A thesis submitted to the
Board of Studies in Physical Sciences

In partial fulfillment of requirements
For the Degree of

DOCTOR OF PHILOSOPHY
of
HOMI BHABHA NATIONAL INSTITUTE

January, 2016

HOMI BHABHA NATIONAL INSTITUTE

Recommendations of the Viva Voce Committee

As members of the Viva Voce Committee, we certify that we have read the dissertation prepared by Shri Arup Biswas entitled **"Deposition and characterization of thin film multilayer structure for application as neutron and x-ray mirror"** and recommend that it may be accepted as fulfilling the thesis requirement for the award of Degree of Doctor of Philosophy.

Sr.No.	Name	Designation	Signature	Date
1	Dr. S. Basu	Chairman		22/01/2016
2	Dr. D Bhattacharyya	Guide & Convener		22/01/2016
3	Dr. H.C. Barshilia	Examiner	22/01/2016	22/01/2016
4	Dr. S.C. Gadkari	Member	22/01/16	22/01/2016
5	Dr. N.K. Sahoo	Technology Advisor		22/01/2016

Final approval and acceptance of this thesis is contingent upon the candidate's submission of the final copies of the thesis to HBNI.

I hereby certify that I have read this thesis prepared under my direction and recommend that it may be accepted as fulfilling the thesis requirement.

Date: 22/01/2016

Place: Mumbai

Dr. Dibyendu Bhattacharyya

(Guide)

STATEMENT BY AUTHOR

This dissertation has been submitted in partial fulfillment of requirements for an advanced degree at Homi Bhabha National Institute (HBNI) and is deposited in the library to be made available to borrowers under rules of the HBNI.

Brief quotations from this dissertation are allowable without special permission, provided that accurate acknowledgement of source is made. Requests for permission for extended quotation from or reproduction of this manuscript in whole or in part may be granted by the Competent Authority of HBNI when in his or her judgment the proposed use of the material is in the interests of scholarship. In all other instances, however, permission must be obtained from the author.

Arup Biswas

DECLARATION

I, hereby declare that the investigation presented in the thesis has been carried out by me. The work is original and has not been submitted earlier as a whole or in part for a degree / diploma at this or any other Institution / University.

Arup Biswas

List of Publications arising from the Thesis

Journals:

1. "Study of interface correlation in W/C multilayer structure by specular and non-specular Grazing Incidence X-ray Reflectivity measurements" *A. Biswas*, S. Maidul Haque, S. Tripathi, Rajnarayan De, S. Rai, D. Bhattacharyya and N.K. Sahoo, J. Appl. Phys. 118, 165312 (2015).
2. "Design and development of an in-line sputtering system and process development of thin film multilayer neutron supermirrors" *A. Biswas*, R. Sampathkumar, Ajaya Kumar, D. Bhattacharyya, N. K. Sahoo, K. D. Lagoo, R. D. Veerapur, M. Padmanabhan, R. K. Puri, Debarati Bhattacharya, Surendra Singh, and S. Basu Review of Scientific Instruments 85, 123103 (2014)
3. "Surface roughness and interface width scaling of magnetron sputter deposited Ni/Ti multilayers" S. Maidul Haque, *A. Biswas*, Debarati Bhattacharya, R. B. Tokas, D. Bhattacharyya, and N. K. Sahoo, J. Appl. Phys. 114, 103508 (2013)
4. "Correlation of interface roughness for Ion Beam Sputter deposited W/Si multilayers" *A. Biswas*, D Bhattacharyya J. App. Phys, 109, 084311 (2011)
5. "Soft x-ray multilayer by ion beam sputtering process", *A.Biswas*, D Bhattacharyya, N. K. Sahoo, Asian J.of Physics Vol. 19, Nos. 2 & 3 (2010) 109-124
6. "Ion energy dependence of interface parameters of ion beam sputter deposited W/Si interfaces", *A. Biswas*, D. Bhattacharyya, Nuc. Ins. and Meth. Phy. Res. B, 268 (2010) 1594–1600
7. "Characterization of ion beam sputter deposited W and Si films and W/Si interfaces by grazing incidence X-ray reflectivity, atomic force microscopy and spectroscopic ellipsometry" *A. Biswas*, A. K. Poswal, R. B. Tokas, D. Bhattacharyya Appl. Surf. Sci, 254 (2008) 3347-3356

Conferences:

AIP Procedings

1. "Installation and Commissioning of a Large Area Coating System for Neutron and X-ray Optical Devices" *A. Biswas*, Sk. Maidul Haque, J. Misal, K.D. Lagoo, R. D.Veerapur, M. Padmanabhan, R.K. Puri, R. Sampathkumar, Ajaykumar, Debarati Bhattacharya, D. Bhattacharyya and N.K. Sahoo, SSPS-2013, AIP Conf 1591, 985 (2014)
2. "Development of W/C Soft x-ray Multilayer Mirror by Ion Beam Sputtering (IBS) System for Below 50Å Wavelength", *A. Biswas* and D. Bhattacharyya, AIP Conf. Proc. 1451, 79-81, 2012

Other Conf.

1. "Development of high 'm-value' neutron supermirror polarizer" *A. Biswas*, D. Bhattacharyya, N.K. Sahoo, Debarati Bhattacharya, S. Singh, S. Basu, Proc. of 5th Conf. on Neutron Scattering, February 2-4 2015, page-123
2. "Development of RF magnetron sputter deposited multilayer neutron supermirror" S. Maidul Haque, *A. Biswas*, D.Bhattacharyya, S. Singh, S. Basu, D. Bhattacharyya and N.K. Sahoo, International Symposium on Neutron Scattering, Mumbai, Jan. 14-17, 2013.

Other Publications[*]:

1. "Optical simulation and fabrication of HfMoN/HfON/Al2O3 spectrally selective coating" N. Selvakumar, K.Prajith, *A.Biswas*, Harish C.Barshilia, Solar Energy Materials & Solar Cells 140 (2015) 328–334
2. "RF plasma MOCVD of Y2O3 thin films: Effect of RF self-bias on the substrates during deposition" S.S. Chopade, S.A. Barve, K.H. Thulasi Raman, N. Chand, M.N. Deo, *A. Biswas*, Sanjay Rai, G.S. Lodha, G.M. Rao, D.S. Patil, Appl. Surf. Science, 285 (2013) 524-531
3. "Structural and Optical Properties of Aluminum Nitride Thin Films Deposited by Pulsed DC Magnetron Sputtering" R. K. Choudhary, P. Mishra, *A. Biswas*, and A. C. Bidaye ISRN Materials Science, Vol 2013, 759462, 1-5
4. "Spectrally selective CrMoN/CrON tandem absorber for mid-temperature solar thermal applications", N. Selvakumar, S.Santhoshkumar, S.Basu, *A.Biswas*, Harish C.Barshilia, Solar Energy Materials & Solar Cells 109 (2013) 97–103
5. "Design and fabrication of highly thermally stable HfMoN/HfON/Al2O3tandem absorber for solar thermal power generation applications" N. Selvakumar, N.T. Manikandanath, *A. Biswas*, Harish C. Barshilia, Solar Energy Materials & Solar Cells 102 (2012) 86–92
6. "Spectroscopic ellipsometry studies of reactively sputtered nitrogen-rich GaAsN films", *A. Biswas*, B. S. Yadav, D. Bhattacharyya, N. K. Sahoo, S. S. Major, and R. S. Srinivasa, J. Non-Crystalline Solids Vol-37, Issue 18, 3293-3300, (2011)
7. "Determination of the optical constants of HfO2eSiO2 composite thin films through reverse fitting of transmission spectra", N.M. Kamble, R.B. Tokas, *A. Biswas*, S. Thakur, D. Bhattacharyya, N.K. Sahoo, Vacuum 86 (2011) 422-428
8. "Microwave ECR Plasma Assisted MOCVD of Y2O3 thin films using Y(tod)3 precursor and their characterization", Shruti Barve, Mukul Deo, Rajib Kar, Nimisha Sreenivasan, Ramaswamy Kishore, Arup Biswas, Bhalchandra Bhanage, Mohan Rao, Lalit Mohan Gantayet, Dinkar Patil, Plasma Process and Polymer, 8, 740-749 (2011)
9. "Structure and optical properties of Ag–Al2O3 nanocermet solar selective", Harish C. Barshilia, N. Selvakumar, K.S. Rajam, *A. Biswas*, Solar Energy Materials & Solar Cells 95 (2011) 1707–1715
10. "Effects of precursor evaporation temperature on the properties of the yttrium oxide thin films deposited by microwave electron cyclotron resonance plasma assisted metal organic chemical vapor deposition" S.A. Barve, Jagannath, N. Mithal, M.N. De*o, A. Biswas*, R. Mishra, R. Kishore, B.M. Bhanage, L.M. Gantayet, D.S. Patil, Thin Solid Films 519 (2011) 3011–3020
11. "Effects of oxygen flow rate on microstructure and optical properties of aluminium oxide films deposited by electron beam evaporation technique", Namita Maiti, *A.Biswas*, R.B. Tokas, D. Bhattacharyya, S.N. Jha, U.P. Deshpande, U.D. Barve, M.S. Bhatia, A.K. Das, Vacuum 85 (2010) 214-220
12. "Effect of argon ion activity on the properties of Y2O3 thin films deposited by low pressure PACVD", S.A. Barve, Jagannath, M.N. Deo, R. Kishore, *A. Biswas*, L.M. Gantayet, D.S. Patil, Applied Surface Science 257 (2010) 215–221

---

[*] Not used in this thesis work

13. “Structure, optical properties and thermal stability of pulsed sputter deposited high temperature HfOx/Mo/HfO2 solar selective absorbers” Harish C. Barshilia, N. Selvakumar, K.S. Rajam, *A. Biswas*, Sol. Energy Mater. Sol. Cells, 94 (2010) 1412-1420
14. “Deposition and characterization of titania–silica optical multilayers by asymmetric bipolar pulsed dc sputtering of oxide targets”, P R Sagdeo, D D Shinde, J S Misal, N M Kamble, R B Tokas, *A Biswas*, A K Poswal, S Thakur, D Bhattacharyya, N K Sahoo, S C Sabharwal, J. Phys. D: Appl. Phys. 43 (2010) 045302
15. “Optical and mechanical properties of diamond like carbon films deposited by microwave ECR plasma CVD”, S B Singh, M Pandey, N Chand, *A Biswas*, D Bhattacharyya, S Dash, A K Tyagi, R M Dey, S K Kulkarni and D S Patil, Bull. Mater. Sci., Vol. 31, No. 5, October 2008, pp. 1–6.
16. “Optical properties and thermal stability of TiAlN/AlON tandem absorber prepared by reactive DC/RF magnetron sputtering”, Harish C. Barshilia, N. Selvakumar, K.S. Rajam, *A. Biswas*, Sol. Energy Mater. Sol. Cells, 92 (2008) 1425-1433
17. “Spectroscopic ellipsometry studies of GaN films deposited by reactive rf sputtering of GaAs target”, *A. Biswas*, D. Bhattacharyya, N. K. Sahoo, Brajesh S. Yadav, S. S. Major, and R. S. Srinivasa, J. Appl. Phys, 103, 083541, 2008
18. “Spectroscopic ellipsometric characterization of TiAlN/TiAlON/Si_3N_4 tandem absorber for solar selective applications” *A. Biswas*, D. Bhattacharyya, H.C. Barshilia, N. Selvakumar, K.S. Rajam Appl. Surf. Sci, 254 (2008) 1694-1699
19. “Substrate bias effects during diamond like carbon film deposition by microwave ECR plasma CVD” R.M. Dey, S.B. Singh, *A. Biswas*, R.B. Tokas, N. Chand, S. Venkateshwaran D. Bhattacharya, N.K. Sahoo, S.W. Gosavi, S.K. Kulkarni, D.S. Patil, Current Applied Physics 8 (2008) 6-12
20. “Structure and optical properties of pulsed sputter deposited Cr*x*O*y*/Cr/Cr2O3 solar selective coatings” Harish C. Barshilia, N. Selvakumar, K. S. Rajam, *A. Biswas*, J Appl. Phys. 103, 023507 (2008)
21. “Spectrally selective NbAlN/NbAlON/Si3N4 tandem absorber for high-temperature solar applications”, Harish C. Barshilia, N. Selvakumar, K. S. Rajam, *A. Biswas*, Sol. Energy Mat. & Sol. Cell, 92, 495– 504, (2008)

Dedicated

To

My Mother

ACKNOWLEDGEMENTS

Foremost, I would like to express my sincere gratitude to my supervisor Dr. Dibyendu Bhattacharyya, his patience, motivation, enthusiasm, and immense knowledge guided me since my joining at Bhabha Atomic Research Centre, Mumbai. Working with him has been a great pleasure and I am thankful to him for believing in me and giving me opportunity. I am deeply grateful to Dr. N.K Sahoo, technology advisor of this thesis work and Head of Atomic & Molecular Physics Division, who is also one of the pioneers of thin film multilayer work in our organization. I would like to express special thanks to all our colleagues in our division, specially, Dr. D.V. Udupa and Dr. S. Thakur for valuable discussions and Shri A.K Poswal, Shri R.B. Tokas, Shri Sk Maidul Haque, Dr. P Rajput, Shri D.D. Shinde, Shri J.S. Misal, Shri N. Dubey and Shri S. Sanaye for their support during deposition and characterization of thin film samples. I also like to thank our colleagues of mechanical, electronics and optical workshops without their unconditional help these experiments would not have been possible. I would like to express my deepest gratitude and appreciation to my collaborators Dr. S. Basu, Dr. S. Singh and Dr. Debarati Bhattacharya of SSPD, BARC and Dr. G.S. Lodha, Dr. S. Rai and Dr. M.H. Modi of RRCAT Indore for neutron and X-ray reflectivity measurements and Dr. P.V Satyam of IOP Bhubaneswar for TEM measurement. I would like to express sincere thanks to Dr. T. Bigault of ILL France and Dr. R. Maruyama of J-PARC Japan for vital discussions on neutron supermirror during my stay at ILL and I am also thankful to Dr. P. Courtois of ILL Grenoble France for giving me opportunity to work at T3 instrument. I would also like to express sincere thank to members of my doctoral committee for their input and valuable discussions. Last but not the least I acknowledge all my teachers, friends and family members for their inspiration and silent support during the course of this thesis work.

CONTENTS

Appendices

SYNOPSIS

Deposition and characterization of thin film multilayer structure for application as neutron and x-ray mirror

Since the discovery of neutron [1] by James Chadwick and X-ray [2] by Rontgen these are excessively used as a probe in understanding the different physical properties of solid and liquid materials under various conditions which later created revolution in technology and modern day life [3-5]. Also worldwide recent developments of high flux research reactors and high intensity synchrotron sources have boosted these techniques enormously. Though some properties and scattering behaviors of neutron and X-ray are similar, their interactions with matters are different, which make the two scattering methods complementary to each other. Other than scattering, neutron and X-ray are excessively used in radiography, tomography and imaging applications also. During these experiments collimating, focusing and controlling X-ray and neutron waves are always challenging and they limit the use of these two probes. In nature, no material is available which can efficiently reflect neutron and X-ray in large wide angle. However, artificial periodic and non-periodic thin film multilayer structures can solve this problem to some extent [6]. For a periodic multilayer with uniform bi-layer thickness, due to the constructive interference of the X-ray or neutron beam reflected from each interface, high reflectivity Bragg peaks appear at some angular positions. Such periodic multilayers having alternate layers of high and low X-ray or neutron scattering lengths, work as high reflecting X-ray or neutron mirror and monochromator. In case of a non-periodic multilayer, where the bilayer thickness varies along the depth, several Bragg peaks due to different portions of the multilayers arise, which subsequently merge and a continuous high reflectivity profile is achieved upto a large value of grazing angle of incidence. Such a structure is known as a supermirror and in case of neutrons it is evaluated by its ‘m-value’ which signifies the ratio of critical angle of the supermirror compared to natural Ni. If these supermirrors are made up with alternate layers of magnetic and non-magnetic elements such that contrast in neutron scattering lengths increases under the presence of magnetic field, then they reflect neutrons of one spin state while neutrons with other spin states are transmitted and in that case these supermirrors are also used as neutron polarizers.

Chapter-1 of my thesis gives a brief introduction and addresses the motivation behind the work. Initially, the necessity of multilayer structures for applications as neutron and X-ray mirrors and monochromators has been pointed out. Subsequently, the sensitivity of the surface and interface parameters on the overall performance of the multilayer device is explained. Along with the surface roughness of the top surface, significance of interface parameters like interface roughness, interface diffusion, correlation length and hurst constant are discussed [6]. In summary, the contents of this chapter provide the basis for the works presented in subsequent chapters.

Chapter-2 is devoted mostly to the measurement and theory of specular and non-specular reflectivity of neutron and X-ray, along with few other thin film characterization techniques which have been used in this thesis work. It is started by the formulation of specular reflectivity pattern of the bulk surface and single layer thin films for neutron and X-rays using Fresnel’s theory and respective expressions of refractive index. Subsequently, the Parratt formalism [7] for computing the reflectivity of a multilayer structure is discussed. Finally, the roughness parameter of a real surface is introduced and how does it affect the specular reflectivity spectrum of bulk surface, single layer thin film and multilayers are shown.

The formulation of the non-specular X-ray reflectivity has been established with simple Born Approximation (BA) which is valid far away from the critical angle of total reflection and with Distributed Wave Born Approximation (DWBA) [8] which is valid for near critical angle. In case of a multilayer structure, similar to specular reflectivity the non-specular reflectivity also interferes constructively in some conditions and it depends on how one interface of the rough multilayer is correlated to other interfaces. So a new correlation function introduced by Holý et. al. [9] having vertical correlation length has been introduced in the formulation of the non-specular reflectivity of a multilayer structure.

All the thin film and multilayer samples described in this thesis work have been prepared by sputtering technique, so chapter-3 of this thesis is started with the theory and mechanism of sputtering phenomena along with some historical over-view. Subsequently, different sputtering processes like DC magnetron, RF magnetron and Ion Beam Sputtering (IBS) which have been used in this thesis work along with the most recently invented High Power Impulse Magnetron Sputtering (HiPIMS) [10] have been explained. It is well understood that neutron and X-ray optical components operate at low grazing angle of incidence, so large area mirrors are essential to cover the large foot prints of the X-ray or neutron beam. In order to meet this practical requirement of neutron and X-ray optical devices, a 9 m long DC/RF magnetron sputtering system has been designed and built indigenously in our laboratory. The development of the above system which is capable of depositing more than 500-layer multilayer thin films on substrate of maximum dimension 1500 mm x 150 mm [11] has also been described in this chapter.

In the last section of this chapter, specular and non-specular reflectivity measurement techniques using neutron and X-ray are explained. The neutron reflectivity measurements have been carried out at the Polarized Neutron Reflectivity (PNR) measurement facility [12] at DHRUVA reactor, BARC, Mumbai and using T3 facility in high flux research reactor at ILL Grenoble, France. The X-ray reflectivity measurements at grazing incidence (GIXR) are done using a commercial XRD instrument with a 1.54 Å CuK_{α} source having grazing incidence measurement facility and the soft X-ray reflectivity measurements have been carried out at the Reflectivity Beamline at INDUS-I synchrotron source at RRCAT, Indore. The techniques of analysis of the measured data by using the fitting software IMD [13] and Parratt32 [7] are also discussed. The other characterization techniques used in this thesis work such as Spectroscopic Ellipsometry (SE), Atomic Force Microscope (AFM) and cross sectional Transmission Electron Microscopy (TEM) are also explained in brief.

In Chapter-4 the design and fabrication of a m=2.5, 312-layer Co/Ti neutron supermirror polarizer based on a graded bi-layer thickness multilayer structure have been described [11]. In the present thesis work, a GUI based computer program has been developed in-house to design multilayer stacks for neutron supermirror application using the Hayter and Mook method [14]. Using this program a process error analysis has also been done for estimating the dependence of neutron reflectivity of supermirrors on the error in layer thickness that may ocur during deposition. It has been observed that more than ±5% thickness error in the layers drastically deteriorates the reflectivity of the supermirrors [15].

After finding out the optimized process parameters for obtaining good quality Co and Ti layers, the 9 m long deposition system has been calibrated by depositing several Co/Ti periodic multilayers with different substrate trolley speeds and characterizing the samples by GIXR technique. It is observed that there is a ‘growth offset’ during the growth of Co and Ti layers in Co/Ti multilayers which is positive for Co and negative for Ti due to the difference in inter-diffusion at Co-on-Ti and Ti-on-Co interfaces. Considering this, Co/Ti supermirror polarizers of m=2.0 (100 layers), m=2.25 (204 layers) and m=2.5 (312 layers) have been deposited as per the design generated by the in-house developed computer code. PNR spectra of all the supermirrors have been measured at DHRUVA, Bhabha Atomic Research Centre, Mumbai, India. It has been found that though the spectral characteristics of the m=2.0 supermirror polarizer closely matches with the theoretically designed spectra, the PNR spectra of the m=2.25 and m=2.5 supermirrors contain undesirable oscillations and the measured reflectivity values of up-spin neutrons are relatively low. On further investigation, it has been observed that presence of magnetic roughness or magnetic dead layer at the Co/Ti interface is the reason for such degraded performance of these supermirrors. The above problems have subsequently been rectified by depositing all the Co layers under a mixed ambience of argon and air and also by depositing Co layers with slightly higher thickness than the nominal value and Ti layers with slightly lower thickness compared to their nominal values. Cross-sectional TEM measurements also show that the Co/Ti samples deposited with air have sharper interfaces which confirms less interface diffusion. Finally high reflectivity (~80%) up to a reasonably large critical wavevector transfer (q) of ~0.06 $Å^{-1}$ has been observed in the above multilayer structures [11,16].

Chapter-5 deals with optimazation of a smaller d.c./r.f. magnetron sputtering system and development of Ni/Ti neutron monochromator and supermirror [17]. Initially Ni and Ti thin films have been deposited at different powers and deposition pressures and have been characterized by GIXR and AFM techniques and the system has been optimized for obtaining single layers with low roughness and bulk-like density. It is found that the top surface roughness of the Ni and Ti films satisfies the power growth law with the thickness of the film. Subsequently, four Ni/ Ti multilayers of 11-layers, 21-layers, 31-layers and 51-layers having different bi-layer thicknesses have been deposited. The multilayers have been characterized by both GIXR and neutron reflectivity techniques with cold neutrons of 7.5Å at ILL, Grenoble France. It is seen that unlike the single layer samples, the top layer roughness of the multilayers does not depend on the total thickness of the multilayer, rather they strongly depend on the bilayer thickness of the multilayers with a power law dependence similar to single layer films. This observation has been explained by the assumption of "restart of the growth at the interface" phenomenon [18].

After successfully depositing the periodic Ni/Ti multilayer, the non-periodic Ni/Ti supermirror is targeted. Prior to deposition using the in-house developed GUI based computer code described above, two Ni/Ti supermirrors of m=1.75 and m=2.0 having 62 and 98 layers are designed. After deposition both the supermirrors have been characterized by measuring neutron reflectivity at DHRUVA reactor at BARC Trombay using 2.5 Å neutron wavelength. The m=1.75 supermirror has shown more than 92% reflectivity while the m=2.0 supermirror has shown more than 71% of reflectivity [19]. The reflectivities of both the supermirrors agree quite well with the theoretically generated reflectivity spectra of the samples.

In chapter 6, the development of an in-house built Ion Beam Sputtering (IBS) system and optimization of process parameter for deposition of W/Si and W/C interfaces are described [20,21]. Subsequent to the installation of the system W, Si single layer thin films, W/Si bi-layer and W/Si/W tri-layer samples have been deposited. The samples have been characterized by GIXR, spectroscopic ellipsometry (SE) and AFM. It has been found that the r.m.s. roughness does not increase from bi-layer to tri-layer samples and the inter-diffusion at the interface is found to be insignificant when Si is deposited on W layer, however it is found to be considerably high when W is deposited on underlying Si layer [20].

In the aim of optimization of the Ar^+ ion energy of the IBS system for depositing W/Si and W/C multilayer mirrors, a set of single layer W film and tri-layer W/Si/W and W/C/W samples are deposited at 1.5×10^{-3} mbar Ar working pressure, 10 mA grid current and at Ar^+ ion energies of 600, 800, 1000 and 1200 eV. Along with the thickness and density of the single-layer W films, interface roughness, interface diffusion and correlation length for all the interfaces have been measured for the tri-layer samples by specular and non-specular (detector scan geometry) GIXR measurements. In this experiment it has been found that the density of W layer initially increases as the sputtering ion energy increases from 600 eV to 1000 eV and above it density goes down. The above observation is explained by simulation of the IBS process using the Monte-Carlo programme ‘‘TRIM” [21]. In case of the tri-layer samples, the interface width and inter-diffusion at W-on-Si interface and W-on-C interface are found to be much higher than that at Si-on-W and C-on-W interface respectively. The interface diffusion decreases as ion energy of W deposition increases for Si-on-W interface and C-on-W interface and is minimum when W-layer is deposited with 1000 eV Ar+ ions since the density of W layer is maximum at this energy. Through this process the optimum ion energy of 1000 eV is reached for deposition of W/Si and W/C multilayer mirrors using the home-built IBS system [21].

In continuation of the above work using the IBS system in Chapter 7, the development and characterization of W/Si and W/C soft X-ray multilayers are described [22-24]. Here the correlation of the interface roughness found from specular and non specular X-ray reflectivity measurements of the W/Si and W/C multilayer are also discussed. Initially, W/Si multilayers having 5, 7, 9, 13 and 17 layers and W/C multilayer having 5, 7, 9 and 13 layers have been deposited on c-Si substrates. The thickness of the multilayer is maintained at a pre-determined value by quartz crystal monitor. These samples have been characterized by specular GIXR measurement with 1.54Å wavelength and non-specular GIXR measurements in detector scan geometry are also done at the 1st Bragg peak position. Fitting these specular and non-specular measured data, it is found the interface widths at the W-on-Si and W-on-C interfaces are higher than that at Si-on-W and C-on-W interfaces due to higher diffusion of W atoms inside Si or C layers. Investigation has been done on the variation of all interface parameters of the W-on-Si and Si-on-W interfaces for W/Si multilayer and W-on-C and C-on-W interfaces for W/C multilayers. It is found that in case of W/Si multilayer there is a smoothening process which is due to deposition of energetic W atom [22], however in case of W/C multilayer high internal stress dominates over the smoothening process.

Subsequently, a 25-layer and a 21-layer W/Si multilayer have been designed and deposited which can give high reflectivities at 45 Å and 130 Å wavelengths respectively at 30° grazing angle of incidence. These soft X-ray mirrors are characterized by soft X-ray at INDUS-I reflectivity beamline at 45 Å and 130 Å wavelengths. The reflectivity has been measured in the 0 to 45° grazing angles of incidence. It is seen that the reflectivity of 25-layer and 21-layer multilayer is 20% and 30% of their theoretical values at their designed condition. Similarly a 21-layer and a 25-layer W/C multilayer are designed and deposited to show peak reflectivity for 44Å soft X-ray at 20° and 25° respectively [24]. The soft X-ray reflectivities of both the W/C multilayer samples have been measured at the Reflectivity beamline at INDUS-1 in the 0 to 40° grazing angles at different wavelengths in the range 43-50Å and the maximum reflectivity has been found at 44Å for both the samples. The value of peak reflectivity for 21-layer sample is found to be ~4.5% at 20° grazing angle of incidence, while for the 25-layer samples it is ~3.5% at 26° grazing angle of incidence [23].

Finally in chapter 8 the conclusion drawn in the all previous chapters on different multilayer systems are summarized. During this work some high *m*-value high reflecting neutron supermirrors, supermirror polarizer and some high reflecting soft X-ray mirrors have been developed. Depositions of these multilayers have been carried out in various in-house built sputtering systems and it has been demonstrated that good quality multilayer devices could be realized in these home-built systems. By characterizing all the samples it has been observed that the interface width as well as interface diffusion in a multilayer thin film is always asymmetric. It is also seen that the top surface roughness of a multilayer does not generally depend on the total thickness of the multilayer, as at each interface the growth process restarts without propagating the bottom layer roughness, except in some case like W/C multilayer where some other effect like inherent stress in the multilayer is found to be more dominating. It has also been found that in case of Co/Ti multilayers, interface roughness can be controlled by depositing Co layers by reactive sputtering technique. In future it is proposed to control the interface roughness by applying some buffer layers at the interfaces of the multilayer. Also as a future work it is proposed to deposit the neutron and X-ray multilayers by the recently invented High Power Impulse Magnetron Sputtering (HiPIMS) technique which imparts higher energies to the adatoms of a growing film.

References

1. J. Chadwick, Possible Existence of a Neutron, Nature, 129 (1932) 312.
2. W.C. Röntgen, On a New Kind of Rays, The British Journal of Radiology, 4 (1931) 32-33.
3. G.L. Squires, Introduction to the Theory of Thermal Neutron Scattering, Dover Publications, 1997.
4. J. Als-Nielsen, D. McMorrow, Elements of Modern X-ray Physics, second Edition ed., Wiley: A John Wiley & Sons, Ltd Publication, West Sussex, PO19 8SQ, United Kingdom, 2011.

5. D.T. Attwood, Soft X-Rays and Extreme Ultraviolet Radiation Principles and Applications, Chambridge University Press, 2000.
6. J. Daillant, A. Gibaud, X-ray and Neutron Reflectivity Principles and Applications, Springer, Berlin Heidelberg, 2009.
7. L.G. Parratt, Surface Studies of Solids by Total Reflection of X-Rays, Physical Review, 95 (1954) 359-369.
8. D.K.G. de Boer, X-ray scattering and x-ray fluorescence from materials with rough interfaces, Physical Review B, 53 (1996) 6048-6064.
9. V. Holý, Diffuse X-ray scattering from non-ideal periodical crystalline multilayers, Appl. Phys. A, 58 (1994) 173-180.
10. V. Kouznetsova, K. Macáka, J.M. Schneidera, U. Helmerssona, I. Petrovb, A novel pulsed magnetron sputter technique utilizing very high target power densities, Surface and Coatings Technology 122 (1999) 290-293.
11. A. Biswas, R. Sampathkumar, A. Kumar, D. Bhattacharyya, N.K. Sahoo, K.D. Lagoo, R.D. Veerapur, M. Padmanabhan, R.K. Puri, D. Bhattacharya, S. Singh, S. Basu, Design and development of an in-line sputtering system and process development of thin film multilayer neutron supermirrors, Review of Scientific Instruments, 85 (2014) 123103.
12. S. Basu, S. Singh, A new polarized neutron reflectometer at Dhruva for specular and off-specular neutron reflectivity studies, Journal of Neutron Research, 14 (2006) 109-120.
13. D.L. Windt, IMD Version 4.1.1, in: http://cletus.phys.co-lumbia.edu/windt/idl, 2000.
14. J.B. Hayter, H.A. Mook, Discrete thin-film multilayer design for X-ray and neutron supermirrors, J. Appl. Cryst., 22 (1989) 35-41.
15. A. Biswas, S.M. Haque, J. Misal, K.D. Lagoo, R.D. Veerapur, M. Padmanabhan, R.K. Puri, R. Sampathkumar, Ajaykumar, D. Bhattacharya, D. Bhattacharyya, N.K. Sahoo, Installation and commissioning of a large area coating system for neutron and X-ray optical devices, AIP Conference Proceedings, 1591 (2014) 985-987.
16. A. Biswas, D. Bhattacharyya, N.K. Sahoo, D. Bhattacharya, S. Singh, S. Basu, Development of high ‘m-value’ neutron supermirror polarizer, in: 5th Conf. on Neutron Scattering, Mumbai, 2015, pp. 123.
17. S. Maidul Haque, A. Biswas, D. Bhattacharya, R.B. Tokas, D. Bhattacharyya, N.K. Sahoo, Surface roughness and interface width scaling of magnetron sputter deposited Ni/Ti multilayers, Journal of Applied Physics, 114 (2013) 103508.
18. D.E. Savage, N. Schimke, Y.H. Phang, M.G. Lagally, Interfacial roughness correlation in multilayer films: Influence of total film and individual layer thicknesses, Journal of Applied Physics, 71 (1992) 3283-3293.
19. S.M. Haque, A. Biswas, D. Bhattacharya, S. Singh, S. Basu, D. Bhattacharyya, N.K. Sahoo, Development of RF magnetron sputter deposited multilayer neutron supermirror, in: International Symposium on Neutron Scattering, Mumbai, 2013.
20. A. Biswas, A.K. Poswal, R.B. Tokas, D. Bhattacharyya, Characterization of ion beam sputter deposited W and Si films and W/Si interfaces by grazing incidence X-ray reflectivity, atomic force microscopy and spectroscopic ellipsometry, Applied Surface Science, 254 (2008) 3347-3356.
21. A. Biswas, D. Bhattacharyya, Ion energy dependence of interface parameters of ion beam sputter deposited W/Si interfaces, Nuclear Instruments and Methods in Physics Research Section B: Beam Interactions with Materials and Atoms, 268 (2010) 1594-1600.
22. A. Biswas, D. Bhattacharyya, Correlation of interface roughness for ion beam sputter

deposited W/Si multilayers, Journal of Applied Physics, 109 (2011) 084311.

23. A. Biswas, D. Bhattacharyya, Development of W/C soft x-ray multilayer mirror by ion beam sputtering (IBS) system for below 50Å wavelength, AIP Conference Proceedings, 1451 (2012) 79-81.
24. A. Biswas, D. Bhattacharyya, N.K. Sahoo, Soft X-ray multilayer by ion beam sputtering process, Asian J. of Physics, 19 (2010) 109-124.

List of Figures

List of Tables

CHAPTER 1

Introduction and Motivation

Since the discovery of neutron [1] by James Chadwick and X-rays [2] by Wilhelm Röntgen these are excessively used as probes in understanding the different physical properties of solid and liquid materials under various conditions which has later created revolution in technology and modern day life [3-5]. Worldwide recent improvements of high flux research reactor and high intensity synchrotron sources have boosted these techniques enormously. Though some properties and scattering behavior of neutron and X-rays are similar, their interactions with the matter are different, which makes the two scattering methods complementary to each other. Other than scattering, neutron and X-rays are excessively used in radiography, tomography and imaging applications also [6, 7]. During these experiments collimating, focusing and controlling of neutron and X-ray waves are always challenging tasks and these limit their use in characterisation of materials. In nature, no material is available which can efficiently reflect neutron and X-rays in large wide angle. However, artificial periodic and non-periodic thin film multilayer structure can solve this problem to some extent [8]. For a periodic multilayer with uniform bi-layer thickness, due to the constructive interference of the neutron or X-ray beam reflected from each interface, a high reflectivity Bragg peak appears at some angular position. Such periodic multilayers with alternate layers of high and low neutron or X-ray scattering lengths, work as high reflecting neutron or X-ray mirror and monochromator. In case of non-periodic multilayer where the bilayer thickness varies along the depth, several Bragg peaks due to different portions of the multilayers arise, which subsequently merge and a continuous high reflectivity profile is achieved up to a large value of grazing angle of incidence [9, 10]. Such a structure is known as a supermirror and in case of neutron it is characterised by its 'm-value' which signifies the ratio of critical angle of the supermirror compared to natural Ni. If these supermirrors are made up with alternate layers of magnetic and non-magnetic elements such that contrast in neutron scattering lengths increases under the presence of magnetic field, then they reflect neutrons of one spin state while neutrons with other spin states are transmitted and in that case these supermirrors are also used as neutron polarizers [11].

Neutrons are unique probe in condensed matter research, due to the fact that it has a de Broglie wavelength ($\lambda=h/mv$), comparable to that of the inter atomic spacing in many physical systems and also that its energy which is in the range of meV to eV is comparable to many atomic and electronic processes, compared to X-rays which has photon of energy in the range of KeV [3]. Since neutrons are chargeless particles, and they have the ability to penetrate far into matter, it is possible to do "in-situ" experiments on samples kept inside specialised sample environment equipments, such as furnaces, cryostats or pressure cells. Intrinsic spin angular momentum of neutron is 1/2 in nuclear units and it has a magnetic moment, μ_n of -1.913 Bohr magnetons, which means that it can interact with other particles, either through a magnetic or through a nuclear interaction. All these properties make neutrons a favorable probe for characterizing a material. Neutrons can be produced in a nuclear reactor through fission process and also can be produced using proton accelerator through spallation reaction which has gained importance in recent years [12]. Whatever may be the process, after moderation these neutrons are transported to the experimental station through a neutron guide to a large distance which is some time hundreds of meter long in order to accommodate variety of instruments and also to achieve an environment of low γ-ray, as shown in Fig. 1.1. This guide is similar to optical guides, where the light is guided through a fiber optic cable. In a neutron guide, vacuum is the core and the outer casing is either float or borofloat glass coated with a single Ni layer or float or borofloat glass coated with Ni/Ti supermirror as discussed in the previous section. By coating the supermirror on an elliptical surface neutrons can also be focused on a small area of the sample. It is already demonstrated that by this technique neutron can be focused with FWHM ~125 μm [13], as shown in Fig. 1.2.

By intelligently choosing the magnetic and non magnetic material combination of the

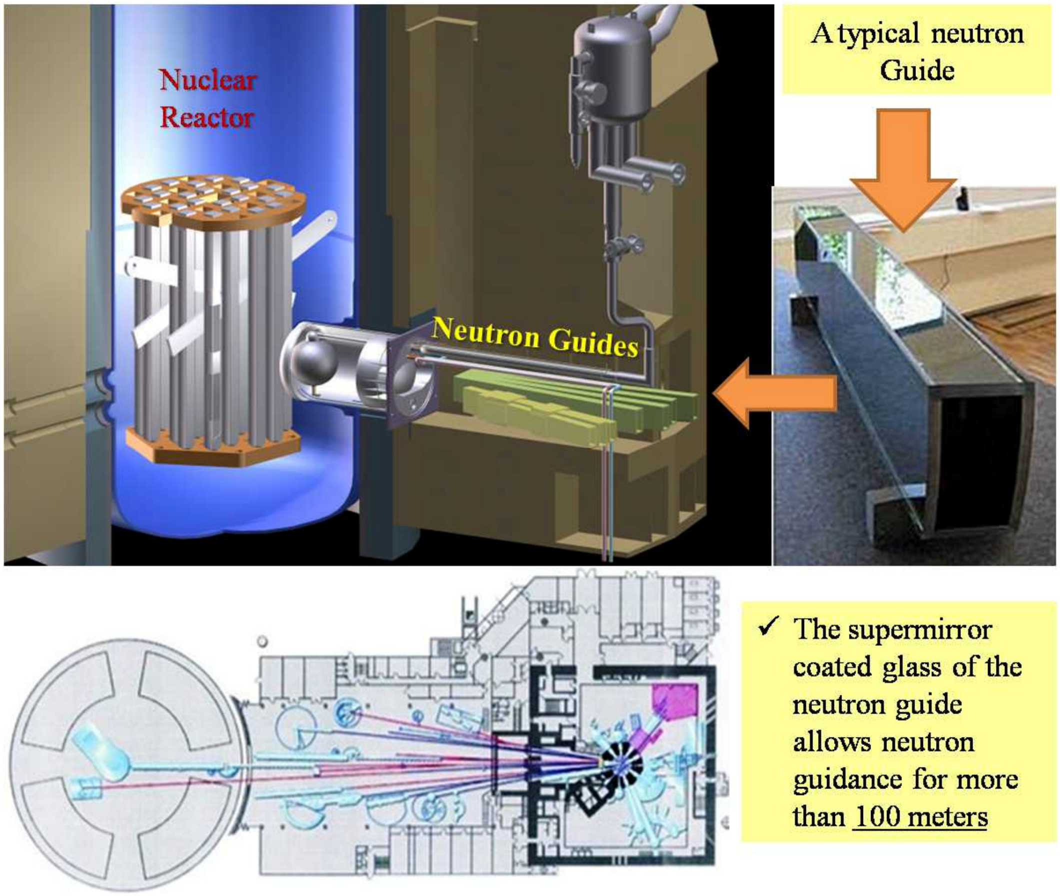

Fig. 1.1: A typical research reactor for neutron generation and its guide tube

multilayer like Co/Ti [14], Fe/Si [15], FeCoV/Ti [16], a supermirror can be used to polarize or analyze neutrons which is very useful for studying the magnetic properties of materials. It not only used to measure the polarized neutron reflectivity (PNR) for measuring magnetization in thin film and multilayer [17, 18], but also for the separation of nuclear, magnetic and nuclear spin-incoherent scattering on a multi-detector neutron spectrometer, so-called 'xyz'-polarization analysis [19] which is the only technique available which provides unambiguous separation of the nuclear, magnetic and nuclear spin incoherent scattering cross sections simultaneously over all scattering angles [20]. It is used in huge number in neutron spin echo (NSE) spectrometer to achieve a very high energy resolution by encoding the neutron velocities in the Larmor

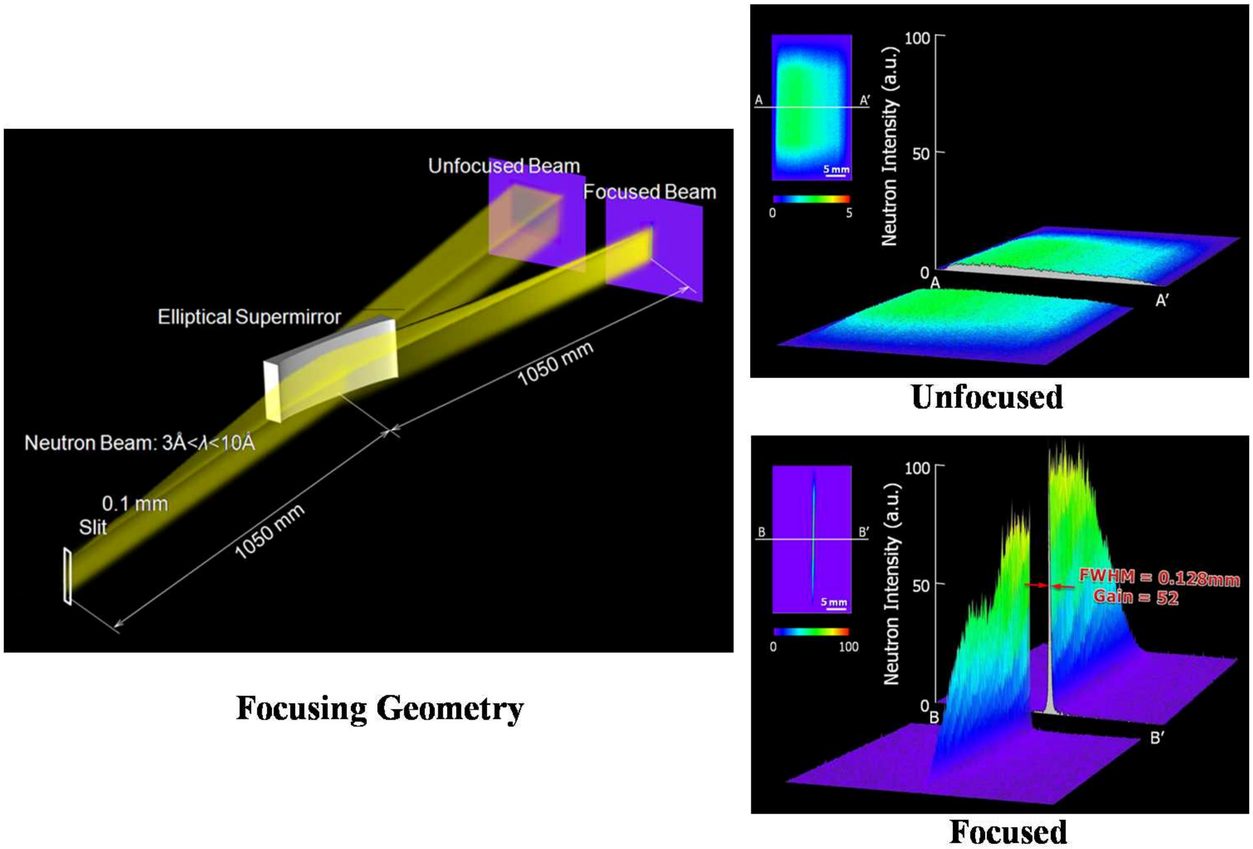

Focusing Geometry

Unfocused

Focused

Fig. 1.2: Neutron focusing by supermirror deposited on elliptical surface
Source: http://legacy.kek.jp/intrae/press/2012/060811

precession angle of the neutron's magnetic moment as the neutron is exposed to well-controlled magnetic fields. By comparing the precession angles of the neutron spins in identical fields before and after scattering from the sample, respectively, tiny velocity or energy changes, can be measured independently of the width of the neutron velocity distribution which is a very efficient technique in neutron inelastic scattering experiment [21].

On the other hand, X-rays which is basically an electromagnetic wave of lower wavelength compared to visible light, can only be reflected at very low grazing angle of incidence using single layer mirror of noble matels like Pt, Au, Rh etc. deposited on polished silicon substrates [22]. As it operates at a very low grazing angle of incidence, large size mirrors, typically ~1.5 meter long are required. As shown in Fig. 1.3 the other type of X-ray mirrors are periodic multilayer structures consisting of one material having high atomic number like, W, Mo, Pt and other material having low atomic number like Si, C, Be etc. These multilayers operate at a high grazing angle of incidence and are very useful in soft X-ray region of wavelength as mirrors and dispersive elements. As the choice of natural crystal having lattice spacing more than 10 Å is very limited and those available (such as pro-chlorite) are likely to be small and of poor quality [22], so in the soft X-ray and EUV region multilayer structure is the only option for reflecting, monochromating or polarizing photons. Incidentally there is a region in the soft X-ray wavelength of 23 Å (above O K edge) to 44 Å (below C K edge) where water does not absorb (the so called "Water Window" region) [23-26]. However organic materials which are dominantly carbon based, show strong absorption in this region. Hence microscope having probe with X-ray within this range are extremely helpful in viewing living cells within their native aqueous medium. Similarly microscope in the "Carbon Window" region i.e. 45 Å to 50 Å can image various carbon containing thick samples easily [27]. On the other hand X-ray not only can see small features of nanometer scale it can also create small features of same scale on a surface using a technique, popularly known as lithography. It uses a set up which is basically a microscope working with soft X-rays of 135 Å wavelength in the reverse optical direction which also uses soft X-ray multilayer mirrors and is unavoidable in semiconductor industry for fabrication of small transistor to meet today's requirement of miniaturization [28]. Other than the above, these X-ray multilayer devices are widely used in the application of astronomy [29], plasma diagnosis [30], microscopic holography [31], synchrotron radiation beamlines [32] etc.

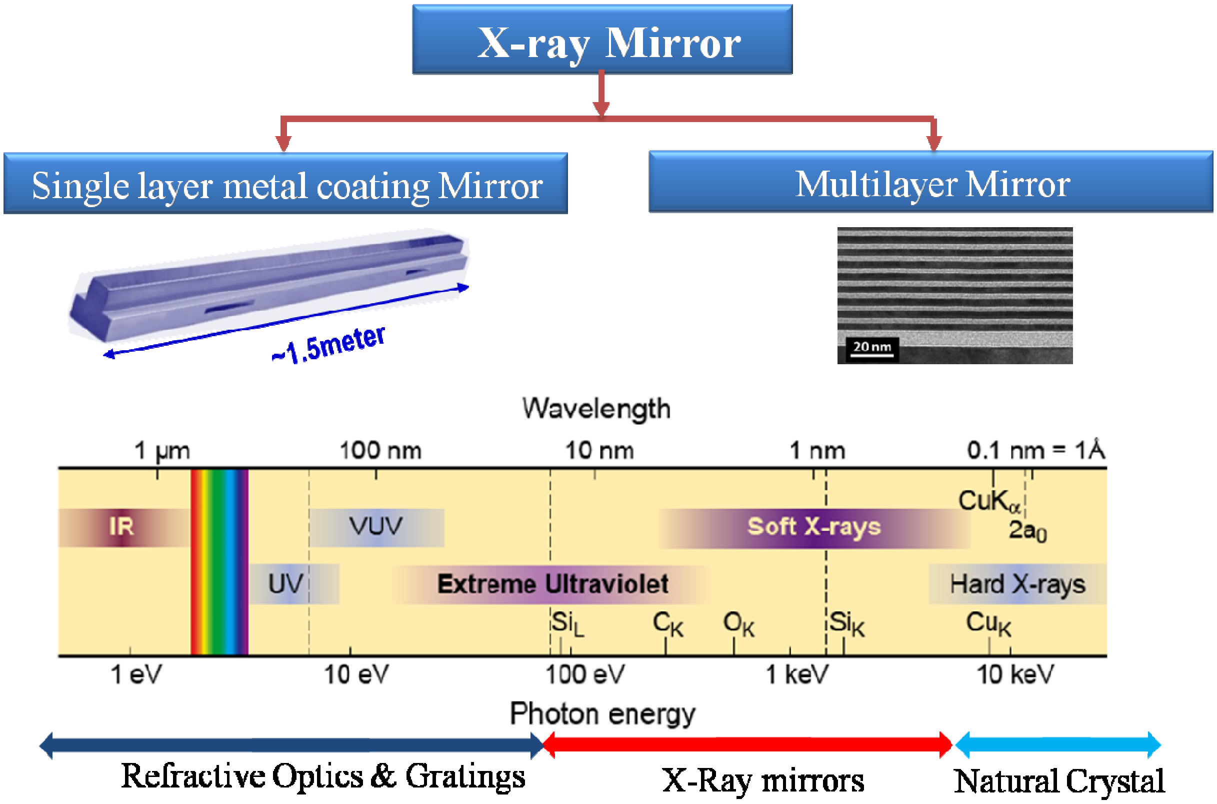

Fig. 1.3: Classification of X-ray mirror

The performance of the above periodic and non periodic neutron and X-ray multilayer devices depends on the quality and features of top surface and internal interfaces. As shown in Fig. 1.4, the neutron reflectivity of a Ni/Ti supermirror and soft X-ray reflectivity of a Mo/Si multilayer decrease drastically with roughness which is quantitatively equal to standard deviation of the interface heights. This roughness not only decreases the specular reflection but also increases the non-specular reflection which reduces the image contrast. The origin of this interface roughness can be due to physical roughness, due to diffusion of one material in to the other or due to the magnetic dead layer and magnetic roughness in between magnetic and non-magnetic layers [8]. In case of single layer film it is predicted that the roughness grows with the thickness of the film under the frame work of Dynamic scaling Theory (DST) [33, 34] which has also been confirmed experimentally and shown that the coefficient of scaling depends on process of growth and material of film deposited [35-38]. In case of multilayers, the recent numerical simulation by Liu and Shen predicted that the same growth law of single layer film is valid [39]. It is also predicted that, in contrast to the monotonous rises of roughness with increase in thickness like in a single layer, in multilayer generally an oscillating variation of roughness is observed due to periodic smoothening and roughening effect at the two different interfaces. Smoothening and roughening effects in multilayers have been observed experimentally also [40-42] though contradictory results have been reported in the literature regarding their origion. Freitag and Clemens [41] have observed that the smoothening effect is in amorphous Si layer, in

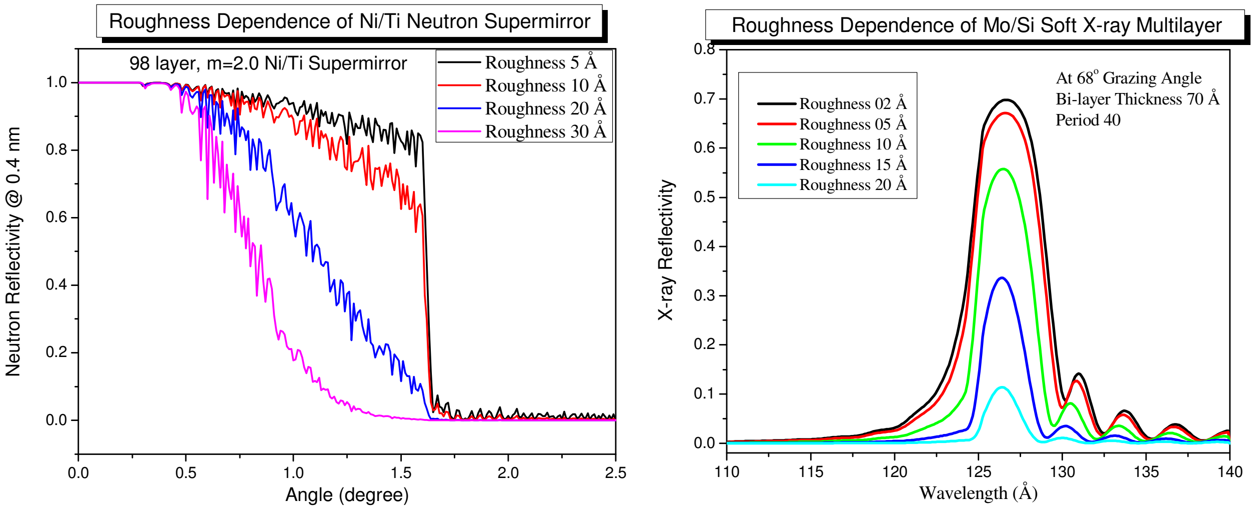

Fig. 1.4: Roughness dependence of neutron and x-ray multilayer devices

case of DC sputtered Mo/Si multilayer, whereas by in-situ X-ray reflectivity study of the growth of WSi_2/Si multilayers, Wang *et. al.* [43] concluded that the smoothening effect is stronger during WSi_2 deposition. Knowledge about the smoothening and roughening layer in any multilayer system can always be beneficial during the growth of multilayer devices for controlling the interface roughness and improving the reflectivity. Not only the interface roughness, the performance of the multilayer device also depends on lateral or in-plane correlation length and how this roughness of one interface is correlated with other interface of the multilayer which is expressed as vertical correlation length [44-47]. It has been shown by studying different multilayer systems that correlation lengths can be completely correlated, uncorrelated or partially correlated [8]. The knowledge of origin and mechanism of growth of all this roughness parameters can give clue to control over the roughness in multilayer systems which at the end can give better performance of multilayer devices. With this aim, in this thesis work two neutron multilayer systems viz., Co/Ti & Ni/Ti and two X-ray multilayer systems viz., W/Si & W/C have been studied in details by specular and non-specular X-ray and neutron reflectivity techniques along with few other complementary techniques. The flow of this thesis work goes as follows:

The theories of specular and non-specular reflectivities of neutron and X-rays, have been discussed in Chapter 2. During this formulation different practical structural and surface parameters of single layer and multilayer films are introduced.

As preparation of high quality thin film multilayer devices by sputtering is a major part of this thesis work, so in Chapter 3 different sputtering configurations are explained. The details of a 9 meter long DC/RF magnetron sputtering system which has been designed and built indigenously in our laboratory in the course of this thesis work, have been described along with the optimization procedures to obtain good quality layers and interfaces. This in-line sputtering system can deposit more than 500 layer multilayer thin films on substrate of maximum dimension of 1500 mm x 150 mm. The deposited single layer and multilayer films are mainly characterized by measureing neutron and X-ray reflectivity in specular and non-specular geometry. The experimental measurement setup of these characterization facilities are described here. The other characterization techniques used in this thesis work such as Spectroscopic Ellipsometry (SE) and Atomic Force Microscope (AFM) are also explained in brief in this chapter.

Chapter 4 of the thesis deals neutron multilayer systems. Subsequent to optimization and calibration of the 9 meter long DC sputtering system, Co/Ti supermirror polarizers of m=2.0 (100 layers), m=2.25 (204 layers) and m=2.5 (312 layers) have been developed using in-house designed structure and have been characterized by PNR measurement. The neutron reflectivities of the m=2.25 and m=2.5 supermirrors have been improved to high values by controlling the interface widths using two different modifications in the process, which have been explained in details.

Chapter 5 is devoted to the study of Ni, Ti single layer, Ni/Ti periodic multilayer and development of Ni/Ti supermirrors using an in-house developed RF sputtering system. After optimization of the process parameters, the roughness scaling of single layer Ni and Ti films with thickness have been probed by GIXR and AFM measurements and roughness scaling for Ni/Ti periodic multilayers has been studied using neutron and X-ray reflectivity techniques. Subsequently two Ni/Ti supermirrors of m=1.75 and m=2.0 having respectively 62 and 98 layers have been designed, deposited and characterized.

The next two chapters deal with deposition and charaterisation of thin film multilayer devices for soft X-ray application which has been done using an in-house developed ion beam sputtering (IBS) system. Subsequent to the installation of IBS system, the process parameters for deposition of W/Si and W/C multilayers have been optimized by depositing single layer W film, tri-layer W/Si/W film and tri-layer W/C/W film at different Ar^+ ion energies in the range of 600 eV to 1200 eV. The above results have been described in detail in Chapter-6 of this thesis along with theoretical corroboration by Monte Carlo simulation using TRIM code.

In continuation with above, Chapter-7 describes the development and characterization of W/Si and W/C multilayers which can be used as soft X-ray mirrors. Analyzing the specular and non-specular GIXR measured data of W/Si multilayer having 5, 7, 9, 13 and 17 layers and W/C multilayer having 5, 7, 9 and 13 layers, the correlation of the interface roughness in the W/Si and W/C periodic multilayers have been discussed. Finally, 21-layer and 25-layer W/Si and W/C multilayer soft X-ray mirrors have been designed and deposited using IBS technique and finally characterized using synchrotron radiation from INDUS-I synchrotron source at RRCAT, Indore, India.

In Chapter-8 the conclusions drawn in the all previous chapters in the different multilayer systems are summarized. Also some future works in continuation with the improvement of performances of multilayer devices are proposed.

CHAPTER 2

Theoretical formulation: specular and non-specular reflectivity of neutron and X-ray

2.1 Introduction

It is well understood that when a wave enters from one medium to another medium, some fraction of it is reflected and transmitted from the interface and rest of it is absorbed depending upon the interaction of the waves with the medium. In case of electromagnetic wave of higher wavelength like visible ray the interaction is mainly polarization of molecules, on the other hand, for lower wavelength electromagnetic wave like X-ray, its interaction with the electrons of the material is necessary to be considered [4, 5]. However for neutron wave the interaction is mainly with the nuclei of the material and in some cases with the electrons of an atom which has magnetic moment [3, 8]. These properties make the X-ray and neutron complementary to each other. Though their mechanism of interactions with matter are different, their nature of propagation in a medium can be formulated by a single optical parameter called complex refractive index, the imaginary part of which signifies the absorption in the medium. In this chapter the expression of complex refractive indices of an isotropic medium for neutron and X-ray have been derived separately considering the above phenomena. Subsequently, the formulations of specular and non-specular reflectivities have been derived for thin film and multilayers starting with Fresnel's equation for an ideal single surface. The effect of surface feature generally observed in real surface has been incorporated thereafter. These two different scattering geometries are important as they probe the interface in two different directions, the specular reflectivity probes the structure along the depth of the film whereas the non-specular reflectivity probes the surface features [8].

2.2 X-Ray and neutron optical properties of material

2.2.1 X-ray refractive index

The vector wave equation for transverse electromagnetic wave of the form $exp[-i(\omega t - k.r)]$, propagating in the *k*-direction can be written from Maxwell's equation

$$\left(\frac{\partial^2}{\partial t^2} - c^2\nabla^2\right)E(r,t) = -\frac{1}{\epsilon_0}\frac{\partial J(r.t)}{\partial t} \tag{2.1}$$

where, *E* and *J* are the electric field and current density in the transverse to the wave propagation direction *k* and *c* is the phase velocity for propagation of wave in vacuum. Now when an electromagnetic wave is incident on a medium, it oscillates the bound electrons of the medium with the same frequency of the wave and the amplitude of the oscillation can be written as

$$x(r,t) = \frac{e}{m}\frac{1}{(\omega^2 - \omega_s^2) + i\gamma\omega}E(r,t) \tag{2.2}$$

where, *m* and *e* are the mass and charge of electron, ω_s is the electron's natural frequency of oscillation according to semi-classical model, γ is the dissipative factor and *E* & ω are the electric field and frequency of the incident wave. For small amplitude oscillations of the electron the oscillation velocity is thus

$$v(r,t) = \frac{e}{m}\frac{1}{(\omega^2 - \omega_s^2) + i\gamma\omega}\frac{\partial E(r,t)}{\partial t} \tag{2.3}$$

Now the total current density *J*(*r*,*t*) of eqn. (2.1) must sum the contributions of all such bound electrons within an atom and sum over all atoms. If we restrict our interest to propagation only in the forward direction, the current density expression can be written as

$$J_0(r,t) = -en_a \textstyle\sum_s g_s\, v_s(r,t) \tag{2.4}$$

where, subscript zero signifies the special case of forward scattering, n_a is the average density of the atoms and the oscillator strengths for the various resonances sum to the total number of electrons per atom (*A*) i.e.,

$$\sum_s g_s = A$$

Combining equ. (2.4), eqn. (2.3) and eqn. (2.1) it can be written

$$\left[\left(1 - \frac{e^2 n_a}{\varepsilon_0 m}\sum_s \frac{g_s}{(\omega^2 - \omega_s^2) + i\gamma\omega}\right)\frac{\partial^2}{\partial t^2} - c^2\nabla^2\right]E(r,t) = 0 \tag{2.5}$$

which can be rewritten in the standard form of wave equation as

$$\left[\frac{\partial^2}{\partial t^2} - \frac{c^2}{n^2(\omega)}\nabla^2\right]E(r,t) = 0 \tag{2.6}$$

where, the frequency dependent refractive index $n(\omega)$ is defined as

$$n(\omega) = \left[1 - \frac{e^2 n_a}{\varepsilon_0 m}\sum_s \frac{g_s}{(\omega^2 - \omega_s^2) + i\gamma\omega}\right]^{1/2} \tag{2.7}$$

It can be shown that for soft X-ray ω^2 is very large compared to the quantity $e^2 n_a/\varepsilon_0 m$, so that to a high degree of accuracy the index of refraction can be written as

$$n(\omega) = 1 - \frac{1}{2}\frac{e^2 n_a}{\varepsilon_0 m}\sum_s \frac{g_s}{(\omega^2 - \omega_s^2) + i\gamma\omega} \tag{2.8}$$

This equation predicts both positive and negative dispersion, depending on whether the frequency ω is less or greater than resonant frequency ω_s. Fig. 2.1 describes a generic refractive index across the electromagnetic spectrum with resonances in the infrared (IR), ultraviolet (UV) and X-ray region.

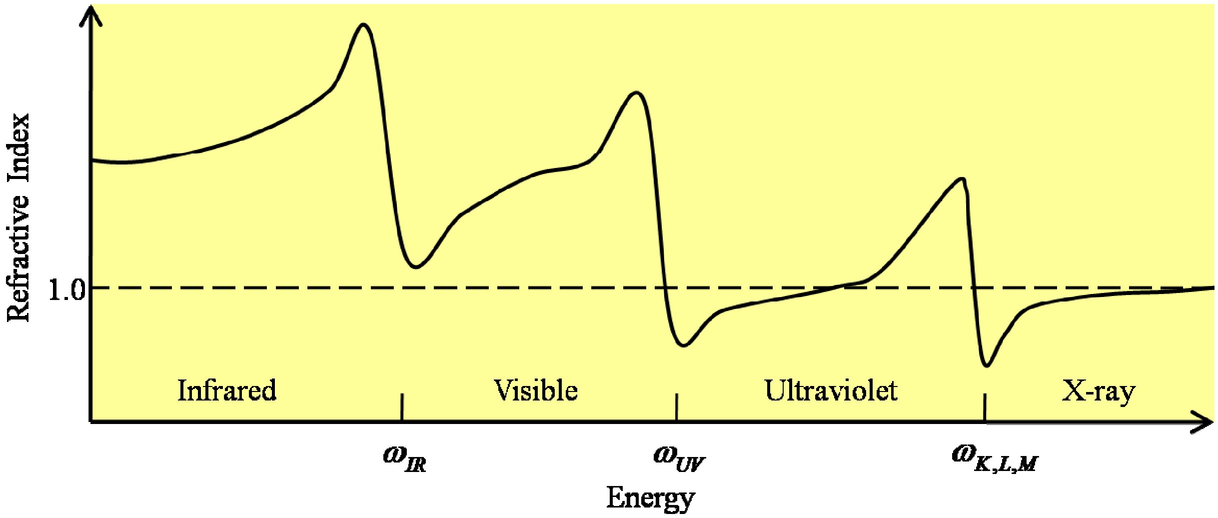

Fig. 2.1: Schematic variation of real part of refractive index in the whole electromagnetic spectrum range

The equ. (2.8) can be written in more simple form in terms of the classical electron radius

$$r_0 = \frac{e^2}{4\pi\varepsilon_0 mc^2}$$

and the complex atomic scattering factor (superscript zero)

$$f^0(\omega) = f_1^0(\omega) - if_2^0(\omega) = \sum_s \frac{g_s\omega^2}{(\omega^2-\omega_s^2)+i\gamma\omega}$$

With these substitutions, the refractive index of equ. (2.8) can be written as

$$n(\omega) = 1 - \frac{n_a r_0 \lambda^2}{2\pi}[f_1^0(\omega) - if_2^0(\omega)] \tag{2.9}$$

so commonly it is written as:

$$n = 1 - \delta + i\beta \tag{2.10}$$

where,

$$\left.\begin{aligned}\delta &= \frac{n_a r_0 \lambda^2}{2\pi} f_1^0(\omega)\\ \beta &= \frac{n_a r_0 \lambda^2}{2\pi} f_2^0(\omega)\end{aligned}\right\} \qquad (2.11)$$

These are very small quantities, for most of the material δ is ~10^{-5} and β is ~ 10^{-6}-10^{-7}. At high energy (larger than k-shell binding energy) $f_1^0 \approx A$, so δ depends on the atomic number A of the material. The β is related to the absorption coefficient (μ) of the material by $\mu = 4\pi\beta/\lambda$, where absorption coefficient is defined by a characteristics length μ^{-1} at which the X-ray beam is attenuated by e^{-1}. The source of this absorption is mostly dominated by the photoelectric ionization for energy less than 10KeV. In this case the energy of X-ray is transferred to the ejected electron. This absorption normally decreases with increasing energy of X-ray except at transition edge (K, L, M) where new photo ionization process starts and absorption increases sharply. At higher X-ray energies Thomson (elastic) and Compton (inelastic) scattering dominate and at very high energy (> 1 MeV) electron positron pair production starts.

2.2.2 Neutron refractive index

It is well known that the neutron can be described by a wave of wavelength λ, of wave vector k_0 and energy E_0 as:

$$k_0 = \frac{2\pi}{\lambda} \qquad (2.12a)$$

$$E_0 = \frac{\hbar^2 k_0^2}{2m} \qquad (2.12b)$$

Its wave function verifies the Schrödinger equation:

$$\frac{\hbar^2}{2m}\frac{d^2\Psi}{dr^2} + [E - V(r)]\Psi = 0 \qquad (2.13)$$

where, m is the neutron mass, E its energy and V the interaction potential. The neutron is a spin 1/2 particle. According to the energy of the neutron, it can be classified as hot, thermal and cold as shown in the Table-2.1. The wavelength of a thermal neutron (~10^{-10} m) is much greater than the size of a nucleus (10^{-14} to 10^{-15} m), which means that the nucleus can be considered as a point scatterer. If a neutron is scattered by a nucleus the resulting scattered wave is therefore spherically symmetric.

	Energy (meV)	Temperature (K)	Wavelength (Å)
Cold	0.1-10	1-120	4-30
Thermal	5-100	60-1000	1-4
Hot	100-500	1000-6000	0.4-1

Table-2.1: Energy, Temperature and wavelength of different neutron

Suppose that at an instant of time neutrons incident on a fixed nucleus is represented by $e^{ik.r}$, which is a plane wave of unit amplitude. The amplitude of the neutron wave scattered by the nucleus depends on the strength of the interaction between neutron and nucleus. Because the scattered wave is isotropic, its wave function can be written as $(-b/r)e^{ikr}$, if the scattering nucleus is at the origin of the coordinate system. The spherical wavefronts of the scattered neutrons are represented by the circle spreading out from the nucleus as shown in the Fig. 2.2. The constant b is referred to as the scattering length of the nucleus which is a measure of the strength of interaction between the neutron and the nucleus. The minus sign means that b is a positive number for repulsive interaction between neutron and nucleus. The scattering length is a complex quantity with the imaginary part corresponding to absorption of the neutron.

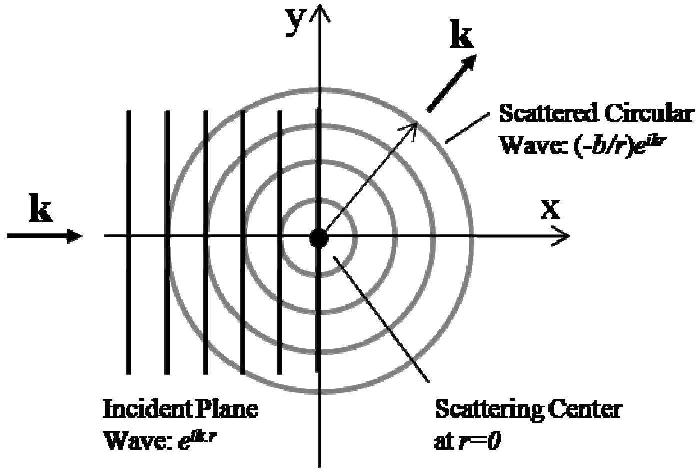

Fig. 2.2: A plane wave incident neutron beam and circular wave after scattering by a point source

It is assumed that the interaction between the neutron and the nucleus is only a small perturbation in the potential field of the system (the Born approximation), and only weakly perturbs the wavefunction outside the nucleus. The implication of this is that for a nucleus at a position, *r*, then any neutron with a wavevector not at that position will not be scattered. We can describe the interaction potential as a delta function, the "Fermi pseudopotential" given below is conventionally used, as it gives the required isotropic scattering.

$$V(r) = \left(\frac{2\pi\hbar^2}{m}\right) b\delta(r) \tag{2.14}$$

The scattering cross section is simply defined as the ratio of the number of neutrons scattered per unit time to the incident neutron flux

$$\sigma_{tot} = 4\pi b^2 \tag{2.15}$$

It is obvious that σ_{tot} has the units of area and the quanity *b,* which has an unit of length, is known as the scattering length, which defines the amplitude of the scattering. However, unlike X-ray scattering strength, it does not follow a systematic variation with atomic number. As shown in the Fig 2.3 the scattering length for elements that are next to each other in the periodic table (and even isotopes of the same element) can be very different and have to be defined empirically. This fact provides a means of distinguishing between individual species within a scattering sample, especially for studying light elements in the presence of much heavier ones, as in metal hydride systems or distinguishing between adjacent elements. Even scattering length of

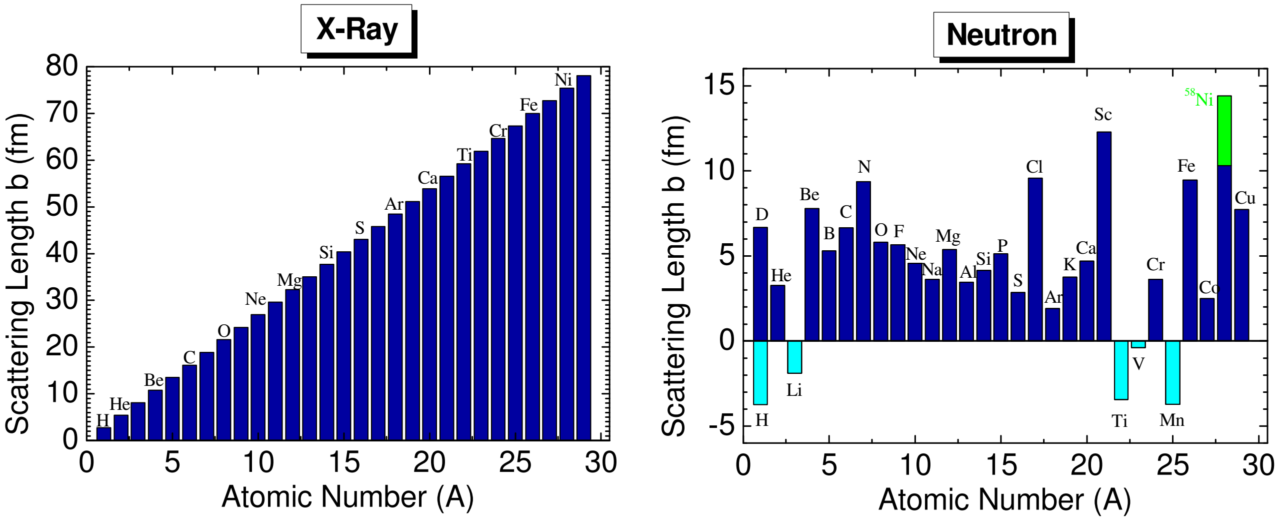

Fig. 2.3: Comparison of scattering length between X-ray and neutron

two isotopes of same element can be different, one of the famous example is Hydrogen and Deuterium. Presence of Deuterium can be realized in Hydrogen through neutron scattering which is not possible with X-ray.

$$V = \frac{1}{v}\int_v V(r)d^3r = \frac{2\pi\hbar^2}{m}\rho b \tag{2.16}$$

Now suppose a neutron of kinetic energy E_0 is moving from vacuum to a medium where it has kinetic energy E, then it can be written

$$E_0 = E + V \Rightarrow \frac{\hbar^2 k_0^2}{2m} = \frac{\hbar^2 k^2}{2m} + V$$

where k_0 and k are the wave vector in the vacuum and in the medium.

Now the neutron refractive index of the material can be written as

$$n = \frac{k}{k_0} = \sqrt{1 - \frac{2m}{\hbar^2}\frac{V}{k_0^2}} = \sqrt{1 - \frac{\lambda^2}{\pi}\rho b} \tag{2.17}$$

The quantity $1 - n$ is ~10^{-5} for most of the material, so the above equation can be written as:

$$n \approx 1 - \frac{\lambda^2}{2\pi}\rho b \tag{2.18}$$

where ρb is called Scattering Length Density (SLD) of the material.

In case of magnetic material along with nuclear interaction potential there is a magnetic interaction which is dipolar interaction of the neutron spin with the magnetic field created by the unpaired electrons of the magnetic atoms as shown in the Fig 2.4. This field contains two terms, the spin part and the orbital part:

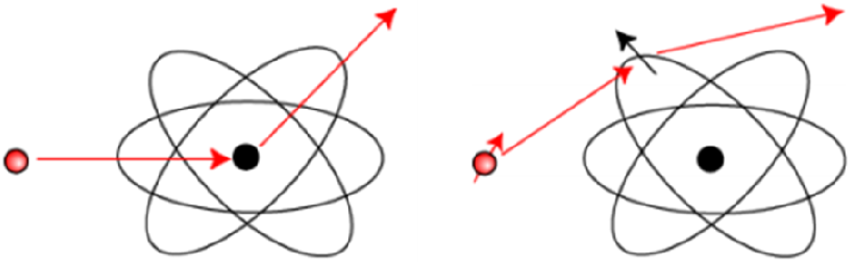

Fig. 2.4: Neutron nuclear scattering and neutron magnetic scattering

$$B = \frac{\mu_0}{4\pi}\left(\nabla \times \left\{\frac{\mu_e \times R}{|R|^3}\right\} - \frac{ev_e \times R}{|R|^3}\right) \tag{2.19}$$

where $\mu_e = -2\pi\mu_B\sigma$ is the magnetic moment of the electron, μ_B is the Bohr Magneton, v_e is the speed of electron.

The magnetic interaction potential is expressed as

$$V_m(r) = -\mu_n . B = \pm\mu_n B \tag{2.20}$$

where μ_n is the magnetic moment of neutron and ± refers to whether the neutron has a spin parallel or anti-parallel to the direction of the materials magnetic field, B.

Using eqn. (2.17) the neutron refractive index of a magnetic material can be written as:

$$n_{\pm} = 1 - \frac{\lambda^2}{2\pi}\left(\rho b \pm \frac{m\mu_n B}{2\pi\hbar^2}\right) \tag{2.21}$$

From the above expression, it is seen that the refractive index for neutrons is spin dependent. This property is extremely important and enables us to construct devices such as optical neutron polarizer, which allows one to select the neutron polarization which will be discussed later.

Thus it can be noted that the refractive index of neutron as shown in eqn. (2.18) and eqn. (2.21) can also be written similar to the refractive index of X-rays given by eqn. (2.10). Here the absorption of neutrons is described by the imaginary part of the scattering length (*b*). Except some material like Gd, Sm and Cd the absorption of neutron for most of the material is negligible. These elements present (*n,γ*) nuclear resonances at thermal neutron energies which strongly increase the absorption.

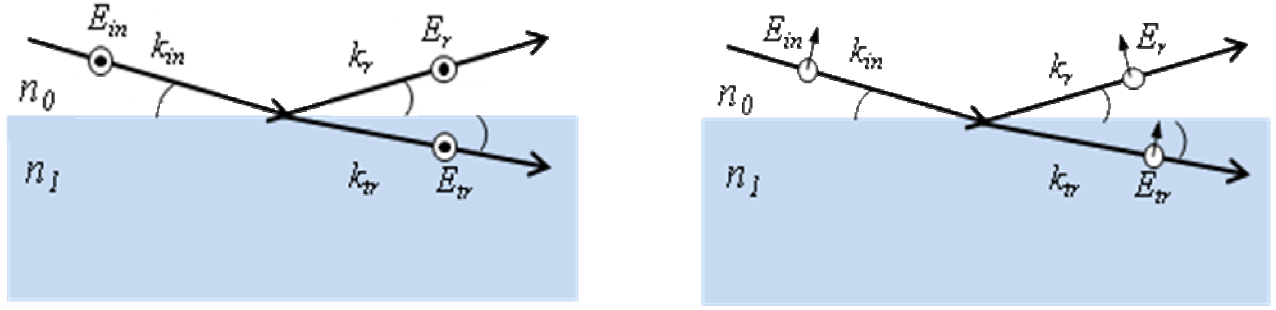

Fig. 2.5: Reflection of s-polaraized and p-polaraized light from a ideal surface

2.3 Theory of specular reflection

2.3.1 Specular reflection from an ideal surface: Fresnel reflectivity

The reflection and transmission coefficient in specular condition can be derived by writing the well known condition of continuity of electric and magnetic fields at the interface. The final expression of reflectivity of X-ray which is an electromagnetic wave is same as particle wave like neutron, so in the following derivation though the X-ray is considered only, similar expressions are applicable for neutron also.

The reflected intensity, which is the square of the modulus of the reflection coefficient, is the quantity measured in an experiment. Suppose that an X-ray wave is reflecting from an ideal surface which is at the interface of two semi infinite, isotropic medium having refractive index n_0 and n_1. As shown in the Fig. 2.5 there may be two different cases of s- and p-polarization. In the case of p-polarization electric field is parallel to the plane of incidence whereas in s-polarization, electric field is perpendicular to the plane of incidence.

If the incident ray is making a grazing angle (θ_i) with the surface then the grazing angle of reflection (θ_r) and transmission (θ_t) can be determined from Snell's Law

$$\theta_i = \theta_r \quad \text{and} \quad n_0 \cos\theta_i = n_1 \cos\theta_t \tag{2.22}$$

When X-ray is incident from vacuum ($n_0 = 1$) to a medium of refractive index $n = 1\text{-}\delta + i\beta$ ($n<1$) the X-ray will be completely reflected up to a critical angle θ_c which can be calculated from eqn. (1.22) putting $\theta_t = 0$,

$$\cos\theta_c = 1 - \delta \;\Rightarrow\; \theta_c = \sqrt{2\delta} \tag{2.23}$$

This phenomenon is called total external reflection, similar to total internal reflection observed in visible light. The position of the critical angle in X-ray reflectivity vs. angle of incidence plot of a sample gives a simple estimate of the electron density close to the surface of the sample.

The well known Fresnel's reflectivity of s- and p-polarization wave from a surface are as follows [48]:

$$r^s = \frac{n_0 \sin\theta_i - n_1 \sin\theta_t}{n_0 \sin\theta_i + n_1 \sin\theta_t} \tag{2.24}$$

$$r^p = \frac{n_0 \sin\theta_t - n_1 \sin\theta_i}{n_0 \sin\theta_t + n_1 \sin\theta_i} \tag{2.25}$$

It is easy to show that at small grazing angle of incidence for X-ray $r^p \approx r^s \approx r$. Though only s-polarization is considered for next calculations, however same is true for both and can be written as:

$$r(\theta_i) = \frac{n_0 \sin\theta_i - \sqrt{n_1^2 - n_0^2\cos^2\theta_i}}{n_0 \sin\theta_i + \sqrt{n_1^2 - n_0^2\cos^2\theta_i}} \tag{2.26}$$

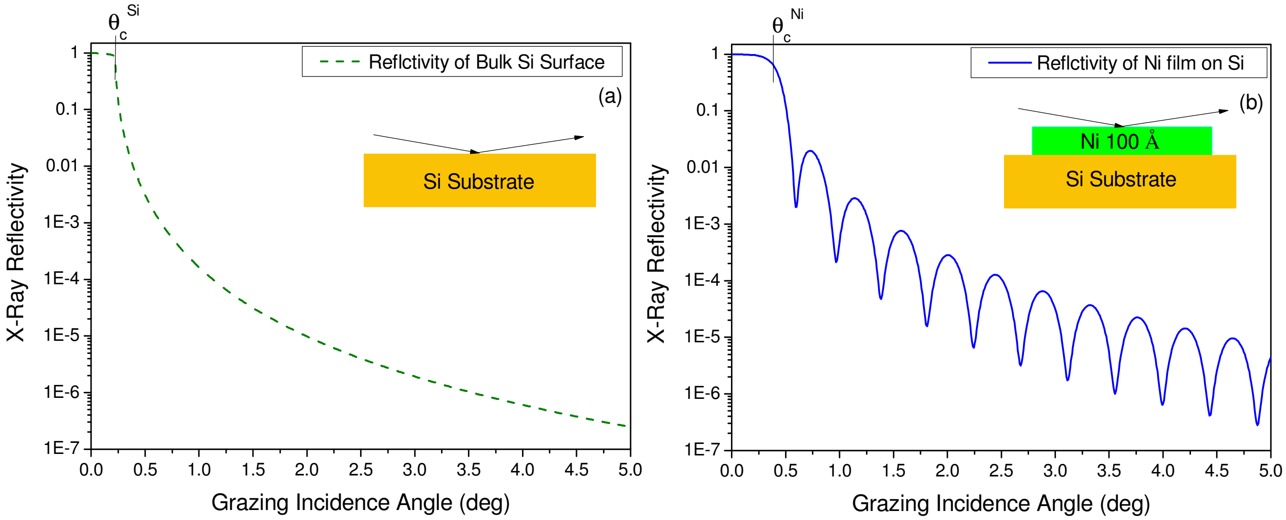

Fig. 2.6: X-ray reflectivity of Cu-Kα radiation from (a) silicon (Si) substrate and (b) a 100Å Nickel (Ni) film deposited on Si substrate

In the case of small incidence angle from vacuum it can be written:

$$\cos\theta_i = 1 - \theta_i^2/2$$

$$n^2 = 1 - 2\delta = 1 - \theta_c^2$$

where, absorption of X-ray in the medium is neglected. Finally using the above equation, reflectivity which is the square of the modulus of reflection coefficient becomes

$$R(\theta_i) = rr^* = \left|\frac{\theta_i - \sqrt{\theta_i^2 - \theta_c^2}}{\theta_i + \sqrt{\theta_i^2 - \theta_c^2}}\right|^2 \tag{2.27}$$

However if the absorption of the X-ray beam by the material is accounted for, the refractive index takes a complex value and the Fresnel reflectivity is then written by

$$R(\theta_i) = rr^* = \left|\frac{\theta_i - \sqrt{\theta_i^2 - \theta_c^2 - 2i\beta}}{\theta_i + \sqrt{\theta_i^2 - \theta_c^2 - 2i\beta}}\right|^2 \tag{2.28}$$

The same expression can be written in terms of wave vector transfer q = 4πsinθ/λ :

$$R(q_i) = rr^* = \left| \frac{q_i - \sqrt{q_i^2 - q_c^2 - \frac{32i\pi^2\beta}{\lambda^2}}}{q_i + \sqrt{q_i^2 - q_c^2 - \frac{32i\pi^2\beta}{\lambda^2}}} \right|^2$$

In the Fig 2.6 (a) the generated X-ray reflectivity of Cu-Kα radiation (wavelength 1.54Å) from a Si substrate is shown. Using the cut off angle the electron density as well as mater density can be measured using eqn, (2.23), similar for neutron reflectivity the scattering length b can be measured. It is seen that after the cut off the reflectivity drops very fast.

2.3.2 Reflection from a single layer film

Let us consider a thin film of refractive index n_1, thickness d, deposited on substrate of refractive index n_2 as shown in the Fig 2.7. An X-ray with wavelength λ¸ and amplitude E_0 is incident from the ambient (with refractive index n_0, usually the vacuum and $n_0 = 1$) on the layer with grazing angle of incidence θ_0, gets refracted in the layer with an angle θ_1 and subsequently in the substrate with an angle θ_2. At the first reflection, the reflected ray has an amplitude $r_{01}E_0$, and the transmitted one $t_{01}E_0$, where r_{01} and t_{01} are the Fresnel's reflection and transmission coefficient when X-ray is incident from medium 0 to medium 1. This transmitted beam will be reflected from the surface of the substrate and the reflected ray will have an amplitude $r_{12}t_{01}E_0$ (the transmitted ray in substrate is absorbed in the substrate by definition) where r_{12} is the reflection coefficient between medium 1 and 2. This reflected ray at the layer surface will be furthermore reflected in the layer and partially transmitted. The amplitudes of the reflected (in the layer) and refracted (in vacuum) are $r_{10}r_{12}t_{01}E_0 = -r_{01}r_{12}t_{01}E_0$ and $t_{10}r_{12}t_{01}E_0 = r_{12}(1-r^2_{01})E_0$. At this point both rays have a phase shift with respect to the incident one (see Fig. 2.7):

$$\Delta\phi = \frac{2\pi}{\lambda} 2n_1 d \sin\theta_1 \qquad (2.29)$$

Repeating all the steps with the reflected ray in the layer and taking into account the phase shift $\Delta\phi$ at each reflection on the substrate, and by summing all the reflected rays, the resulting reflected amplitude is:

$$E_r = E_0\left[r_{01} + r_{12}(1 - r_{01}^2)e^{-i\Delta\phi} - r_{01}r_{12}^2(1 - r_{01}^2)e^{-2i\Delta\phi} + r_{01}^2 r_{12}^3(1 - r_{01}^2)e^{-3i\Delta\phi} \ldots\right] \quad (2.30)$$

By summing the geometric series the complex amplitude of reflection can be found:

$$r_{total} = \frac{r_{01} + r_{12}e^{-i\Delta\phi}}{1 + r_{01}r_{12}e^{-i\Delta\phi}} \quad (2.31)$$

In Fig 2.6(b) the theoretically generated X-ray reflectivity plot of Cu-Kα radiation (wavelength 1.54Å) with respect to the grazing incidence angle for a 100Å thin film of Ni on a Si substrate is shown.

The fringe pattern observed in the spectrum is due to the thickness of the film. When X-ray reflected from the top of the film and from bottom of the film interfere destructively then the minima in the reflectivity is observed and on the other hand, when they interfere constructively a maxima is observed. So from the width of the fringe the thickness of the film can be determined. This interference fringes are also called Kiessig fringes [49], named after the author of first experimental report. Here also from the cut-off angle the density of the Ni film can be measured from eqn. (2.23).

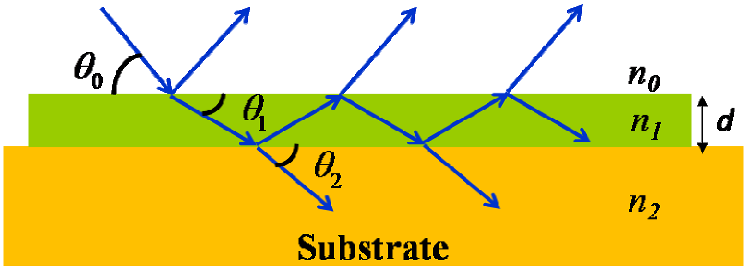

Fig. 2.7: Reflection and refraction of X-ray from a single layer film on a substrate

2.3.3 Reflectivity of multilayer thin film

Periodic multilayer reflectivity: The Bragg law

A periodic multilayer is basically repetition of identical bilayers, each of them being a superposition of thin films with a large refractive index contrast; in case of X-ray it is a contrast in electron density whereas in case of neutron it is a contrast in scattering length density. The typical pairs for X-ray are Mo/Si, W/Si, W/C, Ni/C, W/B_4C etc. whereas, for neutron the widely used pair is Ni/Ti.

As shown in Fig. 2.8 the thickness of the two materials are indicated with symbol d_A and d_B and their corresponding refractive indices are $n_A=1-\delta_A+i\beta_A$ and $n_B=1-\delta_B+i\beta_B$ respectively. The constant bi-layer thickness is called the multilayer period $d=d_A + d_B$, and the Γ factor is defined as the ratio $\Gamma=d_A/d$ ($0<\Gamma<1$). The multilayer is deposited on to a thick substrate of refractive index n_S.

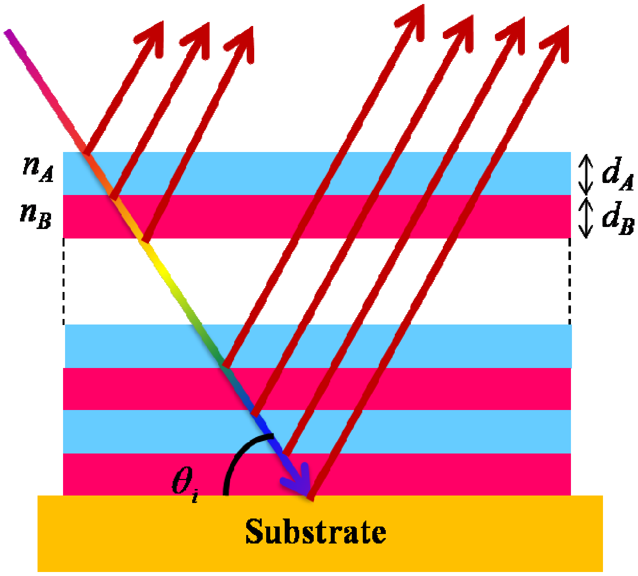

Fig. 2.8: Structure of a periodic multilayer

A periodic multilayer has the interesting property of reflecting X-rays or neutron with a (theoretical) reflectivity close to 100% at larger angles than the critical angles of its materials, where a single interface would have a reflectivity

$$|r_{AB}|^2 = \frac{(\delta_A - \delta_B)^2}{4\sin^2\theta_i} \tag{2.32}$$

of the order of 10^{-2}, and quickly decaying with increasing energy of X-ray. However, in case of a periodic multilayer, because of large number of layers and constructive interference between the waves reflected from each interface when the phase difference is

$$\Delta\phi = \frac{2\pi}{\lambda} 2d \sin\theta_i = 2m\pi \tag{2.33}$$

the film will show narrow reflectivity peak at the condition:

$$2d \sin\theta_i = m\lambda \tag{2.34}$$

where, m is an integer.

Eqn. (2.34) is the Bragg law and it is the most practical approximate formula to evaluate the angular positions of reflectivity peaks (Bragg peaks) of a periodic multilayer. Since the behavior of a periodic multilayer structure is similar to that of crystals, it could be said that a periodic multilayer is an imitation of the crystalline structures made by the nature.

However in practical multilayer mirror due to refraction at the interface the path of waves

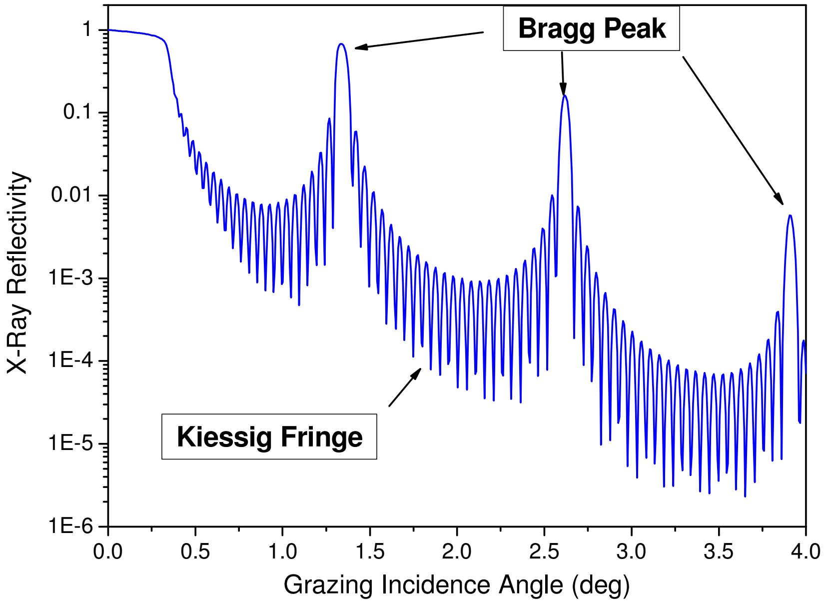

Fig. 2.9: X-ray reflectivity at 1.54Å of a 25 bilayer W/Si multilayer on Si substrate having thickness of W layer 10Å and Si layer 24Å (right)

will be also different. So condition for constructive interference for each bilayer will be,

$$\Delta\phi = \frac{2\pi}{\lambda}(2n_A d_A \sin\theta_A + 2n_B d_B \sin\theta_B) = 2m\pi \tag{2.35}$$

where, θ_A and $\theta_B$are grazing incidence angle in medium *A* and *B* respectively. Using Snell's Law it can be written

$$\cos\theta_i = n_A \cos\theta_A = n_B \cos\theta_B \tag{2.36}$$

Then

$$n_A \sin\theta_A = (n_A^2 - n_A^2 \cos^2\theta_A)^{1/2} = (n_A^2 - \cos^2\theta_i)^{1/2} \tag{2.37}$$

and the same for $n_B \sin\theta_B$. Approximating $n_A^2 \approx 1 - 2\delta_A$, $n_B^2 \approx 1 - 2\delta_B$ the equation (2.35) becomes

$$2d_A(\sin^2\theta_i - 2\delta_A)^{1/2} + 2d_B(\sin^2\theta_i - 2\delta_B)^{1/2} = m\lambda$$

and using the definition of Γ,

$$2d\sin\theta_i\left[\Gamma\left(1 - 2\frac{\delta_A}{\sin^2\theta_i}\right)^{1/2} + (1-\Gamma)\left(1 - 2\frac{\delta_B}{\sin^2\theta_i}\right)^{1/2}\right] = m\lambda \tag{2.38}$$

Now since, $\sqrt{2\delta_A}$ and $\sqrt{2\delta_B}$ are the critical angles of the two materials of the multilayer and the Bragg peaks are observed always at $\sin^2\theta_i \gg 2\delta_A, 2\delta_B$, so it can be approximated as:

$$\Gamma\left(1 - 2\frac{\delta_A}{\sin^2\theta_i}\right)^{1/2} + (1-\Gamma)\left(1 - 2\frac{\delta_B}{\sin^2\theta_i}\right)^{1/2} \approx \left(1 - 2\frac{\Gamma\delta_A + (1-\Gamma)\delta_B}{\sin^2\theta_i}\right)^{1/2}$$

and so we obtained the refraction-corrected Bragg Law

$$2d\sin\theta_i\sqrt{1 - 2\frac{\Gamma\delta_A + (1-\Gamma)\delta_B}{\sin^2\theta_i}} = m\lambda \tag{2.39}$$

which allows to locate the exact position of the Bragg peaks.

In Fig 2.9 X-ray reflectivity of a 25 layer W/Si multilayer of 34Å bilayer thickness is shown. Three narrow Bragg peaks are observed in this spectrum. The first Bragg peak is observed at 1.33°, however according to eqn. (2.34) it should be observed at 1.29°. The small fringe observed in the Fig 2.9 is called Kiessig fringe [49] which appears due to the total thickness of the multilayer.

Non-periodic multilayer reflectivity

As shown in the Fig 2.9 a periodic multilayer can give high reflectivity at a particular angle of incidence for a particular wavelength. However, on deviating from this angle and wavelength the reflectivity falls drastically. So in order to achieve high reflectivity in a broad angular or wavelength region, non-periodic or graded multilayer is necessary. If the thickness of this multilayer vary in such a fashion (as shown in Fig 2.10) that the Bragg peaks obtained in different part of multilayer structure overlap with each other, then a continuous band of high reflectivity is achieved as shown in the Fig 2.11. Such a multilayer which generally consists of hundred of bi-layers with graded thickness is called a supermirror [10]. In case of X-rays such supermirrors are used in astrophysical application whereas neutron supermirrors are widely used in transporting thermal and cold neutrons by hundreds of meter in neutron guide tube in place of single layer Ni film to improve the transmission [50]. Thus a neutron supermirror is basically a non-periodic multilayer of two alternate materials having large

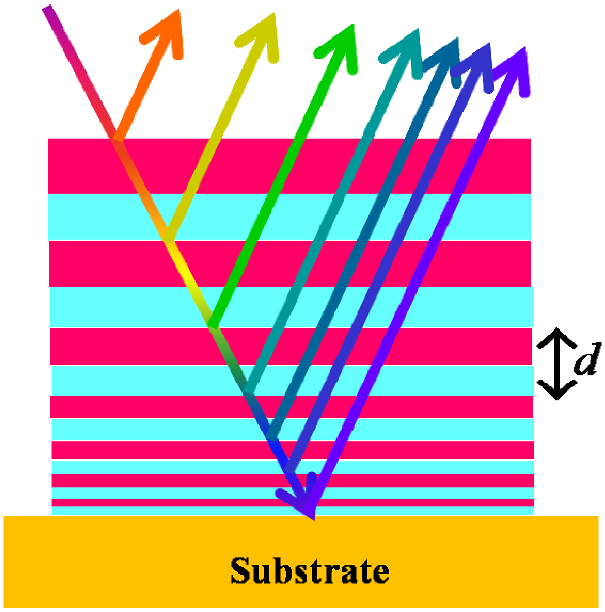

Fig. 2.10: Structure of a supermirror

difference in their neutron scattering lengths like Ni and Ti with varying layer thickness from ~40 Å to 500 Å, which can extend the region of total reflection to a large extent from the critical angle value of the individual layers. The region up to which the critical angle is extended is represented by its *m*-value which is equal to the ratio of critical angle of supermirror and critical angle of Ni, i.e.,

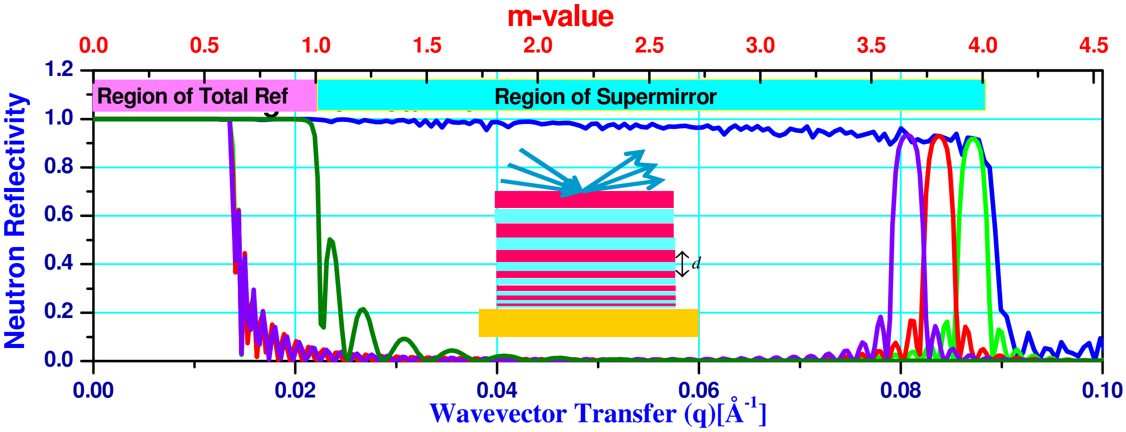

Fig. 2.11: Neutron reflectivity of a *m*=4.0 (956 layer) Ni/Ti supermirror at 4Å wavelength

$$m = \theta_c^{Sup}/\theta_c^{Ni} \tag{2.40}$$

In Fig. 2.11, the reflectivity pattern of a m=4.0 Ni/Ti supermirror is shown for 4Å neutron wavelength. This supermirror was first conceptualized and developed by Mezei [10], later the design structure proposed by Hayter and Mook [50] are widely used which will be discussed in details later.

Thin multilayer supermirrors where the alternate layers are ferromagnetic and non-magnetic can also be used to polarize neutrons and in that case it is called a supermirror polarizer. As shown in eq. (2.21) for a magnetic material the expression for refractive index is modified as follows:

$$n_{\pm} = 1 - \frac{\lambda^2}{2\pi}\rho(b \pm p) \tag{2.41}$$

where, p is the magnetic scattering length. The combination of the two materials (1 and 2) will be such that in the presence of magnetic field parallel to the film surface, the neutron spin parallel to the magnetization will see very large neutron scattering length contrast (i.e., $b_1 + p\rangle\rangle b_2$) between the alternate layers and reflectivity of the supermirror for these neutrons will be very high. However neutrons having spin anti-parallel to the magnetization will have negligible neutron scattering length density contrast between the alternate layers (i.e., $b_1 - p \approx b_2$) and they will pass through the supermirror with very low reflection. In Fig 2.12 the scattering length contrast of Co and Ti for neutrons having spin parallel to the magnetic field and anti parallel to the magnetic field are shown. The simulated neutron reflectivities of a typical Co/Ti supermirror polarizer for both the polarizations are shown in Fig 2.13. In this figure, it is clearly seen that at slightly higher grazing angle of incidence, this can be used as neutron polarizer or analyzer. Fe/Si, Fe/Ge, FeCoV/TiN are some other commonly used material combinations of magnetic/non-magnetic layers for

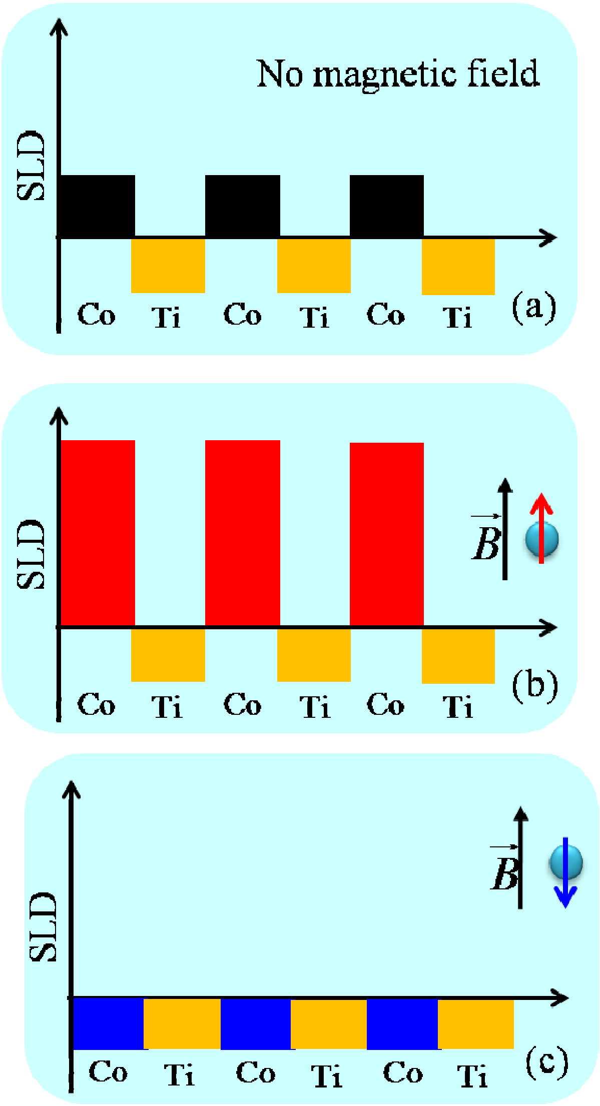

Fig. 2.12: Scattering length contrast of Co/Ti (a) without magnetic field (b) neutron spin parallel to magnetic field (c) neutron spin anti-parallel to magnetic field

realizing thin film supermirror neutron polarizer or analyzer for studying the magnetic property of materials and for use in inelastic neutron scattering experiments [20, 21].

2.3.4 Multilayer reflectivity calculation

There are several methods for calculating the reflectivity of the multilayer. The Fourier method and the matrix method are discussed in Appendix A. The most commonly used method i.e., recursive method is discussed here.

Recursive method: Parratt formalism

To be able to calculate the actual reflectivity of any structure, the Fourier method is not appropriate, since it does not take into account the absorption and multiple reflections in the structure. However recursive calculation method which is well known as Parratt Formalism [51] takes care of this. In this method, the total reflected amplitude r_f of a film on top of another structure is determined by the reflected amplitude r_t of the top interface, to be calculated using eq. (2.31) and the reflected amplitude r_b of the structure underneath:

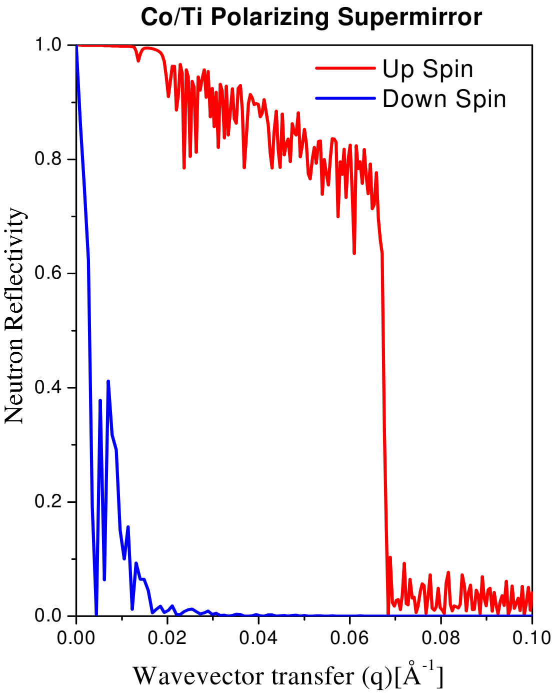

Fig. 2.13: Up spin and down spin reflectivity of a typical Co/Ti supermirror polarizer

$$r_f = \frac{r_t + r_b e^{2i\varphi_j}}{1 + r_t r_b e^{2i\varphi_j}} \tag{2.42}$$

where $\varphi_j = \frac{2\pi}{\lambda} d_j n_j \sin\theta_j$ represents the phase delay produced by the propagation of the wave through the j^{th} film with a thickness d_j and a refractive index n_j. θ_j is the (grazing) angle of the wave within this layer, to be calculated using Snell's law. The reflected amplitude r_b of the structure underneath can recursively be calculated by sub-dividing this structure in another layer on top of the remaining structure, until only one layer on top of the substrate remains. In this last iteration r_b equals the Fresnel reflectivity of the substrate (eq. 2.28).

Since this method includes the influence of absorption by means of the complex part of the refractive index n_j, it gives the exact solution for structures that can be described using sharp boundaries between all layers.

2.3.5 Specular reflection from a real surface

So far in the above formulation, it is considered that the surface of reflection is perfectly flat, however in practice, any surface cannot be perfectly flat. Moreover, in real thin film systems, the interface between the two media or between two layers is neither perfectly smooth nor chemically sharp. As shown in Fig 2.14 there may be two distinct features at the interface between two layers. In one case, represented by the schematic in Fig 2.14(a) physical height of the surface is varying. In that case, if the height at any point is $z(x,y)$, then the surface can be characterized by root mean square (RMS) roughness (σ) in the following way:

$$\sigma^2 = \frac{1}{L}\int_0^L [z(x,y) - z_0]^2 dx \tag{2.43}$$

where, z_0 is the mean height and the integration is performed over a length scale L. In the other

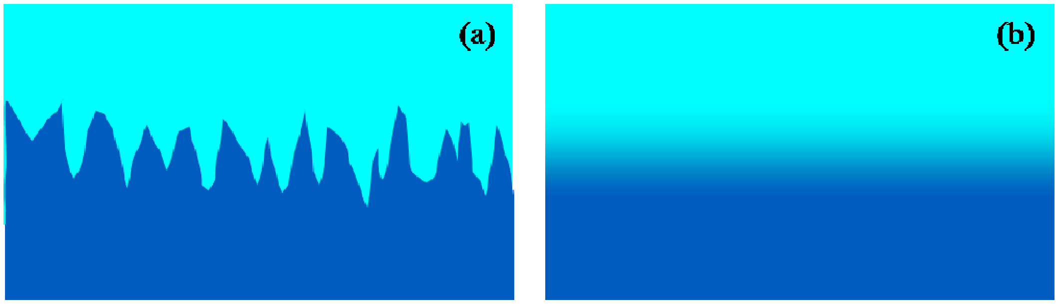

Fig. 2.14: Real surface (a) Physically the height of the surface is varying (b) Density of the interface is changing from one medium to other

case (Fig 2.14(b)) the density of the medium at the interface is changing gradually instead of sharply which is a very usual phenomena in a practical interface between two layers in a thin film multilayer due to diffusion of one material into the other. This can be characterized by the total width of graded region. As in both of the above cases, the refractive index of the medium is varying with depth, z so the specular reflectivity which is sensitive to average refractive index cannot distinguish between the two.

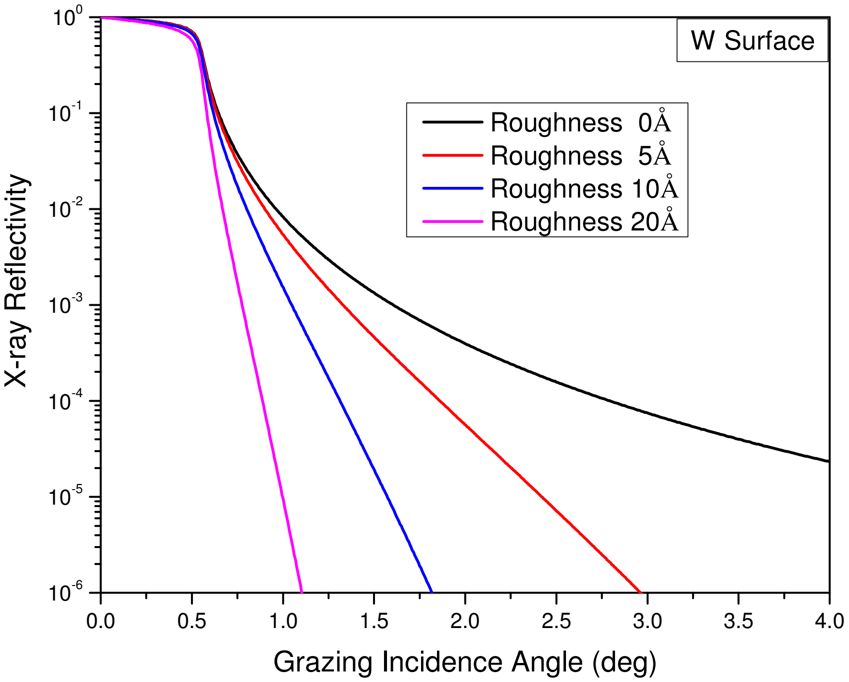

Fig. 2.15: Effect of surface roughness on x-ray reflectivity of tungsten (W) surface

As over an extended interface the phase of the reflected wave will only vary, so it can be shown that for a real interface the master formula for reflection will be:

$$R(q_i) = R_F(q_i)\left|\int_{-\infty}^{+\infty} \frac{d\rho}{dz} e^{iq_i z} dz\right|^2 \tag{2.44}$$

where R_F is the Fresnel's reflectivity of the ideal surface and ρ is the electron density. The above equation tells that the ratio between the actual reflectivity and that for an ideal sharp interface is the absolute square of the Fourier transform of the normalized gradient of the density across the interface.

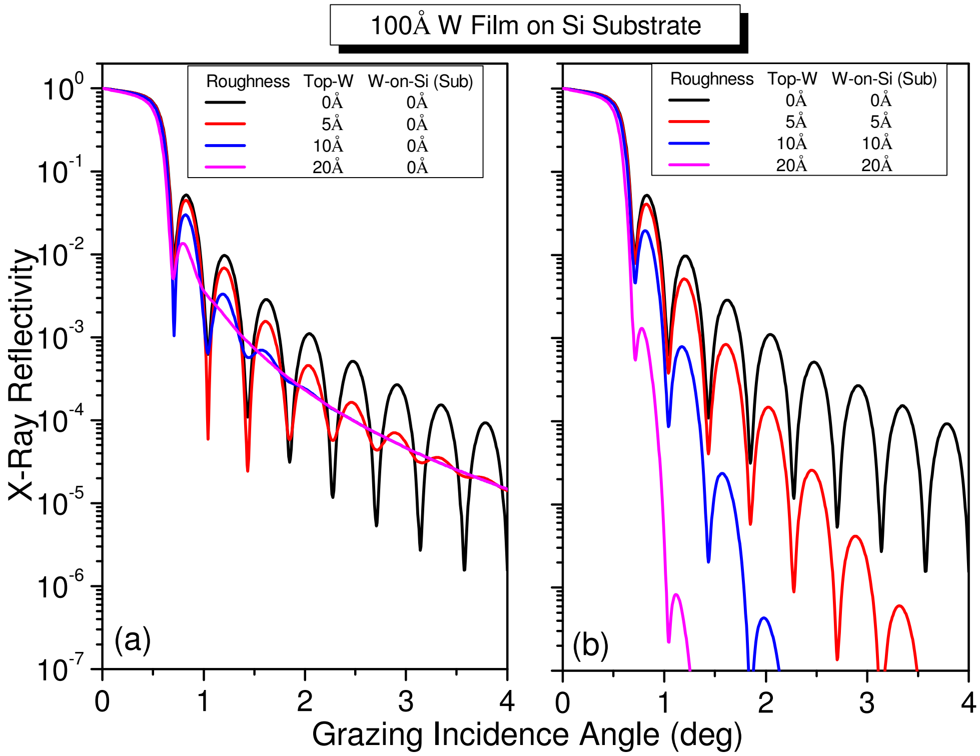

Fig. 2.16: Effect of surface roughness on x-ray reflectivity of 100Å tungsten (W) film deposited on silicon (Si) substrate (a) Top W surface roughness is varying keeping W-on-Si substrate interface roughness 0Å (b) Top W surface roughness and W-on-Si substrate interface roughness both are varying

If we consider that at the interface the electron density is an error function i.e., $\rho(z) = erf\left(\frac{z}{\sqrt{2}\sigma}\right)$ where, σ is the width of the graded region then the derivative of the error function will be a Gaussian given by:

$$\frac{d\rho}{dz} = \frac{1}{\sqrt{2\pi\sigma^2}} e^{-\frac{1}{2}\left(\frac{z}{\sigma}\right)^2}$$

and it can be shown that the Fourier transform of it will be another Gaussian, $e^{-q^2\sigma^2/2}$. So the reflected intensity can be written as

$$R(q_i) = R_F(q_i)e^{-q_i^2\sigma^2} \tag{2.45}$$

In case when the physical roughness and the roughness due to inter-diffusion both are present in an interface then σ of eq. (2.45) will be total roughness i.e.

$$\sigma_{total} = \sqrt{\sigma_{physical}^2 + \sigma_{diffusion}^2} \tag{2.46}$$

In a multilayer of alternate magnetic and non magnetic materials, due to non magnetization of magnetic material at the interface region, there may be a third type of roughness for polarized neutrons which is known as magnetic roughness [52]. It also has similar effect on reflectivity as shown in eqn. (2.45).

The eqn. (2.45) is known as Debye-Waller formula [4], which gives the reflectivity of X-ray or neutron from a surface with roughness. Fig 2.15 shows how X-ray reflectivity of a W surface falls off as the roughness of the surface increases. In connection with it, Névot and Croce [53] pointed out that the eqn. (2.45) violates time reversal and therefore it is incorrect. The correct solution is

$$R(q_i) = R_F(q_i)e^{-q_i q_t \sigma^2} \tag{2.47}$$

where, q_t is the wave vector transfer of the transmitted beam. Later it is concluded that neither form is universally correct, though practical difference is very minor. De Boer [46] pointed out that the Névot-Croce term is more valid around the critical angle and for high spatial frequencies of roughness, while the Debye-Waller form is more applicable for other regimes.

Similarly the reflectivity of thin film and multilayer will also be reduced due to the roughness of the top surface and the roughness of the buried interfaces. In this case the total reflectivity is calculated by replacing the Fresnel's reflectivity of each interface with the eqn.

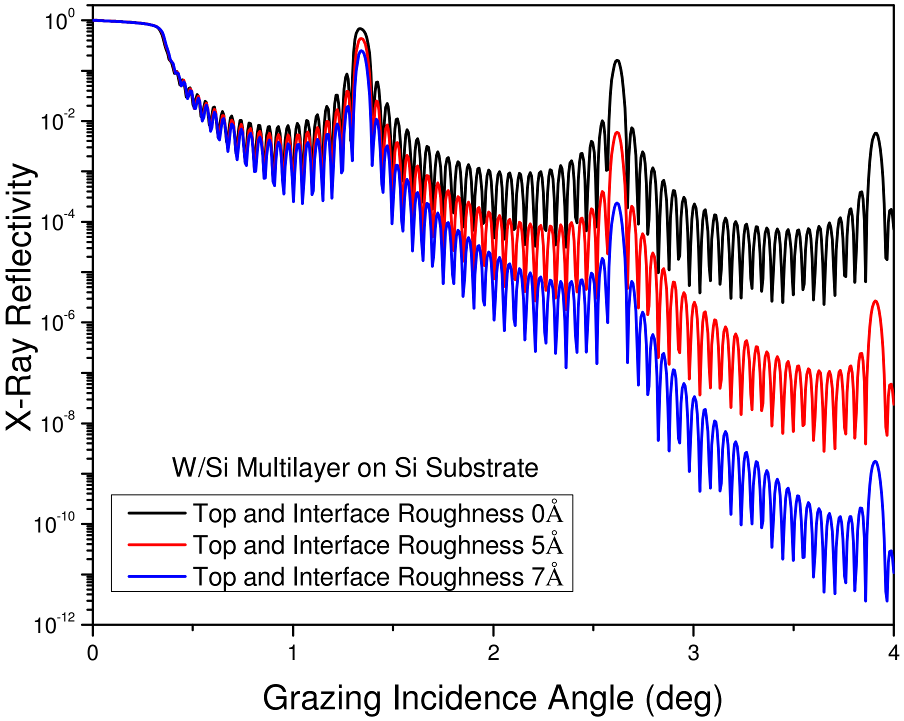

Fig. 2.17: Effect of top surface roughness and interface roughness on x-ray reflectivity of W/Si multilayer of 25 bilayer with10Å and 24Å W and Si layer thickness respectively

(2.45) or eqn. (2.47). In Fig. 2.16 the effect of roughness on X-ray reflectivity (at 1.54Ǻ) of a 100Å W film deposited on Si substrate is shown. In case of Fig. 2.16(a) the top W surface roughness is varying from 0 to 20Å keeping W on Si interface roughness as ideal. It is seen that with the increase in roughness the reflectivity decreases and the contrast of the fringe of reflectivity is vanishing. When the interface roughness also increases, the total reflectivity falls off drastically as shown in Fig 2.16(b). Similarly in Fig. 2.17 the effect of top and interface roughness on multilayer reflectivity is shown for the W/Si multilayer described in Fig. 2.9. It is clear that with the increase in interface roughness the reflectivity at Bragg Peak decreases rapidly, even 5Å average roughness is quite high for this multilayer.

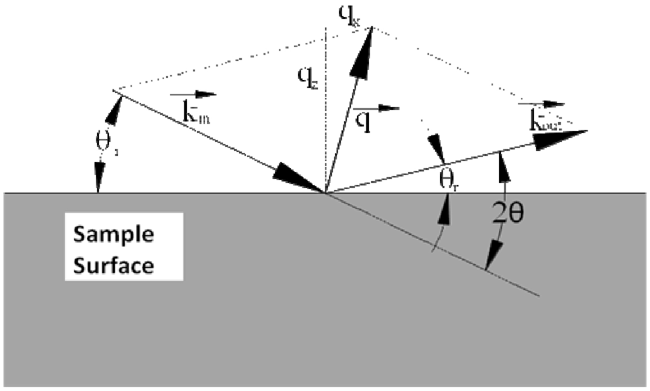

Fig. 2.18: Scattering Geometry

2.4 Theory of non-specular reflectivity

Let us consider that in a scattering experiment as shown in Fig. 2.18, an incident wave vector (k_{in}) makes an angle θ_i with the surface, and in the same scattering plane the scattered wave vector (k_{out}) makes an angle θ_r (=$2\theta - \theta_i$) with the surface where 2θ is called scattering angle which is the angle of the detector in the scattering plane relative to the incident beam. For elastic scattering, k_{in} and k_{out} have same magnitudes: $|k|=2\pi/\lambda$. However the scattering vector q which is the difference between the k_{in} and k_{out} is given below:

$$q_x = |2k| \sin\left(\frac{2\theta}{2}\right) \sin\left(\theta_i - \frac{2\theta}{2}\right) \tag{2.48}$$

$$q_z = |2k| \sin\left(\frac{2\theta}{2}\right) \cos\left(\theta_i - \frac{2\theta}{2}\right) \tag{2.49}$$

So in a specular reflectivity scan when incident and exit angles are same i.e. $\theta_i = \frac{2\theta}{2}$ only q_z is scanned with q_x=0. In this case only the structure normal to the sample surface is probed. However in order to probe in-plane sample structure q_x need to be scanned which is called non-specular reflectivity scan.

The non-specular reflectivity measurement scan can be performed in three different scattering geometries as following:

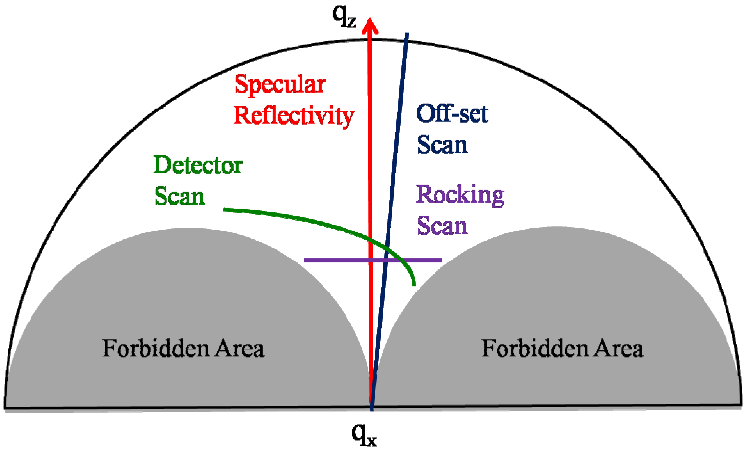

Fig. 2.19: Trajectory of scanning of scattering vector during specular and non specular measurements

- **Rocking scan:** It refers to the case of a measurement of the non-specular reflected intensity wherein the detector is held fixed relative to the incident beam, and the sample is rotated, or 'rocked', with respect to the incident beam. In this case, both the angle of incidence θ_i and the scattering angle 2θ vary simultaneously.
- **Detector scan:** It refers to the case wherein the sample is fixed relative to the incident beam, and the detector is varied. Thus θ_i is constant, while scattering angle 2θ is varied.
- **Offset scan:** Here the sample and detector are both rotated, with the detector offset from the specular direction by a constant offset angle, i.e., 2θ - θ_i =constant.

The trajectories of the scattering vector for the above three nonspecular scans along with specular scan are shown in the Fig. 2.19.

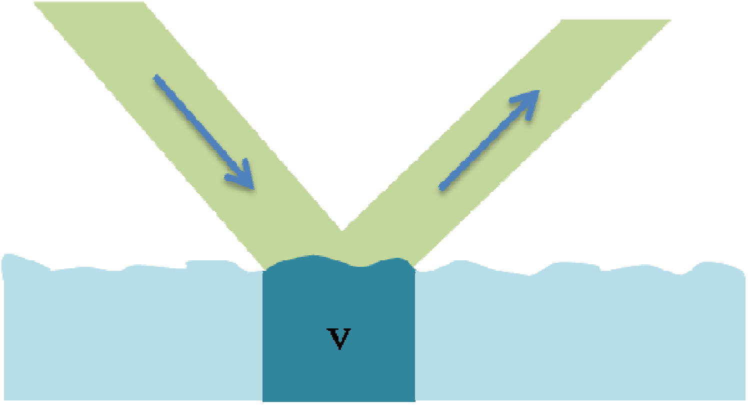

Fig. 2.20: Scattering from a rough surface

2.4.1 Scattering in kinematical approach: Born Approximation (BA)

In Born Approximation (BA) for calculating scattering of neutrons or X-ray only scattering from separate particle is considered and neglecting the processes of extinction, refraction and multiple scattering. This assumption is valid in the weak scattering region which is far from the angular region of the critical angle of total external reflection, where scattering is strong and multiple scattering cannot be neglected. Here scattering amplitude can be modeled as the Fourier transform of the scattering potential which simplifies the mathematical description to a large extent.

Let us consider an X-ray beam illuminating a semi-infinite slab at a grazing angle of incidence as shown in Fig 2.20 where the incident beam illuminates a volume *V* of the sample. Summing the scattering from all the volume elements *dV* and taking into account the phase factors, the total scattered amplitude r_V can be calculated as:

$$r_V(q) = -\, r_0 \int_V \rho(r) e^{iq.r} dV$$

where, $\rho(r)dV$ is the total number of electrons within the volume dV centered at r and r_0 is the Thomson's Scattering length, or classical electron radius as described in eqn. (2.9).

This volume integral can be converted to surface integral using Gauss's theorem and considering that the uppermost surface only contributes to the scattering, it can be written as:

$$r_V(q) = -\, r_0\rho\left(\frac{1}{iq_z}\right)\int_S e^{i(q_x x+q_y y)}.\, e^{iq_z Z(x,y)}dxdy$$

where, *Z*(*x,y*) is the height of the surface at (*x,y*) point. Now the scattering cross-section $d\sigma/d\Omega$ which is the absolute square of the scattering amplitude can be written as [4]:

$$\left(\frac{d\sigma}{d\Omega}\right) = \left(\frac{r_0\rho}{q_z}\right)^2\left(\frac{A}{\sin\alpha_i}\right)\int_S exp\{i[q_x x+q_y y]\}.\langle exp\{iq_z[Z(0,0)-Z(x,y)]\}\rangle dxdy$$

where, $A/\sin\alpha_i$ is the illuminated surface area. It is assumed that the surface is homogeneous such that only the relative coordinate between two points $(x-x', y-y') = (X,Y)$ are relevant. Using this relative coordinates, a statistical height difference function is introduced,

$$g(X,Y) = \langle[Z(0,0)-Z(x,y)]^2\rangle \qquad (2.50)$$

Now considering this function as Gaussian, cross section can be written as:

$$\left(\frac{d\sigma}{d\Omega}\right) = \left(\frac{r_0\rho}{q_z}\right)^2\left(\frac{A}{\sin\alpha_i}\right)\int_S exp\{i[q_x X+q_y Y]\}.\, exp\{-q_z^2 g(X,Y)/2\}dxdy \qquad (2.51)$$

Now let us consider some special cases.

(I) Ideal surface: Perfectly flat

In this case $g(X,Y) = 0$ and the scattering cross section will give Fresnel's Reflectivity:

$$\left(\frac{d\sigma}{d\Omega}\right)_{Fresnel} = \left(\frac{r_0\rho}{q_z}\right)^2\left(\frac{A}{\sin\alpha_i}\right)\delta(q_x)\delta(q_y) \qquad (2.52)$$

Which, describes an infinitely sharp specular reflection at $q_x = q_y = 0$.

(II) Rough and completely uncorrelated surface

In this case the height of two points separated by (X,Y) are statistically independent no matter how close together they are. So the height difference function of eqn. (2.50) become

$$g(X,Y) = \langle [Z(0,0) - Z(x,y)]^2 \rangle = \langle Z(0,0) \rangle^2 + \langle Z(X,Y) \rangle^2 + 2\langle Z(0,0) \rangle \langle Z(X,Y) \rangle = 2\sigma^2$$

In that case the expression for scattering cross-section of a rough surface becomes

$$\left(\frac{d\sigma}{d\Omega}\right)_{\substack{Rough \\ Uncorrelated}} = \left(\frac{d\sigma}{d\Omega}\right)_{Fresnel} exp(-q_z^2\sigma^2) \tag{2.53}$$

The eqn. (2.53) is similar to Fresnel's reflectivity given by eqn. (2.52) with a damping term $e^{-q_z^2\sigma^2}$ of total interface width containing physical roughness and interface diffusion.

(III) Rough surface: without cut-off

Let us consider a rough self-affine fractal surface which is self similar in different in-plane length scales, which can be happen in actual atomic scale thin film deposition process. As introduced by Sinha et. al [54], in this case the height difference function g(R) is given by

$$g(R) = AR^{2h}$$

where $R = \sqrt{X^2 + Y^2}$ and h is the Hurst exponent or Hurst constant, $0<h<1$, describes the jaggedness of the surface.

So the scattering cross section for this surface

$$\left(\frac{d\sigma}{d\Omega}\right)_{\substack{Rough \\ without\, cut-off}} = \left(\frac{r_0\rho}{q_z}\right)^2 \left(\frac{A}{\sin\alpha_i}\right) \int_0^\infty Rexp\left\{-\frac{A}{2}q_z^2R^{2h}\right\} J_0(q_rR)dR \tag{2.54}$$

where $q_r = \sqrt{q_x^2 + q_y^2}$ and J_0 is the Bessel function. The eqn. can be solved analytically for some special case h=0.5 and h=1.0 only.

(IV) Rough surface: with cut-off

The perfect self-affinity is unphysical, as for h>0.5, $g(R)$ diverges for large value of R. Practically there will be cut off and a saturation roughness σ.

So Sinha et al [54] proposed a modified form for $g(R)$:

$$g(R) = 2\sigma^2[1 - exp(-(R/\xi)^{2h})] \tag{2.55}$$

where, ξ is the correlation length or in plane cut-off length for self-affinity. It can be shown for large values of R, $g(R) \rightarrow \sigma^2$, whereas for small R, $g(R) \rightarrow R^{2h}$.

Surface can also be characterized by a correlation function $C(R)$ instead of height-height difference function, such as:

$$C(R) = \langle Z(0,0)Z(x,y)\rangle = \sigma^2 - g(R)/2 \tag{2.56}$$

Appling the both form of equation Sinha et.al [54] has calculated the scattering cross section, which can be written as:

$$\left(\frac{d\sigma}{d\Omega}\right)_{\substack{Rough \\ with\,cut-off}} = \left(\frac{r_0\rho}{q_z}\right)^2\left(\frac{A}{\sin\alpha_i}\right) exp\{-q_z^2\sigma^2\}\int_S exp\{-i(q_rR)\}\, exp\{q_z^2C(R)\}dxdy$$

This is summation of specular and diffuse components. Subtracting the specular component given by eqn (2.52) the diffuse component become

$$\left(\frac{d\sigma}{d\Omega}\right)_{\substack{Diffuse \\ Rough \\ with\,cut-off}} = \left(\frac{r_0\rho}{q_z}\right)^2\left(\frac{A}{\sin\alpha_i}\right) exp\{-q_z^2\sigma^2\}\int_S exp\{q_z^2C(R) - 1\}exp\big(q_xx + q_yy\big)dxdy$$

Using the expression of correlation function as given in eqn. (2.55) it becomes

$$\left(\frac{d\sigma}{d\Omega}\right)_{\substack{Diffuse \\ Rough \\ with\,cut-off}} = \left(\frac{r_0\rho}{q_z}\right)^2\left(\frac{A}{\sin\alpha_i}\right) exp\{-q_z^2\sigma^2\}$$

$$\times\int_0^\infty \Big[exp\Big\{q_z^2\sigma^2 exp\{-(R/\xi)^{2h}\}\Big\} - 1\Big]J_0(q_rR)dR \tag{2.57}$$

where J_0 is the Bessel function of First kind. It is noted from above equation that at q_r=0 also there is a diffuse scattering component.

2.4.2 Scattering in dynamical approach: Distorted Wave Born Approximation (DWBA)

As discussed previously in the region close to the critical angle the Born Approximation (BA) fails, as in this region the multiple scattering phenomenon cannot be neglected. Due to similar cause BA cannot be applied for multilayer samples also. However Distorted Wave Born Approximation (DWBA) [55] which starts with exact Fresnel solution for the perfect interface, and calculate the effect on the wavefront of the perturbing potential due to interface roughness can be applied in these situations. Sinha *et. al*. [54] first applied this approach for neutron and

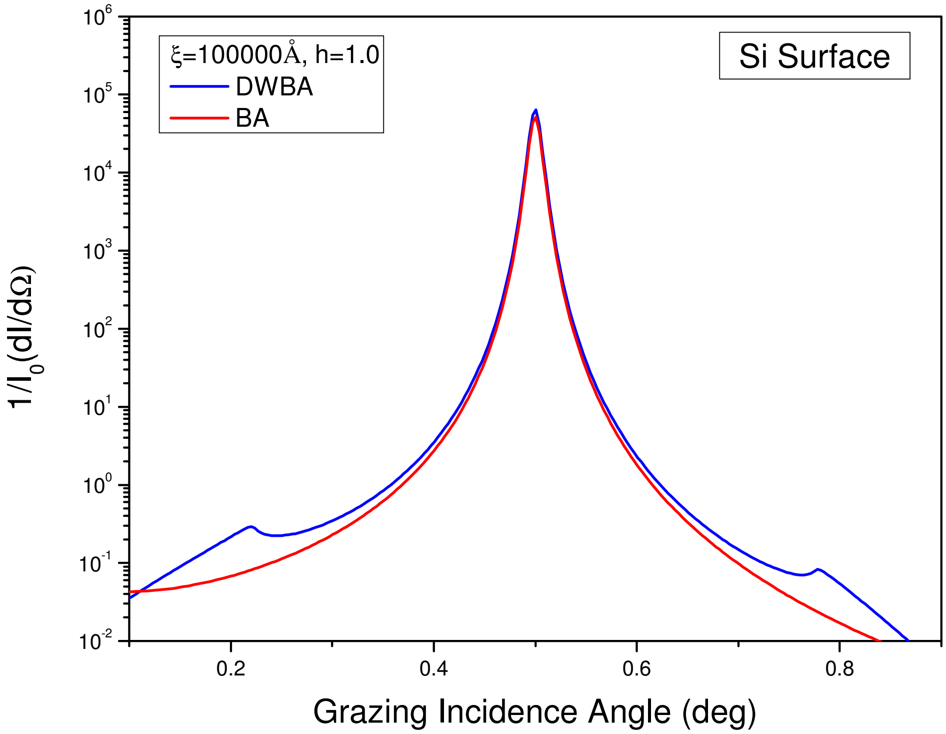

Fig. 2.21: Rocking scan of a silicon surface at scattering angle 0.5° using BA and DWBA approximation

X-ray scattering. Here the scattering potential is separated in two terms V_1 and V_2 where the total potential $V=V_1+V_2$, The ideal surface located at z=0 is described as:

$$V_1 = \begin{cases} k_0^2(1-n^2) & z<0 \\ 0 & z>0 \end{cases} \tag{2.58}$$

The perturbing potential at depth z due to roughness is described by

$$V_2 = \begin{cases} k_0^2(1-n^2) & for\ \ 0<z<Z(x,y) \\ -k_0^2(1-n^2) & for\ \ 0>z>Z(x,y) \\ 0 & Otherwise \end{cases} \tag{2.59}$$

where, *Z(x,y)* is the actual rough surface. Using this perturbing potential Sinha *et. al.* [54] have calculated the diffuse scattering cross section within DWBA, as follows:

$$\left(\frac{d\sigma}{d\Omega}\right)_{\substack{diffuse\\ DWBA}} = \left(\frac{r_0\rho}{q_z^t}\right)^2 \left(\frac{A}{\sin\alpha_i}\right)|t(k_1)|^2|t(k_2)|^2(1-n^2)exp\left\{-\frac{\sigma^2}{2}[(q_z^t)^2+(q_z^{t*})^2]\right\}$$

$$\times \int (exp\{|q_z^t|^2C(R)\}-1)exp\{i(q_xX+q_yY)\}dxdy \tag{2.60}$$

where, $|t(k)|$ is the Fresnel transmission coefficient of the surface which can be calculated from Fresnel's equation and q_z^t is the wave vector transfer in the medium, above the critical angle $q_z^t \approx q_z$.

Comparing diffuse scattering cross sections found from BA and DWBA, it is found that in DWBA the Fresnel's transmission coefficient and modified wave vector transfer have been introduced. The generated rocking curves of a silicon surface at scattering angle 0.5° found from BA and DWDA approximations are compared in Fig. 2.21. In case of DWBA the Yoneda peak [56] is realized at cut-off angle however in case of BA it is not seen as in this small angle BA approximation is not valid. In Fig. 2.22 the variation of non-specular scattering of X-ray from a silicon surface is shown for different correlation lengths of the surface. In the above two figures the non-specular spectrum are generated using IMD [57] software package.

2.4.3 Non-specular scattering from periodic multilayer structure

So far we have discussed about the diffuse scattering from a single surface, however in case of multilayer structure each interface will scatter independently. As in the case of specular reflectivity the reflectivity enhances when the scattered waves of each interface add coherently at the Bragg condition as shown in eqn. (2.34). Similarly the rough multilayer can produce peak of non-specular scattering. This so called Bragg Sheet arises from the interfacial defects that are to some degree replicated from interface to interface. So in order to calculate the diffuse scattering from a multilayer structure it is necessary to know about the roughness correlation function at each interface and their cross correlation is given by:

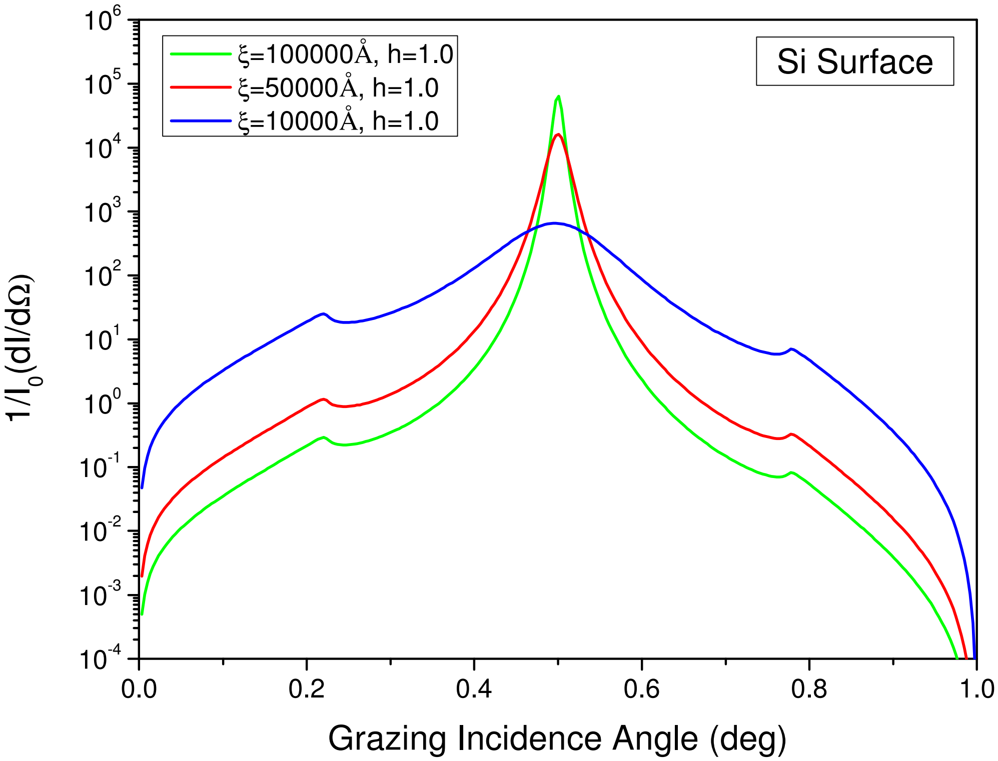

Fig. 2.22: Rocking scan of a silicon surface at scattering angle 0.5^{o} using DWBA approximation for different value of correlation length

$$C_{ij} = \langle Z_i(r) Z_j(r') \rangle \tag{2.61}$$

where (*i,j*) are the interface labels. Fig 2.23 schematically shows the roughness distribution within multilayer: (a) no roughness (b) each layer conformally replicating the underlying roughness and (c) uncorrelated roughness from layer to layer. Here the term 'correlated' is different with the correlation length what discussed in previous section, it refers to how the profile of the consecutive interfaces maps onto one another in the multilayer. In case of uncorrelated interface $C_{ij} = 0$, for $i \neq j$, the scattered wave add incoherently and the average scattering cross section is measured.

Holý *et. al.* [44, 45] have introduced a correlation function with a corresponding out-of-plane correlation length or vertical correlation length ξ⊥ at which the correlation between the i^{th} and the j^{th} layer is *1/e*.

$$C_{i,j}(R) = \sigma_{ij}^2 exp\left\{-\frac{R^{2h}}{\xi_{i,j}^{2h}}\right\} exp\left\{\frac{-|z_i - z_j|}{\xi_\perp}\right\} \tag{2.62}$$

σ_{ij}^2 is the sum in quadrature of the physical roughness of the two interfaces and $\xi_{i,j}^{2h}$ is the mean of $\xi_i^{2h}$and ξ_j^{2h}.

This correlation function is used in place of the previous correlation function to evaluate the scattering cross section of each pair of interfaces *i*, *j* in the formulation of diffuse scattering

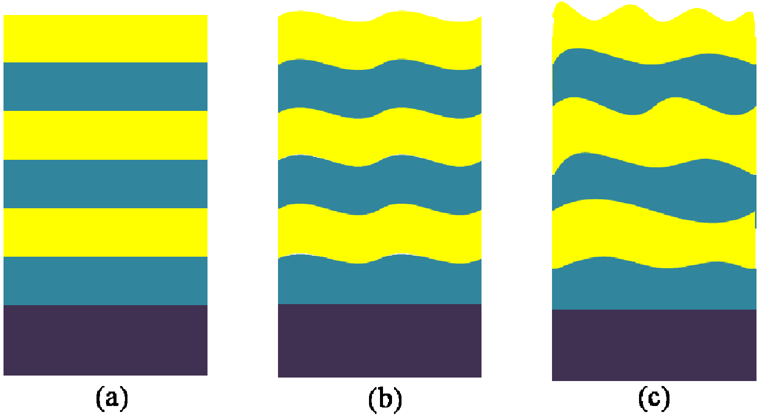

Fig. 2.23: Different type of roughness distribution in multilayer structure (a) no roughness (b) completely correlated (c) completely uncorrelated

used in this work. All pairs of interfaces are summed over to find the total scattering cross-section of the multilayer [58].

2.4.4 Theoretical generation of non-specular X-ray reflectivity spectra

In the present thesis for fitting of the non-specular reflecivity data of the samples, the theoretical non-specular X-ray reflectivity spectrum has been generated using the formalism propsed by Windt *et. al.* [59]. They have used the Power Spectral density (PSD) function of a surface which is equal to the Fourier Transform of the correlation function of a rough surface as defined in eqn. (2.56) and given by following expression:

$$PSD(q_{\parallel}) = \frac{4\pi \exp(-\frac{z}{\xi_{\perp}})(\sigma_r^2 \xi_{\parallel}^2)}{\left\{1 + (abs(q_{\parallel}))^2 \xi_{\parallel}^2)^{(1+h)}\right\}} \tag{2.63}$$

where, $q_{\parallel}$ is the component of the momentum transfer vector on the plane of the sample and each interface is characterized by three parameters viz., the physical or interface roughness (σ_r), the in-plane or parallel correlation length ($\xi_{\parallel}$) and the so called jaggedness factor (*h*). In addition, the vertical correlation function between two interfaces i and j ($j<i$) of a stack is defined by a vertical or perpendicular correlation length parameter ($\xi_{\perp}$) as follows:

$$C_{ji} = \exp(-\sum_{n=j}^{i-1} \frac{d_n}{\xi_{\perp}}) \tag{2.64}$$

d_n being the thickness of the n th layer.

The interface diffusion (σ_d) is used to calculate the modified the Fresnel coefficients at each interface as defined in eqn. (2.45), as the electron density gradient due to slowly varying chemical composition will scatter X-rays out of phase and reduces the overall Fresnel reflectivity as result of destructive interference without contributing to the non-specular reflectivity. However, a perfectly sharp but undulating interface having physical roughness or interface roughness (σ_r) will scatter in phase and increase the diffuse scattering at the expense of specular scattering. The diffused reflectivity of the whole structure is then computed using 1st order Distorted Wave Born Approximation (DWBA) [55] described in eqn. (2.60). So in this technique it is possible to separate out interface roughness (σ_r) and interface diffusion (σ_d) from total roughness (σ) which are related by

$$\sigma = \sqrt{\sigma_r^2 + \sigma_d^2} \tag{2.65}$$

2.5 Summary

The difference in the nature of interaction of X-ray and neutron with matter have been discussed and the expressions for complex refractive indices which describe the propagation of X-ray and neutron in a material have been established. Using the expressions for refractive index, the specular reflectivity of a bulk surface, single layer thin film deposited on a substrate and multilayers samples have been obtained. Subsequently, the effect of surface roughness on the neutron and X-ray reflectivities from a bulk sample and that of interface imperfections for thin films and multilayer samples have been discussed. It has been observed that surface roughness and interface imperfections have strong detrimental effect on the reflectivity of neutron and X-ray multilayer devices. Finally, the expression for non-specular reflectivity of a surface using Born Approximation (BA) in kinematical approach and using Distorted Wave Born Approximation (DWBA) in dynamical approach have been discussed in details. Using this, the surface and interfaces in the lateral direction can also be characterized and hence non-specular reflectivity measurements can be used to distinguish between interface roughness and interface diffusion of multilayer samples and lateral and vertical correlations lengths of the interfaces can also be estimated.

CHAPTER 3

Experimental details: Development of a 9 meter long in-line sputter deposition system and different thin film characterization technique

3.1 Introduction

The technique of deposition for the fabrication of thin film multilayer devices for the application of neutron and X-ray is very critical in order to achieve the desired reflectivity. Initially electron beam evaporation technique was used to deposit these multilayer devices, however due to low adatom energy (~ 0.1 eV) during the growth of the thin film, e-beam evaporation technique leads to a columnar type of growth leading to films with high surface and interface roughness, and from the discussion presented in Chapter 2 it is understood that high roughness is not desirable in neutron and X-ray optical devices. Subsequently however, sputtering techniques have increasingly been used in fabrication of such multilayer devices since in sputtering adatom energies are high (> 1 eV) compared to electron beam evaporation technique which helps them to reorganize themselves upon reaching on the substrate promoting 2-dimensional growth of thin films with roughness below 5Å. Also using sputtering technique it is comparably easier to scale up the dimension of the mirrors which is very much essential in neutron and X-ray application and compared to techniques like molecular beam epitaxy (MBE) this technique is cheaper also. Due to the all above reasons sputtering techniques have only been used for deposition of thin film multilayers in this thesis work.

In this chapter initially the theory of sputtering phenomena and the different type of possible sputtering techniques are described and compared with other deposition techniques. In the next section, a 9 m long DC/RF large area coating system which has been developed in-house during this thesis work is described in details. The 9 m long DC/RF large area coating system is designed in such a way that it can deposit thin films and multilayers on 1500 m x150 m substrate which is very useful for the development of hard X-ray mirrors and large area neutron supermirrors. In this thesis, the thin film samples deposited are mostly characterized by X-ray reflectivity (XRR), polarized neutron reflectivity (PNR), spectroscopic ellipsometry and atomic force microscopy (AFM) techniques. All these techniques have been described in the last section.

3.2 Sputtering phenomena

3.2.1 Theory and mechanism of sputtering

If a surface is subjected to bombardment by energetic ions, it is eroded and surface atoms are ejected, this phenomenon is named "Sputtering". The term “sputtering” was probably created to distinguish the source of vaporization between thermal evaporation and non-thermal (momentum transfer) process [60]. Other expressions proposed to describe the phenomena were, “impact evaporation” by Kay and Guenterschulze [61], “cathodic bombardment” [62] and “cathode disintegration” [63] to refer to the destructive and unwanted effects when the first observations were made on the phenomena.

So far two theoretical models have been proposed for explaining the sputtering phenomena:

A. Thermal vaporization theory: the surface of the target is heated enough to be vaporized due to bombardment of energetic ions.

B. Momentum transfer theory: Surface atoms of the target are emitted when kinetic momentum of the incident particles are transferred to target surface atoms.

The thermal vaporization theory was supported by Hippel in 1926, Sommermeyer in 1935 and Townes in 1944 due to their experimental observations of the Kundsen cosine emission distribution [64]. On the other hand, the momentum transfer theory was first proposed by Stark in 1904 and Compton in 1934. Later the detail studies by Wehner in 1956, including the observation of spot pattern in single crystal sputtering [64], suggested that the most important mechanism is not the thermal vaporaization but momentum transfer process. Still sputtering is believed to be cause by collision cascade in the surface layer of the solids.

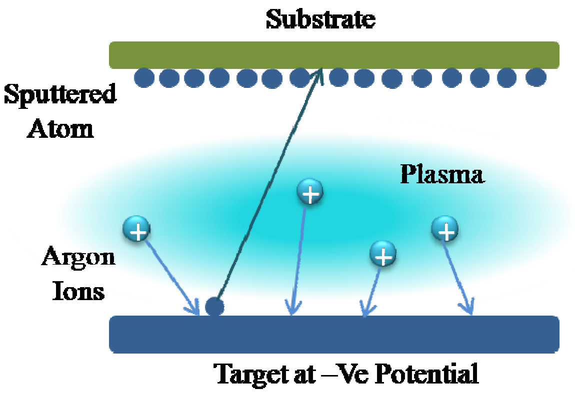

Fig. 3.1: Schematic diagram of a sputtering

In a sputtering system, the source of coating material called “target”, is kept opposite to a substrate on which coating would be done and the energetic particle bombards the surface of the target material with sufficient energy to result in the ejection of one or more atoms from the target, as shown in Fig. 3.1. It is basically a Physical Vapor Deposition (PVD) process and the process is characterized by the sputtering yield, defined as the ratio of emitted atoms to the number of bombarding particles. Generally, inert gas ions (usually Ar^+) are used as bombarding particles while sputtering can also be done with some other type of particles like atoms, molecules, electrons and photons. Ions and neutral atoms of the same element with the same energy produce identical collisional cascades and sputtering happens. This is because the ions become neutralized very close to the surface by attracting an electron. However, since it is easier to generate large fluxes of ions and accelerate them to the desired energy, sputtering systems generally use ions as the bombarding species.

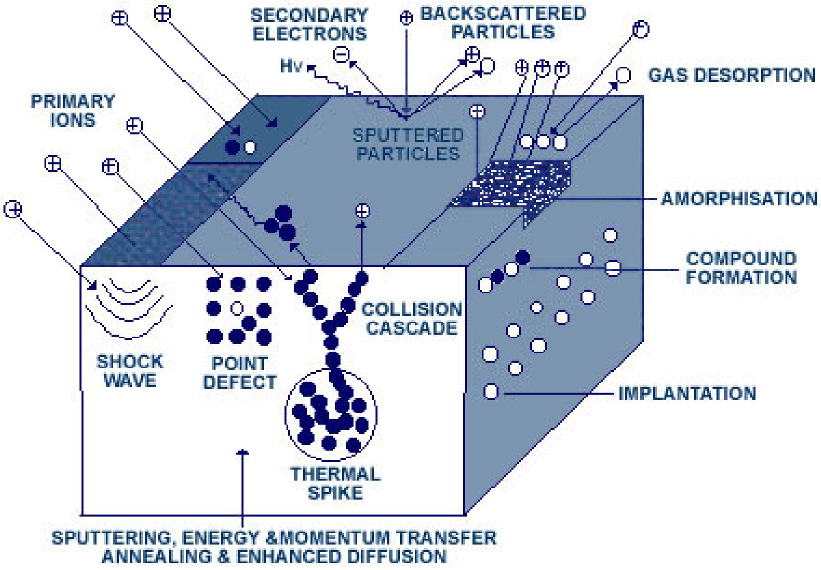

Fig. 3.2: Different events during sputtering at the target surface

When an ion interact with the target many interactions can happen as shown in Fig. 3.2 [65]. These interactions include liberation of neutral atoms, ionized atoms, backscattering, X-ray emission, photon generation, secondary electron emission, and desorption of gas atoms from the target surface. Several other processes can occur also in the target, including the generation of collisional cascades, the creation of point defects, local heating, amorphization, implantation, and compound formation.

Depending on the kinetic energy of the incident ions, the physical process in the sputtering target can be classified as:

(i) Low energy regime (E<20-50 eV): It is also known as the sub threshold region, in this regime the energy of the incident ion is less than the binding energy of the target atoms. Experimentally very low sputtering yield have been observed in this region and normally this regime is not recommended for thin film coating application.

(ii) Moderate energy (50 eV < E < 1000 eV): In this regime, the incident ion impacts a target atom in a primary collision and then generates a cascade of secondary collisions until the energy of the primary ion and all the recoil atoms become less than the displacement energy for an atom in the target material. The sputtering in this regime has been modeled by computer calculations, which follow the trajectories of a large number of incident and impacted particles [66]. Fig. 3.3 shows a computer simulation of such a process resulting from a single bombardment event [67]. It is clear that sputtering cannot result from a single binary collision since the momentum vector of the target atom must be altered by more than 90°. In the simulated collision sequence of Fig. 3.3, the incoming ions strikes target atom 1 and moves it deeper into

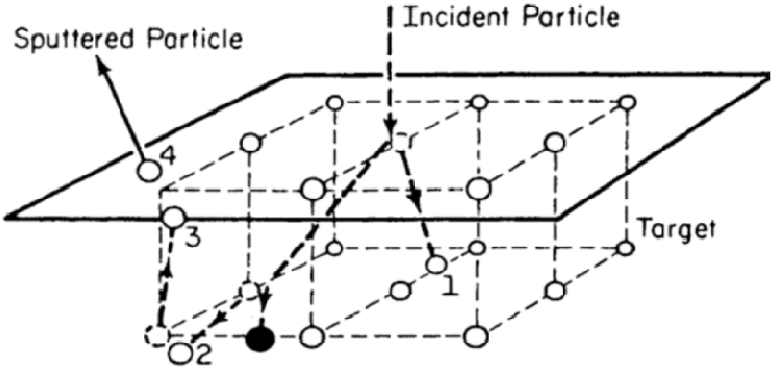

Fig. 3.3: Collision sequence initiated by single ion bombardment on a solid lattice as predicted by computer simulation

the lattice. The collision with atom 2 causes the ions to hit atom 3, which is displaced and collides with surface atom 4. Thus, sufficient momentum is transferred to atom 4 to overcome the surface energy barrier and is ejected [67]. In most of the sputtering applications the ions are used in this region. Along with the sputtered atoms some other particles are also emitted from the target material: reflected particles (neutral atoms, ions), secondary electrons and photons (UV and soft X-ray).

(III) High energy (1 keV < E < 50 keV): At these ion energies the incident ions or particles have sufficient energy to break all the bonds between atoms in a spherical region around the impact point [66]. After the incident ion hit the surface it creates a series of collisions with neighboring atoms in the solid. In many of these collisions, sufficient energy is transferred to displace the atoms. The displaced atoms may displace other atoms and so on, thus creating a cascade of atomic collisions. While this regime has generally higher yields than the previous energy regime, the higher energies (and voltages) make it impractical to use for most sputter deposition applications [66]. This regime is mostly used for analytical characterization of surfaces by techniques such as Rutherford Backscattering Spectroscopy (RBS) and Secondary Ion Mass Spectroscopy (SIMS).

(IV) Very High Energy (E> 50 keV): In this energy the incident particle can travel well into the bulk of the solid before depositing all of its energy. Little or no sputtering occurs as the energy is deposited far away from the surface. In addition, the incident particle is often trapped or implanted within the sample [66]. This regime is used especially in semiconductor device fabrication for ion implantation using dopants ions such as boron, phosphorus or arsenic modifying the conductivity of the semiconductor.

3.2.2 Growth of thin film by sputtering

Thin film on a substrate can be defined as a quasi two-dimensional material created by condensing, atomic/molecular/ionic species of matter. In a typical thin-film deposition process there are three major steps [68], such as (i) production of the appropriate atomic, molecular, or ionic species, (ii) transport of these species to the substrate through a medium, and (iii) condensation on the substrate, either directly or via a chemical and/or electrochemical reaction, to form a solid deposit. Through different theoretical and experimental studies it has been established that the detailed step-by-step process of growth [69] of thin film as shown in Fig. 3.4 is following: 1. Absorption or Physisorption, 2. Surface diffusion, 3.Chemical bond formation or Chemisorption, 4. Nucleation, 5. Island formation and microstructure formation, 6. Bulk change like diffusion and grain growth.

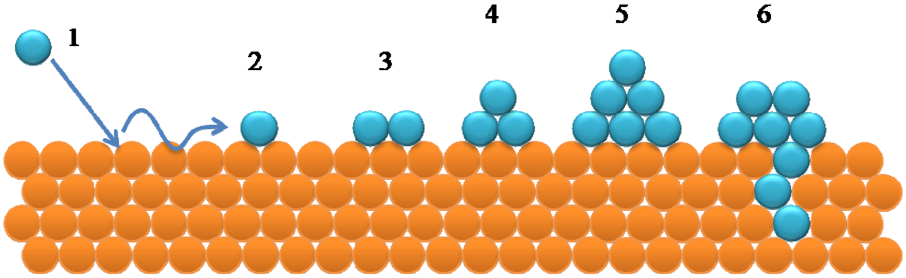

Fig. 3.4: Step by step process of growth of thin film

In the case of sputtering deposition, the primary deposition variables which determine the nucleation and microstructural properties of films are; the film material, the incident material flux, the kinetic energy of adatom at the film growth surface, the film growth temperature or substrate temperature, the flux of contaminants, and the substrate material surface cleanliness, crystallinity and orientation [69].

3.2.3 Different sputtering systems

Over the years, keeping the aim of increasing sputtering rate, depositing films at low pressure, reducing plasma heating of the substrate and depositing non conductive and complex materials several sputtering systems have been invented and used. Some of the standard systems are discussed in the following:

(I) *Planar DC diode sputtering*

Configuration of a DC planar diode sputtering system is shown schematically in Fig. 3.5. This is the most simple and oldest sputtering configuration [67]. Here the target is in the form of a plate, consists of the material which would be deposited as a thin film. A DC power supply capable of supplying several kilovolts (0.5–5 kV) is used to energize the electrodes. The substrate is placed facing the target. Cathode diameters are typically 5 to 30 cm and the cathode to anode spacing is generally 3 to 10 cm [67]. Arrangement for cooling or heating the substrate

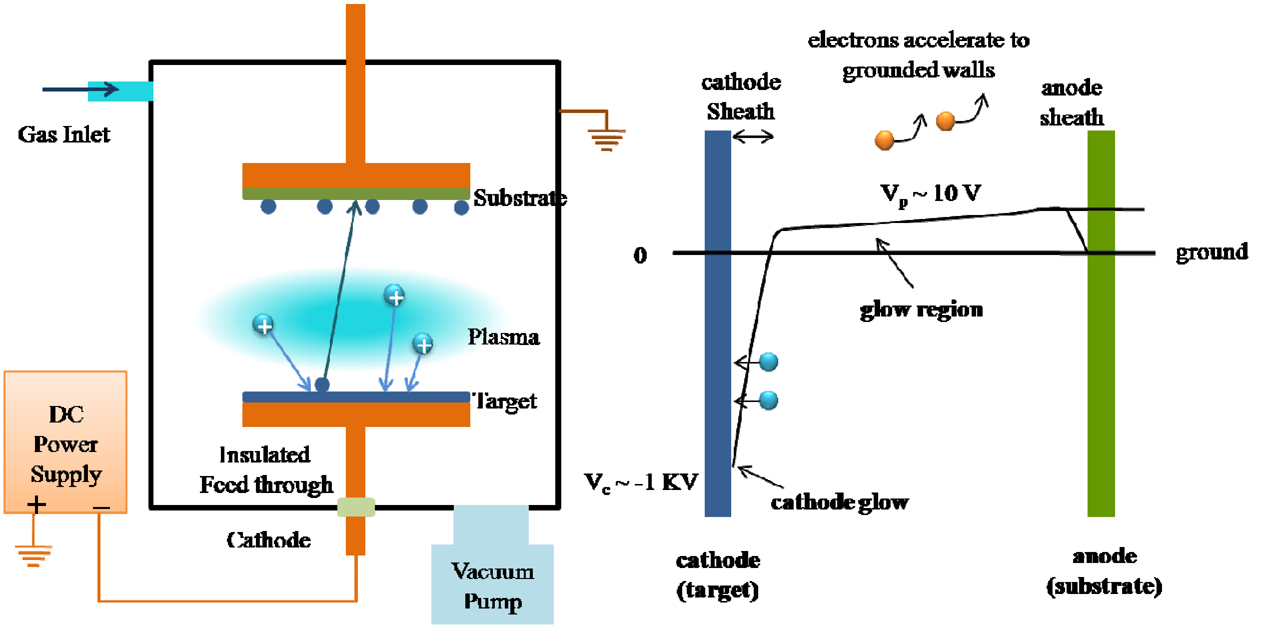

(a) (b)

Fig. 3.5: (a) Schematic diagram of a planer DC diode sputtering system (b) Different plasma region in between cathode and anode

can be used. The substrate can be electrically grounded, biased or floating.

In a typical sputtering process the vacuum chamber is initially evacuated to a base pressure that typically ranges from 10^{-6} to 10^{-8} mbar depending on the specific needs and subsequently it is filled with high purity argon gas up to a pressure of 10^{-1} to 10^{-2} mbar and a DC negative voltage is applied to the cathode which creates glow discharge type plasma. As ions have relatively low mobility compared to the electrons, most of the electrical potential that is applied between the anode and cathode is consumed in the cathode dark space, or sheath region [67] as shown in the Fig 3.5(b). Around 1% of the energy is used to produce the ejection of sputtered particles, and about 75% goes into heating the target, remaining 24% is dissipated by secondary electrons when they bombard the substrate [70]. Due to the strong electric fields in the cathode dark space the ions passing from the plasma volume are accelerated and strike the cathode. These ions not only sputter the target atoms, but also create a small number of

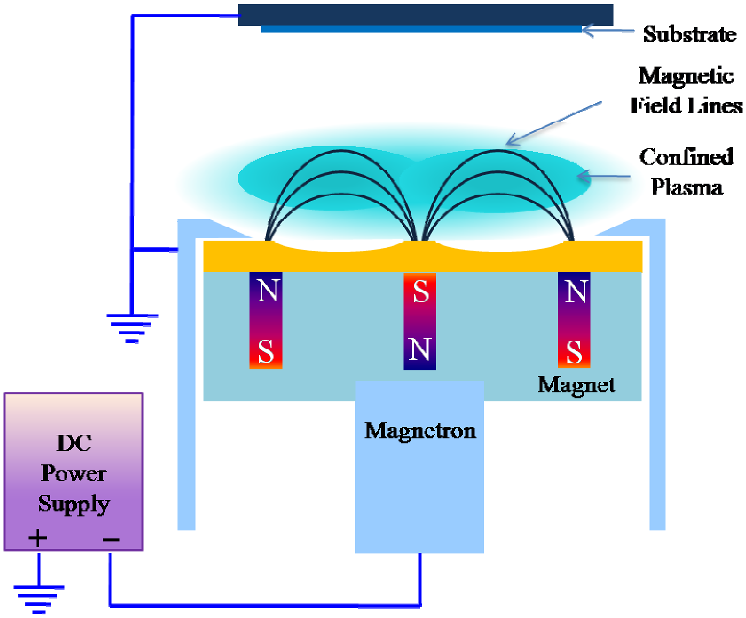

Fig. 3.6: Schematic diagram of a magnetron of a DC magnetron sputtering system

secondary electrons from the target surface (approximately one for every ten ions in the case of Ar ions impacting on a metal cathode). These electrons are accelerated in the cathode dark space and enter the plasma volume (negative glow) where they collide with gas atoms causing the ionization of the gas and sustain the discharge [67]. The atoms sputtered from the target with a momentum as a result of the ion bombardment, propagate to the substrate where they condensate and nucleate to form a thin film. During the propagation, some of the sputtered atoms will be lost due to collision with gas molecules and ions.

(II) ***Magnetron sputtering***

In magnetron sputtering, a magnetic field is created near the target by a proper arrangement of permanent magnets as shown in Fig 3.6, thus forcing the trajectory of an electron into a helical or cycloidal path and thus increasing the possibility of collision and ionization of the residual gas which helps to maintain the plasma at lower pressure. Also because the magnetic field does not increase the energy of the electron, the ionization cross section is the same as in the absence of magnetic fields.

Normally the field geometry used in the magnetron is parallel to the cathode surface as

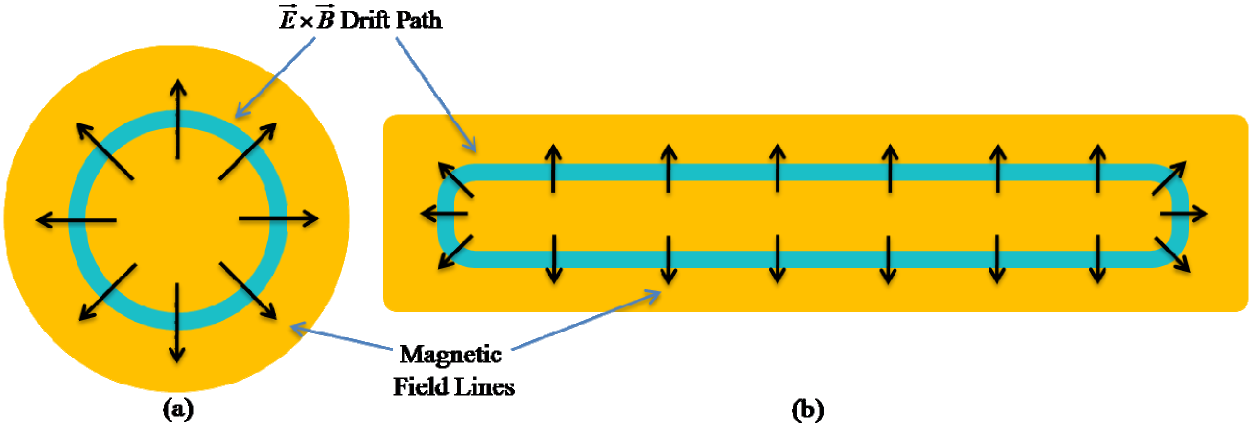

Fig. 3.7: Top view of direction of magnetic field and drift path of electron in (a) circular and (b) rectangular target

shown in the Fig. 3.6. In this way crossed electric and magnetic field are created and the electrons are trapped in a plane perpendicular to the magnetic field using $E \times B$ drift effect. The magnetic field and the drift path are sketched in Fig. 3.7(a) and in Fig. 3.7(b) for a circular and a rectangular magnetron respectively. Magnetron sputtering enhances the sputtering efficiency by enabling deposition of thin films at higher deposition rates, lower pressure, larger deposition areas, lower voltages and lower substrate temperatures than with non-magnetic DC sputtering [60, 67].

However, due to the localized path of the electrons most of the collisions between argon atoms and electrons occur at about half of the target radius for a circular target. Due to this the argon ions are also localized and most of the sputtering happen only in this region [71]. This spatially dependent erosion creates a 'race-track' on the target as shown in the Fig. 3.8 for rectangular target and due to this in magnetron sputtering the full material of the target cannot be utilized. Today's best optimized magnetron can have utilization factor 30-40% for non magnetic target and 20-25% for magnetic target [72]. This certainly limits the use of magnetron sputtering system as it increases the production cost in industry.


Fig. 3.8: Developed race-track in a rectangular Co target after use

(III) ***RF sputtering***

The major drawback of d.c. sputtering technique is its inability to sputter insulating targets due to large accumulation of charge at the target surface. This problem can be overcome by using RF sputtering technique. The use of RF methods for sputtering non-conducting materials is based upon the fact that a self-bias voltage, negative with respect to the plasma potential, develops on any surface that is capacitively coupled to a glow discharge [73]. The basis for this potential, which forms as a consequence of the difference in mobility between electrons and ions, is illustrated schematically in Fig. 3.9.

The current-voltage characteristic for an electrode immersed in plasma is given in Fig. 3.9(a). and when an alternating voltage is applied to an electrode, a net positive/negative potential appears on the surface as shown in the Fig. 3.9(b). During -Ve potential half-cycle positive ions are accelerated to the surface with enough energy to cause sputtering while on the +Ve half-cycles, electrons reach the surface to prevent any charge build up [73].

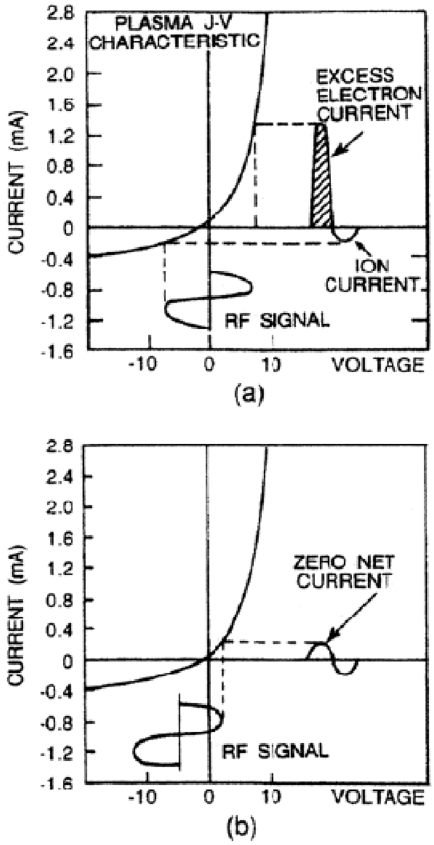

Fig. 3.9: Explanation of development of negative bias during RF sputtering using I-V characteristics

It is a common practice in RF sputtering system to connect the RF power supply to the cathode through a matching network [73] as shown in Fig. 3.10. The purpose of this network is to maximize the power dissipation at the discharge and to protect the power supply. In general, to avoid large RF current flowing around a circuit, generators are designed to have purely resistive output around 50 ohms. However it is seen that the RF discharge normally has larger and partly capacitive impedance which cannot be adjusted without compromising the discharge process. Therefore a load is simulated which is equal to the RF generator's output impedance by combining the discharge load with a variable matching network load. The two loads will be reactive, and the matching network is therefore placed close to the discharge chamber so as to avoid power losses due to the large reactive current flowing between these two components. A typical matching network configuration having capacitance and inductance is shown in Fig. 3.10.

RF frequencies used for sputter deposition can be in the range of 0.5–30 MHz though, most systems are operated at a frequency of 13.56 MHz, since this has been allocated by the Federal Communications Commission (USA) for industrial-scientific-medical purposes [67].

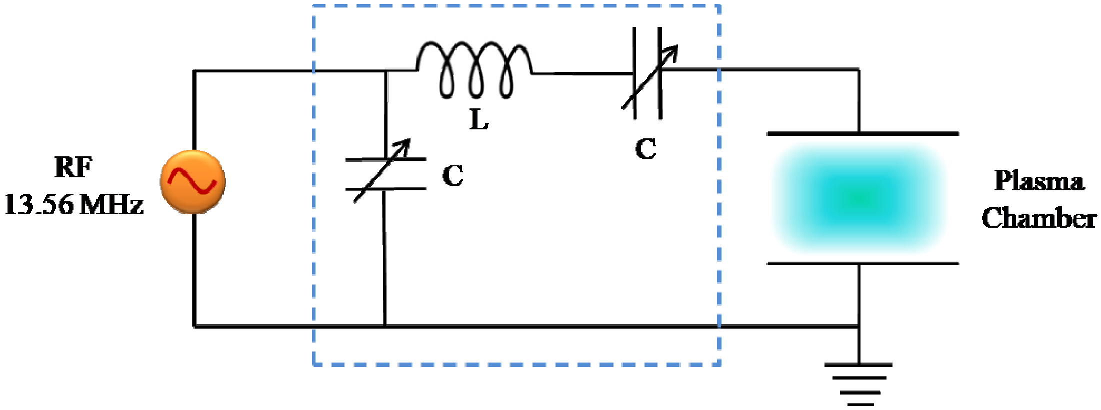

Fig. 3.10: Circuit diagram of an RF sputtering system with matching network

(IV) *Ion beam sputtering (IBS)*

Contrary to three previous type of sputtering the configuration of ion beam sputtering is different with respect to geometry. In this case ions are generated using an ion source in a separate place and using some ion optics it is extracted and carefully focused on a grounded metallic or dielectric target at an oblique incidence [74]. Subsequently, the materials sputtered from the target propagate and get deposited on a nearby substrate as shown in the Fig 3.11. In some of the IBS systems a second low energetic ion source directed towards the substrate is also used to supply extra energy to the deposited atom during growth of the film, in that case it is called dual ion beam sputtering system (DIBS).

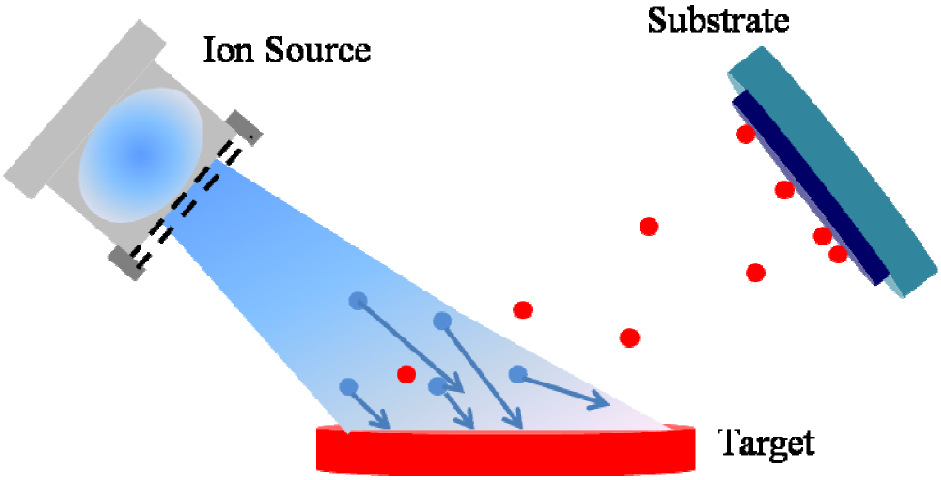

Fig. 3.11: Relative position of ion source, target and substrate in typical IBS system

In ion beam sputtering it is always desirable to deliver as much ion current to the target as possible, in view of this the ion source is made broad and it is placed close to the target. The ions can be generated through different processes. The widely used ion source is Kaufman type [75] where electrons emitted from the heated W or Ta filament (cathode) ionise inert gas molecules (like Ar, Kr) which being positively charged, are attracted to the negatively biased accelerator grid. By controlling the bias applied to the screen and accelerator grids, a certain amount of ion beam can be extracted and focused on target. However there is limitation regarding the lifetime of this filament in this type of ion source. In filament-less ion sources, on the other hand, ions are created by generating plasma using a RF or microwave coupling [76]. Highest plasma densities at relatively low pressures can be obtained under electron cyclotron resonance (ECR) condition in a strong magnetic field. The schematic of a typical microwave ECR ion source as shown in Fig. 3.12 [76] where plasma is generated in a quartz cup surrounded by four water cooled permanent magnets of neodymium-iron-boron (outside the vacuum), which produce ECR zones in a multi cup field. The magnetron is operated at 2.45 GHz and the working inert gas (Ar) is fed in to the discharge cup from outside. In this type of ion source plasma can be generated at pressure ~10^{-4} mbar.

As discussed by various researchers [75] the ion beam sputtering deposition process has some advantages over the other deposition technique like electron beam evaporation and even magnetron sputtering technique for deposition of thin films like,

- Low background pressure results in less inclusion of gas and less scattering of sputtering particles during transit
- Greater isolation of substrate from ion source unlike glow discharge sputtering
- Freedom to change the angle of incident ion beam and angle of deposition
- Narrow energy spread of the ion beam allows us to study the sputter yield as a function of the ion energy
- Process allows accurate beam focusing and scanning
- Change in target and substrate are allowed, keeping the beam characteristics constant
- Independent control of ion beam energy and current are possible
- Less damage due to ion collision as target and substrate are independent of acceleration electrode

Comparative features of all these deposition processes are presented in the Table-3.1.

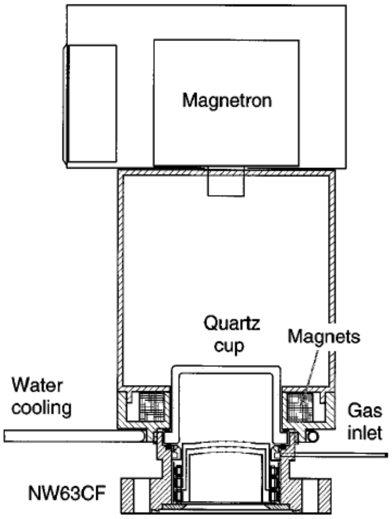

Fig. 3.12: Cross sectional view of a typical ion source used in Ion Beam Sputtering (IBS) System

(V) *High power impulse magnetron sputtering (HiPIMS)*

This is a relatively novel and new sputtering configuration which is also known as High Power Pulsed Magnetron Sputtering (HPPMS). In the year 1999 Kouznetsov *et. al.* [77] first demonstrated this sputtering technique achieving a peak power density 2.8 kWcm^{-2} using a novel pulse power supply and a standard circular magnetron source with Cu target. In this technique, by applying high electric power the plasma density in front of the sputtering source is increased, as a result of which the mean ionization distance of the sputtered particles decreases and high degree of ionization of the sputtered particles and a high rate of molecular gas dissociation are achieved which ultimately results in high density of the deposited films. In practice, the electrical power of the order of $kWcm^{-2}$ are applied to the target surface so electron densities of the order of $10^{19} – 10^{20}$ m^{-3} are achieved close to the sputtering source. However the conventional magnetron sputtering sources cannot be operated at this power in continuous mode.

	Electron Beam Evaporation	**Ion Assisted Deposition**	**Magnetron Sputtering**	**Ion Beam Sputtering**
Surface Roughness	>20Å RMS	>10Å RMS	<5Å RMS	<3Å RMS
Density/Porosity	Porous	Dense	Near Bulk	Near Bulk
Addison/Durability	Low	Good	Very Good	Excellent
Deposition Rate	>10Å/sec	~10Å/sec	~10Å/sec	~3Å/sec
Aging Effect	Yes	Yes, Small	No	No

Table-3.1: Comparison of different deposition system

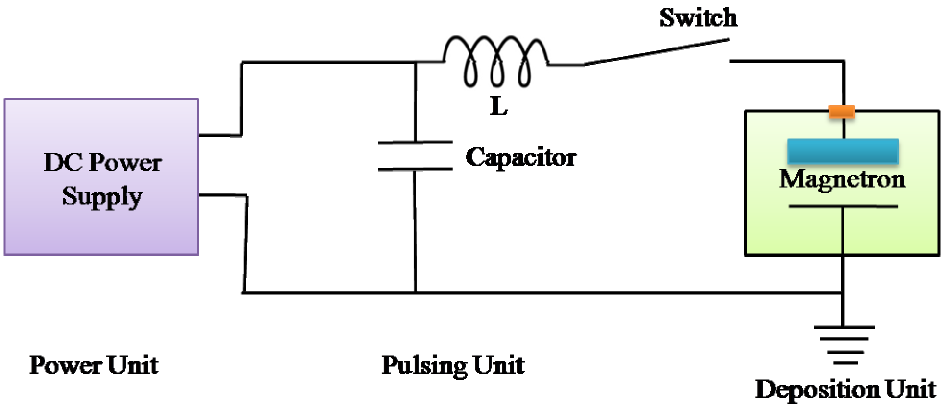

Fig. 3.13: Basic architecture of a HiPIMS system

So this high power is applied in pulsed mode with very low duty factor which is the ratio of the pulse-on time and the cycle time. In Fig 3.13 the basic architecture of a HiPIMS system is shown where the DC generator charges the capacitor bank of a pulsing unit and subsequently, the energy stored in the capacitor is dissipated in the plasma in pulses of pre-defined width and frequency.

3.3 In-house developed 9 m long DC/RF magnetron sputtering systems

As discussed in the previous chapter hard X-rays can be efficiently reflected from a

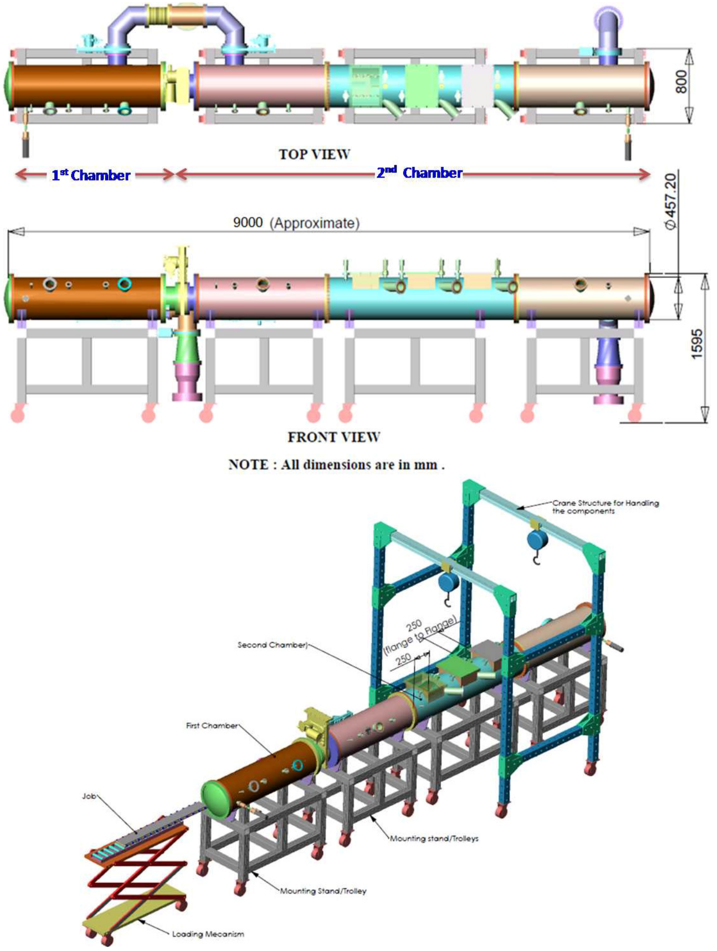

Fig. 3.14: Schematic diagram of the in-house developed 9 meter long magnetron sputtering system.

surface of a thin film if the grazing angle of incidence is below a critical angle. It is very obvious that at such a small grazing angle of incidence, the foot print of the beam will be very large on the reflecting surface or in other words to reflect hard X-rays very long mirrors or coated surfaces are required. Thus in all hard X-ray synchrotron beamlines, mirrors typically of 1-1.5 m length are used to reflect X-rays originating from the Synchrotron source. Similarly for reflecting, polarizing or analyzing thermal and cold neutrons large area supermirrors are required which have also been discussed in previous chapter. In order to meet these requirements a 9 m long DC/RF magnetron sputtering system has been designed and built indigenously under the course of this thesis work [78]. The schematic diagram of this system is shown in Fig 3.14.

3.3.1 Design of in-line sputtering deposition system

The deposition system is designed in such a way that, uniform deposition can be obtained on substrates up to 1500 mm x 150 mm size in sputter down configuration [78]. The system is comprised of two chambers, the first is the load-lock chamber of diameter 450 mm, which is used for loading/unloading and cleaning of the substrates, while the second chamber is the main deposition chamber of same diameter. As shown in Fig. 3.14, the two chambers are connected to two separate turbomolecular pumping systems and isolated by a large gate valve. In the first chamber the substrate is loaded on a substrate trolley and is cleaned by glow discharge cleaning method using a 13.56MHz commercial RF power supply. Subsequently, the substrate is transferred to the second chamber and the gate valve between the chambers is closed.

The second chamber where the deposition is carried out has three compartments. As shown in the expanded view in Fig. 3.15, in the middle compartment three rectangular magnetron cathodes are mounted where three sputtering targets, each having dimensions of 125 mm x 200 mm can be fixed. The actual sputtering process takes place in this compartment while the other two compartments of the second chamber act as dummy space so that the large substrate trolley can undergo a full to-and-fro motion below the target during deposition. In front of each target there is a shutter assembly, comprising of two SS plates fixed in a SS shaft which move in opposite directions by two motors for opening and closing operations. Just beside the each target one quartz crystal monitor with specially fabricated sputtering head sensor is fixed in the shadow region for in-situ monitoring of the static rate of deposition. Each cathode is connected to a 2 kW DC power supply for generating plasma. In order to visualize the plasma

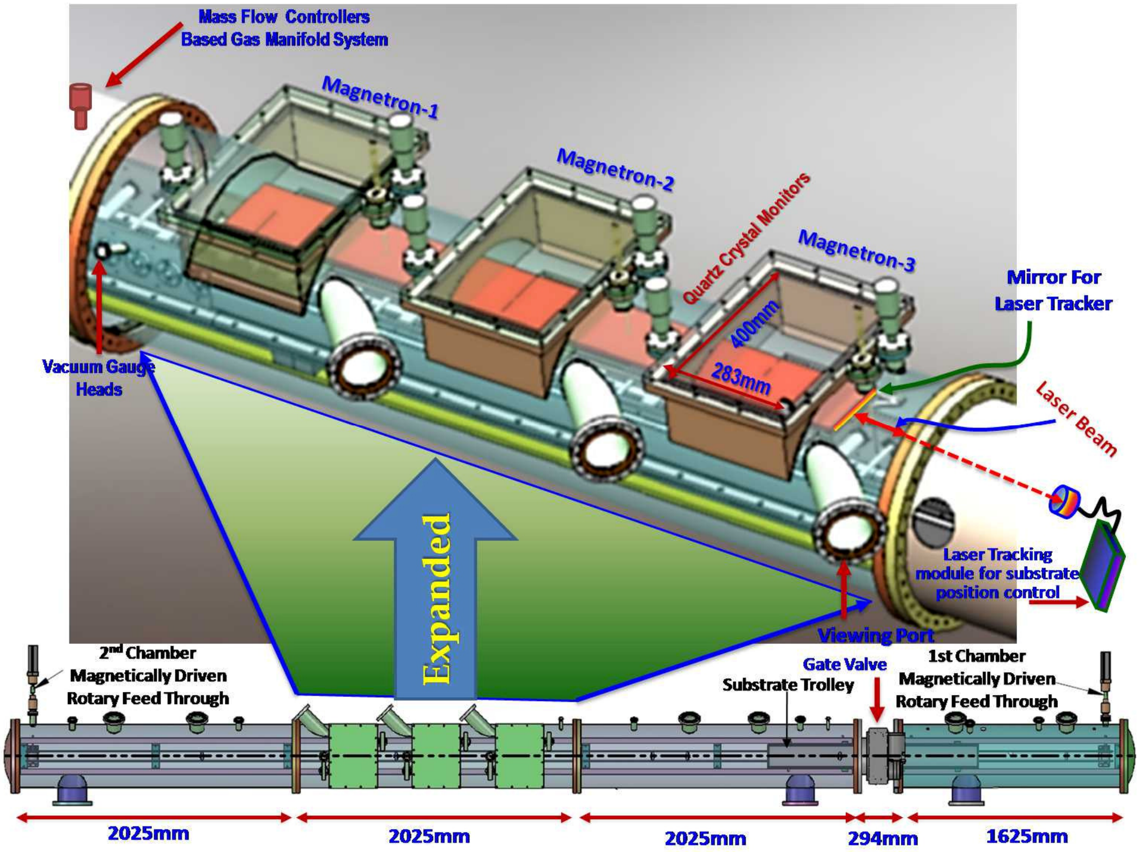

Fig. 3.15: Schematic diagram of the sputtering system with expanded view of the sputtering chamber along with various gadgets

from outside, three viewing ports are mounted on the chamber wall one near each target at an angle as shown in Fig.3.15.

During any deposition, the substrate trolley is moved from one side of the second chamber to the other side with a constant pre-defined speed in order to deposit the whole substrate uniformly. This motion of the substrate trolley is the most critical component of this type of in-line deposition system and hence the motion assembly has been designed very carefully to achieve jerk-free and continuous motion. After testing various options, the S.S. rope based pulley system is chosen where two pulleys are mounted on the opposite ends of each chamber, as shown in the Fig 3.16. At one end, the pulley is connected with a stepper motor placed outside the vacuum chamber and interfaced to the assembly inside through a magnetically driven rotary feed-through. Two parallel SS ropes are tightly fastened over the pulleys and a small guiding trolley is fixed with the rope. Thus, being driven by the stepper motor, when the pulley rotates, the rope moves and the small guiding trolley moves over a fixed rail. The guiding

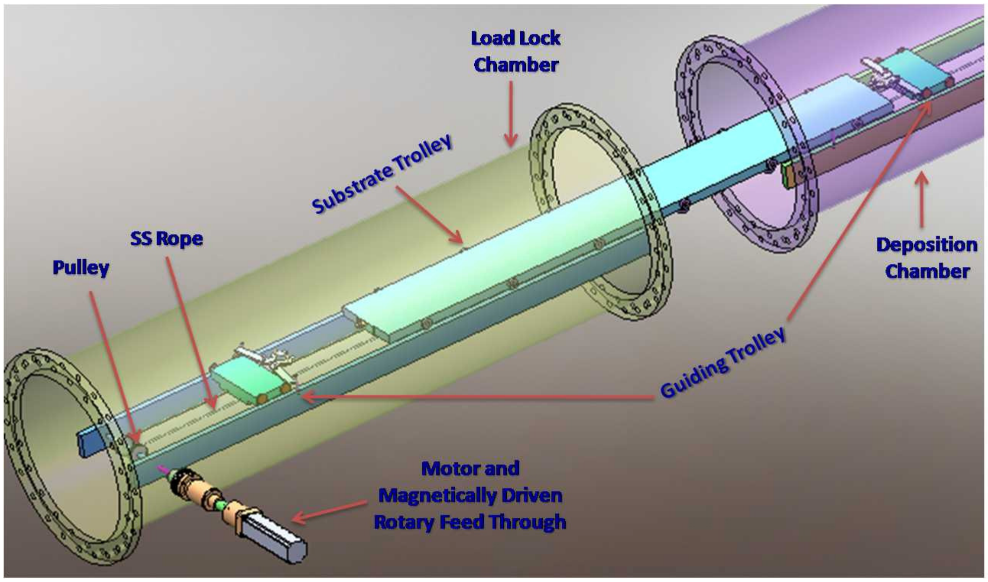

Fig. 3.16: Schematic diagram of the rope and pulley based substrate translation mechanism

trolley is clamped with the big substrate trolley and thus the substrate trolley also moves guided by bearings on side rails on both sides. The spring–loaded clamp between the guiding trolley and the substrate trolley automatically locks/unlocks at the end of the both chambers when the substrate trolley is to be transferred from the first chamber to the second chamber and vice–versa. Fig. 3.16 shows the position of the two guiding trolleys and the large substrate trolley during automatic substrate unloading from the deposition chamber to load lock chamber.

During deposition, in order to track the exact position of the substrate trolley a laser based distance tracker has been fixed just outside the glass view port of one end of the deposition chamber as shown in the Fig. 3.15. The laser beam of the distance tracker passes through the view port and gets reflected back from the substrate tray and thus the exact position of the tray inside the chamber at any point of time during deposition can be measured within an accuracy of 1 mm. The read out of the laser tracker is fed-back to the motion mechanism in a closed loop control.

As discussed earlier, for development of neutron monochromator and supermirror,

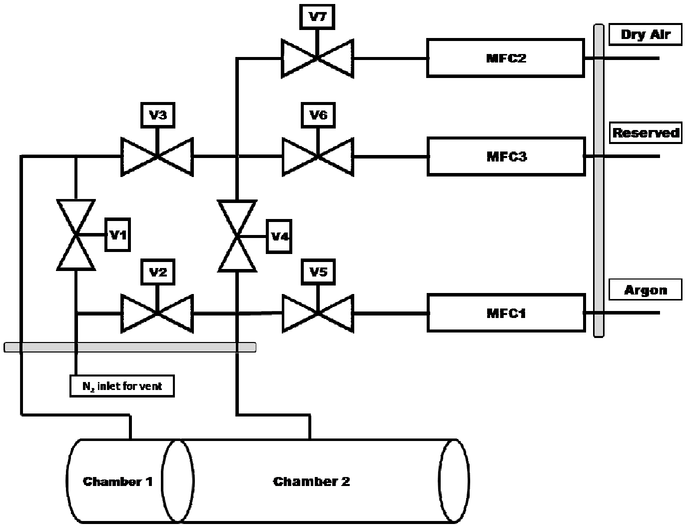

Fig. 3.17: Schematic lay-out of the automatic gas manifold system for reactive sputtering

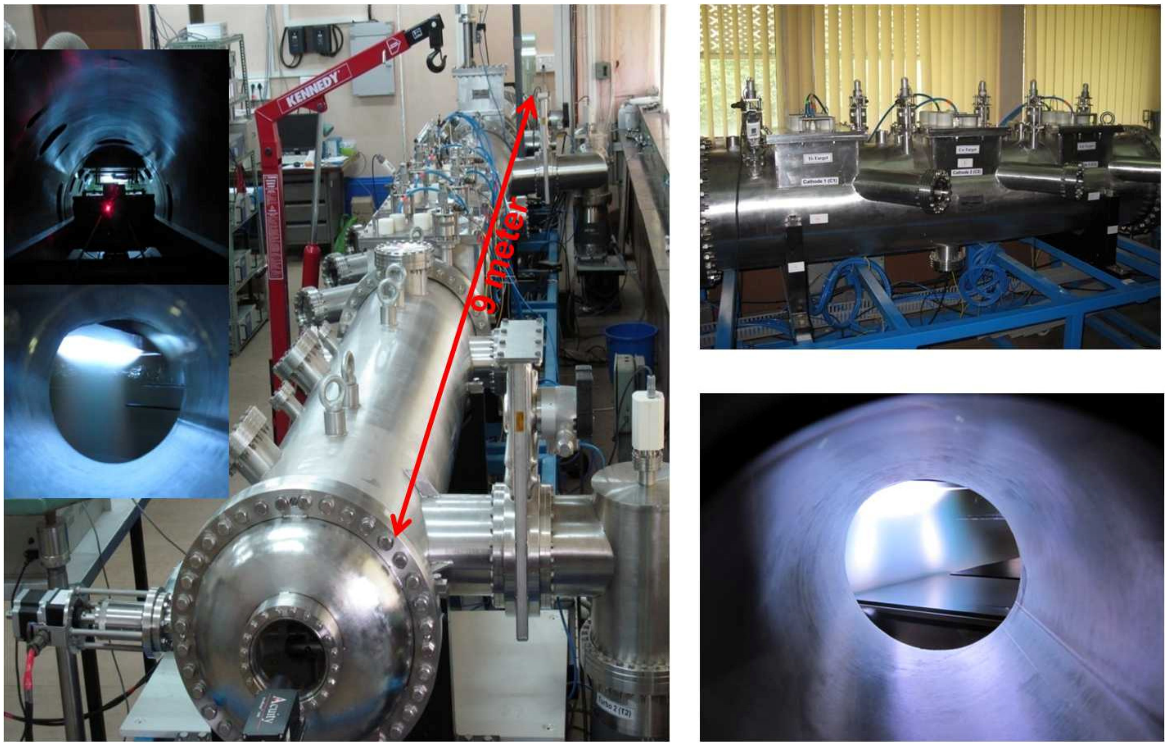

Fig. 3.18: Some photograph of the 9 meter long inline sputtering system

reactive sputtering sometimes become essential where depositions are carried out under a mixed ambience of various gases. In order to meet this requirement, a gas manifold system has been designed so that upto three gases can be mixed at a pre-defined ratio and used as ambience during the deposition. As shown in the Fig.3.17, three Mass Flow Controllers (MFC) and seven pneumatically controlled normally-closed valves are used in the gas manifold system. The fully computer-controlled manifold system helps in choosing a mixed ambience or pure argon ambience as per the requirement since in neutron supermirror deposition, often one layer of the bi-layer stack is deposited under pure argon ambience and the other layer is deposited under mixed ambience of argon/oxygen, argon/nitrogen or argon/hydrogen. The gas manifold has been designed in such a way that when gas mixing is not required, one of the gas (nitrogen, air or hydrogen) can be diverted to the load lock chamber and the MFC’s are not disturbed. For example, when mixture of argon and air is needed in the sputtering (second) chamber, the valves V4, V5 and V7 are to be opened keeping all other valves closed, on the other hand, when only argon is required in the sputtering chamber, the valve V3, V5 and V7 are kept opened keeping all other valves closed so that flow of air can be by-passed to the first chamber. This methodology saves the stabilization time (normally 5-10 sec) of the MFC's starting from the closed state which has a significant cumulative effect in time management for a neutron supermirror fabrication that generally involves deposition of more than 500 layers. Photograph of the complete system installed in our laboratory is shown in Fig. 3.18 [79].

3.3.2 Process automation for multilayer deposition

A labVIEW based process automation software has been developed in the course of this thesis work for the fabrication of neutron supermirrors by sequential deposition of two alternate layers up to 1000 layers or so. As shown in Fig. 3.19, the top level Graphical User Interface (GUI) sequences the interactions with various sub systems such as micro controller based motion

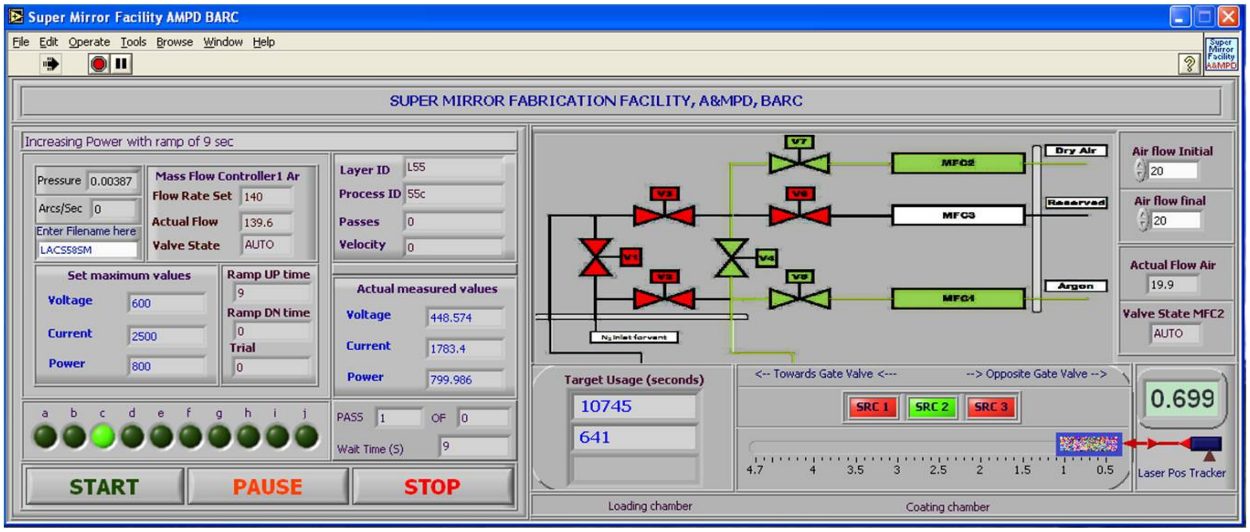

Increasing Power with ramp of 9 sec

Pressure 0.00387
Arcs/Sec 0
Enter Filename here LACS58SM
Flow Rate Set 140
Actual Flow 139.6
Valve State AUTO
Layer ID L55
Process ID 55c
Passes 0
Velocity 0
Voltage 600
Current 2500
Power 800
Ramp UP time 9
Ramp DN time 0
Trial 0
Voltage 448.574
Current 1783.4
Power 799.986
PASS 1 OF 0
Wait Time (S) 9
Air flow Initial 20
Air flow final 20
Actual Flow Air 19.9
Valve State MFC2 AUTO
10745
641
0.699

Fig. 3.19: Snapshot of the GUI of LabVIEW based automation program for multilayer deposition.

controller, laser position tracker for substrate movement, mass flow controllers for monitoring and controlling various gas flow, DC power supplies for plasma generation, Quartz Crystal Micro balance based deposition rate, thickness and crystal life monitor, motorised shutters, microcontroller based gas manifold system and vacuum gauges [78].

Each deposition process has been divided into 11 sub-processes viz., (i) opening of the required set of electro-pneumatic valves of the gas manifolds, (ii) initialization of mass flow controllers and setting up of the required flow rate, (iii) setting up of the upper limits of voltage, current and power, (iii) ramping up of power to the desired level at the set rate, (iv) waiting for stabilization of power, (v) setting up of final gas flow rate through MFC, (vi) logging of the process parameters prior to deposition, (viii) onset of the substrate motion at a pre-defined speed, (vii) opening up of the shutters and performing deposition by shuttling the substrate for a set number of passes at the set speed, (viii) closing of shutters, (ix) logging of the post deposition data, (x) decreasing of magnetron power at the set ramp down rate and (xi) preparation of the next layer by appropriately closing the opened valves and allowing time for residual gases in the chamber to flush out. All these sub processes are depicted via a front panel mimic at every stage and deposition is carried out for the set number of layers.

The process control software runs these sub processes as set in a process table that is automatically generated from the inputs given by the user in two tables. The material property table lists the properties specific to the material of the plasma source such as the voltage, current and power to be applied for plasma generation and the layer information table lists the number of layers and various layer specific parameters such as layer thickness, number of passes, speed of substrate movement, flow rate of Argon and other gases etc. Once these two tables are set, the user has to only run the process control program and click on the start process button after setting the file name for data logging. However, during the course of deposition, an option has been given to the user to modify the process parameters and restart the process at any time for offsetting cumulative process errors.

The automation is implemented by employing in-house developed interface modules for the different components viz., (i) substrate trolley movement mechanism, (ii) laser tracker system, (iii) mass flow controllers, (iv) pneumatic valves and relays of the gas manifold system, (v) quartz crystal monitors, (vi) magnetron power supplies and (vii) vacuum gauges that implement communication employing RS232 interface. For this purpose a 1:8 MOXA serial port extender and a 1:16 USB to serial port HUB were installed for coupling the above sub systems with the control PC. With the development of the fully automated system multi-layer super mirrors having more than 500 layers with graded thickness could be fabricated in a single go at a relatively short span of time making it possible to conduct more fabrication trials under different process conditions. This ultimately helps in arriving at the optimised combination of process parameters for fabrication of super mirrors with the desired optical and polarization properties.

Fig. 3.20: Photograph of the 1500 mm x 150 mm long Ti coated glass.

3.3.3 Measurement of thickness uniformity

Subsequent to the installation of the above system, in order to measure the thickness uniformity of the deposited film, initially a glass substrate of 4mm thickness and dimension of

1500mm x 150mm has been coated with a single layer Ti film. The film has been deposited at Ar pressure of ~1.5×10^{-3} mbar, achieved by flowing Ar at a constant rate of 40 ml m^{-1} after attending the base vacuum of 5×10^{-7}mbar, and at a d.c power of 350 watt applied at constant voltage mode. During deposition the substrate has been subjected to to & fro motion for 8 times below the Ti target at a constant speed of 34 mm sec^{-1}. A visibly uniform Ti coating over the whole area could be achieved at the above deposition condition photograph of which is shown in Fig. 3.20.

However, since the coating made on this large substrate cannot be characterized in standard equipments, several small c-Si substrates of ~30 mm x 20 mm dimensions were loaded on a specially designed substrate holder having dimension of 1500mm x 150 mm, as shown in

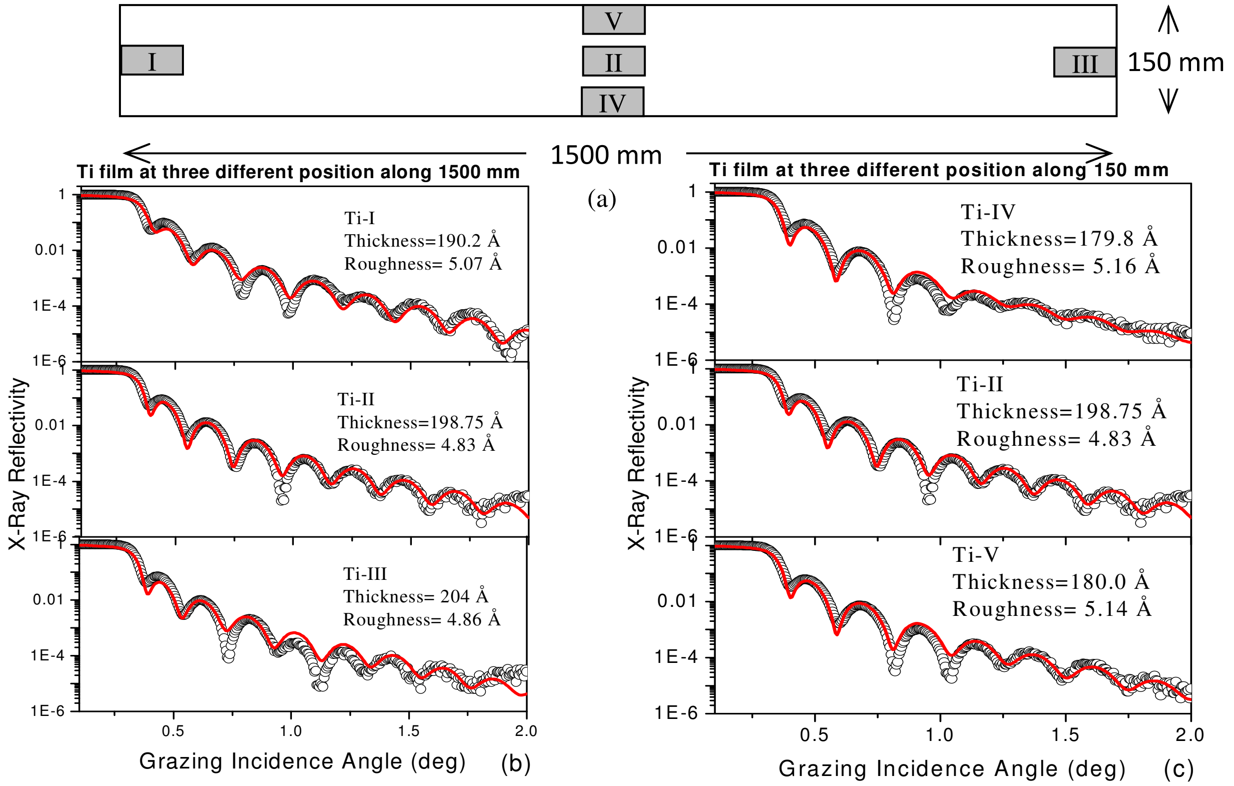

Fig. 3.21: (a) Position of five samples on 1500 mm x 150 mm substrate holder. Measured GIXR spectra (circle) of Ti film along with best fitted simulated spectra (line) (b) along 1500 mm direction (c) along 150 mm direction.

Fig 3.21(a). The substrates were kept on slots spreading over the length and breadth of the substrate holder. Single layer Ti films have been deposited on these substrates at similar deposition conditions as described above and the films have subsequently been characterized by Grazing Incidence X-ray Reflectrometry (GIXR) technique.

Fig. 3.21(b) shows the GIXR spectra of the three Ti-films deposited on c-Si substrates which were placed at the two ends and at middle of the substrate holder along the 1500mm length as shown in Fig. 3.21(a). Width-wise all the three holders were placed on the central axis. The GIXR spectra are fitted with theoretical curves generated using the IMD code [57] which works on the standard Parratt formalism [51] as described in the previous chapter. During fitting thickness, density, Ti-on-Si substrate interface roughness and top surface roughness are varied and from the best fitted spectra these parameter are estimated. The best fit theoretical curves are also shown in Fig. 3.21(b) along with the best fit parameters. It can be seen from the above figure that the average thickness of the Ti films is 197.7Å with a thickness variation ±3.5%. The average density 4.45gm cm^{-3} which is almost 95% of the bulk density and top layer roughness is 4.9Å which is also acceptable for neutron supermirror fabrication. Similarly Fig. 3.21(c) shows the results of GIXR measurements on three samples placed along the 150 mm width on the central axis and it can seen that the thickness non-uniformity in this case is ±4.8% [79].

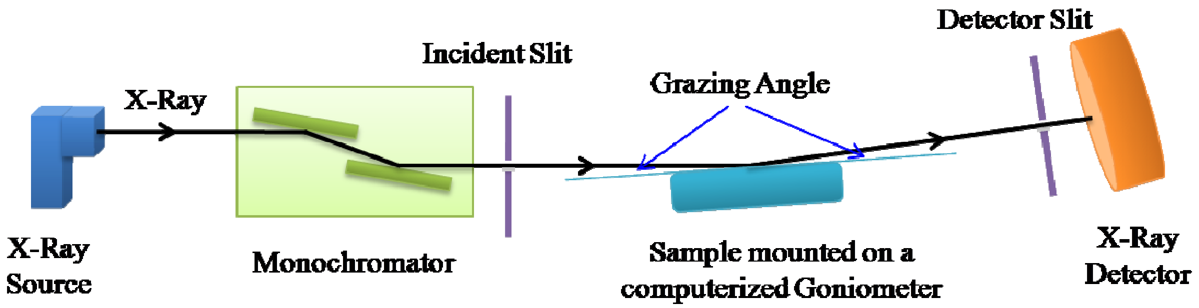

Fig. 3.22: Schematic diagram of grazing incidence x-ray reflectivity (GIXR) measurement set up

3.4 Thin film characterization technique

The thin film and multilayer samples prepared under this thesis work have been characterized by the following techniques:

3.4.1 Specular and non specular X-ray reflectivity measurement

The schematic diagram of grazing incidence X-ray reflectivity measurement set up is shown in the Fig. 3.22. Normally monochromatic Cu Kα_1 (1.54Å) from an X-ray tube is used as source. In our instrument the divergent beam is collimated by some cross beam optics (CBO) technique and the beam is monochomatized by using 2-bounce Ge crystal and Ni filter. The reflected X-ray is passed through a soller slit and detected by a scintillator detector followed by photomultiplier tube. Both the source and the detector are mounted on a high precision goniometer along with the sample. The specular measurement is done in θ-2θ mode where the source arm and the detector arm of the goniometer move synchronously. In non-specular measurement the source arm is kept fixed keeping the angle of incidence constant and the detector arm is moved around specular condition of scattering angle. As discussed previously this geometry of non-specular reflectivity is called detector scan. The photograph of the instrument in our laboratory is shown in the Fig. 3.23.

Fig. 3.23: Actual photograph of grazing incidence x-ray reflectivity (GIXR) measurement set up in our laboratory

Important parameters of the samples are extracted by fitting the measured X-ray reflectivity plot with the theoretically generated spectrum. In case of specular X-ray reflectivity the theoretical spectrum is generated by the well known Parratt formalism [51], described in detail in the previous chapter, where the basic theory of X-ray reflectivity is derived from classical optics and Fresnel theory, modified slightly for X-ray. Analysis of specular X-ray reflectivity spectrum can yield information regarding density and thickness of a thin film/multilayer accurately. Also the surface roughness of a thin film can be estimated from the fitting as the Fresnel's reflectivity gets modified for a rough surface by a 'Debye-Wallar -like' factor, as shown in eqn. (2.45), given by :

$$R = R_F exp(-q^2\sigma^2)$$

where, q is the momentum transfer factor (= $4\pi \sin\theta/\lambda$), R is the reflectivity of the rough surface and R_F is the reflectivity of an otherwise identical smooth surface i.e. Fresnel's reflectivity and σ is the r.m.s. roughness of the surface.

In case of an interface, the above quantity (σ) is called the interface width which includes the contribution of both interfacial roughness and interfacial diffusion. These two contributions cannot be distinguished by specular reflectivity measurement and for that non-specular or diffused reflectivity has been measured on the samples in the "Detector Scan" geometry, as described above.

The non specular or diffused reflectivity is presented here in terms of the quantity $\frac{1}{I_0}\left(\frac{dI}{d\Omega}\right)$, where dI is the intensity of X-rays scattered from the sample within a solid angle $d\Omega$ made by the illuminated portion of the detector at the point of incidence on the sample surface (3 x 10^{-5} Sr in our measurement setting as defined by the slit width) and I_0 is the incident intensity.

In each case, the measured data were fitted with theoretical diffused reflectivity spectra as discussed in the previous chapter and using this technique five fitting parameters: the interface roughness (σ_r), interface diffusion (σ_d), the in-plane or parallel correlation length ($\xi_{\parallel}$), vertical or perpendicular correlation length ($\xi_{\perp}$), jaggedness factor (*h*) can be measured.

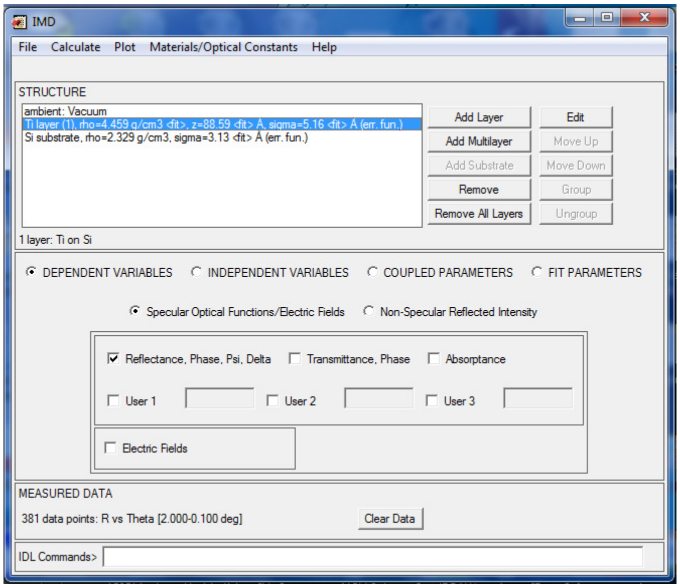

STRUCTURE

ambient: Vacuum
Ti layer (1), rho=4.459 g/cm3 <fit>, z=88.59 <fit> Å, sigma=5.16 <fit> Å (err. fun.)
Si substrate, rho=2.329 g/cm3, sigma=3.13 <fit> Å (err. fun.)

1 layer: Ti on Si

● DEPENDENT VARIABLES ○ INDEPENDENT VARIABLES ○ COUPLED PARAMETERS ○ FIT PARAMETERS

● Specular Optical Functions/Electric Fields ○ Non-Specular Reflected Intensity

☑ Reflectance, Phase, Psi, Delta ☐ Transmittance, Phase ☐ Absorptance

☐ User 1 ☐ User 2 ☐ User 3

☐ Electric Fields

MEASURED DATA

381 data points: R vs Theta [2.000-0.100 deg]

Fig. 3.24: Screen shot of 'IMD' program under 'XOP' package

It should be mentioned here that theoretical simulation and fitting of both specular and diffused reflectivity spectra have been carried out using the "IMD" code as shown in Fig. 3.24 under the "XOP" software package [57] and the best fits are achieved by minimizing the χ^2 value.

3.4.2 Polarized neutron reflectrometry (PNR)

Polarized Neutron Reflectrometry (PNR) is a complementary technique to X-ray reflectivity demonstrated first time used by Fermi and Zinn [80] for measuring the coherent scattering length of different materials. Similar to X-rays, as described in the previous chapter the refractive index of most of the materials for thermal and cold neutron is <1. So the neutron reflectivity of a bulk material is ~1 up to the critical angle and after that it falls rapidly. Similar to the case of X-ray reflectivity, in neutron reflectivity pattern of a thin film also Kiessig oscillations are observed which depend on the thickness of the film. However, as discussed previously unlike X-ray the refractive index of the neutron depends on the coherent scattering length density of the material due to neutron nuclear interaction. The spin of the neutron also interact with the magnetic field created by the unpaired electron of the magnetic material. So in the presence of magnetic field, a magnetic material can have different refractive index for different spin polarization of neutron. So by measuring the polarized neutron reflectivity (PNR) along with the structural parameter like thickness, density, roughness the magnetic structure of the film can also be measured. Also, neutron possesses a magnetic moment of -1.91 μN (nuclear magneton) and so PNR is ideally suited for understanding and depth profiling magnetic structure of thin film and multilayer samples which was first reported by Felcher et. al [81].

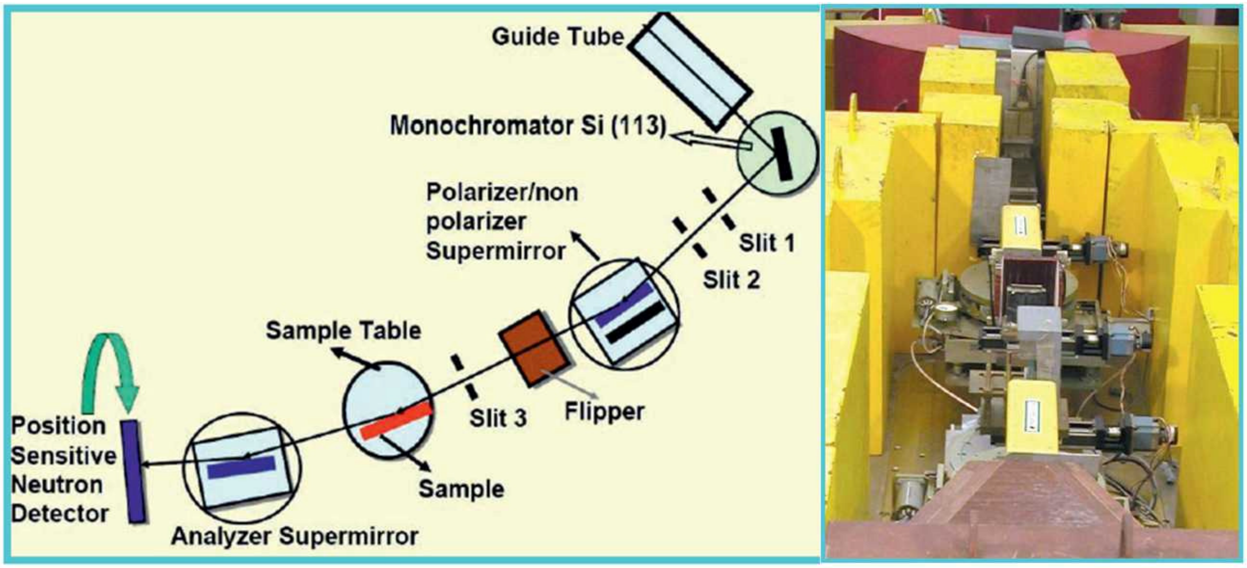

Fig. 3.25: Schematic diagram and actual photograph of Polarized Neutron Reflectivity (PNR) measurement instrument at DHRUVA research reactor BARC Trombay.

In this thesis work, most of the PNR measurements have been carried out at the Polarized Neutron Reflectometer in DHRUVA reactor of Bhabha Atomic Research Center, Mumbai. The photograph and the schematic diagram of the reflectometer are shown in the Fig. 3.25 [82]. Neutron beam of 2.5Å wavelength is used in this reflectometer which is polarized by a FeCo/TiZr supermirror polarizer, subsequently it passes through a DC flipper which helps the measurement of up and down spin simultaneously by reversing the spin of neutrons. The sample is mounted on a high precision goniometer where an external magnetic field is also applied on the sample using a permanent magnet. The reflected neutron beam is detected by a linear He^3 position sensitive detector (PSD).

Some of the neutron reflectivity measurements described in this thesis work have also been done at T3 neutron reflectometer at ILL Grenoble France (www.ill.eu). All the neutron reflectivity measured data have been fitted using *Parratt32* [83] software by the χ^2 minimization technique.

3.4.3 Spectroscopic ellipsometry (SE)

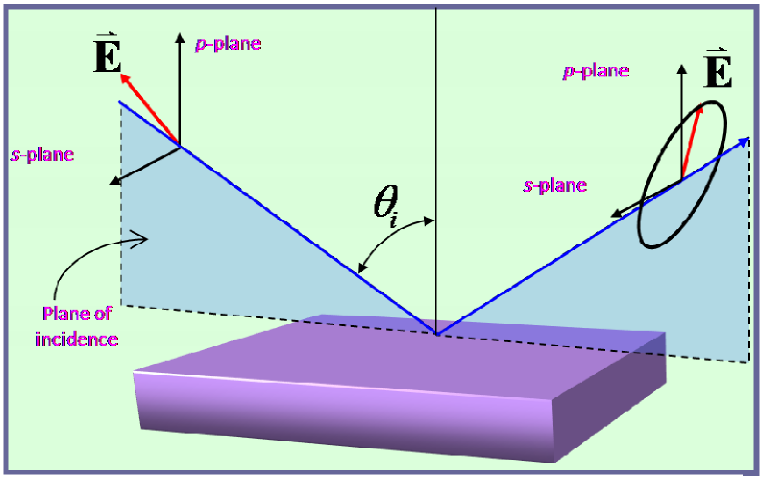

Fig. 3.26: Schematic representation of ellipsometric measured parameter

Unlike the above two techniques spectroscopic ellipsometer use visible light as a probe for characterizing thin film. Since X-ray reflectivity pattern depends strongly on the contrast in electron density (and hence in physical density) of a thin film and its substrate, in some cases like amorphous silicon or carbon film deposited on crystalline silicon wafer, X-ray reflectivity pattern is of no use for determination of the thickness or roughness of the films. However in such cases, since their refractive indices are quite different in visible range, spectroscopic ellipsometry can be used very efficiently.

In ellipsometry, the variation of the amplitude and phase difference between the parallel (*p*) and the perpendicular (*s*) components of the reflected light polarized with respect to the plane of incidence are measured by the two quantities, viz. ψ (which measures the amplitude ratio) and Δ (which measures the relative phase change) as shown schematically in Fig 3.26. These are given by [84]:

$$\rho = {}^{r_p}/_{r_s} = \tan\psi \exp(i\Delta)$$

where r_p and r_s are the reflection coefficients for the *p* and *s* component of the waves respectively. In the phase modulated ellipsometry technique used here [85, 86], the reflected light is modulated by a photo-elastic modulator, which induces a sinusoidal phase shift $\delta(t)$ between the two waves polarized parallel and perpendicular to the strain axis and the modulated signal takes the general form :

$$I(\lambda, t) = I_0 + I_s \sin\delta(t) + I_c \cos\delta(t)$$

where, $\delta(t) = A_0 \sin\omega t$ and A_0 is the modulation amplitude which is proportional to (V_m/λ), V_m being the excitation voltage, λ is the wavelength of light and ω is the modulation frequency (50 kHz in our case) and for the present set of measurements with M=0°, P=45° and A= 45°,

$$I_0 = 1$$

$$I_S = \sin 2\psi \sin\Delta$$

$$I_c = \sin 2\psi \cos\Delta$$

A, P and M being the respective orientations of the analyzer, polarizer and modulator with respect to the plane of incidence. The detected signal is Fourier analyzed to determine the parameters I_s and I_c, which in turn generate the parameters of interest, viz., ψ and Δ.

Assuming the proper dispersion formula of refractive index for thin film and substrate and a model sample structure, theoretical ellipsometric spectra are generated and the measured ellipsometric spectra are fitted by minimizing the squared difference (χ^2) between the measured and theoretically simulated values of the ellipsometric parameters (I_s and I_c) given by:

$$\chi^2 = \frac{1}{2N-P}\sum_{i=1}^{N}\left[\left(I_{s_i}^{exp} - I_{s_i}^{cal}\right)^2 + \left(I_{c_i}^{exp} - I_{c_i}^{cal}\right)^2\right]$$

where, N is the number of data points and P is the number of model parameters. The maximum number of iterations allowed is 100 and the criteria for convergence used is $\chi^2 = 110^{-6}$. For layers containing voids, the calculation of the effective dielectric constant has been done using Bruggeman Effective Medium Approximation (EMA) model [87]. The sub-layer thicknesses,

Fig. 3.27: Photograph of the spectroscopic ellipsometer

volume fractions of void present and the parameters of optical dispersion relations have been used as fitting parameters.

In this thesis work Spectroscopic Ellipsometry measurements are done in a spectroscopic phase-modulated ellipsometer (ISA JOBIN-YVON SPEX, France) in the wavelength range of 300-1200 nm is shown in Fig 3.27. In this ellipsometer, the reflected light is modulated by a photo-elastic modulator. The modulator is actually a fused silica bar which is subjected to periodical stress induced by a piezoelectric transducer. The stress creates an optical anisotropy in the silica bar. As a result, the refractive index corresponding to a light beam with its polarisation parallel to the strain, differs from the index corresponding to a beam with its polarisation perpendicular to the stress. Since the strain is modulated, the emerging beam will also have its polarisation modulated. Conventional ellipsometry technique suffer from the drawback of slow data acquisition process, however, the Phase Modulated Ellipsometry technique employed in this study, offers fast and precise data acquisition over a wide wavelength range.

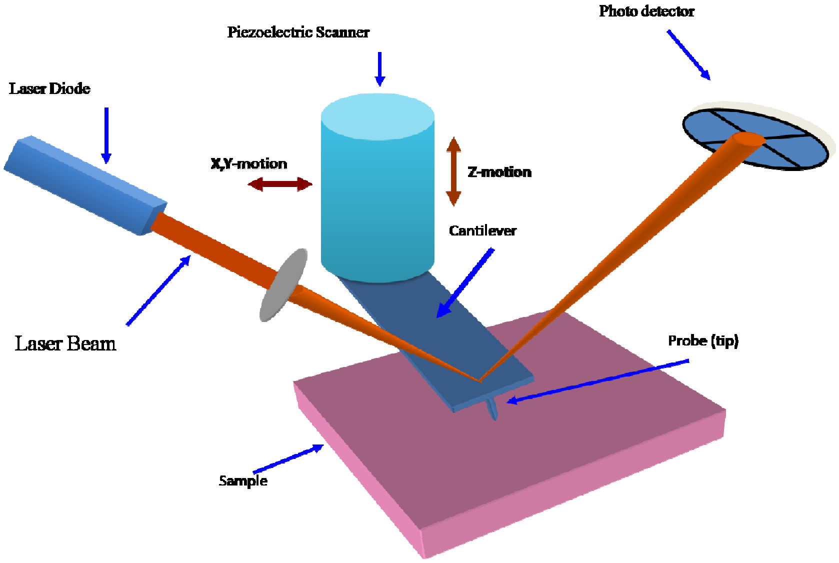

Fig. 3.28: Technique for measuring surface morphology by atomic force (AFM)

3.4.4 Atomic force microscopy (AFM)

Atomic Force Microscopy (AFM) provides quantitative topographic images of surfaces by using a sharp tip which is scanned over the specimen to sense surface forces. Though in principle, either attractive or repulsive forces between the tip and surface can be used for imaging, in practice, the repulsive force mode is predominantly used because it is more stable. The microscopic image produced by AFM is that of a surface, representing the locus of points of constant force between the tip and the specimen. Although functionally similar to a stylus surface profilometer, AFM utilizes much smaller forces between tip and surface (typically 0.1 μN) and the small radius of curvature of the tip (0.03 μm) which gives better spatial resolution. The tip is usually held stationary and the sample is scanned using piezoelectric transducers. An important feature of AFM is its ability to image non-conducting surfaces, whereas the Scanning Tunneling Microscope (STM) requires a conducting surface capable of sustaining a stable tunneling current.

Fig. 3.29: Actual photograph of AFM of our lab

The principle of the AFM microscope is shown schematically in Fig. 3.28. The sample is scanned by a small cantilever of typical length between 100–300 μm, width about 30 μm and holding a sharp pyramidal tip at its end. Such a microprobe senses attractive or repulsive forces while scanned on the surface of a sample and in order to maintain the constant force it gets deflected during scanning. The deflection is most often detected by the laser beam reflected from the back side of the cantilever onto a position sensitive detector. During the measurement the sample or cantilever is moved in X–Y plane by piezoelectric actuators. The whole image is then created in the computer by putting the line–scans together.

In this work, AFM measurements have been carried out in the Solver P-47H multimode AFM system (NT-MDT, Russia) as shown in Fig 3.29. The robust contact mode of the AFM with a soft cantilever of low force constant (0.6 N/m) and low resonance frequency (75kHz) have been chosen for the efficient topographic measurements of thin films [88]. The acquired AFM images have been used to extract surface statistical parameters such as surface roughness, skewness, kurtosis, etc. after a scrupulous software correction from the measured images.

3.5 Summary

Among the various available deposition techniques used in thin film deposition, sputtering is the most efficient and widely used technique for the development of thin film multilayer devices for reflecting neutrons and X-rays due to the stringent requirement of low surface roughness and good interface quality of these devices and hence different sputtering techniques have been used for preparation of thin films and multilayers in this thesis work, the working principles of which have been briefly described here.

During this thesis work, a 9 meter long DC/RF magnetron sputtering system has been designed and developed in-house and commissioned in our laboratory for fabrication of hard X-ray mirror and neutron supermirrors. The coating system has provisions for in-situ to & fro substrate scanning mechanism during deposition so an area of 1500 mm x 150 mm can be deposited uniformly with a thickness variation of <5%. The system is equipped with a load-lock chamber and all other essential gadgets required for good quality thin film deposition and single layer metallic films of Co and Ti with very low roughness and bulk-like density could be prepared in this system. All the gadgets have been interfaced with computer and a robust process control software has been developed so that multilayer thin films with more than 500 layers can be deposited as per a user-defined design within a reasonable time frame.

The thin film and multilayer samples deposited in this work are mostly characterized by specular and non-specular X-ray reflectivity, polarized neutron reflectivity, spectroscopic ellipsometry and atomic force microscopy measurements. All these techniques along with the methodology for data analysis are described here in brief.

CHAPTER 4

Design and fabrication of m=2.5 Co/Ti neutron supermirror polarizer

4.1 Introduction

As has been mentioned in Chapter 2, a supermirror is a thin film non-periodic multilayer device of hundreds of alternate layers of two materials having contrast in their neutron scattering length densities, where the thickness of a bilayer or the *d*-value of the multilayer gradually increases from the substrate to the top of the device [9]. It can thus be conceived as a stack of several multilayers having their individual Bragg peaks whose positions vary continuously and the closely spaced superimposed Bragg peaks push the critical angle of total external reflection by a large extent compared to a single layer film. As discussed previously by choosing proper ferromagnetic and non-magnetic material combination, like Co and Ti, supermirrors can be made such that in presence of magnetic field, neutrons having spins parallel to the magnetic field would face strong scattering length contrast and get reflected, while neutrons having spins anti-parallel to the magnetic field would get transmitted [11, 89]. This can be used as polarizer or analyzer in neutron experiment for separating nuclear and magnetic scattering from a material [20], achieving high energy resolution in neutron spin echo spectrometer [21] and different neutron experiments using polarized neutrons. Mezei [9, 10] first demonstrated the design and fabrication of Fe/Ag neutron supermirror polarizer using electron beam evaporation method.

However, as have been discussed in Chapter 3, compared to evaporation method in sputtering techniques, the energy of the adatoms are generally high enough (~10 eV) so that adatoms can re-organise themselves on the surface of the growing films leading to smoother two-dimensional growth. Hence, presently different variants of sputtering technology are generally used to realize these multilayers [15, 90-92]. Some of the researchers have reported deposition of very large m-value supermirrors by Ion Beam Sputtering (IBS) technique [90, 91]. In spite of several advantages of IBS technique like low air pressure plasma, higher stability of process and non-contact of plasma with deposited film as discussed in previous chapter, IBS technique is not suitable for large area and high throughput deposition due to the enormous cost involved in procurement of large size ion guns and low deposition rate of the ion beam sputtering process. DC magnetron sputtering which can yield higher sputtering rate and which has easy scalability and provisions for reactive sputtering in various gaseous ambience is thus a preferred technique for depositing these multilayer neutron supermirrors for actual applications [15, 92].

In this chapter, the design, fabrication of high m-value Co/Ti multilayer supermirror neutron polarizers using the in-house developed 9 m long in-line DC magnetron sputtering system (discussed in the previous chapter) are presented [78]. These supermirrors are characterized by Polarized Neutron Reflectivity (PNR) measurement at DHRUVA reactor at Bhabha Atomic Research Center, Mumbai [82]. Though there are some reports on optimization of process parameters for neutron supermirror polarizers [15, 89, 92-94], reports with the details of process development and optimization of an in-line sputtering system for development of large area supermirrors are scanty. In some report the initial development of the Co/Ti supermirror polarizers using electron beam evaporation method [14, 89] has been described, however deliberations on the development of Co/Ti supermirror by magnetron sputtering technique are not available in the literature.

4.2 Design of neutron supermirror

Mezei *et. al.* [9] first gave the design structure of the supermirror for increasing the critical angle of total external reflection as well as spin polarization of neutrons. His design is based on the idea of continuously depth graded multilayer such that successive bilayers vary in thickness. The thickness is chosen by a method analogous to that used in the design of broad band filter for visble optics as following:

$$d(n) = d_c/n^{1/4} \tag{4.1}$$

where $d(n)$ is the n^{th} bilayer thickness in the structure and d_c is the constant equal to 280Å for Fe ferromagnetic layer for a supermirror polarizer. Using this structure, Mezei *et. al.* [9] first demonstrated Fe/Ag multilayer supermirror polarizer using an electron beam evaporation system, though it was not very satisfactory. Soon after that Ebisawa *et. al.* [95] also proposed another design structure like

$$t_j - t_{j+1} = 5\text{Å}\left(\frac{195\text{Å}}{t_j}\right)^{-2} \qquad t_1 = 195\text{Å} \tag{4.2}$$

where, t_j represent the j^{th} layer from the substrate. Using this structure Ni/Mn supermirror with low ‘m-value’ has been demonstrated. These derivations of the supermirror layer sequence are based only on the real part of the neutron refractive index of the materials. However, in case of high-m supermirrors the effect of extinction becomes significant which affects the maximum achievable reflectivity. Since then different design structures have been proposed for achieving high reflectivity in the case of high-m supermirrors [50, 96, 97]. Among them the most frequently used is the Hayter and Mook model [50].

4.2.1 Development of design program using Hayter and Mook model

Hayter and Mook [50], have proposed a discrete thin film multilayer (DTFM) model where the thickness of successive layers change by discrete amount instead of varying continuously and the stack of the supermirror is constructed by choosing the thickness of successive bi-layer such a way that their reflectivity profile intersects at half height point as following.

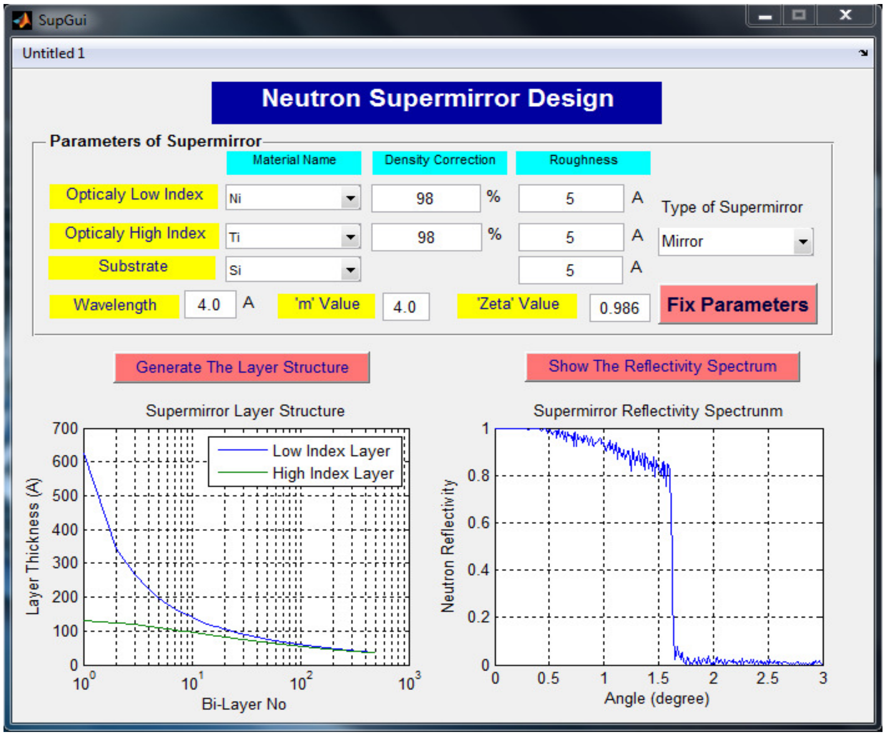

	Material Name	Density Correction	Roughness
Opticaly Low Index	Ni	98 %	5 A
Opticaly High Index	Ti	98 %	5 A
Substrate	Si		5 A

Type of Supermirror: Mirror

Wavelength: 4.0 A
'm' Value: 4.0
'Zeta' Value: 0.986

Fig. 4.1: Screen shot of the in-house developed neutron supermirror design program

$$\tau_k - \Delta\tau_k^- = \tau_{k-1} + \Delta\tau_{k-1}^+ \tag{4.3}$$

Where, τ_k is the scaled grazing angle of incidence at the kth bilayer corresponding to the Bragg condition and

$$\tau_k \pm \Delta\tau_k^\pm = \{4(\omega_k \pm \Delta\omega_k)^2 \times [(\omega_k \pm \Delta\omega_k)^2 + 1] - h_1^2\}^{1/2} \times [2(\omega_k \pm \Delta\omega_k)]^{-1}$$

where $\Delta\omega_k = \left(\frac{2\omega_k}{\pi}\right)\sin^{-1}\left(\frac{3\bar{\rho}_k}{2\sqrt{2}}\right)$, $\tau_k = \frac{\theta_k}{\gamma_1}$, $\omega_k = \frac{\Psi_k}{\gamma_1}$, $\gamma_1 = \sqrt{2\alpha_1}$, $n_1 = 1 - \alpha_1 + \beta_1$, $h_1 = \frac{\beta_1}{\alpha_1}$, θ_k is the grazing angle of incidence from air corresponding to the Bragg condition. During this calculation a parameter ζ is taken which is equivalent to the reflectance level to be achieved by the supermirror and $\bar{\rho}_k$ is the effective reflectivity of the kth bilayer in the aperiodic supermirror which is calculated using the parameter ζ. Equ.(4.3) is solved by Newton iteration method to calculate ω_k starting with $\tau_0 + \Delta\tau_0^+ = 3/2\sqrt{2}$ which is defined by the intersection of the profile of the thickest bilayer and the critical edge of the additional capping layer. Using this ω_k value, the value of ψ_k, which is the grazing angle of incidence at the kth bilayer corresponding to the Bragg condition, is derived, and then thickness of one layer (optical index n_1) of the kth bi-layer is calculated using the following relation such that each layer is a λ/4 plate:

$$d_k^{n_1} = \frac{\lambda_0}{4\Psi_k} \qquad (4.4)$$

Subsequently, using Snell's law ψ_k for the second material (optical index n_2) is calculated and $d_k^{n_2}$ is derived using eqn. (4.4), so that it is also a λ/4 plate.

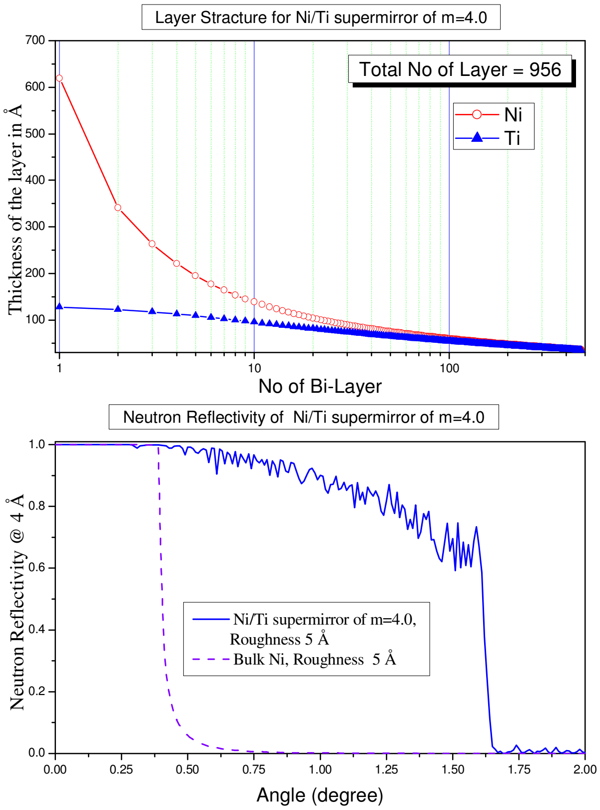

Fig. 4.2: Layer structure and neutron reflectivity of m=4.0 Ni/Ti neutron supermirror

Following this, thickness of each layers in successive bilayers are calculated and the program is terminated according to the desired 'm-value' of the supermirror such that:

$$d_k^{n_1} + d_k^{n_2} = \frac{2\pi}{m \times 0.022} \text{Å} \qquad (4.5)$$

Under this thesis work, a graphical user interface (GUI) based user friendly computer program has been developed using MATLAB to design the supermirror stack following the Hayter and Mook method described above [98]. The flow chart of the program and MATLAB code is given in the Appendix B while the screen shot of this program is shown in the Fig. 4.1. In the same GUI program, neutron reflectivity pattern of the designed structure can also be simulated by using Parratt formalism described in Chapter 2. Using this program a Ni/Ti supermirror of m=4.0 is designed assuming ζ=0.986 which signifies the reflectance label to be achieved, along with 'm-value' it also decide total number of layer. The designed structure and the simulated neutron reflectivity pattern of this supermirror for neutrons of 4 Å wavelength are shown in Fig. 4.2 assuming 5 Å interface roughness throughout the multilayer structure. It is a multilayer of 956 layers where Ni layer thickness is varying from 36.38 Å at the substrate end to 618.89 Å at the top and similarly Ti layer thickness is varying from 36.35Å to 340.79Å.

4.2.2 Process error analysis

It is obvious that during actual deposition of the multilayer thin films due to fluctuations in process conditions always there is a chance of thickness error. In the above design structure of m=4.0 Ni/Ti supermirror, a random thickness error of ±5%, ±10% and ±20% have been introduced and the reflectivity profiles simulated for neutrons with 4 Å wavelength are compared with that of an ideal supermirror in Fig. 4.3. It is observed that more than ±5% thickness error drastically deteriorates the optical performance of a neutron supermirror [78]. In the in-line sputtering system, described in the previous chapter, this thickness uniformity is mainly controlled by the mechanical repeatability of the substrate trolley motion mechanism and hence significant effort has been given to improve this.

The effect of reflectivity of a supermirror due to some missing layers during the deposition process is also analysed and it is seen that even a single missing layer introduces a hole in the reflectivity spectrum as shown in the Fig. 4.4, it is also shown that if several layers are missed arbitrarily in the structure, the reflectivity spectrum degrade drastically. The above in-house developed custom-made code has been very useful to estimate the process errors, which might have been occurred during deposition of a multilayer supermirror, from the post-deposition analysis of its neutron reflectivity pattern. It should be noted that such a computer code is not available commercially and it is very useful not only to design the structure and

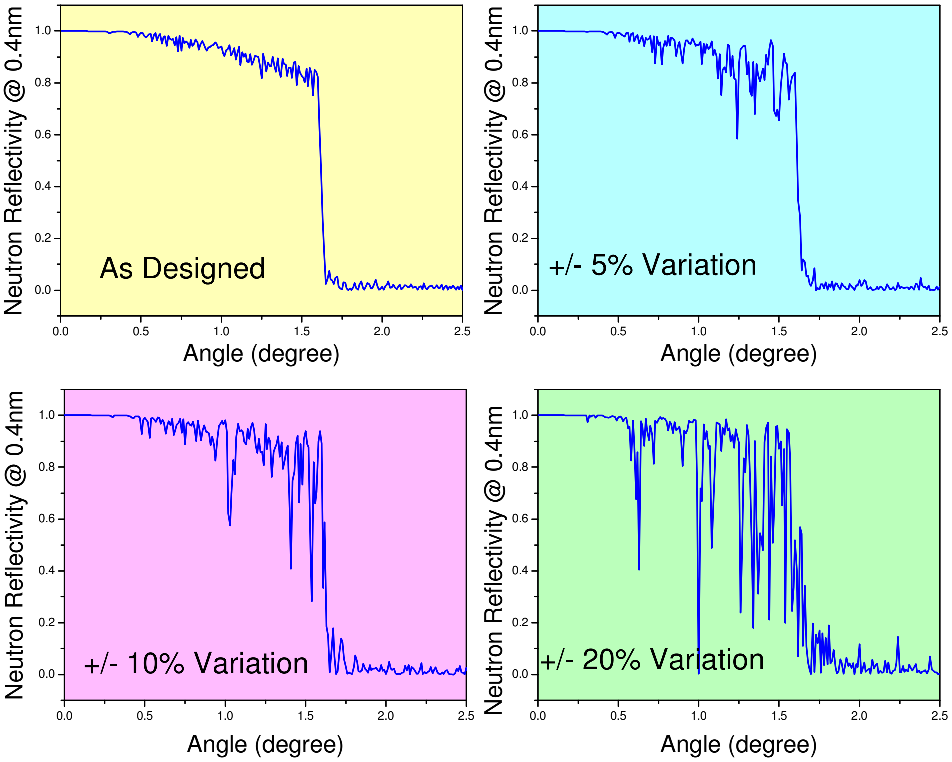

Fig. 4.3: Comparison of neutron reflectivity of as designed Ni/Ti supermirror with ±5%, ±10% and ±20% thickness errors.

simulate the neutron reflectivity pattern but also in reverse engineering during the process optimization.

4.2.3 Design of *m*=2.0, *m*=2.25 and *m*=2.5 Co/Ti supermirror polarizer

Co/Ti is a very unique material combination for fabrication of supermirror polarizer due to its polarizing capability at low angles as pointed out by Stewart *et.al.* [20] since –ve scattering length densities of Ti and Co for spin down neutrons do not support the total external reflection phenomena. Though the use of this material combination is limited by the fact that Co strongly

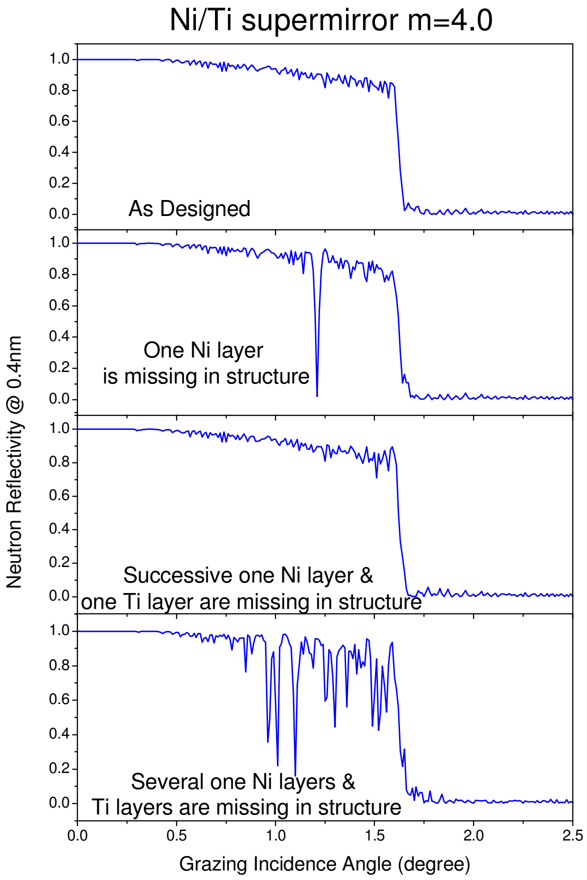

Fig. 4.4: Effect of missing layer on the neutron reflectivity of Ni/Ti supermirror

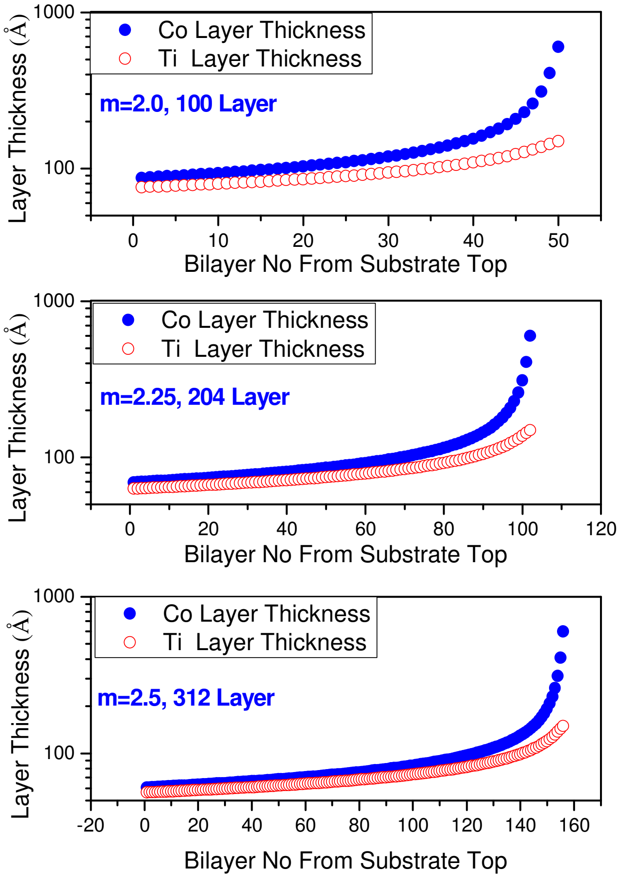

Fig. 4.5: Designed layer structure of m=2.0, m=2.25 and m=2.5 Co/Ti supermirror polarizer

activates in intense neutron flux environment, it can be used as analyzer [20] at neutron flux ~1.5 × 10^6 n cm^{-2} s^{-1} in neutron experiments, where it can isolate the spin of neutrons at very small grazing angles of reflection which other material combinations like Fe/Si fails to do.

Using the in-house developed computer code described above, Co/Ti supermirror polarizers of m=2.0, m=2.25 and m=2.5 have been designed and as shown in the Fig 4.5 these require 100, 204 and 312 layer Co/Ti multilayer respectively. The variations of the Co and Ti layer thickness with layer number for the all three supermirrors are also shown in the above figure. It is seen that in this structure Ti layer thickness is always less than the Co layer thickness in a Co/Ti bilayer. According to Hayter and Mook model [50] the optical thickness of every layer would be $\lambda/4$ for a particular angle of incidence. This makes Ti thinner as it has higher neutron refractive index than Co. Initially thin Co and Ti layer thicknesses are very close as they correspond to the high grazing angle of incidence. However the top few thick layers have large thickness difference as they correspond to very low grazing angle of incidence.

4.3 Fabrication of Co/Ti supermirror polarizer

4.3.1 Process optimization

9 meter long in-line DC/RF sputtering system described in the previous chapter is used for the fabrication of Co/Ti supermirror polarizer [78, 98]. Initially, gas flow rates were optimized so as to obtain a sustainable plasma with no arcing and the optimized gas flow rates of 40 mL min^{-1} and 100 mL min^{-1} have been obtained for Ti and Co respectively. The flow rates are different for the two elements as ions in the plasma behave differently for the non-magnetic and magnetic targets fixed on similar magnetron cathodes. In these flow rates, stable and uninterrupted plasma has been observed and several films have been deposited at different d.c.

power levels at a constant substrate trolley speed of 34 mm s^{-1}. The films deposited have been characterized by measuring grazing incidence X-ray reflectivity (GIXR) spectra at 1.54Å wavelength and the thickness, density and top surface roughness have been estimated. In Fig. 4.6(a) the variation of thickness of Ti films deposited per pass of the substrate trolley with cathode power is shown. It is clear from this figure that the rate of deposition increases linearly with cathode power which confirms the linearity of this plasma system. In Fig. 4.6(b) the top surface roughness and the total thickness of the above films deposited at different DC power levels are shown which shows that we are able to deposit films with very low roughness using

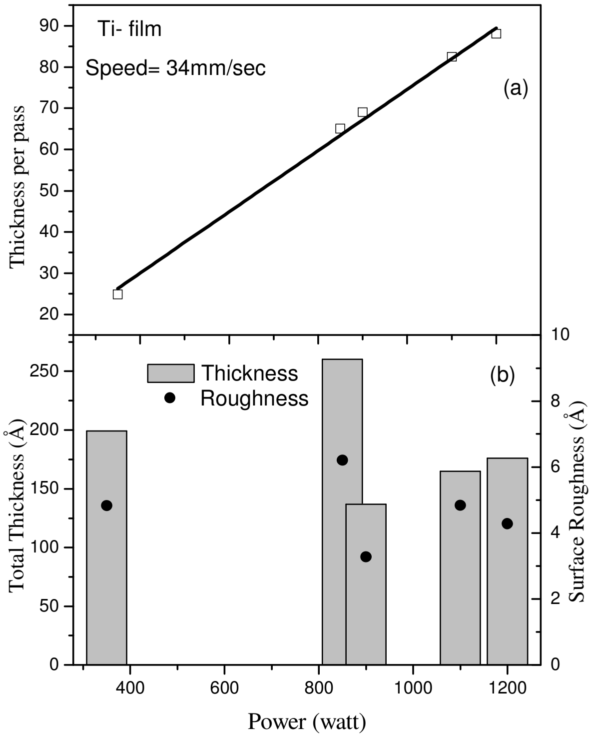

Fig. 4.6: (a) Variation of thickness of Ti films deposited per pass of substrate trolley as a function of magnetron power along with least square linear fit. (b) Variation of top surface roughness of Ti films as a function of magnetron power

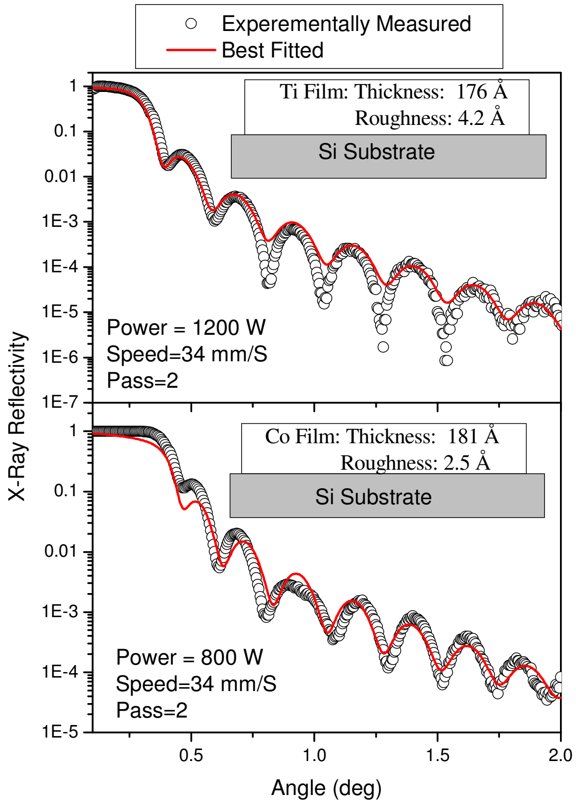

Fig. 4.7: GIXR spectra along with best fit theoretical spectra of Ti and Co films deposited at optimized deposition conditions.

the present deposition system which is very important for the fabrication of thin film multilayer neutron optical devices. It further shows that roughness does not increase in proportionality to the thickness of the films which implies two-dimensional non-columnar growth of the films.

Subsequently, the d.c. power levels of the magnetron cathodes have been optimized for both Co and Ti. The consideration of this optimisation has been the ability to deposit minimum thickness of the smooth and continuous film per pass of the substrate trolley which is a requirement for high m-value neutron supermirror where films of very low thickness have to be deposited. The time spent in each pass of the substrate trolley is again governed by the lower and upper limits of its speed for having smooth and jerk-free motion. The optimized power of deposition for Ti films has been found to be 1200 W while that for Co films is found to be 800 W. In Fig.4.7, the GIXR spectra of the Ti and Co films deposited at these selected powers with 34 mm s^{-1} substrate trolley speed and two passes of the substrate trolley are shown along with their best fit theoretical spectra [78].

4.3.2 Speed calibration of substrate trolley

Subsequently, the thickness of the films deposited has been calibrated with the speed of the substrate trolley required for a particular layer during fabrication of a multilayer supermirror. Three 20 layers Co/Ti periodic multilayers have been deposited with three different substrate trolley speeds i.e. 34 mm s^{-1}, 51 mm s^{-1} and 68 mm s^{-1} respectively in which every layer of Co and Ti is deposited by a single pass of the substrate trolley. In Fig. 4.8, GIXR spectra of the above three periodic multilayer samples are shown along with their best fit theoretical spectra. It can be observed from fig. 4.8 that several Kisseig oscillations arising from the total thickness of the multilayer are observed in the figure alongwith few Bragg peaks correspding to the different order of reflections of X-rays by the peroiodic multilayers as has been discussed in detail in Section 2.3.3 of Chapter 2. By fitting the experimentally measured spectra thickness of every layer, top surface roughness and interface roughness are estimated. In Fig. 4.9(a) the measured thicknesses of individual layers of Co and Ti are plotted with inverse of trolley speed. In both the cases it can be seen that the dependence is linear which again establishes the reproducibility of the deposition system. The slope of the linear curve gives the dynamic rate of deposition at this condition; for Co it is found to be 2987.1 Å mm sec^{-1} and for Ti it is found to be 2652 Å mm sec^{-1}. As shown in the Fig. 4.9(a), the intercept of the straight line on the zero speed^{-1} axis is +4.21 Å for Co and -2 Å for Ti. Similar observations have also been found by Høghøj et. al. [15] for Fe/Si periodic multilayer by GIXR technique and Houdy et.al. [99] for W/Si multilayer by

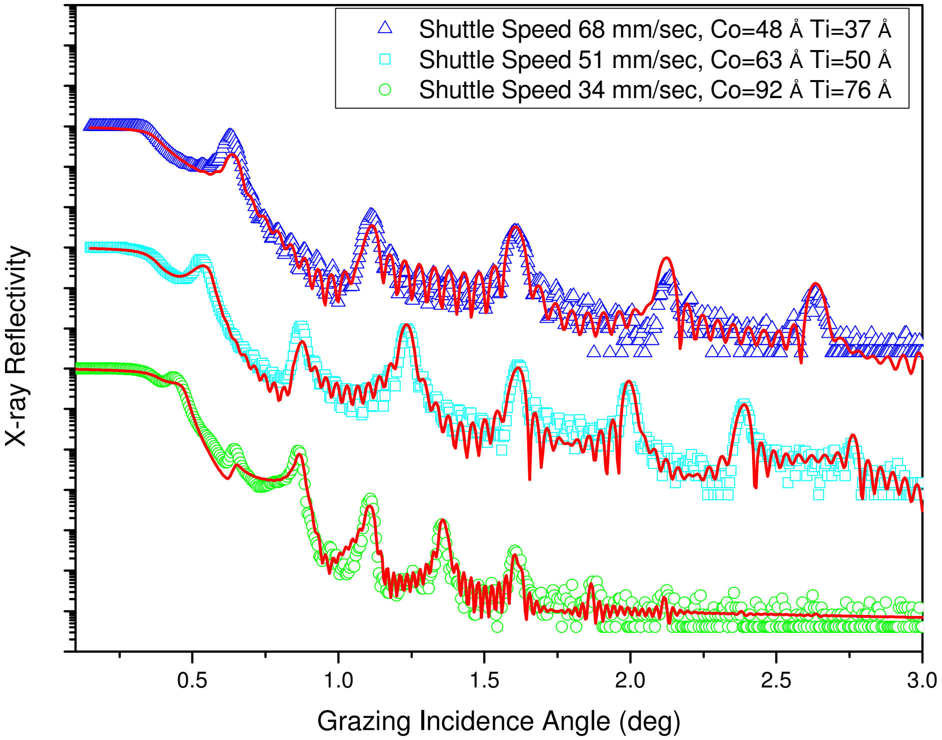

Fig. 4.8: GIXR spectra of 20 layer Co/Ti periodic multilayer samples deposited at three different substrate trolley speeds viz., 68 mm s^{-1}, 51 mm s^{-1} and 34 mm s^{-1} along with best fit theoretical spectra.

ellipsometric technique. This offset, known as the "growth offset" arises due to the inter-diffusion at the interface of Co and Ti and the opposite signs of growth offset for Co and Ti is due to the asymmetry of diffusion at the Co-on-Ti and Ti-on-Co interfaces [78]. The diffusion of one material into the other is controlled by relative values of surface free energy of the materials. As Ti has lower surface free energy of 2.1 J/m^2 than 2.5 J/m^2 of Co, Co diffuses more at the Co-on-Ti interface compared to Ti at Ti-on-Co interface. It can also be explained in this way that due to the high density i.e. lower size of Co atom it penetrates more in to the Ti layer than Ti into the Co layer. This phenomenon decreases the effective thickness of Ti in the multilayer structure and increases the effective thickness of Co. Similar phenomena of asymmetric diffusion have also been found in our reports on ion beam sputtered deposited W/Si multilayer [100] and RF sputtered Ni/Ti multilayer [101].

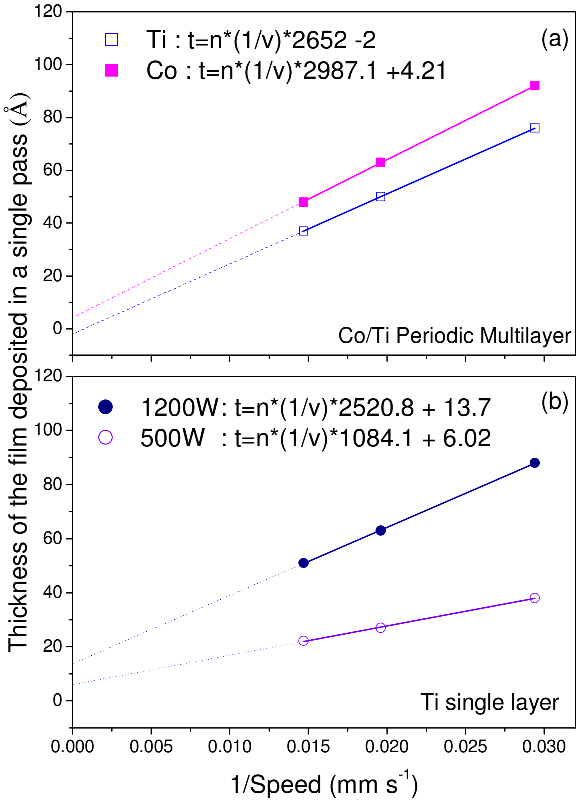

Fig. 4.9: Measurement of dynamic rate and growth off-set for (a) Co and Ti layers in Co/Ti multilayer (b) Ti in single layer film deposited on Si substrate.

In order to investigate the initial growth of Ti film, similar experiments have been carried out for single layer Ti film deposited on crystalline Si (111) substrate at two different d.c power (i.e., at two different rates of deposition) levels keeping all the other parameters same. In Fig. 4.9(b), thickness of two set of single layer Ti films has been plotted as a function of speed^{-1}. In both the cases, linear relations have been found which again confirm the repeatability of the deposition system. The dynamic deposition rates found for 1200 W and 500 W d.c. power levels are 2520.8 Å mm sec^{-1} and 1084.1 Å mm sec^{-1} respectively and the growth offsets are 13.7 Å and 6.02 Å respectively. The higher dynamic deposition rate for 1200 W is due to increase in rate of deposition which is well understood for sputtering. On the other hand, the positive values of growth off-set signifies that for both the d.c. power levels, the initial rate of growth of the film i.e. just adjacent to the substrate surface is higher compared to the region away from the substrate surface. This may be due to the trapping of voids during initial growth of Ti film on the Si(111) substrate, as in this case, island-like growth is more favorable than layer by layer growth. Similar observations have been made by Yang et.al. in case of Ge film [102], where ellipsometric measurements show different optical constant of the material at the film-air interface and at the film-substrate interface which has been attributed to trapping of voids during the initial growth of the film which creates the growth off-set as shown in the Fig. 4.9(b). The higher value of growth off-sets for 1200 W power in this case may be due to higher rate of deposition. This higher value of growth off-set obtained at higher power suggests that that for depositing very low thickness films, lower magnetron power with low speed of substrate trolley is more preferable compared to high substrate speed and higher magnetron power for this in-line sputtering system.

4.3.3 Deposition of m=2.0, 2.25 and 2.5 Co/Ti supermirror polarizer

Supermirror polarizers of m=2.0 (100 layers), m=2.25(204 layers) and m=2.5 (312 layers) have been designed using the in-house developed computer code as shown in Fig. 4.5, the material property table and the layer information table have been generated and the multilayers have been deposited using the automatic in-line dc sputtering system described in the previous chapter. The depositions have been carried out using the previously described in-house developed process control software on 2 inch diameter silicon substrate and 240 mm x 140 mm glass substrates with maximum 6 substrates loaded at a single shot. Subsequent to the deposition, the supermirror polarizers have been characterized by measuring Polarized Neutron Reflectivity (PNR) with neutron beam of 2.5 Å wavelength at DHRUVA reactor BARC, India; the details of the reflectrometer [82] have been described in Chapter 3. The reflectivity spectra of the supermirrors, both for up-polarised neutrons ($R_{\uparrow}$) and down polarised neutrons ($R_{\downarrow}$) are shown in the Fig. 4.10 which shows that for m=2.0 supermirror, the reflectivity value decreases gradually with increase in q_z and at cut-off value of q_z reflectivity is ~70% which agrees well with the reflectivity pattern obtained by other workers on similar supermirror structures [20].

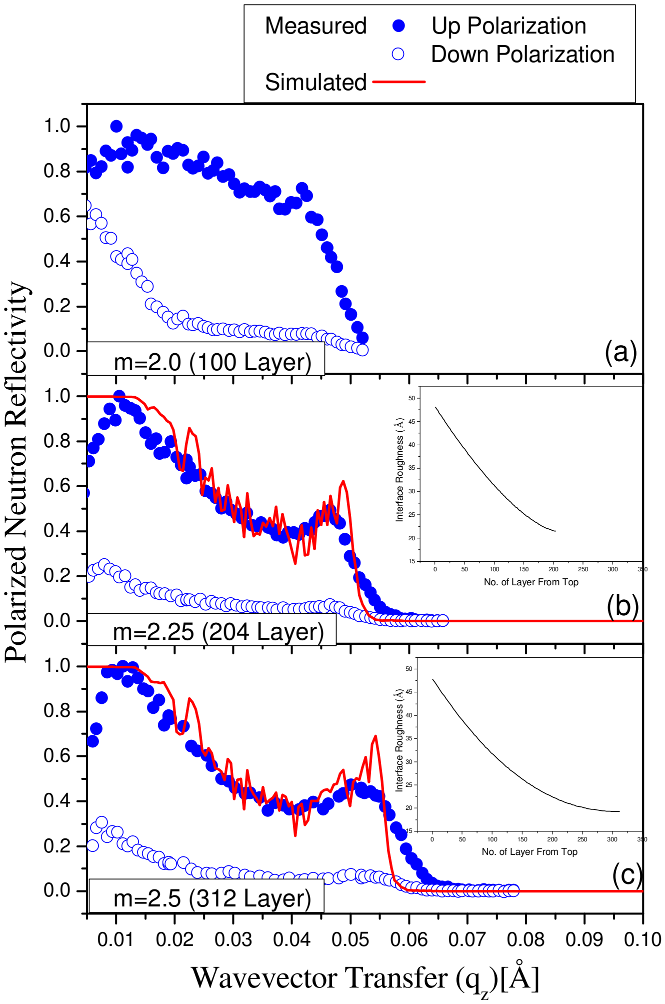

Fig 4.10: Polarized neutron reflectivity of (a) m=2.0, (b) m=2.25 and (c) m=2.5 Co/Ti supermirror polarizer. The interface roughness variation with layer no. required to fit the PNR spectra of the respective supermirrors are shown in the inset of (b) and (c).

However, in case of m=2.25 (204 layers) and m=2.5 (312 layers) supermirrors, we have observed an oscillatory behaviour in reflectivity pattern where reflectivity gradually falls till a q_z range of ~0.04 Å^{-1} and increases again at higher q_z range before falling off sharply above the respective critical q_z value. In order to analyze the cause of this type of unusual variation of reflectivity, the experimentally measured neutron reflectivity spectra of the above two samples are fitted with theoretically generated spectra. However, fitting of such reflectivity spectrum with standard fitting algorithm is quite impossible because of the large number of fitting parameters i.e., density and thickness of each layer, roughness of each interface etc. Thus the experimental reflectivity patterns have been tried to be simulated with by varying the parameters manually in the in-house developed theoretical reflectivity simulation code described above. Several iterations have been carried out by incorporating errors in thickness in a particular layer or a set of layers, by dropping a layer from the stack etc. However, a reflectivity pattern similar to the experimental one could only be generated when a variable interface roughness is introduced in the multilayer stack in such a way that it increases from layers with lower thickness to layers with higher thickness in a certain fashion. The theoretically generated PNR spectrum of spin-up neutrons for m=2.25 (204 layers) supermirror having stepwise variation of interface roughness from 20 Å to 50 Å with nominal layer thickness structure is shown (straight line) in Fig. 4.10(b) along with the experimental data. In the inset of Fig. 4.10(b) the polynomial fit of the variation of interface roughness with layer number is shown. Similarly in Fig. 4.10(c) the theoretically generated PNR spectrum of spin-up neutrons for m=2.5 (312 layers) supermirror is shown as straight line along with the experimental data. Here the interface roughness is varied stepwise from 17 Å to 50 Å with increase in the thickness of the layers as shown in the inset of Fig.4.10(c). So it is concluded from these two spectra that the interface roughness values for m=2.25 and m=2.5 supermirrors are quite high which is responsible for the unusually oscillatory behaviour in the reflectivity spectra of neutrons.

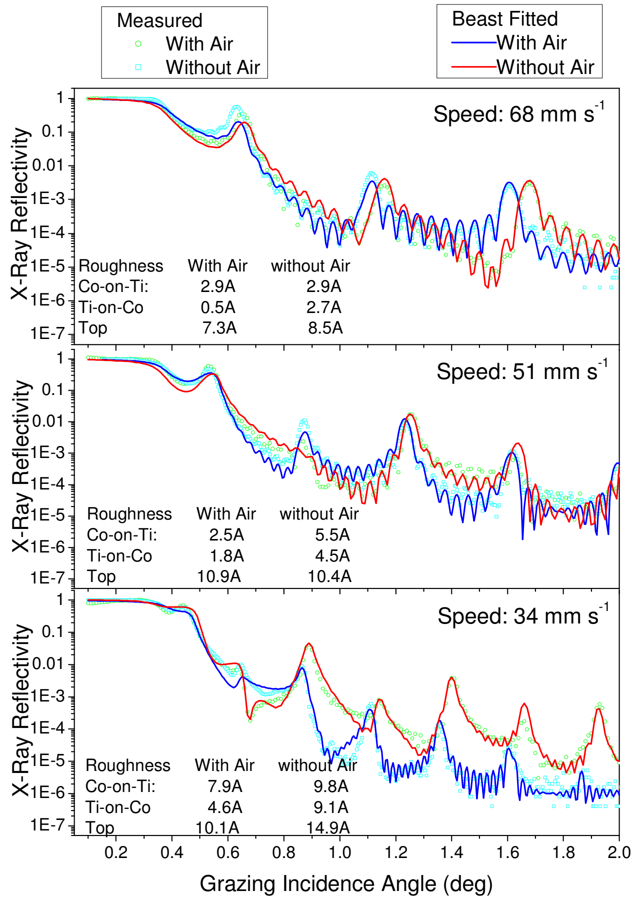

Fig. 4.11: GIXR spectra of 20 layer Co/Ti periodic multilayer samples deposited with air and without air during Co deposition at three different substrate trolley speeds viz., 34 mm s^{-1}, 51 mm s^{-1} and 68 mm s^{-1} along with best fit theoretical spectra.

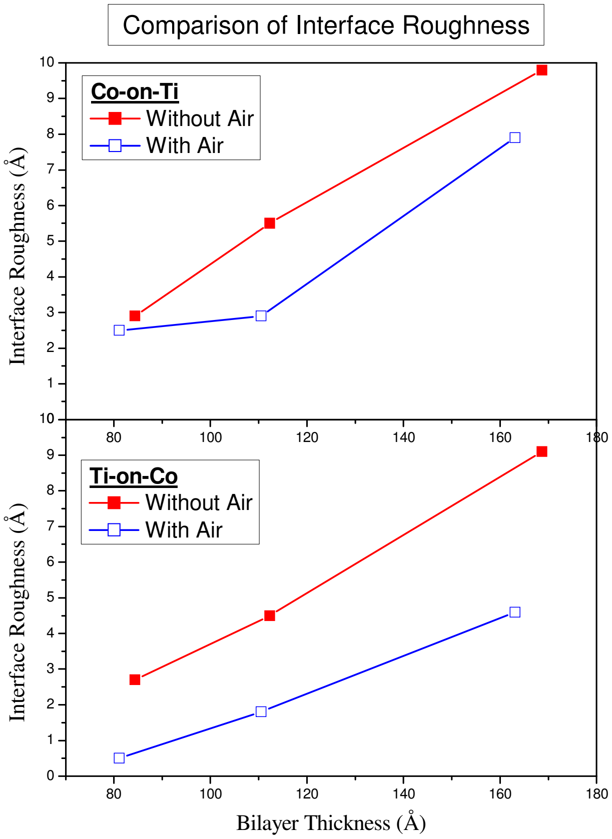

Fig. 4.12: Comparison of measured interface roughness (a) Co-on-Ti and (b) Ti-on-Co, with air and without air in sputtering ambience

However from the X-ray reflectivity measurement of the Co/Ti periodic multilayers, shown in Fig. 4.8, it is found that even for periodic multilayer of 176 Å bi-layer thickness the interface roughness is ~10 Å. So the high value of interface roughness observed in the PNR spectra of the above two supermirrors might be due to magnetic roughness at Co/Ti interface.

Similar observations had also been made by Schärpf *et. al.* [14] for their Co/Ti supermirror deposited by evaporation technique. Diffusion of Co into Ti layer creates a non-magnetic layer at the Co-Ti interface which leads to reduction in magnetic contrast at the interface. Senthil Kumar *et. al* [16] have shown that for FeCoV/Ti multilayer also two magnetic phases exist in the magnetic layer, one in the bulk region and other at the interface, magnetic moment at the interface being less than that inside the bulk. Due to mixing or alloy formation at the interface, this region behaves almost like a non-magnetic material. This is known as magnetic roughness which increases the total interface roughness [14]. In this context, Smardz *et. al.* [103] had studied the variation of magnetization of Co layers in Co/Ti multilayer samples having different Co layer thicknesses, where they have observed that Co layers get fully magnetized like bulk samples only if the thickness of the layers are more than a certain cut-off value. It seems that for Co layers having thickness lower than this, the interface effect dominates and magnetic moments of all Co atoms do not get aligned to the external field.

In order to decrease such magnetic roughness in the interface of magnetic/non-magnetic materials, two techniques have generally been reported in the literature which are described below:

(i) Reactive sputtering technique

Senthil Kumar *et. al.* [92] had demonstrated improvement of reflectivity of Ni/Ti multilayer and m=3.65 (600 layers) Ni/Ti supermirrors by reactive sputtering of Ni layer with synthetic air in their dc magnetron sputtering system.

In order to check the applicability of the above recipe for the present Co/Ti multilayer system, periodic multilayers of 20 layers have been prepared by mixing dry air with argon during the deposition of Co layer. Three multilayer samples have been prepared at three different substrate trolley speeds viz., 34 mm s^{-1}, 51 mm s^{-1} and 68 mm s^{-1} respectively with a single pass of the substrate trolley similar to multilayers shown in Fig 4.8 keeping the power of deposition and all other process conditions same. The samples have subsequently been characterized by GIXR technique at 1.54 Å X-ray wavelength and the measured spectra have been fitted with theoretically simulated spectra using the IMD [57] code as shown in Fig 4.11 and information have been extracted for individual thicknesses of Co and Ti layers, top layer roughness, interface roughness when Co is deposited on Ti (Co-on-Ti) and interface roughness when Ti is deposited on Co (Ti-on-Co). In Fig 4.12 the Co-on-Ti and Ti-on-Co interface roughness found from the best fitted spectra are plotted with bilayer thickness for multilayers deposited with air and without air in sputtering ambience. It is seen that deposition of the Co layer by reactive sputtering under mixed ambience of air and argon decreases the interface roughness of both Co-

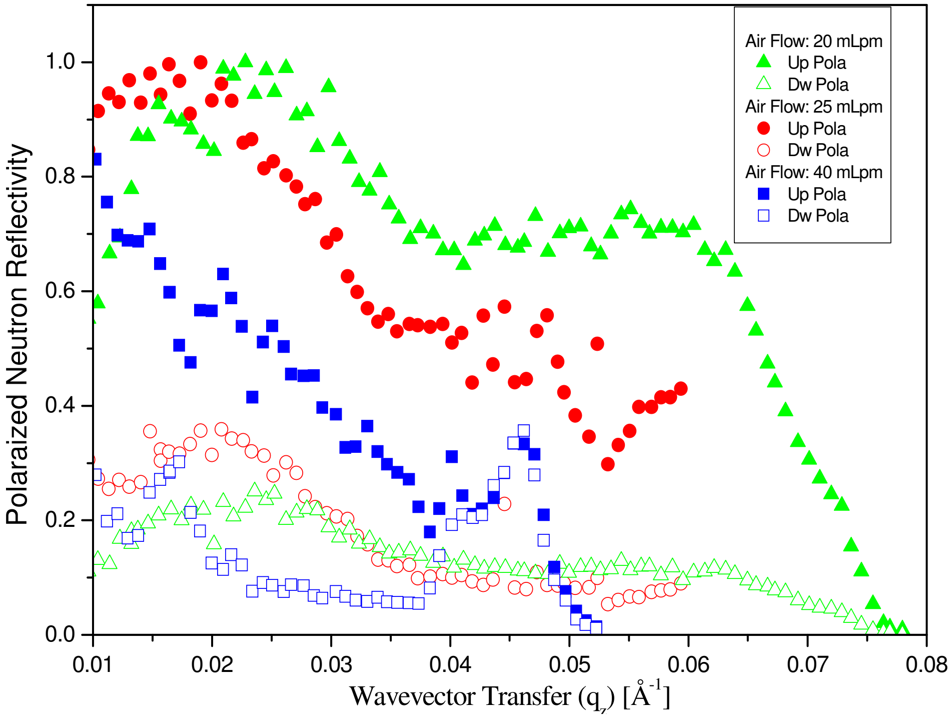

Fig. 4.13: Polarized neutron reflectivity of Co/Ti supermirror deposited at different air flow 20 ml m^{-1} 25 ml m^{-1} and 30/40 ml m^{-1}

on-Ti and Ti-on-Co substantially and this effect is more significant in case of higher bilayer thickness. Such a reactive sputtering process might decrease the grain size of the Co layer which in-turn decrease the inter diffusion at the interface [15, 92, 104]. This observation has been very useful for the deposition of the Co/Ti supermirror polarizer of high 'm-value'. Subsequently, in order to find out the optimum air flow rate required in the sputtering ambience to obtain good reflectivity from the multilayers, three Co/Ti supermirrors have been deposited at three different air flow rates (viz., 20 ml m^{-1}, 25 ml m^{-1} and 40 ml m^{-1}) used during the deposition of Co layers. The air flow rates have been kept constant at pre-defined values during the deposition of the supermirrors using a computer controlled mass flow controller (MFC). After measuring the polarized neutron reflectivity of all the samples at DHRUVA, Trombay as shown in Fig 4.13 it is observed that at very high air flow (40 ml m^{-1}) the up ($R_{\uparrow}$) and down ($R_{\downarrow}$) polarization neutron are not separated. So it is concluded that the Co layers get oxidized completely and lose their magnetic properties at this air flow rate. The difference in $R_{\uparrow}$ and $R_{\downarrow}$ increases as the air flow rate is lowered and it is found that at 20 ml m^{-1} air flow rate, substantially high reflectivity for up-spin neutrons ($R_{\uparrow}$) can be obtained. So this air flow rate (20 ml m^{-1}) is accepted for further deposition of Co/Ti supermirrors.

(ii) Compensating layer technique

In this technique, on the other hand, non-magnetic region at Co/Ti interface is compensated by increasing Co layer thickness by small amount and decreasing Ti layer thickness by similar amount in each bi-layer [14] keeping the bilayer thickness same. Schärpf et. al. [89] had reported improvement of reflectivity of evaporated m=1.5 (80 layers) Co/Ti supermirror by increasing thickness of each Co layers by 10% and decreasing thickness of each Ti layers by

10%. They have also reported [14] improvement of reflectivity of m=2.5 (300 layers) Co/Ti polarizing supermirror by increasing each Co layer thickness by 7 Å and decreasing each Ti layer thickness by 7 Å. In both the cases the authors have vented the deposition system periodically, which according to them has helped in obtaining better reflectivity for the supermirrors.

4.3.4 Improvement of reflectivity of *m*=2.25 and *m*=2.5 Co/Ti supermirror polarizer

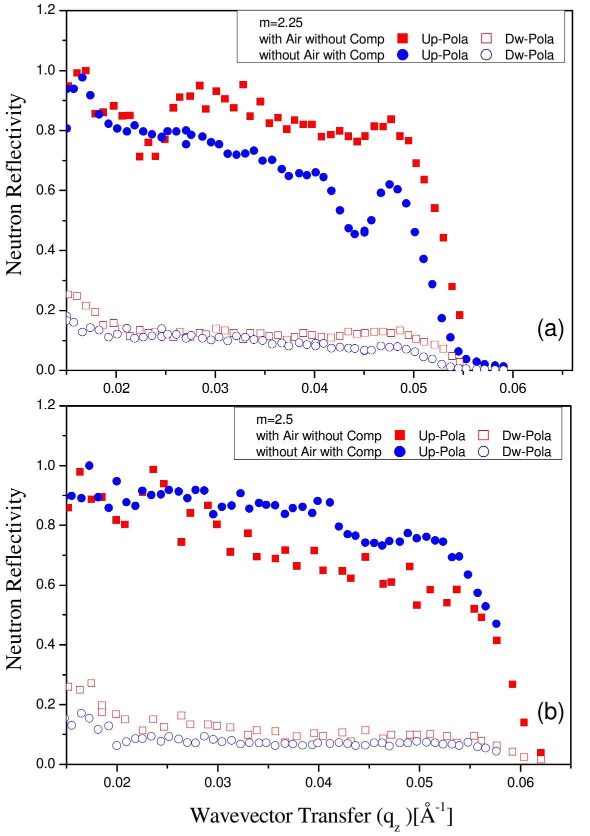

Fig. 4.14: Polarized neutron reflectivity of (a) m=2.25 and (b) m=2.5 supermirrors deposited with air without compensation layer thickness and without air with compensation layer thickness.

We have deposited m=2.25 (204 layers) and m=2.5 (312 layers) Co/Ti supermirror polarizers adopting both the above techniques and the measured PNR spectra of the samples are shown in Figs. 4.14 (a) and 4.14(b) respectively. It can be noticed that in all the four cases, the reflectivity spectra do not show the unusually oscillatory behavior as observed in Figs. 4.10(b) & (c). In the case of compensation technique, we have increased the thickness of each Co layer by 10 Å and decreased the thickness of each Ti layer by 10 Å. In the other set, we have deposited each Co layer of the supermirror with an optimized air flow rate of 20 mL m^{-1} during the sputtering process. The above four supermirrors are also found to yield reasonably good reflectivity (~80%) at the critical values of wavevector transfer

(q_z) and the polarization efficiency $(R_{\uparrow} - R_{\downarrow})/(R_{\uparrow} + R_{\downarrow})$ of the supermirror polarizers are estimated to be ~85% [78]. However the measured polarization efficiency of the supermirrors is also limited by the flipper efficiency of neutron reflectometer used in this study which is ~90% and hence actual polarization efficiency of the supermirrors would be higher than this.

It should also be noted that in Fig. 4.14(a), the reflectivity spectrum of up-polarized neutrons of the m=2.25 supermirror deposited with a compensating Co layer thickness has a dip in high q_z range while that of the supermirror deposited with mixed ambience of air and argon has a dip at a low q_z range. These aberrations are due to some missing layers which occurred due to accidental problems during deposition of the supermirrors and are not really intrinsic characteristics of the supermirrors.

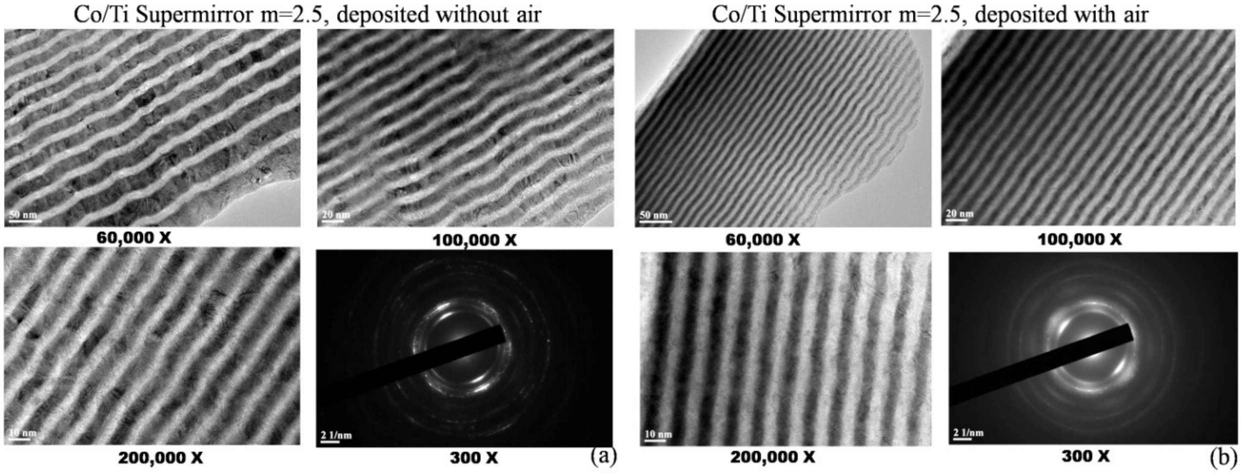

Fig. 4.15: HRTEM image capture at different resolution of m=2.5 Co/Ti supermirror deposited at condition (a) without air (b) with air

4.4 Characterization supermirror by cross sectional HRTEM

Cross sectional high resolution transmission electron microscopy (HRTEM) have been carried out on two 'm=2.5' Co/Ti supermirror samples, in which Co layers are deposited respectively under pure argon ambience and mixed ambience of argon and air as shown in Fig. 4.10(a) & 4.14(c) respectively. The measurements have been carried out using a 200 keV ultra high resolution transmission electron microscope (JEOL-2010) at the Institute of Physics (IOP), Bhubaneswar, India. In Fig 4.15 the cross sectional images of both the supermirrors are shown at different resolutions from where it is clearly seen that the thickness of the individual layers are varying very slowly with layer number. Comparing all the images of the supermirror deposited under argon ambience and mixed ambience of argon and air, it is clearly observed that the sample deposited with air has sharper interfaces which confirms less interface diffusion as found from X-ray and neutron reflectivity measurements also and discussed above. It is also seen that, the layers of the supermirror deposited without air are more wavy in nature compared to other sample, which may be due to the presence of more stress in this sample. In Fig 4.16(a) the images of the two samples taken at same resolution and at similar thickness range are compared. From this figure the distinct difference between the two samples is clearly visible. The depth profiling of the two samples from this image is compared in Fig 4.16(b) where it is seen that due to diffusion, in the supermirror deposited without air the contrast between the layers are less and interfaces are diffused, compared to the supermirror deposited with air.

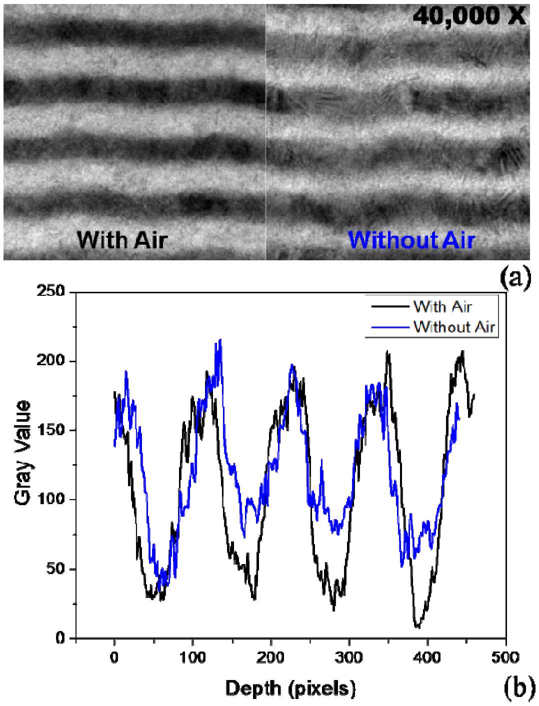

Fig. 4.16: (a) Side by side comparison of cross sectional TEM photo of supermirror deposited without air and with air (b) Comparison of depth profiling of the above supermirrors.

4.5 Conclusion

Using Hayter and Mook model a GUI based computer program has been developed for designing of neutron supermirror and using this code process error analysis has been done. It is seen that the thickness variation of more than ±5% is not tolerable during the deposition of the supermirror. Subsequent to optimization of various process parameters, viz., deposition pressure, magnetron power and rate of deposition, the calibration of the speed of substrate trolley has been done by depositing Co/Ti periodic multilayer of 20 layers at different substrate speeds. Measuring the variation of the deposited individual thickness of Co and Ti with substrate trolley, the calibration curve between the speed of the trolley and deposited layer thickness is established. During this experiment it is also seen that there is a 'growth offset' in the Co and Ti layer thickness which is due to asymmetric diffusion at Co-on-Ti and Ti-on-Co. Considering this, Co/Ti based thin film multilayer supermirrior polarizers of up to m=2.5, have been fabricated successfully in the 9 m long in-line sputtering system using the design structure generated by the in-house developed computer code. The Co/Ti supermirror shows high reflectivity up to a reasonably large critical wavevector transfer (q_z) of ~0.06 Å^{-1}. It has been observed that use of a mixed ambience of argon and air while depositing Co layers or increasing the Co layer thickness from its nominal value by ~10 Å improves the reflectivity pattern of the supermirrors significantly. Cross-sectional TEM measurements confirm that deposition of Co layer in the mixed ambience of argon and air increases the sharpness of the interface between the layers.

CHAPTER 5

Scaling of surface and interface roughness of single layer and multilayer films & development of Ni/Ti neutron supermirror

5.1 Introduction

As seen in the previous chapter the surface and interface roughness are the key parameters which control the performance of a multilayer device, so knowledge of the mechanism that controls the roughness of a growing surface can help in developing better device. A significant amount of theoretical and experimental work has been carried out that ultimately led to the theory of kinetic roughening in the thin film and yielded scaling relation of roughness with growing thickness under the frame work of Dynamic Scaling Theory (DST) [33, 105, 106]. The scaling exponents found are roughness exponent α and growth exponent β which characterize the growth dynamics of the surface. However, the growth exponents obtained by X-ray scattering, Atomic Force Microscopy (AFM) or Scanning Tunneling Microscopy (STM) techniques by various workers on different systems suggest that the exponents of roughness scaling are very much material and process dependent. For example, He *et. al*. [36] have reported α=0.79 and β=0.22 for single layer Fe films deposited on Fe(001) substrate by MBE technique, while for Mo films deposited on Si substrate by DC magnetron sputtering, Wang *et. al*. [37] have obtained α=0.89 and β=0.42. You *et. al.* [38] have found that β varies from 0.40 to 0.42 as the deposition temperature varies from 300K to 220K for sputter deposited Au films while Jeffries *et. al*. [35] have found α=0.9 and β=0.26 for Pt films deposited by ion beam sputtering technique.

In case of multilayer samples, where two materials are deposited alternately, growth of roughness is coupled with total thickness, bilayer thickness and thickness ratio of two materials. It is predicted that in case of multilayers also same type of roughness scaling exists as described by DST for single layer film. However there are also some experimental studies using specular and non-specular X-ray reflectivity of W/C [40], Mo/Si [41] and Pt/C [42] multilayers where it has been shown that the roughness does not depend on the total thickness of the multilayers. Recently, a numerical simulation has been reported using nonlinear continuum theory [39] where it has been shown that the surface roughness of the multilayer experience oscillating growth, with smoothening of the interface width existing at one type of interface and growth-induced roughening observed at another type of interface. The phenomena of smoothening and roughening at alternate interfaces in case of multilayer samples have also been observed by Paul and Lodha [42] for their d.c. magnetron sputtered Pt/C multilayers and by us in case of ion beam

Fig 5.1: Photograph of RF magnetron system installed in our laboratory

sputter deposited W/Si multilayer samples [100].

Due to strong contrast of neutron scattering length density for thermal and cold neutrons, Ni and Ti pairs are widely used as neutron optical components (mirrors and monochromators) in neutron delivery systems [91, 107, 108]. Periodic multilayers, where bilayer thickness are constant, are used as monochromators and non-periodic multilayers, where bilayer thickness gradually increase from the bottom to the top of the multilayers, act as supermirrors as described in previous chapters and are used in neutron guide tubes for transporting neutrons from its source to the experimental station efficiently. Apart from as neutron reflector, Ni/Ti multilayers can also be used as a mirror in the water window region (23-44Å) for soft X-ray radiation. Experimentally [109] it is shown that Ni/Ti mutilayers can give higher reflectivity compared to Ni/Sc, Ni/C, and W/C multilayers at 2.74 nm of X-ray wavelength which is in the water window region. Thus we have chosen this important system of Ni/Ti multilayer for our present study. After optimizing the process parameters of a home-built RF sputtering system, single layer Ti and Ni films are deposited for different deposition time and their roughness scaling are measured by Grazing Incidence X-ray Reflectometry (GIXR) and Atomic Force Microscopy (AFM) techniques. Subsequently, under the similar deposition conditions, Ni/Ti periodic multilayers of 11-layer, 21-layer, 31-layer and 51-layer have been deposited and characterized by GIXR and neutron reflectivity measurements [101] and finally Ni/Ti supermirror devices are designed, fabricated and characterized by neutron reflectivity method [110]. It should be mentioned here that the odd number of layers have been considered here so that we have high density layer on the top of the substrate as well as at the top surface of the multilayer. Presence of higher density layer at the top surface helps in proper alignment of the sample during GIXR measurement. For example, in case of the 11-layer multilayer, the first layer on the substrate is of Ni, and subsequently 5- bilayers of Ti/Ni have been deposited.

5.2 RF magnetron sputtering system

For this particular work, a home-made RF magnetron sputtering system, as shown in Fig. 5.1, is used for deposition of single layer and multilayer films. The system is equipped with a turbo molecular pump backed by a rotary pump and a base pressure of 1×10^{-6} mbar is regularly achieved in the system. The sputtering system is provided with two water cooled cathodes which can hold circular targets of 3 inch diameter. A RF power supply (max. power 1kW, frequency 13.6 MHz) has been used to supply RF power to the cathodes and an automatic impedance matching network has been used between the cathode and power supply to supply maximum power to the cathode. The other plate (anode) facing the cathodes, which supports the substrate is grounded. The substrate holder is also water-cooled to cancel out the temperature rise by the plasma during the sputtering process. A motorised movement is provided to the substrate holder from the top of one cathode to the other for enabling sequential deposition of two materials. For controlling the deposited film thickness and for allowing pre-sputtering of the targets a shutter has been introduced between the cathodes and the anode. Two quartz crystal thickness monitors have also been used in the deposition system near each target to monitor the rate and the total thickness deposited by respective targets. High quality Ni (99.95%) and Ti (99.95%) discs of 75 mm diameter were used as the target materials in the present system. Substrates used for all the depositions are crystalline silicon (111) wafer of 50mm diameter and the depositions are carried out under high purity argon ambience. The Ar flow rate was controlled by using a mass flow controller.

5.3 Optimization of process parameter

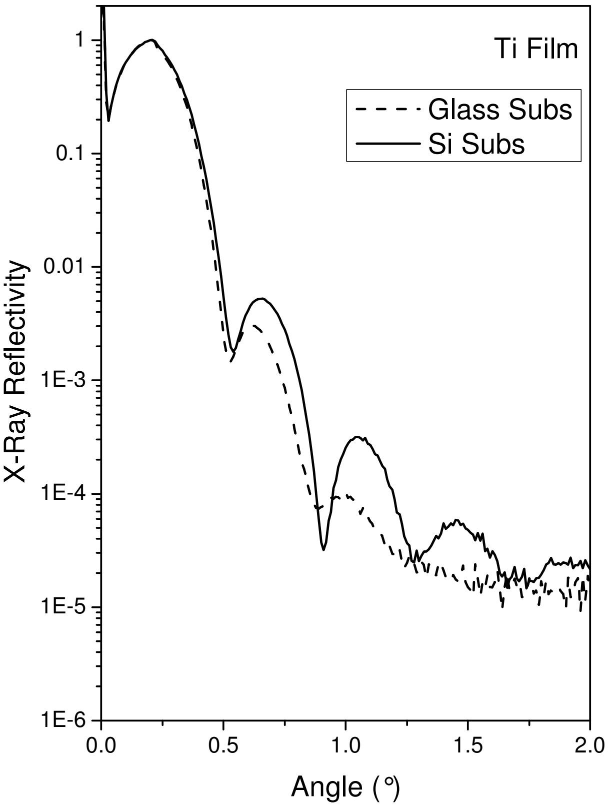

Fig. 5.2: Measured GIXR spectrum of Single layer Ti film deposited on glass and Si substrate

Initially single layer Ti films have been deposited at 50W RF power on crystalline Si (111) and glass substrate and the samples have been characterized by Grazing Incidence X-ray Reflectivity (GIXR) technique with X-rays of 1.54Å wavelength. In Fig 5.2 the GIXR spectra of both the samples are shown, from which it is very clear that the sample deposited on silicon substrate has less roughness. Hence subsequently all the single layer and multilayer samples have been deposited on silicon substrates. Several Ni and Ti single layer films have been deposited at different deposition conditions and were characterized by GIXR measurements to estimate the thickness, density and top surface roughness of the films. The aim of this exercise was to obtain reproducible optimized condition to deposit good quality films with bulk-like density and low surface roughness. Finally the optimum deposition pressure found for Ni was 4x10^{-3} mbar and for Ti was 2x10^{-3} mbar with an optimum substrate to target distance of 4.5 cm. The optimum RF power for both the materials was found to be 50 Watt with minimum reflected power.

5.4 Roughness scaling of Ti & Ni single layer films

In general, a rough surface can be described statistically by the height-height correlation function as shown in eqn, (2.50) in Chapter 2 which is defined as mean square height difference between two surface positions separated by a lateral distance r. In eqn. (2.55) it is also defined in terms of measurable quantities, the lateral correlation length (ξ), the roughness exponent (h or α) which controls the short range fractal dimension of the surface and the average interface width or r.m.s roughness (σ) defined as

$$\sigma(r,t) = \left\langle \left(Z(r,t) - \langle Z \rangle \right)^2 \right\rangle_r^{1/2} \tag{5.1}$$

Where, $Z(r,t)$ is the surface height, t is the deposition time and $<\ldots>_r$ denotes the average over all r in a system of size L and $r \leq L$. Generally, dynamics of a growing surface follows simple Dynamics Scaling Theory (DST) according to which the interface width follows Family-Vicsek (FV) dynamic scaling as [33]:

$$\sigma(r,t) = t^{\beta} f\left(r/t^{\beta/\alpha} \right) \tag{5.2}$$

and the scaling function $f(x)$ behaves as:

$$f(x) \alpha \begin{cases} x^{\alpha} & if \ x << 1 \\ const & if \ x >> 1 \end{cases} \tag{5.3}$$

where, β is called growth exponent which gives scaling for long range. It can be shown from the scaling theory that lateral correlation length scales with time of deposition or thickness as [13]:

$$\xi \ \alpha \ t^{\beta/\alpha} \tag{5.4}$$

According to KPZ [111] model, the value of exponent is α=1/2 and β=1/4 for d=1+1 dimension. However, Lai and Das Sharma [112] have generalized it by predicting α=(5-d)/3 and β=(5-d)/(7+d) in d dimension.

5.4.1 GIXR characterization

In order to measure the roughness scaling parameters single layer Ti and Ni films have been deposited for different deposition times. In Fig.5.3 the measured grazing incidence X-ray reflectivity (GIXR) spectra of four single layer Ti films have been shown along with their respective best fit theoretical spectra generated using Parratt formalism and IMD code as explained in Chapters 2 &3. During fitting the density, thickness and top surface roughness of the films are varied and the best fit values are shown for respective films in the inset of Fig. 5.3 along with their deposition time. The densities found are around 95% of bulk density in all the films. From the above figure, it can be seen that with increasing thickness, the frequency of

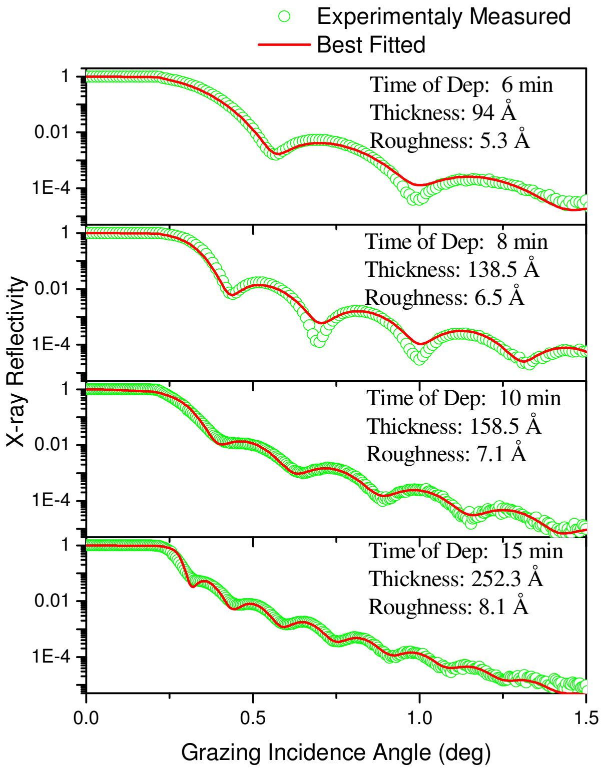

Fig. 5.3: GIXR spectra with best fitted theoretical curve of single layer Ti film deposited at different time of deposition.

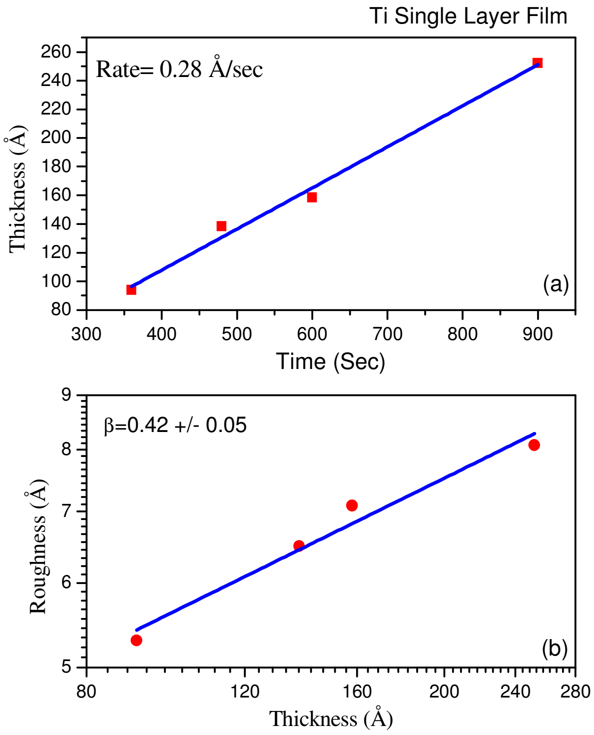

Fig. 5.4: (a) Variation of thickness of Ti single layer film with time of deposition (b) Variation of surface roughness of single layer Ti film as a function of thickness

oscillation of the GIXR spectrum increases and also the value of the reflectivity drops faster which signifies that the top surface roughness of the films increases with increase in thickness.

In Fig. 5.4(a) measured thicknesses of these films have been plotted with the deposition time. These data can be fitted reasonably well with a straight line and from the slop of the straight line the rate of deposition of Ti 0.28 Å/sec can be found. It signifies the stability and reproducibility of the home-made RF sputter deposition system. In Fig. 5.4(b) the top surface roughness of Ti films is plotted with the thickness of the film found as above. These variation of roughness is fitted by the power law behavior of roughness (σ) with thickness (d) i.e. $\sigma \alpha d^{\beta}$ and the value of growth exponent (β) found is 0.42±0.05. This value of growth exponent agrees

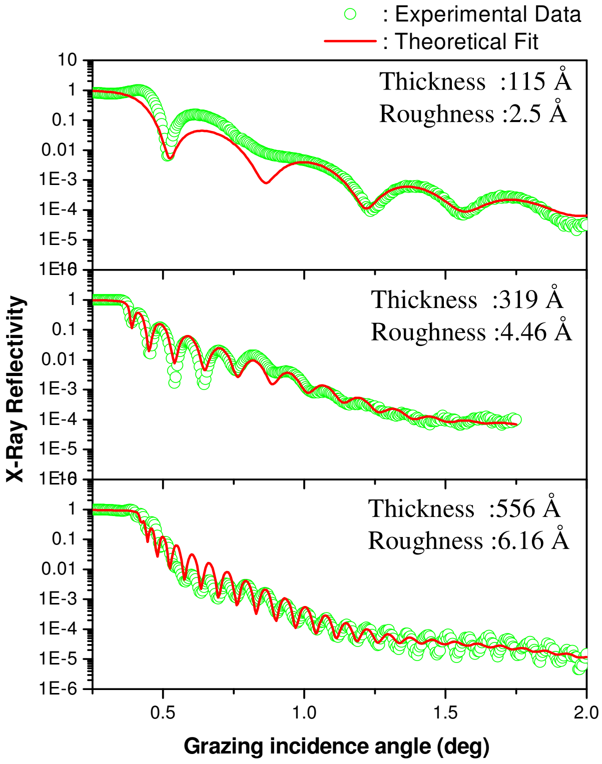

Fig. 5.5: GIXR spectra with best fitted theoretical curve of single layer Ni film deposited at different time of deposition.

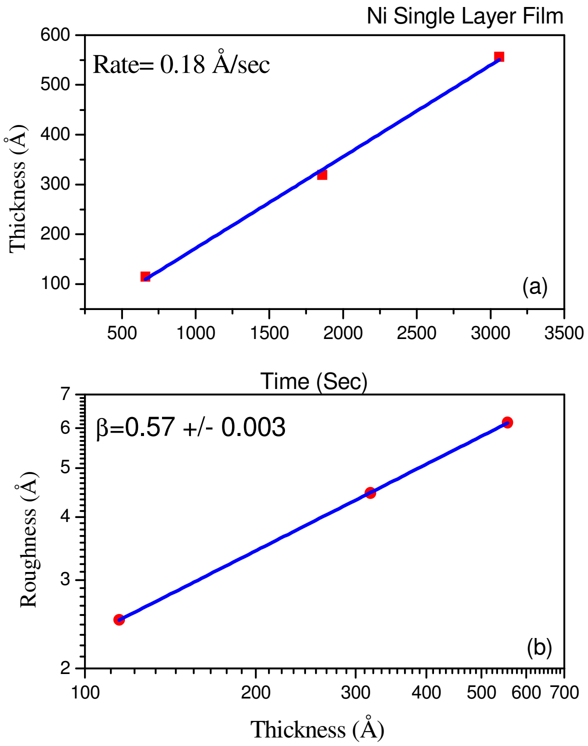

Fig. 5.6: (a) Variation of thickness of Ni single layer film with time of deposition (b) Variation of surface roughness of single layer Ni film as a function of thickness.

well with the previously reported growth exponent values of sputter deposited Mo films (0.42) [40] and sputter deposited Au films (0.40-0.42) [41]. Thus it can be concluded that our RF sputter deposited single layer Ti films are found to follow the DST theory of scaling of surface roughness.

In Fig. 5.5, the GIXR data of three single layer Ni thin films are presented. The measured densities of all the films, as obtained from the critical angle of the GIXR spectra, have been found to be almost equal to the bulk density of Ni. Like Ti films, in case of RF sputtered Ni also

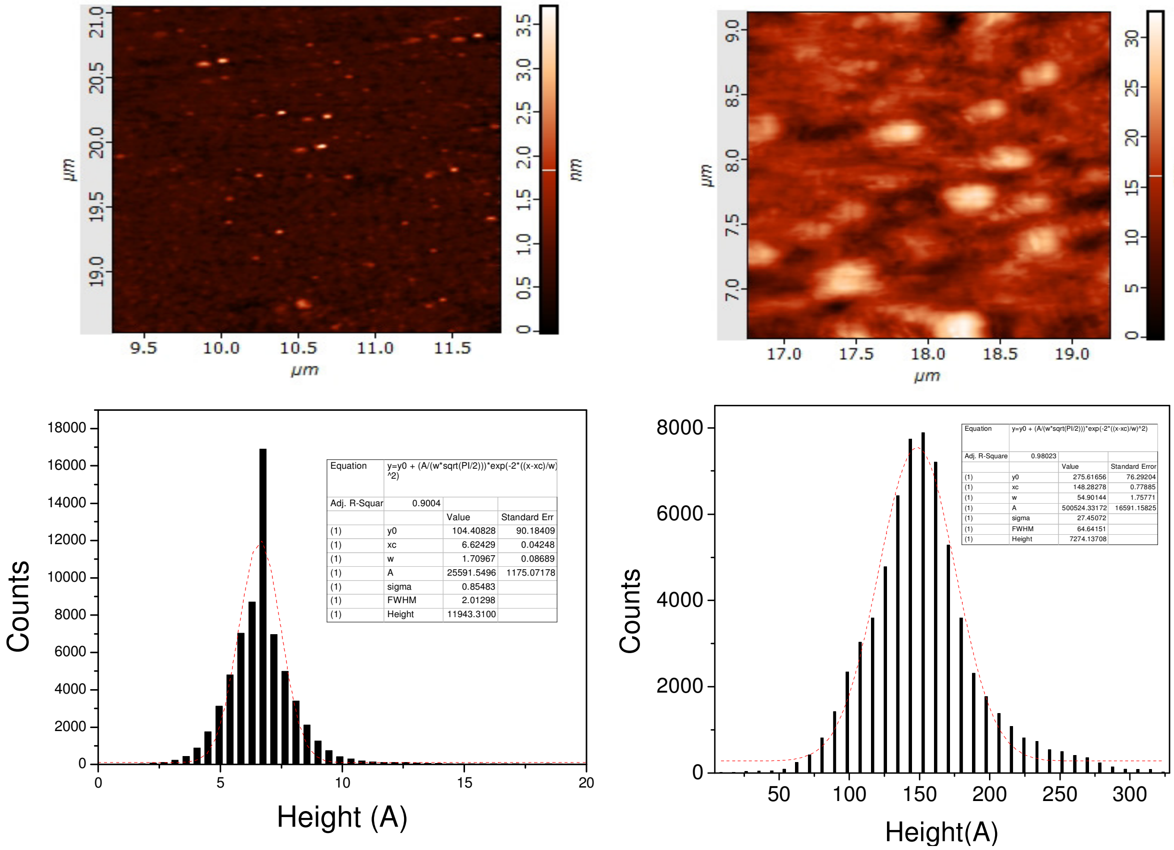

Equation	y=y0 + (A/(w*sqrt(PI/2)))*exp(-2*((x-xc)/w)^2)		
Adj. R-Squar	0.9004		
		Value	Standard Err
(1)	y0	104.40828	90.18409
(1)	xc	6.62429	0.04248
(1)	w	1.70967	0.08689
(1)	A	25591.5496	1175.07178
(1)	sigma	0.85483	
(1)	FWHM	2.01298	
(1)	Height	11943.3100	

Equation	y=y0 + (A/(w*sqrt(PI/2)))*exp(-2*((x-xc)/w)^2)		
Adj. R-Square	0.98023		
		Value	Standard Error
(1)	y0	275.61656	76.29204
(1)	xc	148.28278	0.77885
(1)	w	54.90144	1.75771
(1)	A	500524.33172	16591.15825
(1)	sigma	27.45072	
(1)	FWHM	64.64151	
(1)	Height	7274.13708	

(a) (b)

Fig. 5.7 AFM micrograph and histogram of height distribution of the surface of a representative (a) Ti film (b) Ni film

it can be seen that with increasing thickness the frequency of oscillations of the spectrum increases and also the value of the reflectivity drops fast which signifies that the top surface roughness of the films also increases with increasing thickness of the film. The rate of deposition as obtained from Fig. 5.6(a) for Ni films is found to be 0.18 Å sec^{-1} which is less than that for Ti films under similar r.f. power condition. Surface roughness values of the Ni films have been plotted as a function of thickness in Fig. 5.6(b) and is fitted by a power law behavior viz., $\sigma \alpha d^{\beta}$ and the value of growth exponent (β) in this case is found to be 0.57±0.003, which is higher than the value obtained in case on Ti films (0.42±0.05). The higher value of β obtained for Ni compared to Ti films deposited under similar condition may be due to the higher atomic mass of the Ni. During the growth of the films, on reaching the substrate surface diffusion of adatoms i.e., their probability of hoping from one site to another decreases due to higher mass. So the shadowing effect dominates for the Ni film compared to Ti films which leads to the higher growth exponent of surface roughness. As has been pointed out by Yu and Amar [113], in their simulation study of two dimensional balastic deposition with shadowing, for cosine angular distribution of flux (as in case of sputtering), the value of growth exponent lies in the range of 0.52-0.64 which is higher than the value for KPZ model [111] without shadowing effect.

5.4.2 AFM characterization

Figs. 5.7(a) and 5.7(b) show the AFM micrographs of representative Ti and Ni single layer films of ~100 Å and 550 Å thickness, respectively. First order statistical analysis of the surfaces has been carried out using the AFM micrographs and histograms of the surface heights over the whole scanned area of the samples are also shown in the respective figures. It can be seen that in both the cases the surface height distribution is Gaussian and no asymmetry is observed in the histograms. Similar Gaussian distribution of surface heights has been observed for all other Ti and Ni films also.

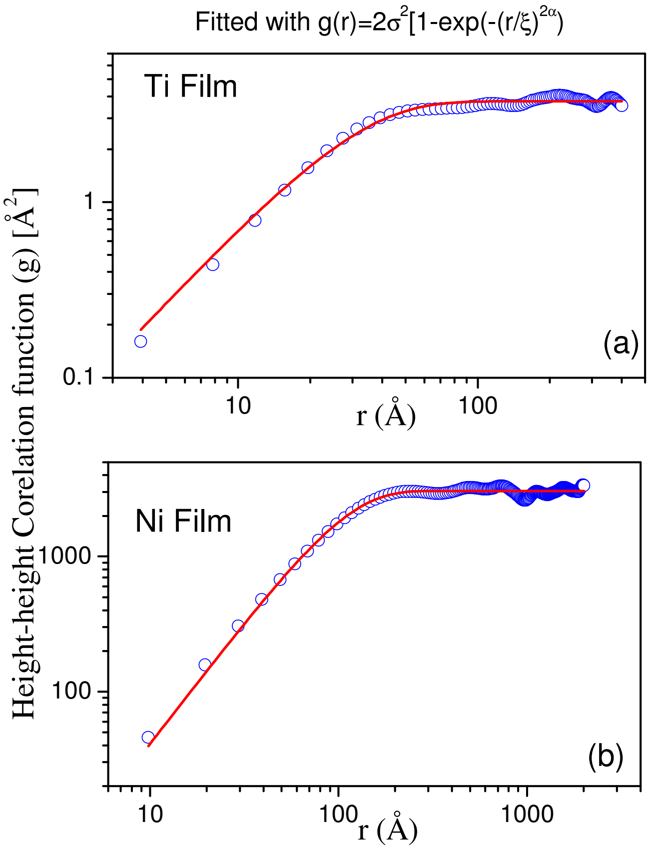

Fig. 5.8 Height-height correlation function as a function of distance along with best fitted theoretical curve of representative (a) Ti film and (b) Ni film

Figs. 5.8(a) and 5.8(b) show the measured height-height correlation functions of the same Ti and Ni single layer films respectively, as obtained from their AFM micrographs, along with best fit theoretical curves following eqn. (2.55) given in Chapter 2. The above exercise has been carried out for all the Ti and Ni films and it has been observed that the average value of roughness exponent (α) for Ti films is 0.73, while that for Ni films is 0.90. The above values of α for Ni and Ti films are found to agree well with that reported by Wang *et. al*. for their sputter-deposited Mo films on silicon substrates [37] and by Jeffries *et. al.* for their sputter-deposited Pt films on glass substrates. From GIXR analysis described above, it has been found that β is ~0.42 for Ti films and ~0.57 for Ni films. With the α values obtained from the above AFM measurements, we have found β/α (scaling exponents of correlation length ξ) values for Ti films to be 0.57 and for Ni films to be 0.63, respectively.

5.5 Characterization of Ni/Ti multilayer

5.5.1 X-ray reflectivity

In Fig. 5.9 the measured specular GIXR spectra of 11-layer, 21-layer, 31-layer and 51-layer Ni/Ti periodic multilayers are shown along with the best fit theoretical spectra. During fitting the theoretical reflectivity spectra of these multilayer films are generated by modeling with a 4-layer structure as shown in the inset of the Fig. 5.9. The first Ni layer on the substrate and Ti layer on the top of it, in all the samples have been considered as two individual layers in the model to separate the initial layers from the rest of the multilayer. The third layer has been considered as a Ni/Ti bilayer repeated for 4, 9, 14 and 24 times respectively for the 11-layer, 21-layer, 31-layer and 51-layer samples. This will give information about thickness uniformity of

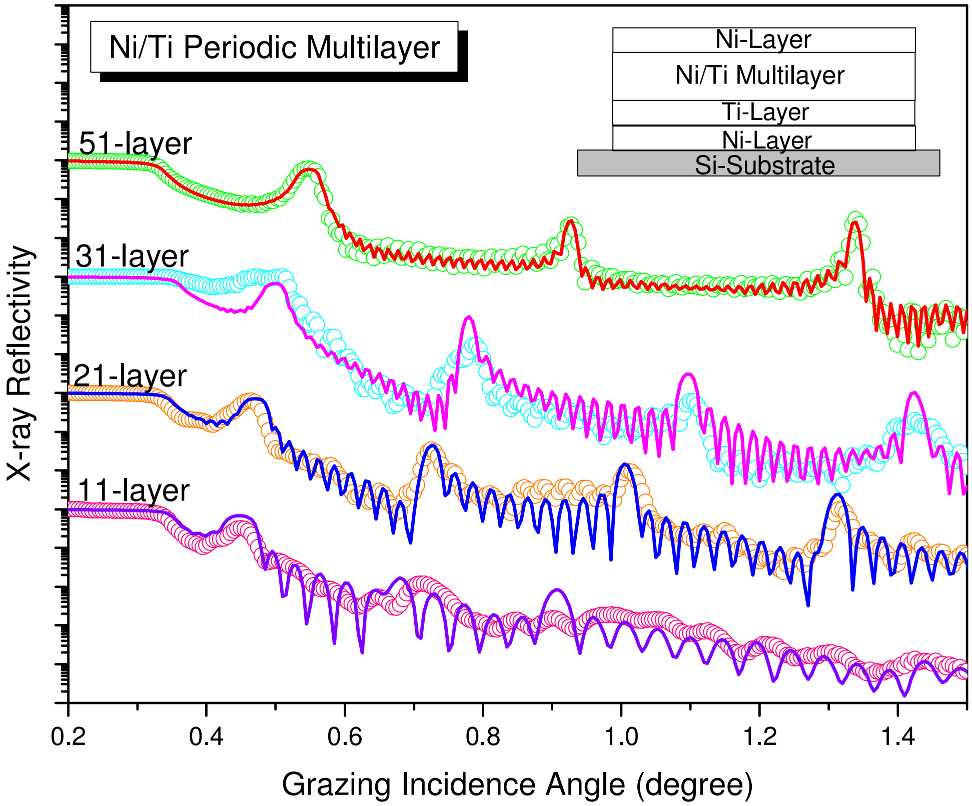

Fig. 5.9 Measured GIXR spectra (circle) with best-fit (line) theoretical curve for Ni/Ti Multilayer of 11-layer, 21-layer, 31-layer and 51-layer

the multilayer. The fourth layer has been considered as an individual Ni layer which is the top layer of the sample and has been considered separately. Assumption of such a 4-layer structure not only helps us to find out the density and thickness uniformity of the samples but we can also estimate the average interface width and top layer surface roughness of the multilayer separately. In Table-5.1 the thickness of the initial Ni and Ti layers, average interface width of Ni-on-Ti and Ti-on-Ni interfaces (σ), density of each layer (ρ), top layer surface roughness (σ_{top}) and substrate roughness (σ_{sub}) found from these fittings are given for the four multilayer samples. The nature of fitting of the theoretical spectra with the measured GIXR spectra using the above 4-layer model confirms the depth uniformity of the multilayer and hence it can be concluded that the thickness variation of individual Ni and Ti layers in the multilayer is negligible in all the samples.

5.5.2 Neutron reflectivity

In Figs. 5.10(a) and 5.10(b), the neutron reflectivity spectra for the 31-layer and 51-layer multilayer samples, measured with neutron wavelength of 7.5 Å are respectively shown. The reflectivity at the first Bragg peak found for the 31-layer multilayer is ~48% at 1.7° grazing angle of incidence and for 51-layer multilayer it is found to be ~36% at 2.23° grazing angle of incidence. In the above figures, along with the measured data, the best fit theoretical spectra are

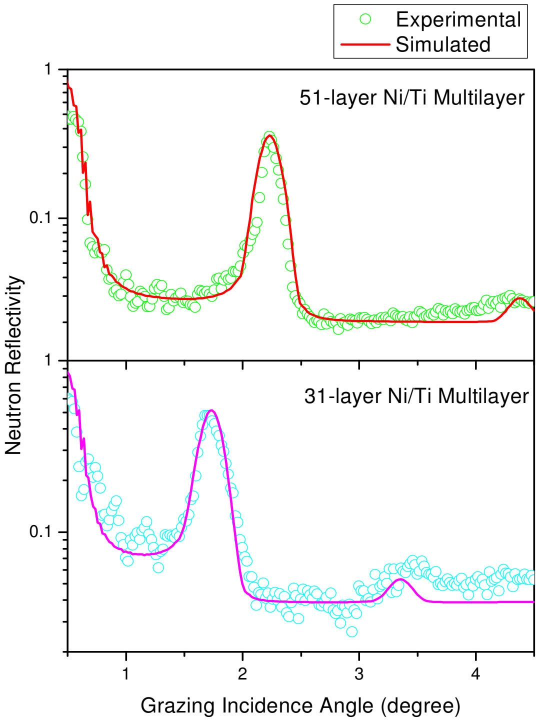

Fig. 5.10: Measured neutron reflectivity (circle) at 7.5 Å wavelength with best-fit (line) theoretical curve for Ni/Ti Multilayer of 31-layer and 51-layer

also shown which have been generated with the same 4-layer model used for fitting of the GIXR data. During fitting, the detector resolution has been considered to be 0.005 $Å^{-1}$ and a constant background, found by measuring the background counts for long time, has also been consideredwhich was 0.03 for the 31-layer sample and 0.02 for the 51-layer sample. The thickness of initial Ni and Ti layers, widths of Ni-on-Ti and Ti–on-Ni interfaces, density of each layer, top layer roughness, and substrate roughness found from this fitting are also shown in Table 5.1 along with the data found from GIXR measurements. It is found that the values of the parameters of the multilayer samples measured from X-ray and neutron reflectivity techniques are consistent with each other.

Method			X-ray Reflectivity				Neutron Reflectivity	
Multilayer Sample			11-layer Sample	21-layer Sample	31-layer Sample	51-layer Sample	31-layer Sample	51-layer Sample
Ni layer		Thickness (Å)	89.8	80.4	77.9	56.3	80.4	51.9
		ρ (gm/cc)	8.3	8.3	8.7	7.8	8.6	8.7
		σ_{top} (Å)	10.7	8.2	9.5	3.2	10.6	5.2
Multilayer	Ti layer	Thickness (Å)	66.9	56.7	45.1	49.0	49.2	46.8
		ρ (gm/cc)	4.5	4.2	4.5	4.1	4.5	4.0
		σ (Å)	13.8	10.1	12.6	10.7	17.7	15.5
	Ni layer	Thickness (Å)	91.9	83.2	82.8	53.2	80.5	52.4
		ρ (gm/cc)	8.3	8.1	8.5	8.1	8.7	8.9
		σ (Å)	8.5	7.6	8.1	3.6	9.0	5.0
Ti layer		Thickness (Å)	71.4	60.5	48.5	50.1	52.6	48.6
		ρ (gm/cc)	9.5	3.8	4.5	4.2	4.4	3.8
		σ (Å)	4.5	9.5	10.6	7.3	17.7	15.5
Ni layer		Thickness (Å)	73.2	75.6	87.6	49.4	80.2	52.1
		ρ (gm/cc)	8.7	9.8	8.7	8.5	8.7	8.9
		σ (Å)	8.5	8.8	11.9	1.8	8.1	6.6
Substrate		σ_{sub} (Å)	4.1	3.3	7.6	7.3	7.3	7.3
Thickness ratio Γ =Ni/(Ni+Ti)			0.47	0.40	0.35	0.42	0.37	0.47

Table-5.1: Best fit parameters obtained for Ni/Ti multilayer films from fitting of X-ray reflectivity and Neutron Reflectivity data.

5.6 Multilayer roughness scaling

As shown in Table-5.1, it is found from both the characterization techniques that for all the cases the average interface width of Ni-on-Ti interfaces is more than the corresponding width of Ti-on-Ni interfaces. Since both interface diffusion and interface roughness contribute in determining the interface widths and since from Figs. 5.4 and 5.6, it can be seen that for similar thickness, the roughness of Ti layers is more than that on Ni layers, it can be concluded that the higher interface width for the Ni-on-Ti interfaces might be due to higher roughness of Ti layers as well as higher penetration of Ni atoms inside the Ti layers leading to higher inter-diffusion.

As stated previously about the variation of roughness with the thickness for multilayer films, Liu and Shen [39] predicted by numerical simulation that same growth law of single layer film according to DST is also valid for multilayer interface width. However, in contrast to the monotonous rise of roughness in case of single layer films, in multilayers generally an oscillating variation in roughness is observed due to periodic smoothing and roughening effect at the two different interfaces. This leads to the fact that the roughness of multilayers generally becomes independent of the total multilayer thickness, which has been reported by several other authors also [40, 41]. For example, Savage *et. al.* [40] prepared two sets of W/C multilayers, one with same bilayer thickness but different period of multilayer and other set with same period but bilayer thickness varying from 19 Å to 166 Å. After characterizing all the samples by specular and nonspecular GIXR measurements, they concluded that the roughness of the multilayer is independent of the total thickness of the film contrary to the predicted scaling law by numerical simulation. We have also made similar observations for ion beam sputter deposited W/Si samples, discussed in Chapter-7, where it has been seen that there is no significant increase in the top surface roughness or interface width with the increase in number of layers and the roughness at the Si-on-W interface gradually decreases from the bottom to the top of the multilayer [100]. In case of the present set of samples also, as shown in Table-5.1, the top Ni-layer surface roughness for the 11-layer sample is considerably larger than the 51-layer sample though the total thickness of the 11-layer sample is 870 Å and that of the 51-layer sample is 2608 Å. It has also been observed for the present set of samples that the top surface roughness of the samples is quite similar to the interface width of the multilayers. All the above observations support the assumption that unlike single layer films, surface roughness in case of multilayer does not increase as the multilayer grows. The above phenomenon may be explained, as pointed out by Savage *et al.* [40], by the assumption that at the interfaces, the growth "restarts" every time. So interface width does not depend on the thickness of the multilayer already deposited, rather it depends on bilayer thickness. Similar observations was also found for Mo/Si multilayer film [41], where it is shown that the roughness is dependent on thickness ratio Γ (=Mo-thickness/(Mo-thickness+Si-thickness)) and due to change of Γ from 0.2 to 0.8, roughness changes from 2.4Å to 4.2Å.

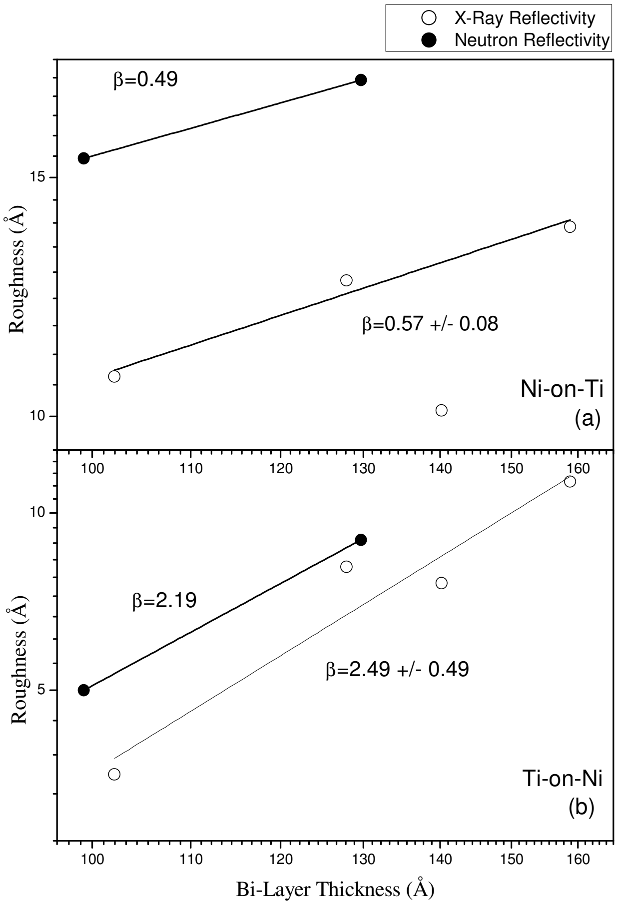

Fig 5.11: Variation of interface width as a function of bi-layer thickness for Ni/Ti multilayers: (a) Ni-on-Ti interface (b) Ti-on-Ni interface

In Fig. 5.11(a) & (b) the Ni-on-Ti and Ti-on-Ni interface widths as obtained from GIXR and neutron reflectivity measurements are plotted as a function of bilayer thickness (i.e., sum of Ti and Ni-layer thickness) of the samples from where is can be seen that the interface widths vary significantly due to the variation of the bilayer thickness from 102Å to 160Å where the thickness ratio Γ (=Ni-thickness/(Ni-thickness + Ti-thickness)) is around 0.4. If we imagine that the same growth law as predicted by the Dynamic Scaling Theory (i.e. $\sigma \alpha D^{\beta}$, where D=bilayer thickness) is also applicable here and fit the data as shown in Fig.5.11(a), it is found that from GIXR measuremrent β=0.57 and from neutron reflectivity measurement β=0.49 for Ni-on-Ti interface width. It is interesting to note that the exponent is similar to that obtained for surface roughness of Ti films (0.42, as shown in Fig. 5.4(b)) showing that the inter-diffusion component almost remain constant irrespective of bilayer thickness. However, as can be seen from Fig. 5.11(b), the Ti-on-Ni interface exponent (2.19 & 2.49) are much higher than the growth exponent for surface roughness of Ni films (0.57, as shown in Fig. 5.6(b)). This shows that Ti on Ni interface is dominated by interface diffusion much more significantly than interface roughness. Similar phenomenon has also been observed in our work on W/Si multilayers [100, 114] deposited by ion beam sputtering technique and discussed in Chapter 6 & 7 where, by fitting the measured specular and non-specular GIXR spectra and separating the interface diffusion and interface roughness components, it has been found that W diffuses more into the Si layers compared to Si into W layers.

5.7 Development of Ni/Ti supermirror

After successful deposition and characterization of Ni/Ti periodic multilayers, non-periodic multilayers i.e. supermirrors have been deposited using the above r.f. sputtering system. Prior to deposition the supermirror structures are designed using our in-house developed GUI based computer code which uses Hayter & Mook [50] method. The details about the design and computer code have been described in the previous chapter. The *m*=1.75 supermirror which can reflect up to 1.75 times of the critical angle of Ni consists of 62 layers of Ni and Ti where the

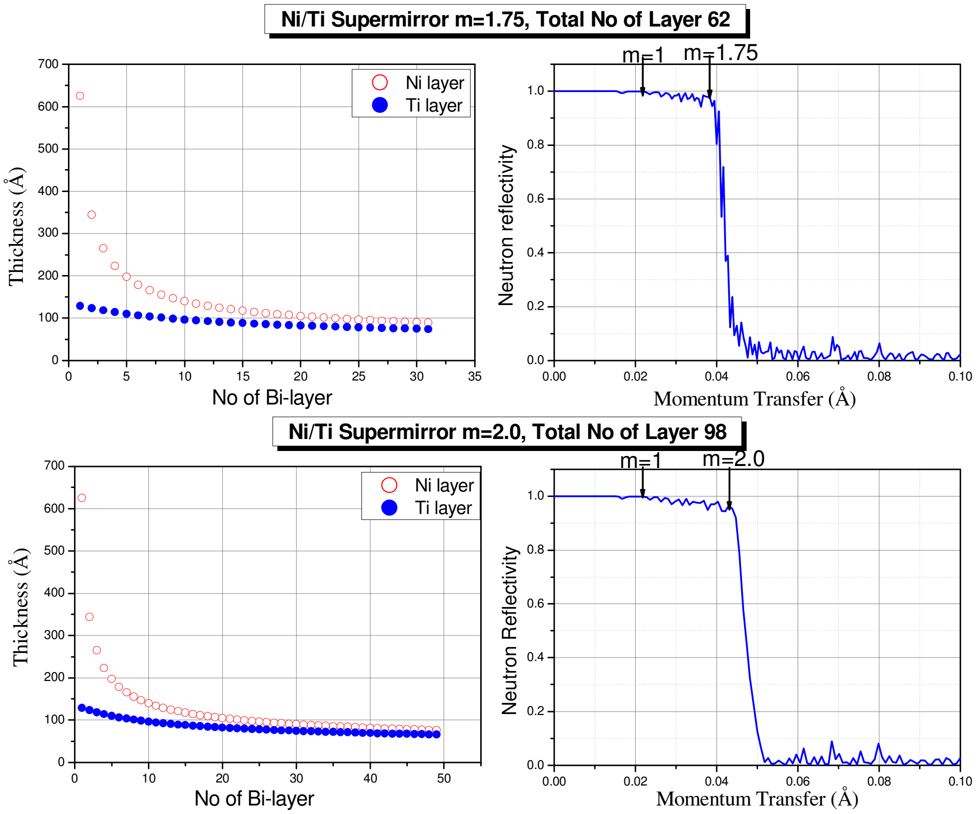

Fig. 5.12: Variation of layer thickness of Ni & Ti layers according to designed structure and simulated neutron reflectivity of the same designed structure for m=1.75 and m=2.0 supermirror.

thickness of Ni varies from ~89 Å to ~625 Å and thickness of Ti varies from ~74 Å to ~128 Å. In Fig. 5.12 the nature of variation of Ni and Ti layer with layer no (from top) is shown along with the simulated reflectivity spectrum of the designed supermirror structure. Similarly the *m*=2.0 supermirror which can reflect up to 2.0 times critical angle of Ni is also designed which contains 98 layers of Ni and Ti where the thickness of Ni varies from ~76 Å to ~625 Å and thickness of Ti layers varies from ~66 Å to ~128 Å. Again in the Fig 5.12 the variation of layer thickness and the simulated neutron reflectivity of this structure are shown. The two multilayer structures have been deposited by using the rf sputtering system on silicon wafers of 50 mm diameter. During deposition, all the deposition parameters are kept fixed at optimum condition and the thickness of the layers are maintained at their nominal values by using in-situ quartz crystal thickness monitor. After deposition both the supermirrors have been characterized by measuring neutron reflectivity at DHRUVA reactor at BARC. Trombay using 2.5 Å neutron wavelength [82]. The details about the measurement setup have been described in Chapter 3. The measured neutron reflectivities of both the samples are shown in Fig. 5.13 along with simulated neutron reflectivity of bulk Ni surface. The *m*=1.75 supermirror has shown more than 92%

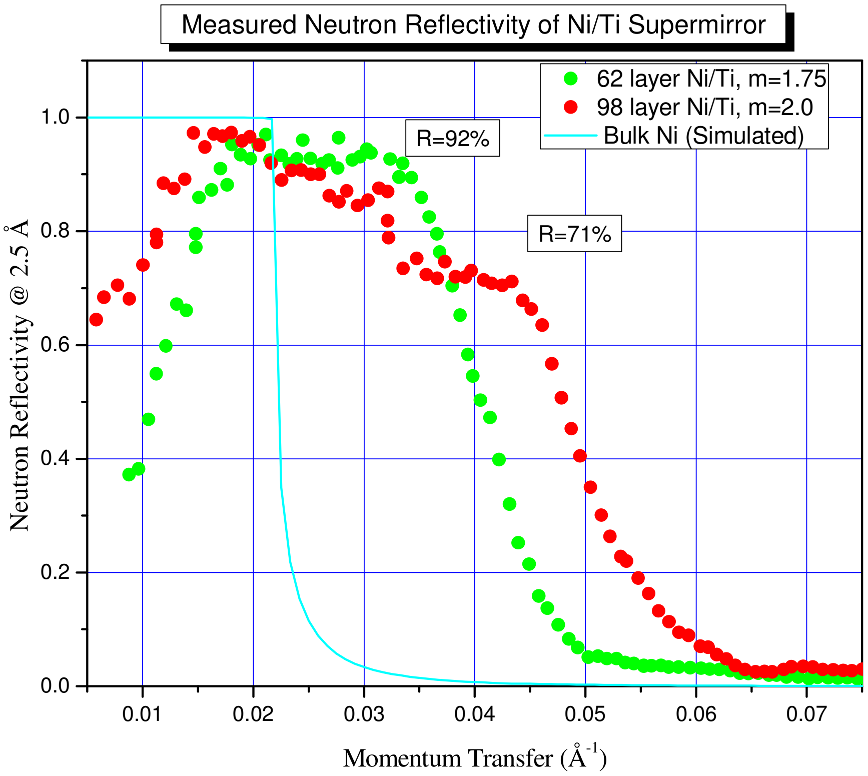

Fig 5.13: Measured Neutron reflectivity of m=1.75 and m=2.0 Ni/Ti supermirror measured at 2.5 Å wavelength at DHRUVA, BARC.

reflectivity at the cut off while the *m*=2.0 supermirror has shown more than 71% of reflectivity at its cut off angle [110]. The reflectivities of both the supermirrors agree quite well with the theoretically generated reflectivity spectra of the samples as shown in the Fig. 5.12.

5.8 Conclusion

Using an indigenously built r.f. magnetron sputtering system, several single layer Ti and Ni films have been deposited at varying deposition conditions. All the samples have been subjected to AFM and GIXR measurements to obtain thickness, density and roughness of the Ni and Ti films and the deposition conditions have been optimized to obtain good quality layers with bulk-like density and low surface roughness. It is found that the top surface roughness of the Ni and Ti films is homogeneous and satisfies the power growth law with the thickness of the film. The values of growth exponent (β) for Ti and Ni films are found to be 0.42±0.05 and 0.57±0.003, respectively. From AFM measurements, the roughness exponents related to the evolution of the correlation length have also been obtained, which are found to be ~0.73 for Ti films and ~0.90 for Ni films.

Subsequently, at optimized deposition condition of Ti and Ni, four Ni/Ti multilayers of 11-layer, 21-layer, 31-layer, and 51-layer having different bilayer thicknesses have been deposited. The multilayers have been characterized by both GIXR and neutron reflectivity measurements with cold neutron of 7.5 Å. The GIXR data of all multilayer films have been fitted with a 4-layer model where the first Ni and Ti layers and the top Ni layers are modeled separately, while the rest of the structure is assumed to be a repetition of a Ni/Ti bilayer. Along with the measurement of average bilayer thickness, average density of layers, average interface width, and the top layer roughness of the multilayers have also been estimated using this model. It is seen that unlike the single layer samples, the top layer roughness of the multilayers does not depend on the total thickness of the multilayers. On the other hand, it has been observed that the interface width of layers strongly depends on the bilayer thickness of the multilayers. This observation has been explained by the assumption of “restart of the growth at the interface” phenomenon. Similar power law for growth of roughness in single layers has been applied for multilayer interface width as a function of bilayer thickness and the value of growth exponent of the interfaces has been obtained. It is found that the growth exponent in case of Ni-on-Ti interface almost agrees with the growth exponent of surface roughness in case of single layer Ti film. However, for Ti-on-Ni interface, the growth exponent is much higher than the surface roughness of single layer Ni film, showing that inter-diffusion plays more significant role in Ti-on-Ni interfaces.

Subsequently, Ni/Ti supermirrors of m=1.75 and m=2.0 having 62 and 98 number of layers respectively have been deposited in the home-made rf sputtering system following the design structure generated by an in-house developed computer code. These supermirrors are characterized by measuring neutron reflectivity with neutrons of 2.5 Å wavelength and both the samples are found to show high reflectivity up to their respective cut off angles.

CHAPTER 6

Development of Ion Beam Sputtering (IBS) system and optimization of process parameter for W/Si & W/C interfaces

6.1 Introduction

As has been discussed in Chapter 3, Ion beam sputtering (IBS) technique has certain advantages over other physical vapour deposition processes viz., vacuum evaporation and magnetron sputtering. Vacuum evaporation technique suffers from an inherent problem that the energy of the evaporated adatoms reaching the substrate is less than 1 eV. Monte-Carlo simulation and molecular dynamics studies show that if the kinetic energy of the incident adatoms are in the range few eVs, adatoms can migrate significantly on a growing film surface to change the morphology of the film from a columnar growth to a two-dimensional smooth structure [115]. This does not happen in a vacuum evaporation process and thus films grow in a columnar fashion resulting in higher surface roughness. There are efforts to overcome this difficulty by using a separate ion beam made incident on the growing film during the evaporation process to deliver extra energies to the adatoms [116]. However, this has led to ion beam induced modifications at the interfaces of the multilayer stacks [116-118]. This problem is not present in magnetron sputtering technique, where the energy of the adatoms are high enough to allow rearrangement on the surface during growth, leading to films with very smooth surfaces which has already been seen in the two previous chapters where using magnetron sputtering system

Co/Ti and Ni/Ti multilayer film of low roughness films have been successfully deposited. However, in magnetron sputtering technique, since an inert gas (generally, Ar) plasma has to be generated and sustained in the sputtering zone, the deposition has to take place at a relatively higher Ar partial pressure (typically, 5 x10^{3}-5x10^{-2} Torr) leading to contamination and Ar trapping inside the growing film. In Ion Beam Sputtering (IBS) deposition technique, on the other hand, ions are generated inside an independent source which is kept away from the sputtering zone and the ions are then made incident on the target by using proper extraction and focusing mechanism [119]. Hence, IBS process can take place at a working pressure of at least one order of magnitude lower than that in magnetron sputtering process which ultimately results in higher purity, packing density and better morphology of the deposited films. Since the ion sources generally have independent control over energy and current density of the bombarding ions, deposition by IBS technique also has better reproducibility and control. Considering these advantages an IBS system have been developed in-house in our laboratory, under this thesis work, for the development of soft X-ray multilayers. As will be discussed in details in the next chapter, these multilayers are used to reflect soft X-rays having wavelength in the range of 10-150 Å and hence according to Bragg relation they can operate at higher grazing angle of incidence (~20^{o}-40^{o}). Thus required dimensions of these multilayer devices are smaller compared to the neutron supermirrors which work at much smaller grazing angle of incidence as discussed previously and hence ion guns of reasonable size and cost can be employed to realize these mirrors.

In this chapter initially details regarding the in-house developed Ion Beam Sputtering (IBS) system have been described and subsequently, optimization of process parameters by depositing single layer W films and W/Si/W, W/C/W trilayer films at different ion energies in the range of 0.6-1.2 KeV and their characterization by specular and non-specular X-ray reflectivity, spectroscopic ellipsometry and atomic force microscopy techniques have been thoroughly discussed. This exercise has been done to obtain good quality single layer films and interfaces for the deposition of W/Si and W/C soft X-ray multilayer devices described in the next chapter.

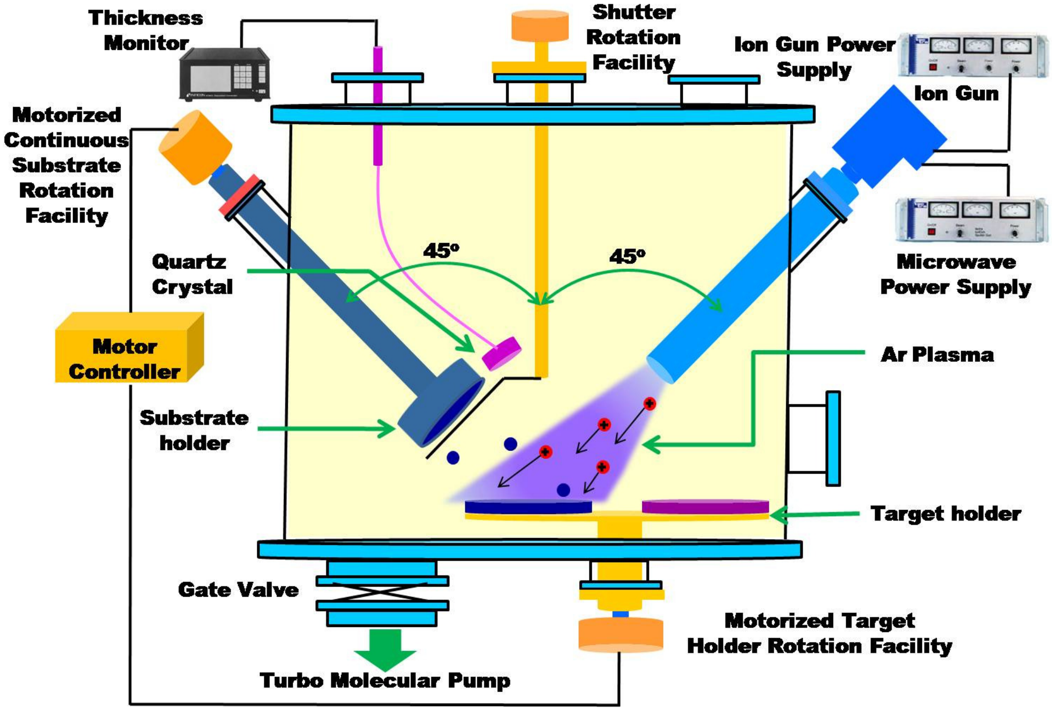

Fig. 6.1: Schematic diagram of Ion Beam Sputtering (IBS) system

6.2 Development of IBS system

The schematic diagram of the Ion Beam Sputtering system set up in our laboratory is shown in Fig. 6.1 [120]. The cylindrical UHV S.S. grade sputtering chamber is of 300 mm diameter and is equipped with turbomolecular based pumping system and cold cathode gauge and base pressure of 5 x 10^{-7} Torr is regularly achieved in the system. The chamber has two 63 CF ports at angle of 45° with each other for introducing the ion gun and the substrate holder. An ECR microwave based filament-less plasma ion source (TECTRA GmbH, Germany) is used in the system. The advantage of using an ECR based source is that dense plasma at relatively low pressure can be obtained under the electron cyclotron resonance (ECR) conditions [76]. The ion source uses microwave power of 250 W @2.45 GHz to produce an Ar plasma within a hemi-spherical alumina plasma chamber. High purity Ar gas is fed into the ion gun at a controlled rate through a mass flow controller to generate the plasma. A permanent magnet based axial magnetic field around the chamber increases the plasma density via the Electron Cyclotron Resonance (ECR) effect. The ions are then extracted out by molybdenum acceleration grids. With the present ion source Ar ions can be extracted at different energies in the range of 50–2000 eV and with a maximum ion current of 20 mA. With plane extraction grids, an ion beam having 50 cm diameter can be made incident on the targets at an angle of about 45°. As shown in Fig.1, two 3" diameter sputter targets are mounted on a horizontal tray which can be rotated by a stepper motor and the targets can be placed sequentially in the ion beam by two limit switches

Fig. 6.2: Actual photograph of the IBS system in our laboratory

mounted at pre-defined positions. The substrates are mounted on the substrate holder shaft about 75 mm above the targets making an angle of 45° to the horizontal. Substrates can be continuously rotated during deposition by a d.c. motor mounted on the shaft outside vacuum. In Fig. 6.2 the actual photograph of the IBS system installed in our laboratory is shown, while a photograph of the ion beam coming out of the gun is shown in the inset of the figure. The extraction grid voltage and grid current values used for depositing the films are 1000 V and 10 mA respectively. A constant Ar working pressure of ~ 1×10^{-3} Torr is maintained in the chamber during deposition. Films have been deposited on c-Si substrates kept at room temperature. It has been observed that under similar deposition conditions of 1000 eV Ar^{+} ion energy and 10 mA grid current, deposition rates of 0.03 Å sec^{-1} and for 0.07 Å sec^{-1} have been achieved for W and Si targets respectively.

6.3 Deposition of single layer, bi-layer and tri-layer films

6.3.1 Single layer W film

Subsequent to the installation of the system single layer W, Si and C films are deposited. Fig. 6.3 shows the GIXR spectrum for a representative W film (W-1) deposited on crystalline silicon (c-Si) substrate, the deposition has been carried out for 30 mins. with Argon ions having energy of 1000 eV.

The experimental spectrum has been fitted with the theoretically simulated spectrum derived using the formalism described in Chapter 2. The best fit theoretical simulation along with the sample structure obtained from the best fit for the W layer are also shown in Fig. 6.3. It should be noted that the c-Si substrate used in the deposition processes has also been characterized by GIXR separately. The GIXR spectrum of a bare c-Si substrate along with the best theoretical fit has been shown in the inset of Fig. 6.3. It is observed that the c-Si substrate is characterized by the presence of a ~10Å Si oxide over layer. This has been used in the subsequent analysis of all thin film structures and kept invariant during the fitting process.

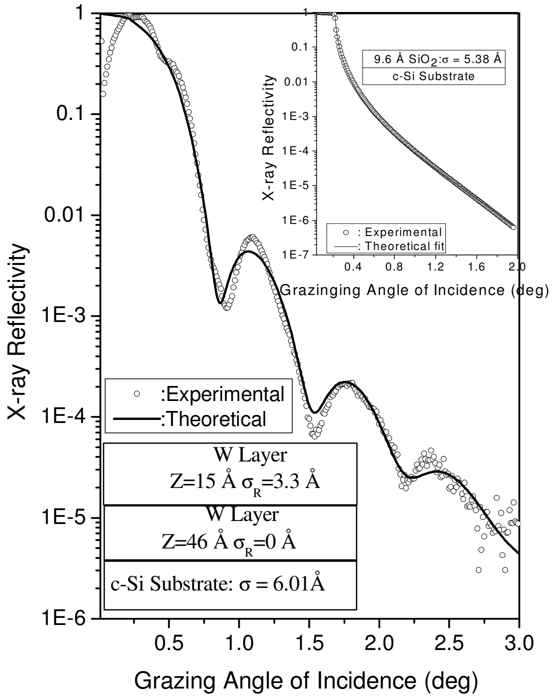

Fig. 6.3: Grazing Incidence X-ray Reflectivity spectrum with best-fit theoretical curve for a representative W film (W-1) deposited on c-Si substrate. Inset: Grazing Incidence X-ray Reflectivity spectrum with best-fit theoretical curve for a c-Si substrate.

It has been observed that the GIXR spectrum of the W-1 sample is best fitted with a two-layer model with a relatively low-density surface layer above the top of a bulk-like compact layer. The densities of the bottom W layer and top W layer correspond respectively to 90% and 75% of the bulk density of W [120]. This observation is very common for thin film structures deposited by any technique. As the film thickness increases during deposition, the deeper lying atoms are subjected to stronger inter-atomic forces and form a compact structure whereas the atoms near the surface are subjected to less inter-atomic force and thus form a spongy loose packed structure [51]. Total thickness of the W-1 film is found to be 61Å yielding a rate of deposition of 0.03 Åsec^{-1} which is typically used for depositing multilayer stacks for X-ray mirror applications [121]. It has been further observed that the r.m.s. surface roughness (σ_R) of the top layer of the W film is 3.3 Å. As mentioned above, the morphology of the W-1 film has also been investigated by AFM technique.

Fig. 6.4 shows the AFM micrograph of the W-1 film along with the r.m.s. roughness. It has been seen that r.m.s. roughness (σ_R) values obtained from the two techniques (GIXR and AFM) for the W-1 film agree well.

The above results show that the present Ion Beam sputtering System is capable of producing good quality films with low surface roughness required for fabrication of multilayer devices. It suggests that the film growth is not totally columnar is fashion, rather, two-dimensional layer formation with smoothening of the surface by surface diffusion of adatoms also takes place to some extent, which should be the case for an ideal sputtering process where the adatom energies are generally high.

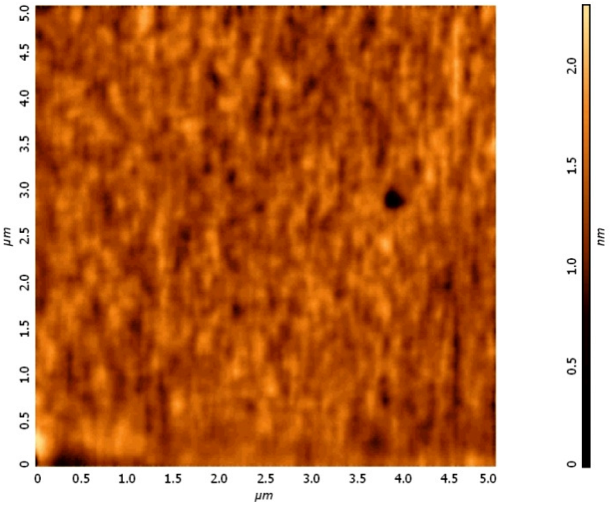

Area of scan	5 μm X 5 μm
Amount of sampling	65536
Root Mean Square, Sq	0.215106 nm

Fig. 6.4: Atomic force micrograph of a representative W film (W-1) deposited on c-Si substrate.

6.3.2 Single layer amorphous a-Si film

Single layer a-Si films deposited by Ion Beam Sputtering at ion energy of 1000 eV on c-Si substrates have been characterized by Spectroscopic Ellipsometry in the wavelength regime of 300-1200 nm [120]. Density of the a-Si film is very close to that of the c-Si substrate manifesting very little contrast in the GIXR spectra and thus determination of thickness becomes almost impossible. However, a-Si and c-Si have large difference in optical constants in the visible optical regime [122] showing good contrast in ellispometric spectra.

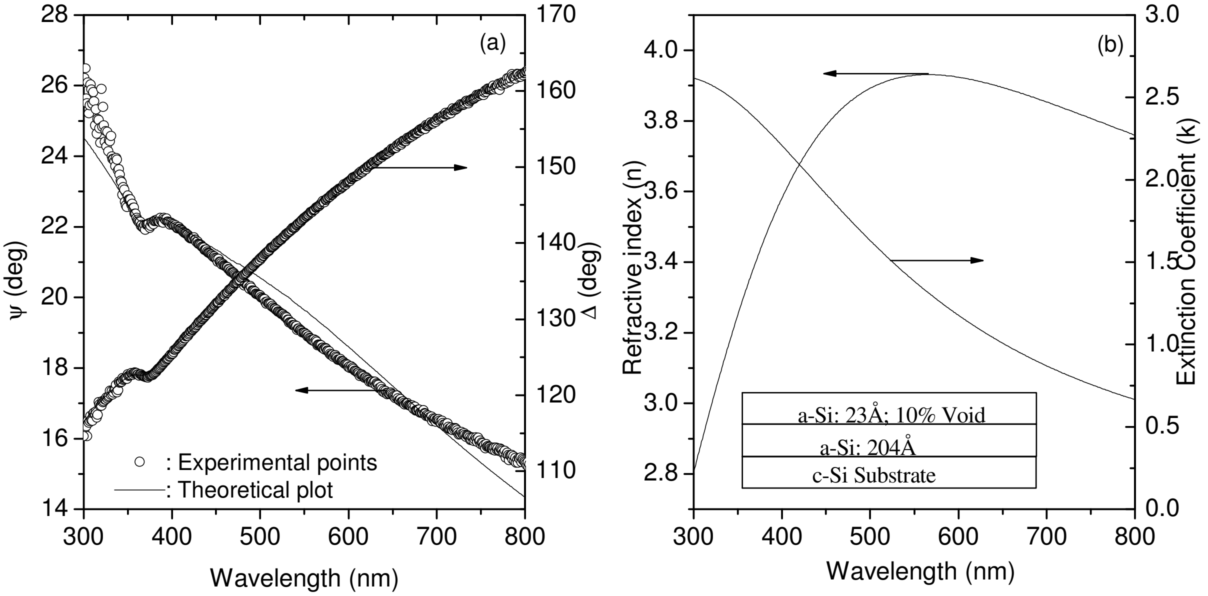

Fig. 6.5: (a) Experimental Ψ and Δ spectra with wavelength along with best fit theoretical plots for a representative a- Si film (Si-1) deposited on c-Si substrate. (b) Variation of Refractive index (*n*) and Extinction Coefficient (*k*) with wavelength and the best fit sample structure

The principle of the SE technique [85, 86] has been discussed in detail in Chapter 3. Fig. 6.5(a) shows the experimental Ψ and Δ spectra with wavelength along with the best-fit theoretical simulation for a representative a-Si film (Si-1) deposited on c-Si substrate for 50 mins with Ar ion energy of 1000V. Variation of refractive index (n) and extinction coefficient (k) with wavelength for the a-Si sample (Si-1), generated with the best fit values for the parameters of the dispersion relation, have been shown in Fig. 6.5(b). The optical constants of the a-Si film agree well with earlier reported values for a-Si films produced by e-beam evaporation [123]. The best fit sample structure obtained for the film is also shown in Fig. 6.5(b). It has been found that, the best fit is obtained with a two sub-layer structure with a bulk-like compact layer on the substrate with no void and a top surface layer with less density manifesting loose packing and presence of voids. Total thickness of the Si-1 sample as obtained by ellipsometric analysis is found to be ~227 Å which manifests a deposition rate of 0.07 Å $\sec^{-1}$. Similar measurements have been carried out on the seven positions of 20 mm x 25 mm substrate and it is seen that the thickness of the film is within the variation of ±4.5%.

As have been mentioned above, morphology of the films have also been characterized by AFM in the contact mode. The AFM micrograph of the Si-1 film is shown in Fig. 6.6 along with the r.m.s. roughness of the film. It has been seen that though the SE analysis shows the presence of a top layer of thickness (d_s= 23 Å) with 10% void, AFM measurement shows a very smooth surface with r.m.s. roughness (σ_R) of 1.01 Å. Significant disagreement exists also in the literature regarding the actual quantitative interpretation of the thickness of the surface roughness layer (d_s), as obtained from the SE measurements, in the context of surface height irregularities. Some authors have shown that d_s values agree well with the r.m.s roughness [124, 125] of the layers while others have found that d_s either corresponds to the peak to peak roughness [126] or gives a value in between [127].

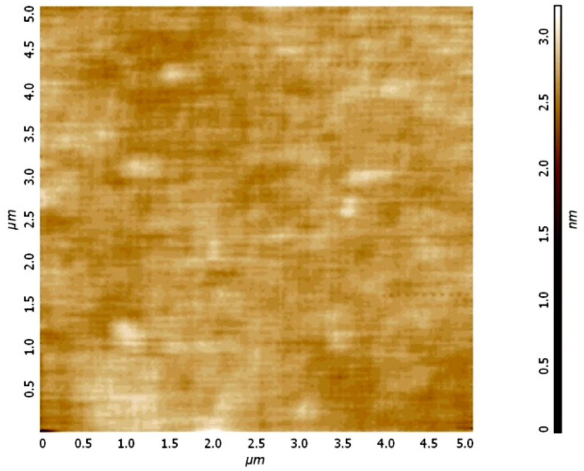

Area of scan	5 μm X 5 μm
Amount of sampling	65536
Root Mean Square, Sq	0.101228 nm

Fig. 6.6: Atomic force micrograph of a representative a-Si film (Si-1) deposited on c-Si substrate.

6.3.3 Single layer C film

The single layer C-film deposited on c-Si substrate at ion energy of 1000 eV has also been characterized by Spectroscopic Ellipsometric (SE) method in the wavelength range 300-1000nm at seven (07) positions of the 25 mm x 20 mm film [128]. Similar to a-Si films, the density of the a-C film is very close to that of the c-Si substrate manifesting very little contrast in the GIXR spectra, while a-C and c-Si have large difference in optical constants in the visible optical regime [122] showing good contrast in ellipsometric spectra. Hence, the a-C films discussed here have been characterized by SE.

In Fig. 6.7 the experimental Ψ and Δ versus wavelength along with best fitted theoretical spectra of a representative measurement point (among 7 points) of the a-C film is shown. In the inset of the figure the refractive index (*n*) and extinction coefficient (*k*) of the a-C film found from best fitted data is shown. The values of *n* & *k* are found to be comparable with the previously reported value of a-C film [122]. The thicknesses found at the seven points are 6.77 nm, 6.72 nm, 6.46 nm, 6.37 nm, 6.22 nm, 6.54 nm and 6.49 nm. So it is clear that the specially

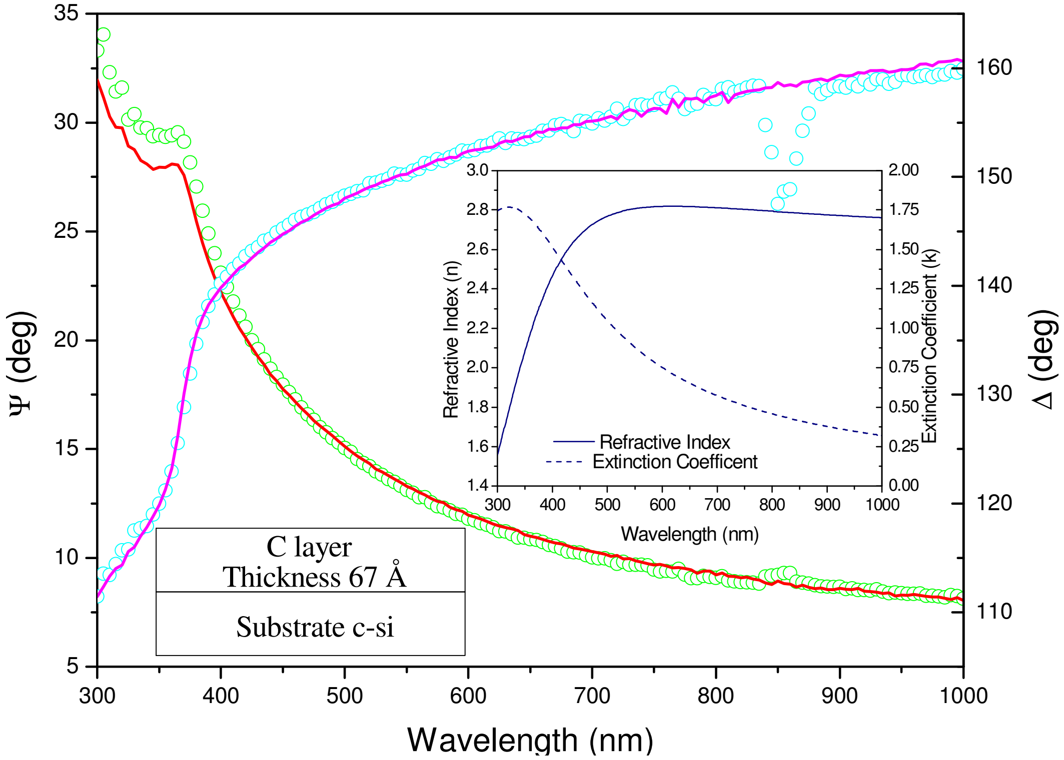

Fig. 6.7: Experimental ψ and Δ vs wavelength along with best-fit theoretical curve for a representative points of a-C films. oooo: Experimental Data;———: Theoretical Spectrum. The inset shows variation of Refractive index (*n*) and Extinction Coefficient (*k*) with wavelength and the best fit sample structure

uniform thin film have been deposited with uniformity of ±3.8%. The rate of deposition found is 0.02 Å/Sec [128].

The above results on a-Si and a-C films manifest the capability of the home-made Ion Beam Sputtering system in producing layers with uniform thickness over a substrate of 50 mm diameter apart from very low surface roughness of the layers [120].

6.3.4 W/Si bi-layer film

Once the single layers are characterized, measurements have been carried out on the bi-layer a-Si/W sample (B-1) deposited on c-Si substrate, where the W film has been deposited for 20 mins. and a-Si film has been deposited for 25 mins [120]. All the depositions have been carried out at an Ar partial pressure of 1×10^{-3} Torr and with a grid voltage of 1000 V and grid current of 10 mA. The GIXR spectrum of the bi-layer sample with the best fit theoretical spectrum and the best fit sample structure have been shown in Fig. 6.8. As has been found from the above measurement, the bi-layer sample is characterized by a 37 Å W film, having two sub-layers of 27 Å and 10 Å respectively on the substrate, with a 92 Å thick a-Si layer on top. The two sub-layer model of the W film is consistent with the earlier observation made on the single layer W film

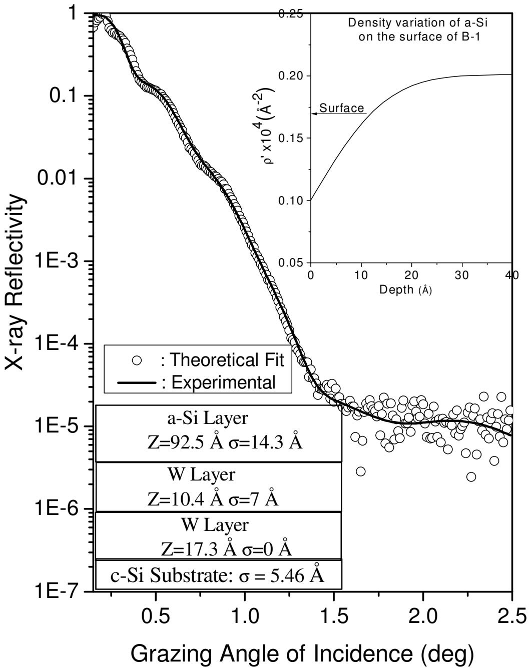

Fig. 6.8: GIXR spectrum along with the best-fit theoretical curve and the best-fit sample structure for a a-Si/W bi-layer structure (B-1) deposited on c-Si substrate. Inset: density profile of the top a-Si layer of the B-1 sample as obtained from the best fit of the GIXR spectrum.

(Section 6.3.1) and the total thickness of the W layer agrees with the expected deposition rate of 0.03 Å sec^{-1}.

It has been discussed previously that by the specular X-ray reflectivity studies, the effect of interfacial roughness and interface diffusion cannot be distinguished and the parameter σ in case of an interface is generally called as interface width [59]. The interface width (σ) at the Si/W interface in case of the B-1 sample, as obtained from the GIXR analysis is 7Å. If we assume the roughness of underlying W layer to be 3 Å as obtained from the analysis of the single layer W film discussed earlier in section 6.3.1, the interface diffusion width is 4Å. Thus it can be concluded that Si diffuses very slightly inside the W layer. In case of r.f. sputtered samples, as reported earlier, Si diffuses upto 10 Å inside W layer [129].

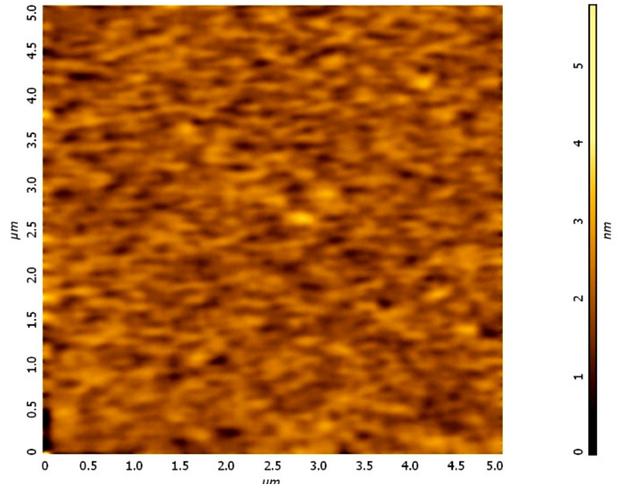

Area of scan	5 μm X 5 μm
Amount of sampling	65536
Root Mean Square, Sq	0.41113 nm

Fig. 6.9: Atomic force micrograph of the a-Si/W bi-layer sample (B-1) deposited on c-Si substrate.

However, as can be seen from Fig. 6.8, GIXR measurement reveals a relatively higher roughness at the top surface of Si in the B-1 sample. Fig. 6.9 shows the AFM micrograph of the B-1 sample which reveals a r.m.s roughness of 4 Å for the top Si layer, slightly higher than the single layer Si film discussed earlier in section 6.3.2. This is expected since the single layer Si film was deposited on singly crystalline Si substrate, while the Si layer of the B-1 sample is deposited on an underlying thin W film.

The r.m.s. roughness value (σ_r) of the B-1 sample obtained from the AFM measurement does not match with the high value obtained from the GIXR measurement. It may be because of the fact that, the low density void prone top layer of the a-Si film contributes to the σ value of the top surface of B-1 as obtained from GIXR measurement. To investigate it further, a continuously varying density gradient has been assumed at the surface of the top a-Si layer and the fitting of GIXR data has been carried out. The result of the best fit density profile is terms of ρ (= $2\pi\ \delta/\lambda^2$) has been shown in the inset of Fig. 6.8. This shows that the density of the a-Si layer gradually falls off over a thickness of 15 Å towards the surface showing the presence of void prone surface layer. As described above, SE analysis of the single layer Si sample shows the presence of a low density layer of 23 Å on the surface of a 200 Å a-Si film. Presence of a 10 Å thick low density layer on the surface of a 100Å thick r.f. magnetron sputtered a-Si film has also been reported earlier [129].

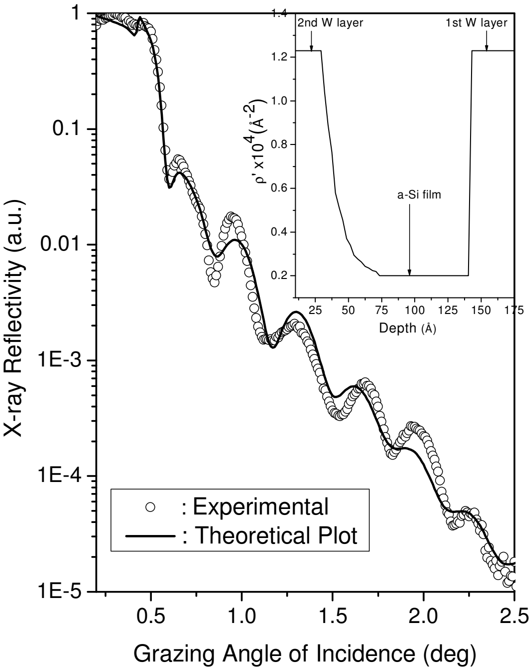

Fig. 6.10: GIXR spectrum along with the best-fit theoretical curve and the best-fit sample structure for a W/a-Si/W tri-layer structure (T-1) deposited on c-Si substrate. Inset: Density profile of the two W/Si interfaces of the T-1 sample as obtained from the best fit of the GIXR spectrum.

6.3.5 W/Si/W tri-layer film

Fig. 6.10 shows the results of the GIXR measurement on a tri-layer (W/a-Si/W/c-Si) sample (referred to as the T-1 sample), where the W layers are deposited for 20 min [120] each and the a-Si layer is deposited for 25 min. The r.m.s. roughness (σ_R) of the top W layer is found be 3.6 Å, which also agrees with the AFM micrograph of the T-1 sample as shown in Fig. 6.11.

In order to estimate the inter-diffusion at the W/Si and Si/W interfaces, the fitting of the GIXR data of the tri-layer sample has been carried out by breaking up the two interfaces in 20 nos. of sub-layers and assuming continuously varying density gradients at these two interfaces. The best fit density profile is terms of ρ (= $2\pi \delta/\lambda^2$) as obtained from the fitting has been shown in the inset of Fig. 6.10.

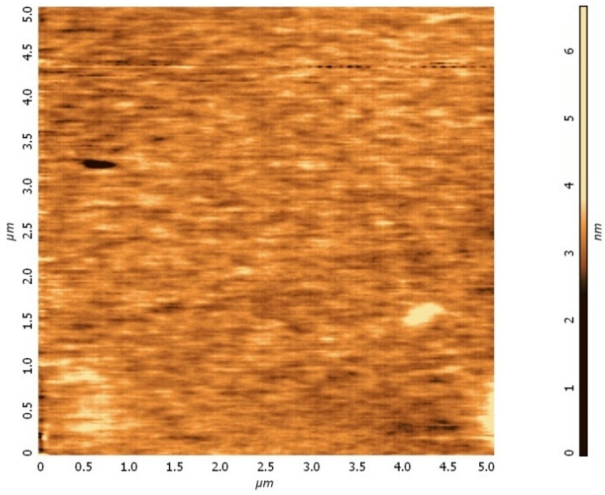

Area of scan	5 μm X 5 μm
Amount of sampling	65536
Root Mean Square, Sq	0.227687 nm

Fig. 6.11: Atomic force micrograph of a W/a-Si/W tri-layer sample (T-1) deposited on c-Si substrate.

From the density profile it has been observed that the 1st interface where a-Si layer is deposited on W layer (Si-on-W), the density is varying over a distance of 4-5 Å, which shows very small inter-diffusion at this interface. However, at the 2nd interface where the W layer is deposited on a-Si layer (W-on-Si), the density is varying gradually over a thickness of ~40Å. If we assume that the r.m.s. roughness of the a-Si layer deposited on a W-layer, as observed in the AFM micrograph of the W/Si bi-layer (B-1) sample (discussed above in the section 6.2.4) to be 4 Å, the width of the inter-diffusion layer at the W-on-Si interface is found to be much higher than the estimated thickness of the low density layer on the top of the 90 Å thick a-Si layer. Thus it shows that W when deposited on a-Si layer penetrates significantly inside the underlying Si layer. This is also manifested by the less thickness obtained by GIXR analysis for the top W layer compared to the bottom W layer of the T-1 sample. It may be mentioned here that in case of r.f. sputtered sample, it had been found from Secondary Ion Mass Spectrometry (SIMS) study that the width of inter-diffusion layer at W-on-Si interface is still larger [129].

The interface width of the W-on-Si interface is found to be much higher than that of Si-on-W interface which is consistent with our earlier findings on similar systems deposited by r.f. magnetron sputtering [129]. Kessel et al. [118] have also observed that the W/Si interface is generally asymmetric with interface width of W-on-Si is more than Si-on-W. Other workers have also reported the fact that in case of sputter-deposited multilayers, the interface width depends on the order of deposition, e.g., in case of Mo/Si multilayers the interface is sharper when Si is deposited on Mo than when Mo is deposited on Si [129, 130]. Similar asymmetric diffusion of one material in to the other has also been observed for Co/Ti and Ni/Ti multilayer as discussed in previous chapters, where it is seen that in case of Co/Ti multilayer Co-on-Ti interface is larger than Ti-on-Co and similarly in case of Ni/Ti multilayer Ni-on-Ti interface is more than Ti-on-Ni.

The larger value of interface width at the W-on-Si is also consistent with the fact that the average atomic volumes of W atoms are smaller and W atoms can penetrate through a larger distance in the underlying disordered amorphous Si layer [131] than the Si atoms inside the W film. However it has been felt that the optimization of the deposition parameters are essential so that the inter-diffusion at the interfaces are reduced.

6.4 Optimization of process parameters

The morphological properties of surfaces and interfaces of multilayer systems deposited by IBS process depend mostly on the energy dissipated at the growing surface by the sputtered atoms which in turn depends on the energy of the primary ions used for sputtering. For example, Ji *et al.* [132] have found that penetration and diffusion across the interfaces in their IBS-deposited Co/Pt multilayer increases with the increase in primary ion energy. Apart from the kinetic energy of the sputtered atoms, the energy of the adatoms would also be enhanced by the ions reflected or backscattered from the target surface and this also would have an effect on the morphology of the growing film. This effect is similar to that of an ion beam directed onto the substrate in an ion-assisted e-beam evaporation process which is known to change the surface morphology and interface properties in a multilayer sample significantly [118]. The effect of back scattered ions have been observed by Cevro and Carter [133] in case of their IBS deposited TiO_2 films, where the authors have found Ar^+ ions upto a density of 0.4% get trapped inside the growing films. Effect of reflected ions has also been observed and discussed by Balu *et. al.* [134] on the properties of their IBS-deposited Cr thin films.

However, there are discrepancies in the literature regarding the dependence of energy of sputtered particles and back scattered ions on the energy of the projectile ions. Duchemin [135] has simulated the IBS process using the TRIM Monte-Carlo code and showed that both the energy of the sputtered atoms and the backscattered/re-sputtered ions increase with the increase in the projectile energy for Ion Beam Sputtering of Mo by Xe ions. However, Franke *et al.* [136] by putting an energy-selective mass spectrometer inside an IBS chamber, have measured the energies of different ions and neutrals involved in a typical IBS process and have found that the energy of the re-sputtered Ar^+ ions from the target surface follows a distribution whose maxima shifts towards lower energy as the energy of the projectile species increases, while the maxima of energy distribution of Ti neutrals sputtered from a Ti target almost remains constant. However, they have also observed that the energy distribution of the species strongly depends on the projectile-target combination. Thus determination of the optimum energy of primary ions is very important for establishing the process parameters for deposition of a particular multilayer system by IBS technique.

Hence prior to the deposition of W/Si and W/C multilayers we have prepared single layer W films, W/Si/W tri-layer and W/C/W tri-layer samples where W layers have been deposited at different ion energies in the range of 600-1200 eV and thoroughly analysed the dependence of the surface and interfaces of the samples on the energy of the primary Ar^+ ions, the results being described below. In this whole exercise, Si and C films have always been deposited at an intermediate ion energy of 1000 eV since it has been observed that the properties of Si or C films do not vary much with the change in energy of the Ar^+ ions.

6.4.1 Ion energy dependence of single layer W film

Fig. 6.12(a) and (b) show the specular and non-specular GIXR spectra of a representative single layer W film deposited on c-Si substrate by the IBS technique in the home-built system described above with an ion energy of 1200 eV [114]. The non-specular X-ray reflectivity spectrum has been measured at the angle of incidence corresponding to the maxima of the 1st oscillation in the specular X-ray reflectivity spectrum. The experimental spectra have been fitted with theoretically simulated spectra using the formalism discussed in Chapters 2 and 3 and the best fit theoretical simulations have also been shown in Fig. 6.12(a) and (b). Similar measurements and theoretical fittings have been carried out on all the W films deposited at different ion energies. The thickness measured by the in-situ thickness monitor (40Å) during deposition has been taken as the starting value for the theoretical fitting of the specular GIXR spectrum. The thicknesses of the samples as obtained from the GIXR analysis are found to be 41, 39, 37 and 39 Å for films deposited at ion energies of 600, 800, 1000 and 1200 eV respectively which shows good calibration of the in-situ monitoring system.

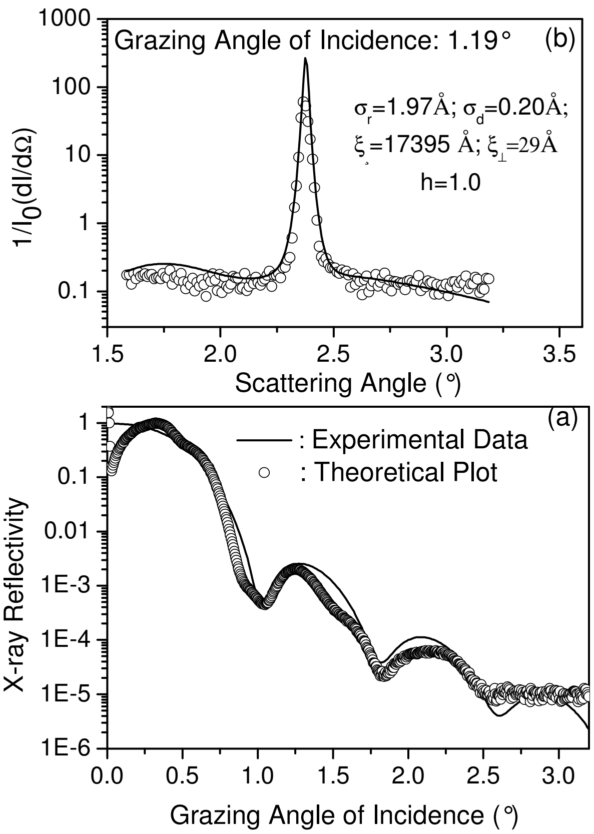

Fig. 6.12: (a) Specular and (b) non-specular Grazing Incidence X-ray Reflectivity spectra with best-fit theoretical curves for a representative single-layer W film deposited on c-Si substrate with Ar$^+$ ion energy of 1200 eV.

The other parameters obtained from the specular GIXR spectra of the samples are surface roughness, interface roughness and densities of the films. The interface width (σ) at the W/c-Si substarte interface and the surface roughness at the Vacuum/W interface as obtained from the fitting of the specular GIXR data have been shown in Fig. 6.13(a) as a function of the ion energy used during deposition of the W films. It should be mentioned here that, considering strong correlation between density and roughness in the GIXR spectrum near the critical angle, roughness values obtained independently from Atomic Force Microscopy (AFM) measurements on the films have been taken as starting guess values for the fitting. It has been found from Fig. 6.13(a) that interface width of W/c-Si interface reduces as the ion energy for W sputtering increases. This may be due to the fact that at lower ion energy of 600 eV and 800 eV, adatoms reaching the substrate surface do not obtain sufficient energy to redistribute themselves resulting in the three-dimensional island-like structure on the surface leading to higher interface roughness. As the ion energy increases, mobility of adatoms also increases leading to two-dimensional smooth interface. The best fit parameters of the non-specular reflectivity measurement are shown in Fig. 6.12(b), from where it is found that the roughness component (σ_r) is the major contributor to the width of the W/c-Si interface and contribution of interface diffusion (σ_d) is insignificant. From Fig. 6.13(a) it is also found that the roughness of the top vacuum/W interface increases continuously as the ion energy increases from 600-1200 eV because of the increase in grain sizes at the surface of the W layer with increase in ion energy.

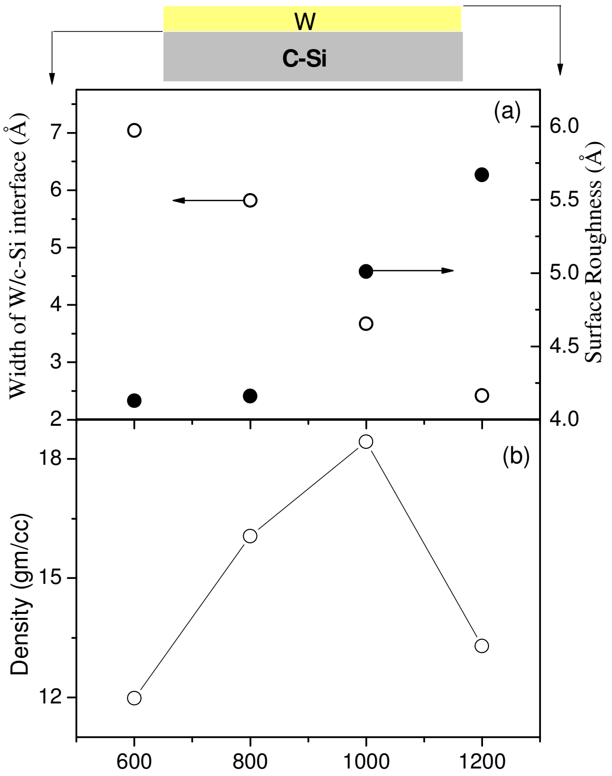

Fig. 6.13: (a) Variation of interface width of W/c-Si interface and surface roughness of single-layer W films as a function of ion energy used for W sputtering. (b) Variation of density of the single-layer W films as a function of ion energy used for W sputtering

The densities of the W layers have also been estimated from the specular GIXR fittings and are shown in Fig. 6.13(b) as a function of ion energy of sputtering. It shows that density of the films initially increases as the ion energy increases upto 1000 eV above which the density goes down. To obtain an insight into the above phenomenon, we have carried out simulation of the IBS process by using the Monte Carlo Programme "TRIM", which works on the principle of binary collision dynamics, to estimate the yield and energy of the sputtered atom and backscattered ions [137]. The results are shown in Fig. 6.14(a) & (b) for the sputtered atoms and backscattered ions respectively. It shows that with increase in energy of the incident particles, the positions of the maxima in the energy distributions of the sputtered atoms and backscattered ions remain almost constant though the distributions change. In case of sputtered atoms, the number of W atoms emitted with maximum energy increases with increase in the energy of the primary ions, while the reverse trend is observed for the backscattered Ar^{+2} ions. However, if total energy of the sputtered atoms and the back scattered ions emitted for a particular flux of incident Ar^{+2} ions are calculated from the area of the respective curves shown in Fig. 6.14(a) and (b), it is found that the sum total of the energy of the sputtered atoms and back-scattered ions with which they strike the growing surface of the film increases monotonically as the energy of the primary projectiles increases. The increase in kinetic energy in the sputtered adatoms with increase in energy of the incident ions, results in higher mobility of the adatoms on the growing surface and thus promotes two-dimensional growth and enhanced smoothness of the layers. However, with the increase in the energy of the incident ion beam, sputtering yield of the target also increases which increases the rate of deposition and results in faster growth of grains, enhanced surface roughness and low density of the films. The simulated sputtering yields from W target under Ar^{+2} ion bombardment at different energies are shown in Fig. 6.15, which follows similar trend as observed in case of Ti sputtering by Ar^{+2} ions [136]. Thus the above two competitive processes, viz., the faster rate of deposition and movement/re-adjustment of adatoms on the growing surface, result in the optimised value of 1000 eV Ar^{+2} ion energy to obtain highest density in the W layers.

6.4.2 Ion energy dependence of W/Si/W tri-layer

The specular and diffused GIXR measurements have also been carried out on the tri-layer samples. Fig. 6.16(a) show the specular and Fig. 6.16 (b) and (c) show the non-specular X-ray reflectivity spectra of a representative tri-layer W/Si/W sample where the W layers have been deposited at an ion energy of 1200 eV [114]. It should be mentioned here that considering higher number of unknown parameters for a tri-layer sample, diffused reflectivity spectra have been measured at two angles of incidences corresponding to the maxima of 1st and 2nd oscillations of the specular GIXR spectrum.

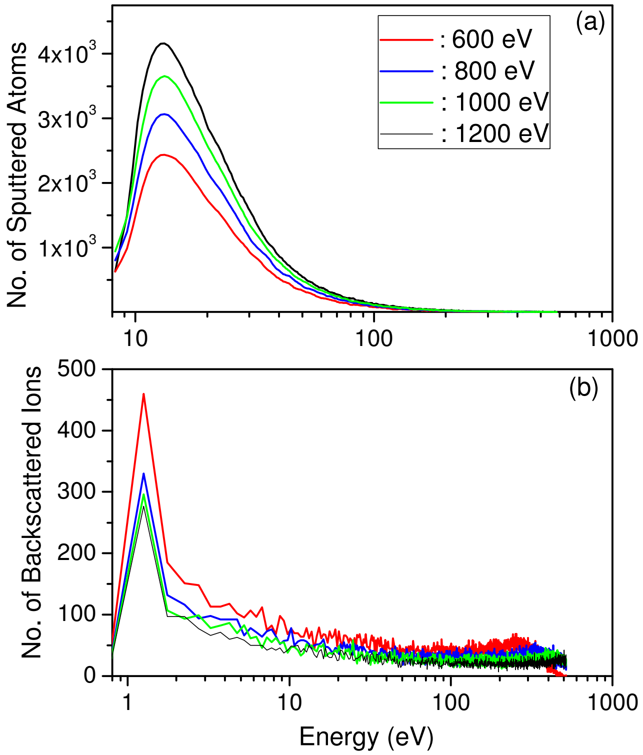

Fig. 6.14: Simulated Energy Distribution of (a) sputtered W atoms and (b) back scattered Ar^{+2} ions from a W target under bombardment of Ar^{+2} ions at different energies

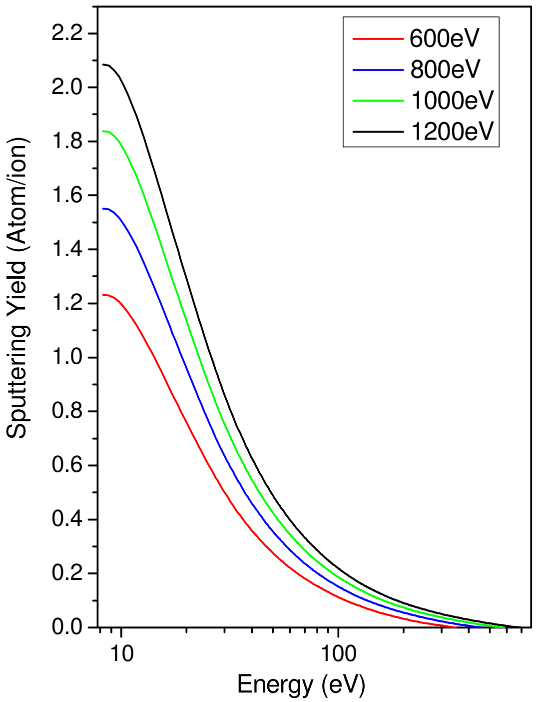

Fig. 6.15: Simulated Sputtering yield of a W target under bombardment of Ar^{+2} ions at different energies.

The best fit theoretical plots obtained following the formalism given in Chapters 2 and 3 for the measured specular and non-specular spectra are also shown in the above figures. Since it had been observed in case of single layer samples that the thickness estimations by quartz crystal monitors and GIXR measurements agree quite well with each other, in case of tri-layer samples we have assumed the in-situ measured thicknesses as the true thicknesses of the layers and have kept them invariant during fitting. Densities of the layers have also been taken from the GIXR measurements of respective single layer films as discussed in the previous section. Also the h values of the different layers have been taken as 1 for all the samples during fitting of the diffused reflectivity spectra. This is justified since lower h value generally defines a relatively more jagged layer corresponding to columnar growth, characteristic of vacuum evaporation technique, however IBS deposited layers generally have relatively smoother texture manifesting two-dimensional growth which justifies the choice of h=1. Ulyanenkov *et al.* [138] have also found a value of h=1 by fitting the diffused X-ray scattering spectra of their Mo/So multilayers prepared by Ion Beam Sputtering on c-Si wafers.

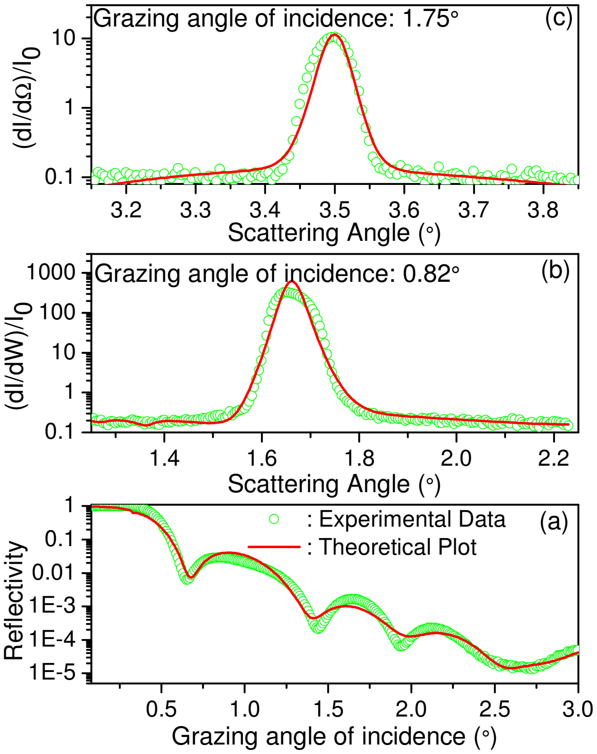

Fig. 6.16: (a) Specular and (b) & (c) non-specular Grazing Incidence X-ray Reflectivity spectra with best-fit theoretical curves for a representative tri-layer W/Si/W sample deposited on c-Si substrate where the W films have been deposited with Ar^+ ion energy of 1200 eV

The above exercise has been carried out for all the four tri-layer samples and the interface width (σ) values as obtained from the fitting of specular GIXR data and the interface roughness (σ_r) and the interface diffusivity (σ_d) values as obtained from the fitting of non-specular GIXR spectra are shown in Fig. 6.17(a) and (b). The other parameters viz., the in-plane

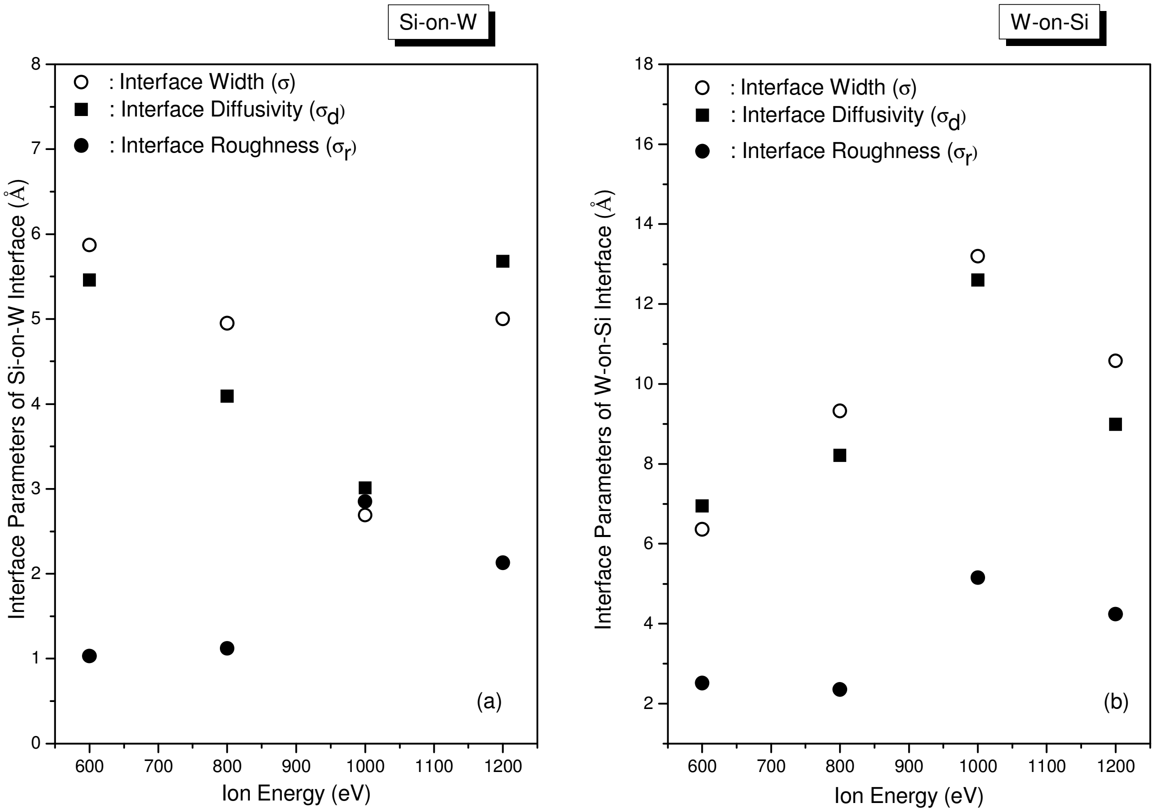

Fig. 6.17: Variation of the interface parameters viz., interface width (σ), interface diffusion (σ_d) and interface roughness (σ_r) of the (a) Si-on-W interface and (b) W-on-Si interface of the W/Si/W tri-layer samples as a function of ion energy used for W sputtering.

($\xi_{\parallel}$) and the vertical ($\xi_{\perp}$) correlation lengths of the layers derived from the fittings and surface roughness of the top W layer (σ_{top}) have been given in Table-6.1. It should be mentioned here that, for a particular sample, the values of the interface parameters ($\sigma_r, \sigma_d, \xi_{\parallel}$ and $\xi_{\perp}$) required to fit the measured diffused reflectivity data at two angles of incidences are found to be almost same and hence the average values of the parameters have been presented in Table-6.1 and Fig. 6.17(a) and (b).

It can also be seen from Fig. 6.17(b) that the major contributor to the interface width of the W-on-Si interface is interface diffusion (σ_d) i.e., diffusion of W atoms in underlying Si layer which is much higher than the diffusion of Si atoms in underlying W layer as shown in Fig. 6.17(a). The above findings is consistent with the fact that the average atomic volumes of W atoms are smaller and W atoms can penetrate through a larger distance in the underlying disordered amorphous Si layer [117] than the Si atoms inside the W film. However, it also shows that the energy of the W atoms and also of the back scattered Ar^+ ions may be much higher in case of W sputtering compared to that of Si sputtering. Teyssier *et al.* [139] have carried out simulation of IBS process of Mo/Si multilayers by TRIM Monte Carlo code and observed that the peak of the energy distribution of sputtered Mo atoms is ~5 eV while that of Si atoms is ~2 eV. Also the energy distribution of the re-sputtered or back-scattered Ar^+ ions spreads upto very high energy (~ 450 eV) in case of sputtering from a Mo target. In case of r.f. sputtered W/Si samples also, we had found earlier from dynamic Secondary Ion Mass Spectrometry (SIMS) study that the width of inter-diffusion layer at W/Si interface is larger for W-on-Si interface than on Si-on-W interface [129].

The variation of interface parameters (σ, σ_d and σ_r) for the Si-on-W interface where the Si film is deposited on the underlying 1st W layer, is shown in Fig. 6.17(a) as a function of the ion energy used during deposition for the W layers. It is found that the interface width (σ)

Sample No.	**Ar^+ Ion energy of W sputtering (eV)**	**$(\xi_{\parallel})_{\text{Si-on-W}}$ (Å)**	**$(\xi_{\parallel})_{\text{W-on-Si}}$ (Å)**	**$\xi_{\perp}$ (Å)**	**$(\sigma_r)_{\text{top}}$ (Å)**
1.	600	245	251	55	2.67
2.	800	170	255	33	2.89
3.	1000	520	287	32	4.20
4.	1200	132	60	30	4.95

Table-6.1: Results of non-specular reflectivity measurements on W/Si/W tri-layer films.

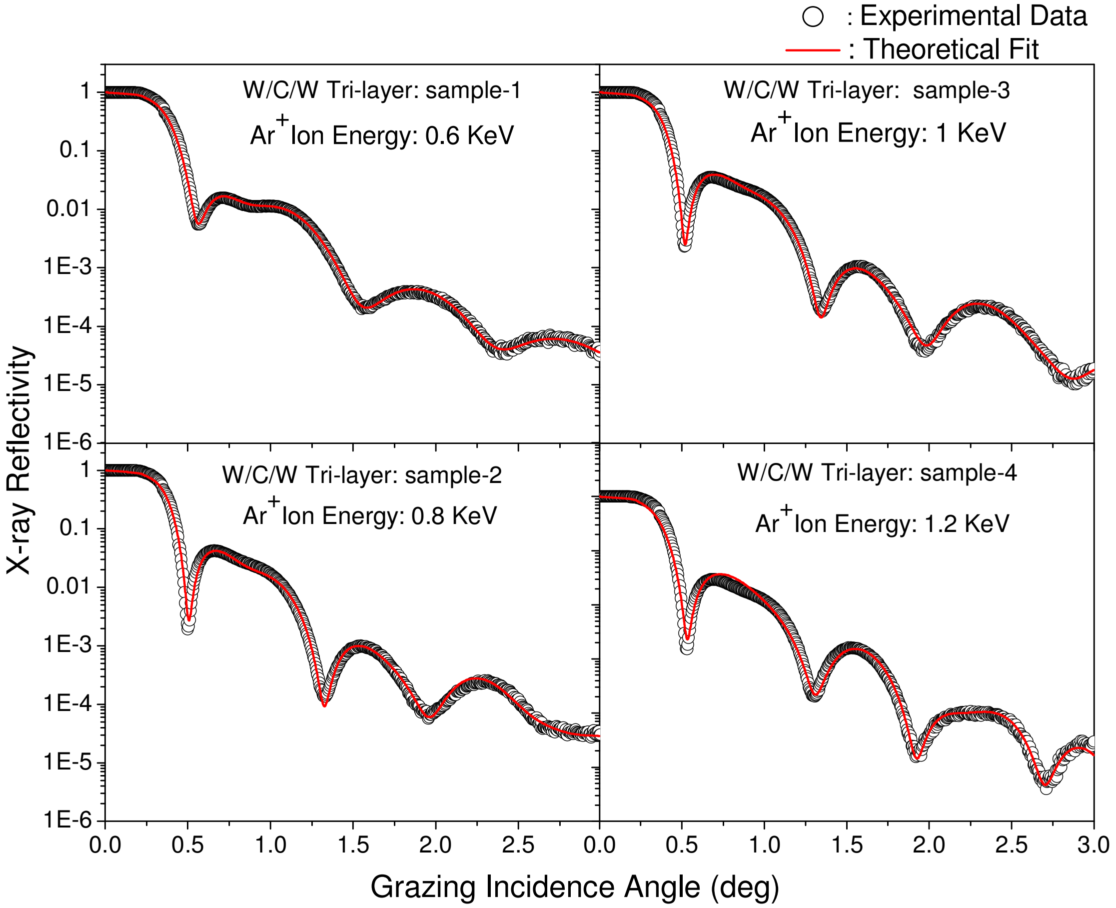

Fig. 6.18: Specular GIXR spectra for W/C/W tri-layer samples along with best-fit theoretical plots where W layers have been deposited at different ion energies.

decreases as the ion energy increases and it is minimum when the W film is deposited at 1000 eV after which it again increases. It is also observed that the major contributor to the width of the Si-on-W interface is the diffusivity (σ_d) and the diffusivity parameter also decreases as the ion energy used during W sputtering increases and reaches a minimum at 1000 eV. This is consistent with the fact that Si being lighter element can only penetrate into the voids present in the underlying W layer and as obtained from our analysis on the single layer films shown in Fig. 6.13(b), the density and compactness of the W layer is maximum when the film is deposited with an ion energy of 1000 eV. However, the interface roughness parameter (σ_r) increases as the ion energy for W sputtering increases, which is consistent with the fact that roughness on the W layer increases with increase in the ion energy of deposition.

The interface parameters for the W-on-Si interface of the tri-layer samples, where the 2nd W layer is deposited on the underlying a-Si layer, have been plotted in Fig. 6.17(b) as a function of energy of Ar^+ ions used during deposition of the W layers. It is found that the interface roughness parameter (σ_r) of the W-on-Si interface does not increase significantly with increase in ion energy for W sputtering, while the interface diffusivity (σ_d) increases considerably with sputtering ion energy upto 1000 eV, beyond which the diffusivity decreases again. This might be because of the increase in sputtering yield and rate of deposition of the W_2 layer at sputtering ion energy above 1000 eV. This agrees well with the results reported by Largeron et al.[140] on simulation by Cellular Automation (CA) and measurements on IBS grown Mo/Si multilayers. Largeron et al. [140] have observed that there is a competition between deposition of Mo atoms to form a Mo layer and growth of Mo/Si interface zone by inter-diffusion. It is found that the interface layer is decreased with increase in sputtering rate of Mo since the higher rate of deposition enhances formation of Mo clusters or nano-crystalline grains which prohibits inter-diffusion across the interface.

6.4.3 Ion energy dependence of W/C/W tri-layer

In Fig. 6.18 the specular GIXR spectra of four W/C/W tri-layer samples where W films are deposited at different ion energies in the range 600 to 1200 eV are shown along with the best fit theoretical spectra. The densities of the individual layers have been obtained from the GIXR measurements of the single layer C and W films deposited at respective ion energies as obtained from Fig. 6.7 and Fig. 6.13. The thicknesses of the films as measured by the in-situ crystal monitor during deposition have been used as initial guess values for the fitting and the best fit thicknesses of the layers are found to be close to it. The variation of the surface roughness of the top W-layer and interface widths (σ) of W-on-C and C-on-W layers found from these fittings are shown in the Fig. 6.19 as a function of energy of Ar$^+$ ions used during deposition. It is seen that all the above three parameters decrease with an increase in Ar$^+$ ion energy till 1000 eV, beyond which they increase again.

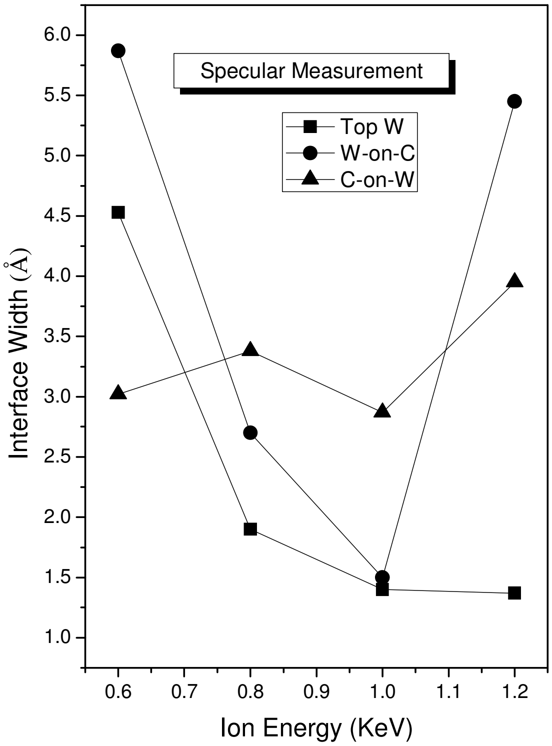

Fig. 6.19: Variation of interface widths and surface roughness of W/C/W tri-layer samples as a function of Ar$^+$ ion energy used for the deposition of W layers

In Fig. 6.20, non-specular reflectivity spectra in the detector scan geometry are shown along with the best fit theoretical spectra of the above four tri-layer samples. During fitting of these non-specular spectra, thickness and densities of each layer are kept fixed at the values found from the specular measurements as discussed above. Also the h values of the different layers have been taken as 1 for all the samples during fitting of the diffused reflectivity spectra due to the reasons discussed in the previous section. The above exercise has been carried out for all the four tri-layer samples and the variation of the values of interface diffusion (σ_d) for both W-on-C and C-on-W interfaces as obtained from these fitting are shown in Fig. 6.21 as a function of Ar$^+$ ion energy. The other parameters viz., interface roughness (σ_r), in-plane correlation length ($\xi_{\parallel}$), vertical correlation length ($\xi_{\perp}$) of the layers and surface roughness of the top W layer (σ_r) derived from the fittings have been given in Table-6.2. It is noticed that the values of these parameters are not varying significantly with ion energy. It can also be seen that the values of interface roughness (σ_r) are much smaller than the values of interface diffusion (σ_d) which implies that the main contributor in the interface width (σ) is interface diffusion (σ_d).

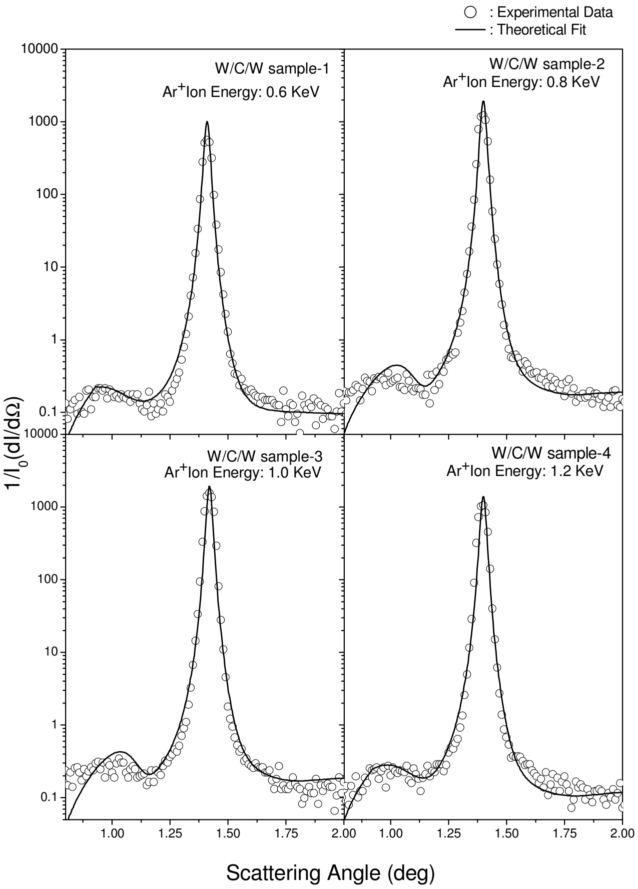

Fig. 6.20: Non-specular GIXR spectra for W/C/W tri-layer samples along with best-fit theoretical plots where W layers have been deposited at different ion energies.

As shown in Fig. 6.21, the interface diffusion of W-on-C is more than the interface diffusion of C-on-W interfaces as observed in previous section for W/Si/W multilayer. Such asymmetric behavior of the two interfaces has been seen in DC sputtered Co/Ti [78] multilayer and RF sputtered Ni/Ti multilayer [101] samples also in the Chapters 4 and Chapter 5 respectively. This may be due to the fact that average atomic volumes of W atoms are smaller and hence W atoms can penetrate through a larger distance in the underlying disordered amorphous C-layer than the C atoms inside the W film. Previously, in Fig. 6.13(b), it has been found from specular X-ray reflectivity measurements of single layer W films deposited at different ion energies that the density of W layer is maximum for films deposited with 1000 KeV Ar$^+$ ion energy, so the diffusion of C atoms inside the W layer is minimum in this case. Similar results have also been obtained from the non-specular reflectivity study of W/Si/W tri-layer samples deposited at different ion energies, as shown in Fig. 6.17(a). Thus the above optimization process has enabled us to achieve an optimum Ar^+ energy of W deposition for realization of W/C multilayers with low interface width.

Ion Energy (eV)	**Top W**		**W-on-C**		**C-on-W**		$\xi_\perp$ (Å)
	σ_r (Å)	$\xi_{\parallel}$(Å)	σ_r (Å)	$\xi_{\parallel}$(Å)	σ_r (Å)	$\xi_{\parallel}$(Å)	
600	2.15	48.9	0.41	5.18	1.00	62.1	8.0
800	2.16	61.7	0.82	14.7	0.92	29.3	6.5
1000	2.15	61.0	1.08	5.22	1.0	31.6	7.64
1200	2.16	61.7	0.49	5.29	1.01	29.1	7.0

Table 6.2: Various interface parameters for W/C/W tri-layer samples as obtained from non-specular GIXR measurements

6.5 Conclusion

An Ion Beam Sputtering (IBS) system have been developed and installed in our laboratory for deposition of soft X-ray multilayers. Initially single layer W, Si & C films, bi-layer W/Si films and tri-layer W/Si/W & W/C/W films have been deposited and characterized by Grazing Incidence X-ray reflectivity (GIXR), Atomic Force Microscopy (AFM) and Spectroscopic Ellipsometry (SE) techniques. It has been found that thin films with near-bulk density and very smooth surfaces with r.m.s. roughness < 4Å could be deposited in the home-made Ion Beam Sputtering system. In the aim of optimization of the process parameters of the IBS system, a set of single layer W films, W/Si/W and W/C/W tri-layer films have been deposited, where the W layers of the different samples have been deposited at different ion energies in the range of 600-1200 eV. Along with the thickness and density of the single-layer W films, interface roughness and interface diffusion for both the Si-on-W (C-on-W) interface and W-on-Si (W-on-C) interface have been measured, in case of the tri-layer samples, by specular and non-specular GIXR measurements.

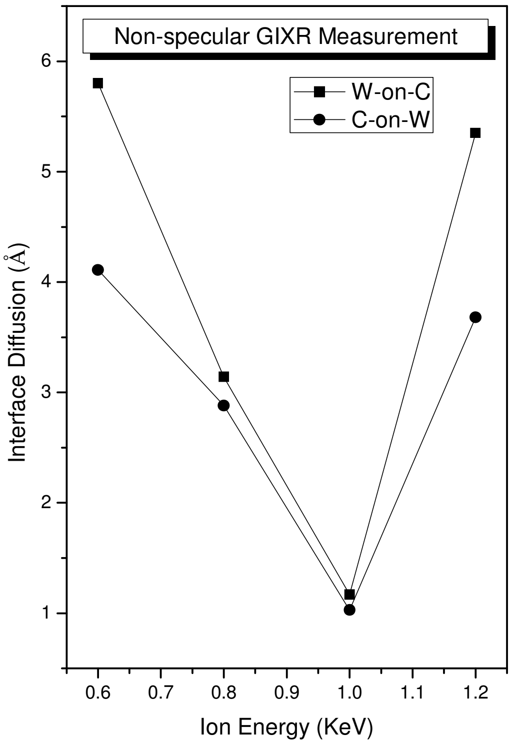

Fig. 6.21: Variation of interface diffusion at W-on-C and C-on-W interfaces of W/C/W tri-layer samples as a function of Ar$^+$ ion energy used for the deposition of W layers.

In this ion energy dependence studies, it has been found that the density of W layer increases as the sputtering Ar$^+$ ion energy increases from 600 eV because of enhancement in the mobility of the adatoms on the growing surface and is maximum for 1000 eV beyond which the enhanced rate of deposition does not allow proper rearrangement of the adatoms resulting in lower density of the films. In case of the tri-layer samples, the interface width and inter-diffusion at W-on-Si interface and W-on-C interface are found to be much higher than that at Si-on-W interface and C-on-W interface respectively. The interface diffusion at Si-on-W interface or C-on-W interface decreases as ion energy of W deposition increases and is minimum when W layer is deposited with 1000 eV Ar$^+$ ions since the density of W layer is maximum at this energy. Through this an optimum Ar$^+$ ion energy of 1000 eV have been reached for deposition of W/Si and W/C soft X-ray multilayer.

CHAPTER 7

Development of W/Si and W/C soft X-ray multilayers and study of interface roughness correlation

7.1 Introduction

The basic concept and working principle of periodic multilayers, which are basically artificial one dimensional Bragg crystals made up of alternate thin layers of low index (high atomic Number) and high index (low atomic number) materials, used for reflecting X-rays has already been introduced in Chapter 2. Due to the unavailability of suitable natural crystal or grating, in the soft X-ray band of 10–150 Å, thin film multilayers, are the only optical devices which are used as mirrors and monochromators in the application of lithography [28], astronomy [29], plasma diagnoses [30], microscopic holography [31], X-ray microscopy [24] and synchrotron radiation beamlines [32] etc.

As observed in previous chapters for the case of neutron multilayer devices, here also the performance of a soft X-ray multilayer is limited by the quality of its interfaces. Few studies have already been reported in the literature on the interface roughness of W/Si and W/C soft X-ray multilayers [40, 59, 116, 141-144] probed by X-ray reflectivity. However, in most of the studies correlation of W/Si and W/C interface roughness have been obtained by fitting the measured reflectivity data using multilayer model assuming every interface to be identical and thus results are conflicting. For example, by studying 40 layer W/C multilayer structures deposited on Si and fused silica substrates by DC magnetron sputtering, Savage *et. al.* [143] noticed that the roughness correlation depends on the substrate surface and the value of the lateral correlation lengths are in the range of 20-200 Å. Later the same group [142] has studied W/C multilayers of 20 bilayer with 37 Å periodic thickness, 55 bilayer with 30 Å periodic thickness and 70 bilayer with 23 Å periodic thickness by measuring non-specular reflectivity for hard X-ray and soft X-ray. It is concluded by fitting the data using multilayer model that the average interface roughness does not change with change in bi-layer thickness and the roughness are correlated. However Modi *et.al.* [144] have measured the variation of interface roughness of a W/C multilayer by specular X-ray reflectivity measurement and it is observed that there is a continuous increase of W-on-C and C-on-W interface roughness from bottom to the top of the multilayer and it is changing with annealing temperature of the sample. Keeping these conflicting results in mind and to have a greater insight into the interface phenomena, in the current study, we have deposited multilayers with less number of layers so that during fitting of the measured X-ray reflectivity spectra the parameters of every individual layers and interfaces can be varied without making any ad-hoc assumptions. Thus in the present study, W/Si and W/C periodic multilayers of different number of layers have been deposited using the home-built ion beam sputtering (IBS) system on c-Si substrates using the optimised parameters discussed in the previous Chapter and these samples have been characterized by specular GIXR measurement and non-specular GIXR measurements in detector scan geometry at the 1st Bragg peak position with 1.54 Å wavelength. These specular and non-specular measured data have been fitted by varying the parameters of every individual layers and interfaces, without making any ad-hoc assumptions. Through this technique the interface width, interface roughness, interface diffusion, in-plane correlation length and vertical correlation length of multilayers are measured and the correlations between them have been studied.

Finally 21-layer and 25-layer W/Si and W/C multilayer mirrors have been designed and deposited in the above system and the performances of these multilayers have been tested at INDUS-I synchrotron source at RRCAT, Indore.

7.2 Deposition of W/Si and W/C periodic multilayer mirrors

W/Si and W/C multilayers have been deposited at the optimized process conditions of Ar^+ ion energy of 1000 eV and ion current of 10 mA, which have been found by studying the W single layers and W/Si/W and W/C/W tri-layer samples deposited at different ion energies, as has been discussed in Chapter 6. W/Si multilayers having 5, 7, 9, 13 and 17 layers have been deposited with nominal thicknesses of the W and Si layers maintained at 20 Å and 28 Å respectively by using the in-situ quartz crystal thickness monitor during depositions. Similarly, at the same condition W/C multilayers having 5, 7, 9 and 13 layers have been deposited on c-Si substrates keeping the W and C layer thickness of nominal values at 12 Å and 58 Å respectively. Subsequently, a 25-layer and a 21-layer W/Si multilayer having bi-layer thickness of 48 Å and 120 Å respectively have been designed and deposited which can give high reflectivity at 45 Å and 130 Å wavelengths respectively at 30^o grazing angle of incidence. Following this a 25-layer and a 21-layer W/C multilayer sample with bi-layer thickness of 50 Å and 62 Å respectively are deposited, which are designed to show peak reflectivities for soft X-ray of 44Å wavelength at 25^o and 20^o grazing angle of incidences respectively. The general design criterion for the soft X-ray mirror is described in Appendix-C.

7.3 Characterization of W/Si and W/C periodic multilayer

7.3.1 Correlation of interface roughness of W/Si multilayer

Specular reflectivity

The measured specular GIXR spectra of 5, 7, 9, 13, 17 and 25 layers of the W/Si multilayer samples have been shown in Fig. 7.1(a). As has been mentioned earlier these multilayer samples have been grown in the IBS system with a 20 Å W/28 Å Si nominal thickness combination, which is a design value for reflecting mirror at soft X-ray wavelength of 45 Å at 30^{o} grazing angle of incidence. Fig. 7.1(a) shows the presence of first Bragg peak at 0.92^{o} for all the samples in the GIXR spectra measured with 1.54 Å hard X-ray source, which is close to the theoretical value, showing good thickness uniformity achieved in the IBS system. The value of reflectivity obtained for 5, 7, 9, 13, 17 and 25-layer samples at the first Bragg peak are 4%, 6%, 13%, 21%, 38% and 60% respectively [100]. In the Fig. 7.1(b) the GIXR spectra of a 21-layer

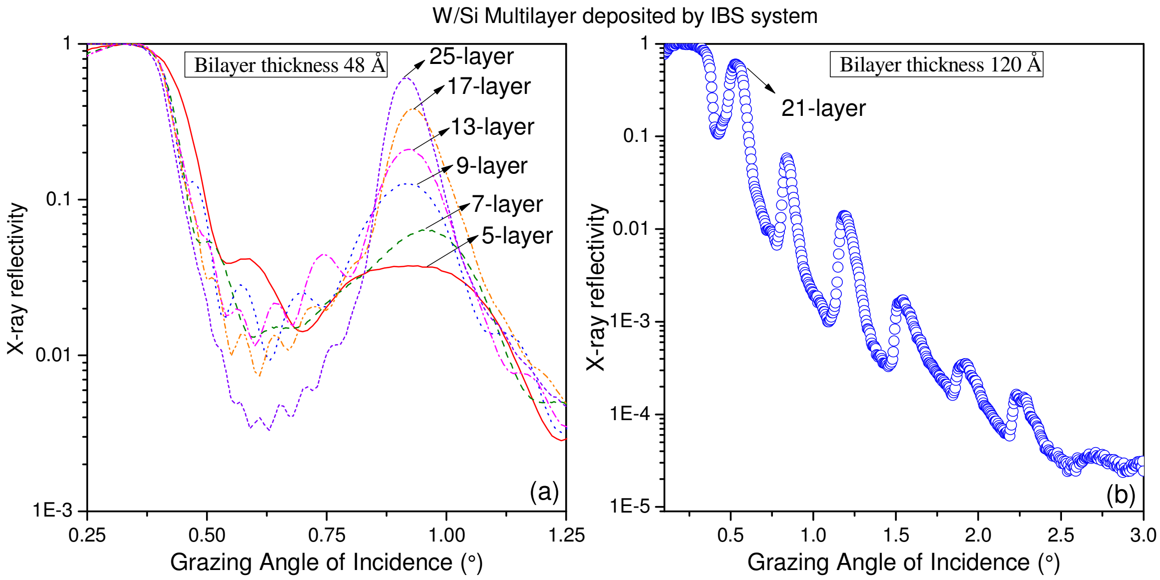

Fig. 7.1: Specular X-ray reflectivity spectra of the W/Si multilayer structures, (a) 5, 7, 9, 13, 17 and 25 layer of bilayer thickness 48 Å (b) 21 of bilayer thickness 130 Å

W/Si multilayer is shown, this sample has bilayer thickness of 120 Å and it is showing ~62% of reflectivity at 0.63° grazing angle of incidence [145].

The multilayer devices have been characterized thoroughly by fitting the respective GIXR spectrum with theoretical spectrum, generated using a suitable sample structure. For samples having 5, 7, 9, and 13 layers, fitting of the GIXR spectra have been carried out using separate parameters for individual layers. Figure 7.2 shows the fitting of the experimental GIXR spectrum with the theoretical simulation for a representative 5-layer W/Si structure. The density, thickness and interface width of the individual layers as obtained from the best-fit have been shown in Table-7.1 for the four samples having 5, 7, 9, and 13 layers. The χ^2 values achieved in the fitting of the present samples are ~0.001 and considering the errors in measurements and the fitting process, the overall uncertainties in the estimated parameters are found to be less than 5%. However, for samples having 17 and 25 layers, the fitting have been carried out using a multilayer model with successive repetition of a W/Si bi-layer, with the first layer on the substrate and the top surface layer taken separately in the model. The specular GIXR data for the 17-layer sample could be fitted with an average W layer thickness of 21.8 Å and Si layer thickness of 30.13 Å, while the average widths (σ) of Si-on-W and W-on-Si interfaces are found to be 5.7 Å and 9.52 Å respectively. The GIXR data for the 25-layer sample, on the other hand, could be fitted with an average W layer thickness of 22.11 Å and Si layer thickness of 31.39 Å with an average Si-on-W interface width of 5.52 Å and W-on Si interface width of 7.88 Å. It should be noted here that since the possibility of diffusion of the W atoms into crystalline Si substrate is minimal, for all the samples the interface width (σ) of the first W/Si-substrate interface has been taken to be 3Å which is the roughness of the bare Si substrates used in this experiments as obtained from separate measurements. Also it should be noted that in Table-7.1, the σ value given for the top W layer in each sample is really the surface roughness of the multilayer sample.

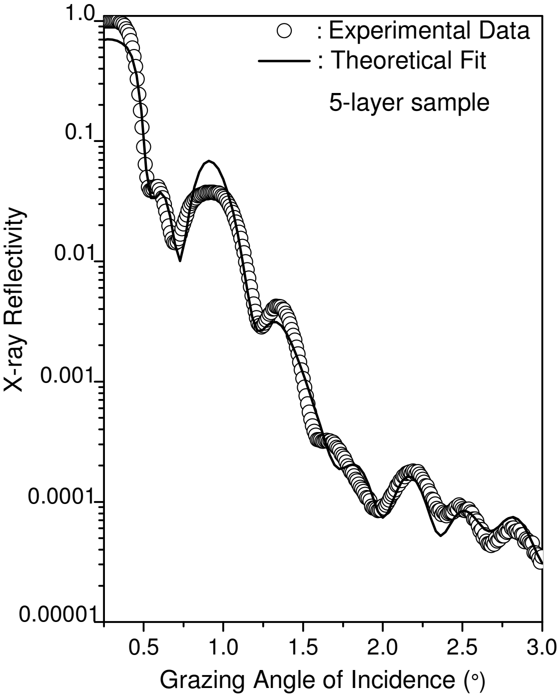

Fig. 7.2: Specular X-ray reflectivity spectrum with best-fit theoretical curve for the 5-layer multilayer structure.

From the best fit results of all the samples the following observations were made. It has been observed that the actual thickness values of the individual layers, as determined from the fitting, are close to the nominal values showing good thickness calibration of the thickness monitors. The densities of the W layers adjacent to the substrate and at the top are lower than the density of other W layers of the stack. It has also been observed that for all the samples, the interface width of the W-on-Si interfaces are higher than that of the Si-on-W interfaces due to higher inter-diffusion of W in Si as had been discussed in details in previous chapter [114, 120, 129]. Similar observations have been made for Ni/Ti and Co/Ti multilayers also deposited by magnetron sputtering technique and discussed in Chapters 4 and 5. Though as has been observed by Stearns et al [131], for their e-beam evaporated Mo/Si multilayers, for the present IBS-deposited samples also it is observed that the inter-diffusion is not a bulk phenomenon and is only restricted to the surfaces of individual layers since the interface width is almost constant throughout the multilayer.

For all the samples it has been observed that the width (σ) of the Si on W interfaces are

~5-6 Å, though however, the top W surface roughness (σ_r) of the multilayers are ~2-3 Å, enabling the multilayers to manifest good reflectivity in the soft X-ray region. The roughness of the top layer is almost comparable to that of the substrate or sometimes less than the substrate, manifesting good quality smooth two-dimensional deposition by the IBS technique. Similar result has also been reported by Feng et al. [121] for their IBS deposited Co/C and W/Si multilayers. It has also been observed that there is a gradual decrease in interface roughness of the Si-on-W layers from the substrate to the top of the multilayer showing some evidence of smoothening as the number of layers is increased and the effect is more visible for multilayers with higher number of layers.

	5-layer			7-layer			9-layer			13-layer		
	ρ (g/cc)	d (Å)	σ (Å)	ρ (g/cc)	d (Å)	σ (Å)	ρ (g/cc)	d (Å)	σ (Å)	ρ (g/cc)	d (Å)	σ (Å)
W										18.66	21	2
Si										2.07	26	7
W										19.10	20	5
Si										2.18	26	9
W							18.79	18	2	19.21	20	5
Si							2.1	28	9	2.10	31	11
W				19.0	21	2	19.0	21	5	19.20	22	6
Si				2.1	27	9	2.10	30	11	2.19	31	6
W	19.13	18	3	19.13	22	3	19.20	22	5	19.20	21	7
Si	2.07	28	12	2.07	28	8	2.06	31	9	2.20	30	7
W	19.28	20	7	19.25	18	5	19.22	21	7	19.23	27	7
Si	2.11	28	11	2.11	26	7	2.05	30	8	2.11	30	11
W	18.95	21	5	18.95	21	4	18.95	19	6	18.79	20	6
	Si substrate (σ_r =3Å)			Si substrate (σ_r =3Å)			Si substrate (σ_r =3Å)			Si substrate (σ_r =3Å)		

Table 7.1: Density, thickness and interface width values of different sub-layers of the W/Si multilayer structures as obtained from the best-fit of the GIXR spectra

Similar observations of smoothening of the interfaces during the growth of a multilayer have been observed by several other workers also. Paul and Lodha [146] have observed that for d.c. magnetron sputtered Pt/C multilayers, there is almost no or very little increase in the roughness from the substrate to the surface due to smoothening effect at C-on-Pt interfaces and the surface roughness almost replicates that of the substrate roughness. Savage *et al.* [40] have observed for d.c .magnetron sputter deposited W/C multilayers very little increase in roughness with the increase in number of periods and replication of the substrate roughness across the interface of the multilayers showing smoothening of the high frequency roughness. There are distinctly two different observations made by the workers on the origin of the above smoothening process during the growth of a multilayer. As pointed out previously, Freitag and Clemens [41] have shown that the smoothening effect of amorphous-like Si layer prohibits the scaling of the interface roughness across the interfaces for d.c. magnetron sputtered Mo/Si multilayers. Theoretical simulation of the growth of a crystalline/amorphous multilayer by Liu and Shen [39] using nonlinear continuum theory also shows that interface roughness varies in an oscillatory fashion where roughening of the interfaces takes place at the growth of the polycrystalline layer on the amorphous layer while smoothening of the interfaces takes place during deposition of the amorphous layer on the polycrystalline layer. Wang *et al.* [43], on the contrary, by in-situ X-ray reflectivity study of the growth of WSi_2/Si multilayers have concluded that it is the intrinsic smoothening process of the thin film deposition which leads to the smoothening of the layers and in their case the smoothing effect is more stronger during WSi_2 deposition. In our case also, it can be observed from the Table-7.1 that the surface roughness of the top W layers are always lower than roughness at the Si-on-W interfaces and the surface of the top W layer gets rougher with further growth of another Si layer. This can be clearly seen if the 7-layer sample is compared with the 9-layer sample or the 9-layer sample is compared with the 13-layer sample. Thus it can be inferred that for the present set of IBS deposited W/Si mulilayers, the intrinsic smoothening effect of the W layers due to the rearrangement of energetic W adatoms is responsible for the smoothening effect observed at the Si-on-W interfaces. The effect is more pronounced during the growth of the W layers since, as has been observed by us earlier also [114], the energies of the adatoms are more in case of W deposition than Si deposition. In any case, the smoothening process results in canceling out of the high frequency component of roughness with a decrease in the over-all roughness of the layers towards the top of the mulitilayers.

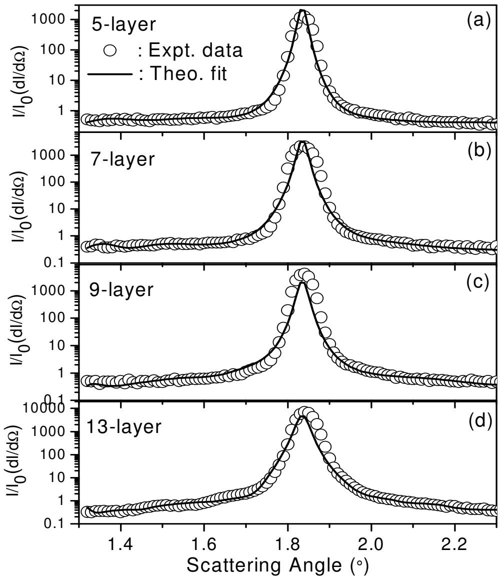

Fig. 7.3: Non-specular X-ray reflectivity spectra of the multilayer structures with best-fit

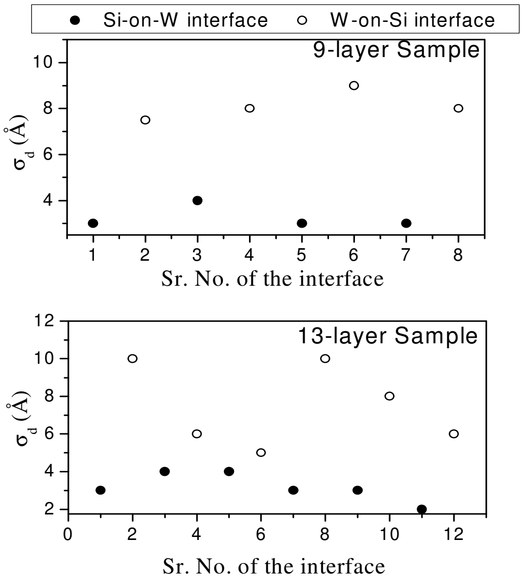

Fig. 7.4: Interface diffusivity (σ_d) values at the different interfaces of the 9-layer and 13-layer W/Si multilayer samples as obtained from the non-specular x-ray

Non-specular Reflectivity

In order to completely understand the above phenomenon of alternating roughening and smoothening of the interfaces which leads to the correlation of interface roughness across the depth of the multilayers, non-specular X-ray reflectivity measurement of the above multilayer samples have been carried out [100]. Fig. 7.3 shows the non-specular reflectance (detector scan) of the multilayer structures taken in the geometry described in Chapter 2. The detector scans were taken by keeping the angle of incidence fixed at the position of the 1st Bragg peak (i.e., ~0.92°). The non-specular reflectivity spectra of the 5-layer, 7-layer, 9-layer and 13-layer samples have been fitted using the DWBA model described in Chapter-2 [47, 55] and the best fit theoretical plots have also been shown in Fig. 7.3 for the above four samples along with the experimental data. It should be noted here that the thickness of the layers obtained from the best fit of the specular reflectivity spectra have been used for fitting of the non-specular spectra and these values have been kept invariant in the above fitting process. For each sample, the interface roughness (σ_r) values has been used as fitting parameter and the interface diffusivity (σ_d) as dependent parameter so that the condition $\sigma^2 = \sigma_r^2 + \sigma_d^2$ is always satisfied, where, σ is the interface widths of the layers obtained from the fitting of the specular reflectivity plot of the sample. As has been mentioned earlier, it has been observed from the fitting of the non-specular X-ray reflectivity of the samples that the diffusion at the W-on-Si interfaces is higher than that at the Si-on-W interfaces. The interface diffusivity (σ_d) values obtained at the different interfaces counted from the bottom for the two representative samples viz., the 9-layer and the 13-layer samples have been shown in Fig. 7.4.

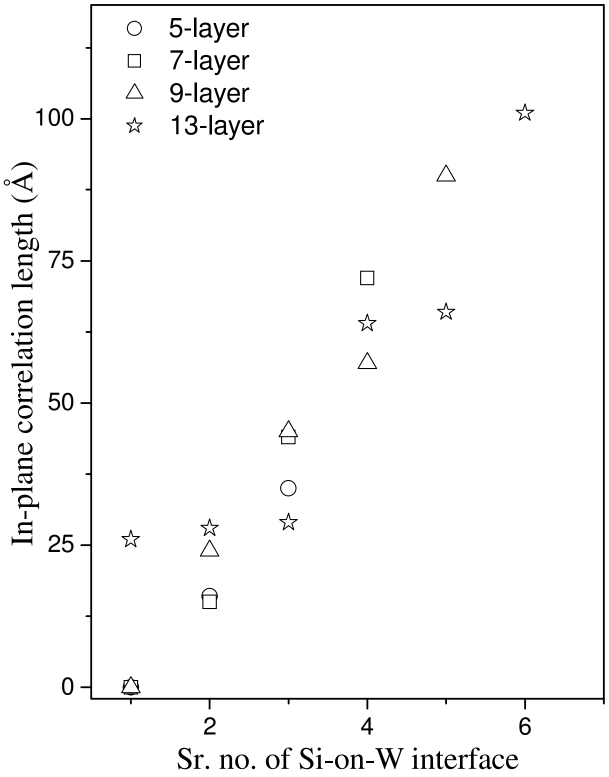

Fig. 7.5: In-plane correlation length in Si-on-W interface of the 5-layer, 7-layer, 9-layer and 13-layer W/Si multilayer as obtained from non-specular x-ray reflectivity

The other parameters used during fitting were the in-plane correlation lengths of the interfaces ($\xi_{\|}$) and the vertical correlation length ($\xi_{\perp}$) for the whole structure. From the best fit parameters obtained for the above four samples, it has been observed that the in-plane correlations of the W-on-Si layers are low due to the high rate of diffusion by the W adatoms into the Si layers, though however, the in-plane correlations of the Si-on-W layers are found to be significant. The in-plane correlation lengths ($\xi_{\|}$) for the different Si-on-W interfaces (at an ascending order from the substrate to the surface) for the four samples have been shown in Fig. 7.5. It should be noted that the last point for each sample corresponds to the top surface layer. It has been observed that the in-plane correlation lengths of the Si-on-W interfaces including the surface of the multilayer structure increase as we approach the top of the multilayer structure. It has also been observed that the vertical correlation length ($\xi_{\perp}$) of the multilayer structure increases from 15.29 for the 5-layer sample to 313.33 for the 13-layer sample. It should be noted here that the fitting of the non-specular reflectivity data of the 17-layer and 25-layer samples have not been carried out due to the involvement of large number of fitting parameters.

The above phenomenon of correlation of interface roughness across the depth of the multilayers has been reported by several other workers also for different other multilayer systems. Freitag and Clemens [41] have found that the interfaces of their d.c. magnetron sputtered Mo/Si multilayers are highly correlated. Ulyanenkov *et al.* [138] have observed that the vertical correlation of interface roughness decreases with an increase in interface roughness for their IBS deposited Mo/Si multilayers when deposited on substrates with higher surface roughness. Chládek *et al.* [147] have also observed from specular and diffused X-ray reflectivity measurements that the roughness is highly correlated across the interfaces for their e-beam evaporated Au/Ni-Co multilayers. Savage *et al.* [40] have observed that for their d.c. magnetron sputter-deposited W/C multilayers, the vertically correlated roughness component (σ_{correl}) obtained from X-ray transverse rocking scan measurements and the total roughness (σ) obtained from specular reflectivity measurement do not increase significantly with the increase in the number of layers in the multilayers indicating smoothening effect of high frequency roughness at one of the interfaces. Paul and Lodha [42], have observed that for d.c. magnetron sputtered Pt/C multilayers, the interfaces are vertically correlated with the correlated roughness increasing with number of layers and uncorrelated or random roughness remaining the same. Jergel *et al.* [148, 149] have also found that the interfaces of the as-deposited e-beam evaporated W/Si multilayers are highly correlated and their diffused reflectivity (detector scan) spectra are well simulated using the model presented by Holý and Baumbach [45] assuming complete vertical correlation among the interfaces which decreases as the multilayer samples are annealed.

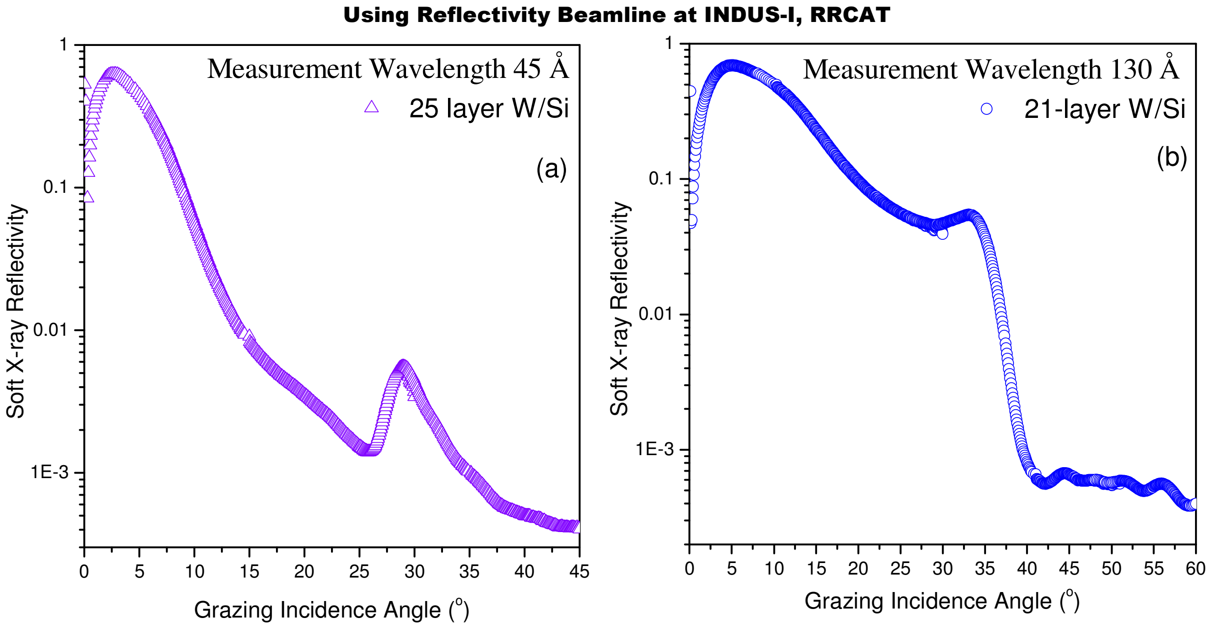

Fig. 7.6: Soft X-ray reflectivity spectrum of W/Si multilayer measured at INDUS-I synchrotron source RRCAT, Indore (a) 25-layer (b) 21-layer

7.3.2 Characterization W/Si multilayer by soft X-ray reflectivity at INDUS-I

The 25-layer W/Si multilayer mirror which is designed to work at a grazing angle of incidence of 30^{o} and for a wavelength of 45 Å has been characterized at the Reflectivity beamline [150] at INDUS-1 synchrotron source at RRCAT, Indore. In Fig 7.6 (a) the soft X-ray reflectivity of the 25-layer sample is shown, the specular GIXR spectrum of this sample at hard X-ray has already been shown in Fig 7.1(a). The soft X-ray reflectivity has been measured with 45 Å wavelength X-ray in the grazing angle of incidence range of 0 to 45^{o}. In this spectrum a Bragg peak at ~30^{o} grazing angle of incidence is clearly seen. The measured absolute value of the reflectivity at this Bragg peak is ~20% of the theoretical value. Another 21-layer sample which is designed to operate at 30^{o} grazing angle of incidence and for 130 Å wavelength has also been characterized and its soft X-ray reflectivity profile with 130 Å wavelength in the angular range 0 to 70^{o} grazing angle of incidence is shown in Fig 7.6(b). At an angle of ~30^{o} a Bragg peak has been observed which is as per the design structure and the measured absolute reflectivity at the Bragg peak is found to be ~30% of its theoretical value.

7.3.3 Correlation of interface roughness of W/C multilayer

Specular reflectivity

The specular X-ray reflectivity spectra of 5-layer, 7-layer, 9-layer and 13-layer W/C multilayer samples, measured with 1.54 Å of X-ray wavelength are shown in Fig 7.7 along with their best fit theoretical spectra. In the measured spectra of these samples up to a grazing angle of incidence of 3°, 3 to 4 Bragg peaks are clearly visible, which manifests proper periodic structure of the multilayers. During fitting of these experimentally measured spectra, the thickness of the individual layers found from the in-situ quartz crystal monitors have been used as starting guess values and subsequently thickness and roughness of the individual layers have been varied.

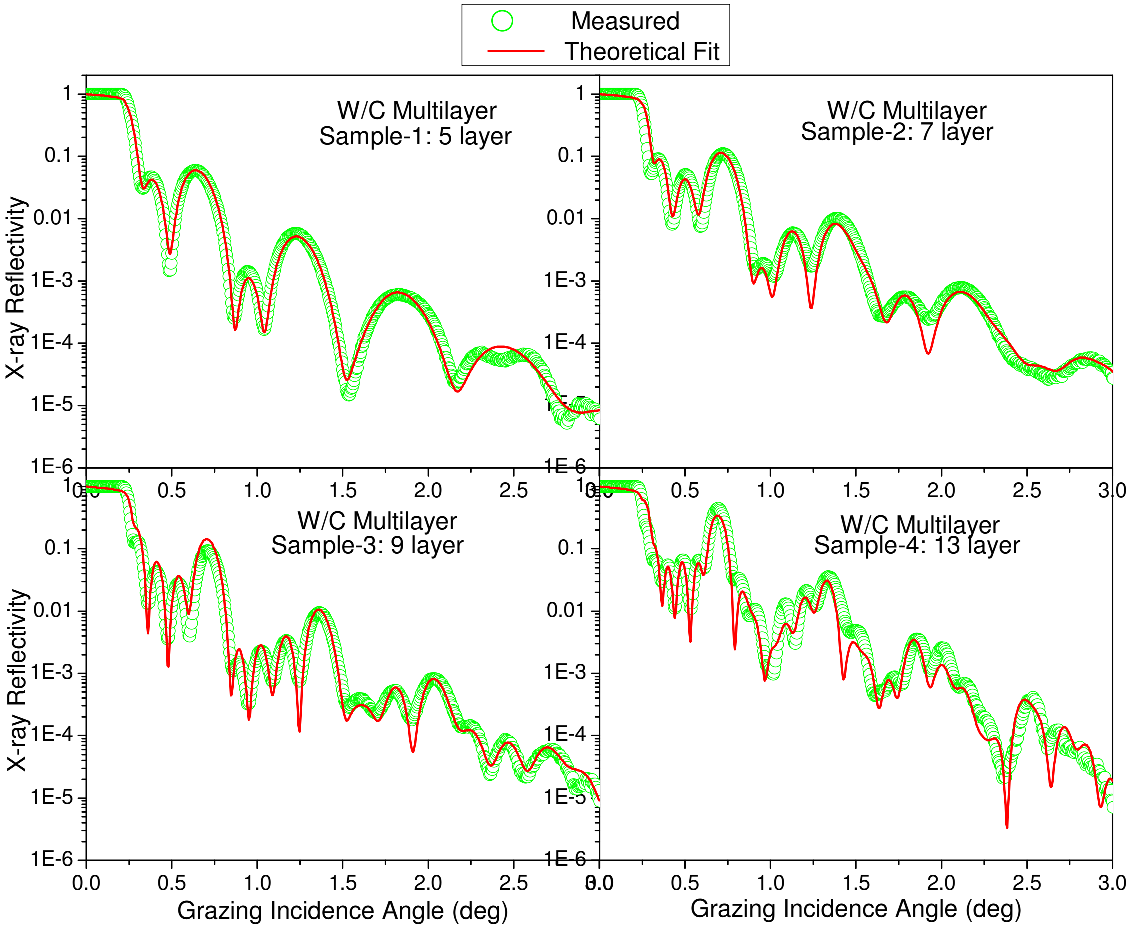

Fig 7.7: Specular GIXR spectra for four W/C multilayer samples having (a) 5-layer, (b) 7-layer, (c) 9-layer and (d) 13-layer along with best-fit theoretical plots.

In Fig. 7.8 the interface widths of C-on-W and W-on-C interfaces found from above specular GIXR measurements are shown as a function of interface serial number (counted from bottom to top) for two representative multilayer samples with 9-layers and 13-layers. It is observed that for the multilayer samples the W-on-C interface width is more than the C-on-W interface width for most of the interfaces which has also been observed in case of the W/C/W tri-layer samples discussed in previous chapter, This observation of asymmetric interfaces in case of

W/C multilayers agree also with our results on W/Si [100, 114, 120], Ni/Ti [101] and Co/Ti [78] multilayer as discussed in the previous chapters and sections. From Fig. 7.8, it is also clear that though C-on-W interface width (σ) is almost constant throughout the multilayer structure with some fluctuation, the W-on-C interface width (σ) increases slowly with layer number towards the top of the multilayers. Similar trend have been observed by Modi *et. al.* [144] in their W/C multilayers through the specular X-ray reflectivity measurements.

Non-specular reflectivity

In order to investigate the interfaces further, non-specular GIXR measurements have been carried out at the first Bragg peak of the four samples in detector scan geometry. In Fig. 7.9 the non-specular X-ray reflectivity spectra of the 5-layer, 7-layer, 9-layer and 13-layer samples are shown along with the best fit spectra. It should be noted that the structure of the multilayer obtained from the best fit model of the specular reflectivity spectrum is kept invariant during the fitting of the non-specular reflectivity spectrum and also the hurst constant (h) is fixed at the value 1.0, the justification for which has been given in the previous section. The other parameters viz., interface roughness

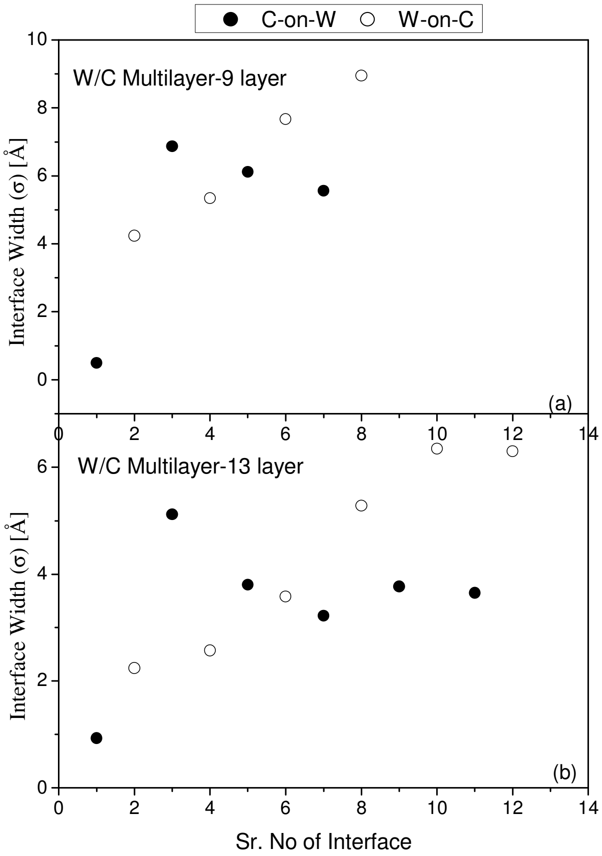

Fig 7.8: Variation of interface widths of W-on-C and C-on-W interfaces of W/C multilayer samples as a function of sr. no. of interface (counted from bottom to top): (a) 9-layer sample, (b) 13-layer sample.

(σ_r), interface diffusion (σ_d), in-plane correlation length ($\xi_\parallel$) and vertical correlation length ($\xi_\perp$) of each interface are however varied during the fitting. It is found that the vertical correlation length ($\xi_\perp$) of these multilayer are very low ~10Å, similar observations are made for W/C multilayers by Macrender *et.al.* [151] also after analyzing the non-specular X-ray reflectivity measured data of sputtered W/C multilayers. In Fig. 7.10 the variation of in-plane correlation length ($\xi_\parallel$) values across the depth of the multilayers for both C-on-W and W-on-C interfaces are shown for the 9-layer and 13-layer samples. It is seen that for both the samples initially the $\xi_\parallel$ values for both W-on-C and C-on-W interfaces are higher and they decrease towards the top of the multilayers. The initial higher values of $\xi_\parallel$ are possibly due to the very large in-plane correlation length of the substrate. These measured values are also consistent with the measured average in-plane correlation lengths of W/C multilayer samples by Savage *et. al.* [142, 143]. They have also shown that the average lateral correlation length depends on the substrate surface, from the measured data of the W/C multilayer films deposited on Si (100) and fused silica substrate [143].

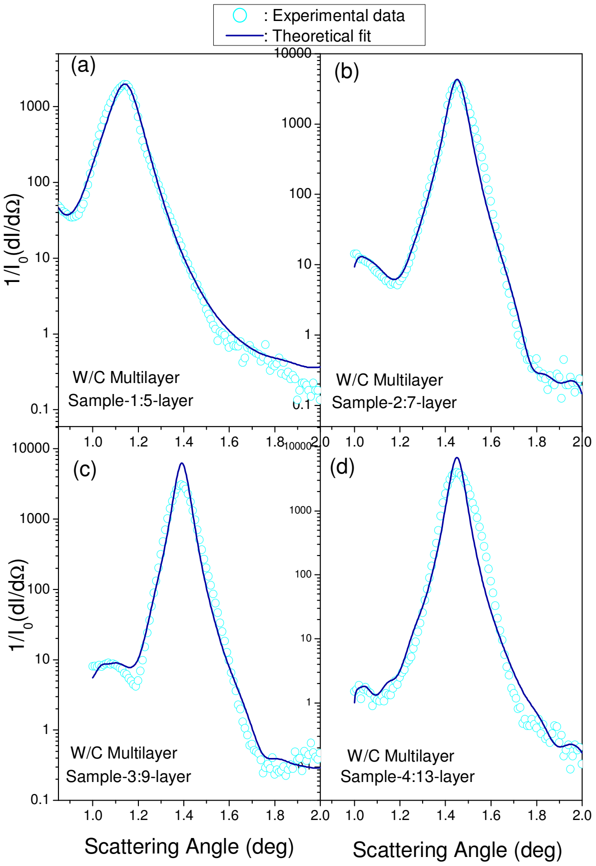

Fig.7.9: Non-specular GIXR spectra for four W/C multilayer samples having (a) 5-layer, (b) 7-layer, (c) 9-layer and (d) 13-layer along with best-fit theoretical plots.

The variation of interface diffusion (σ_d) and interface roughness (σ_r) of W-on-C and C-on-W interfaces across the depth of the multilayers are shown for two representative 9-layer and 13-layer samples in Fig. 7.11 and Fig. 7.12 respectively. It is seen from the above figures that the values of interface diffusion are quite large compared to the values of interface roughness, depicting that interface diffusion is more dominating than physical roughness in these samples. It can also be found from Fig. 7.11 that the interface diffusion of W-on-C interface is more than the interface diffusion of C-on-W interface. This is consistent with the results obtained for the tri-layer samples described in the previous section. Though in case of multilayer samples, the value of W-on-C interface diffusion is larger than that obtained for the tri-layer samples, which might be due to large C layer thickness of the multilayer samples. This is consistent with our findings on Ni/Ti multilayer samples [101], as described in Chapter 5, that the interface roughness of a multilayer depends on the bilayer thickness and it can also be scaled by similar power law like the top surface roughness of single layer films.

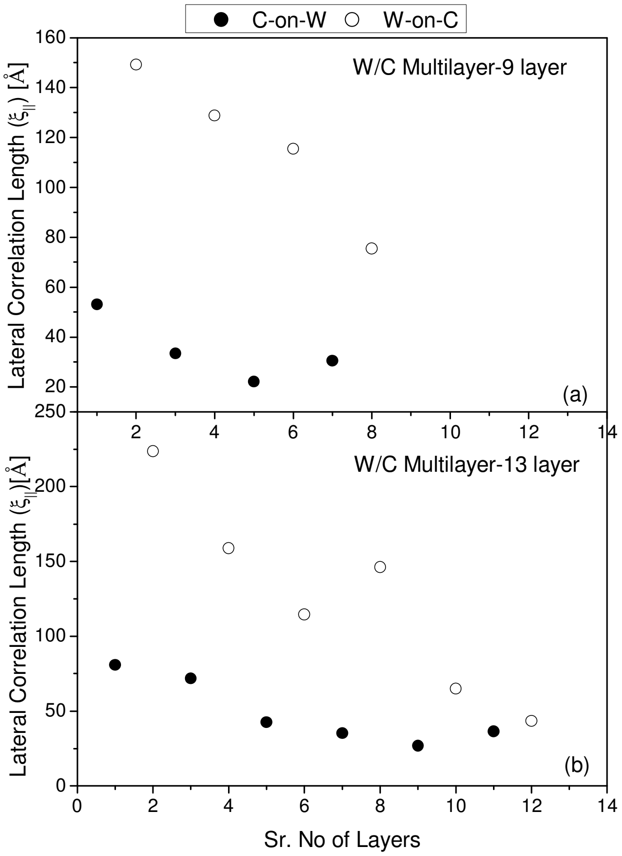

Fig. 7.10: Variation of in-plane correlation length ($\xi_{\|}$) of W-on-C and C-on-W interfaces of two representative W/C multilayer samples as a function of sr. no. of interface (counted from bottom to top): (a) 9-layer sample, (b) 13-layer sample.

Though the interface diffusion values for W-on-C interface and C-on-W interface are not varying significantly across the depth

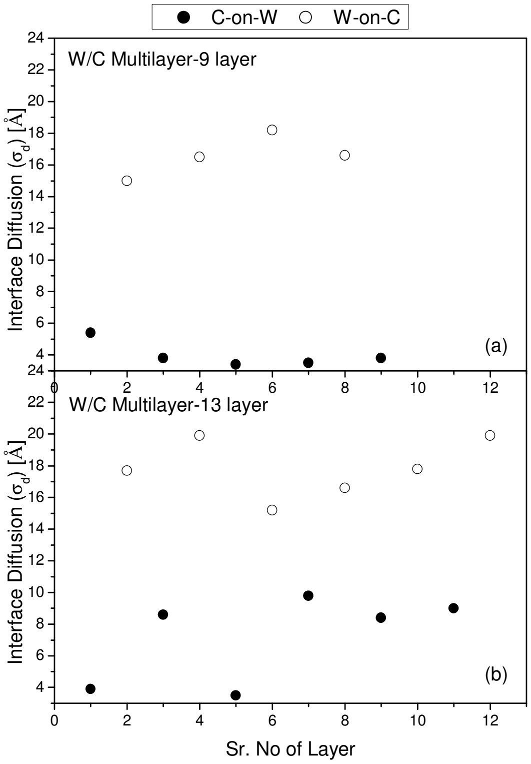

Fig. 7.11: Variation of interface diffusion (σ_d) of W-on-C and C-on-W interfaces of two representative W/C multilayer samples as a function of sr. no. of interface (counted from bottom to top): (a) 9-layer sample, (b) 13-layer sample.

of the samples in the multilayer structure as shown in Fig. 7.11, the interface roughness (σ_r) value of a W-on-C interface has some dependence on the position of the particular interface in the multilayer structure as shown in the Fig. 7.12. It is seen that after a few initial layer, σ_r values for of W-on-C interfaces start increasing. This increase of roughness does not follow the assumption of the 'restart of the growth at the interface' proposed by Savage *et. al.* [40] according to which the interface roughness or interface width at an interface should not depend on the position of the particular interface in the multilayer structure. This may be due to the high stress in the W/C multilayer structure. Comparing W/C and W/Si multilayers, Vidal *et. al.* [152] have concluded that W/C multilayers always have more internal stress than the W/Si multilayer. It has also been pointed out [152] that during the deposition of W/C multilayers, unintentional increase in substrate temperature is more than that occurs in case of deposition of W/Si multilayers. This increase in temperature and generation of high stress on the substrate might be the reason of cumulative increase in roughness at the interfaces in case of W/C multilayers. The increase in interface roughness in W-on-C interfaces towards the top of the multilayers results in the increase in interface widths of W-on-C interfaces as shown in Fig. 7.8.

7.3.4 Characterization W/C Multilayer by soft X-ray reflectivity at INDUS-I

Subsequent to the detail characterisation of the W/C multilayer system as described above, two W/C multilayer mirrors have been deposited using the home-built IBS system, one is a 25-layer W/C sample, designed to have peak reflectivity at 25^{o} grazing angle of incidence for 44Å soft X-ray and the other is a 21 layer sample which is designed to have peak reflectivity at 20^{o} grazing angle of incidence for 44Å soft X-ray. The samples have initially been characterized by hard X-ray GIXR measurement with Cu K_{α} radiation of 1.54 Å wavelength and the hard X-ray reflectivity of the 25-layer W/C sample along with best fitted theoretical spectrum is shown in Fig. 7.13. The first Bragg peak for this sample is found to appear at 0.93^{o} grazing angle of incidence with peak reflectivity of 17%. The appearance of sharp Bragg peaks and clear Kiessig fringes manifest the realization of good quality W/C multilayer structure by the IBS technique. Subsequently, the soft X-ray reflectivity of the 25-layer and 21-layer samples have been measured at the Reflectivity beamline [150] at INDUS-1 synchrotron source at RRCAT, Indore which are shown in Fig. 7.14 (a) & (b) resprctivrly. The soft X-ray reflectivity measurements for both the samples have been carried out in the 0 to 40^{o} range of grazing angle of incidence and at wavelengths of 43Å, 43.25Å, 43.5Å, 43.75Å, 44Å, 45Å, and 50Å. The

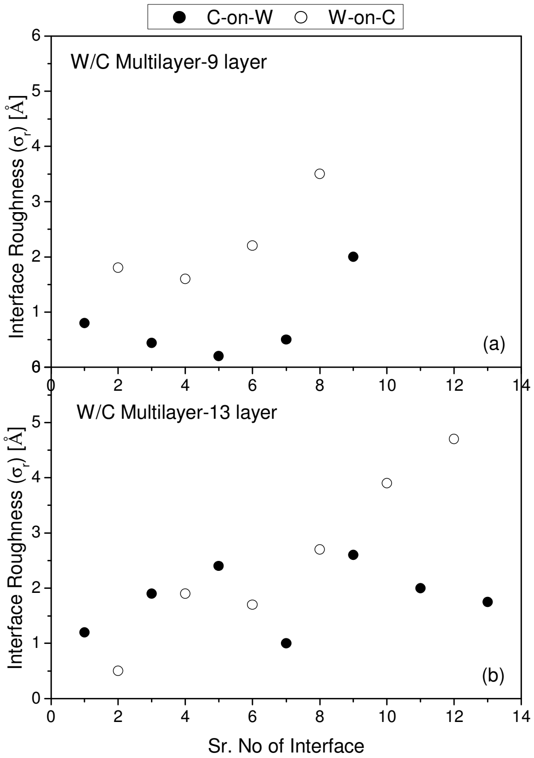

Fig. 7.12: Variation of interface roughness (σ_r) of W-on-C and C-on-W interfaces of two representative W/C multilayer samples as a function of sr. no. of interface (counted from bottom to top): (a) 9-layer sample, (b) 13-layer sample.

maximum reflectivity has been found at 44Å for both the samples which agrees well with the design value. The value of peak reflectivity for 21-layer sample is found to be ~4.5% at 20^{o} grazing angle of incidence, while for the 25-layer samples it is ~3.5% at 26^{o} grazing angle of incidence. Below 44 Å wavelength due to absorption of C-layer the reflectivity drops very fast.

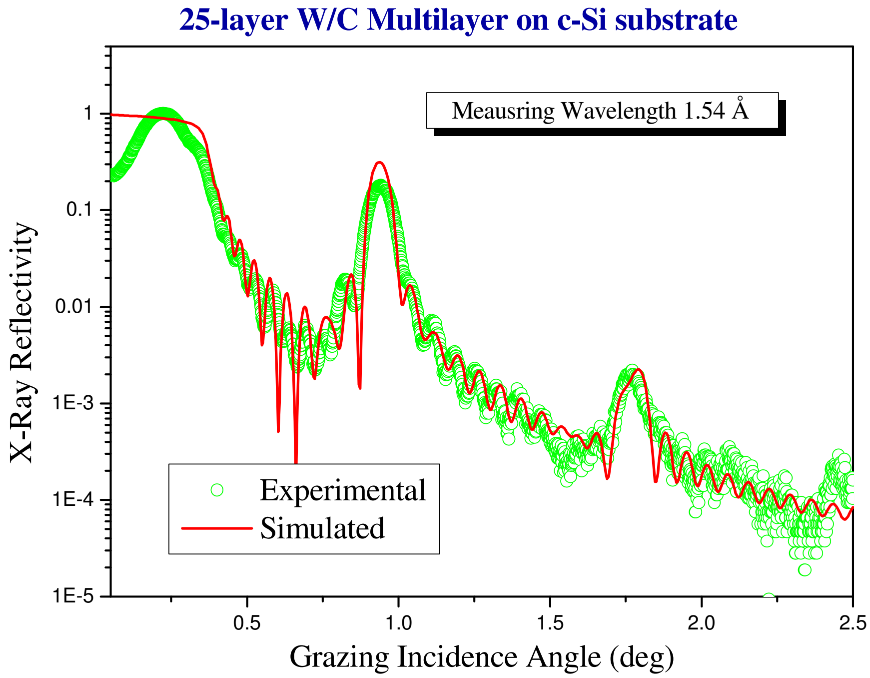

Fig. 7.13: GIXR reflectivity spectrum of 21-layer W/C multilayer mirror along with best fitted simulated spectrum

7.4 Conclusion

W/Si multilayers having 5, 7, 9, 13 & 17 layers and W/C multilayer having 5, 7, 9 and 13-layer have been deposited on c-Si substrates by in-house developed Ion Beam Sputtering technique and characterized by specular and non-specular grazing incidence X-ray reflectivity measurements and information have been obtained regarding interface width, interface roughness and interface diffusivity at the W-on-Si and Si-on-W interfaces for W/Si multilayer, as well as W-on-C and C-on-W interface for W/C multilayer. The interface widths at the W-on-Si interfaces and W-on-C interface are found to be higher than that at Si-on-W interfaces and C-on-W interface respectively due to higher diffusion of W atoms inside Si layers or C layer. In case of W/Si multilayer, it has been observed that there is no significant increase in the interface roughness with the increase in number of layers and the roughness at the Si-on-W interfaces gradually decrease from the bottom to the top of the multilayer. The in-plane correlation lengths are higher at the Si-on-W interfaces which again increase from the substrate to the top of the multilayers and the vertical correlation length of interface roughness increases with the increase in number of layers. Since it has also been observed that the roughness of the top W layers get worsened with further deposition of Si layers on it for the multilayer samples, it has been concluded that smoothening process of the Si-on-W interfaces is due to the intrinsic smoothening process of the W layers due to rearrangement of energetic W adatoms during deposition. This smoothening process results in canceling out of the high frequency component of roughness and the low frequency roughness propagates in a correlated fashion from the substrate to the top as a result of which the top surface roughness does not increase much from that of the substrate.

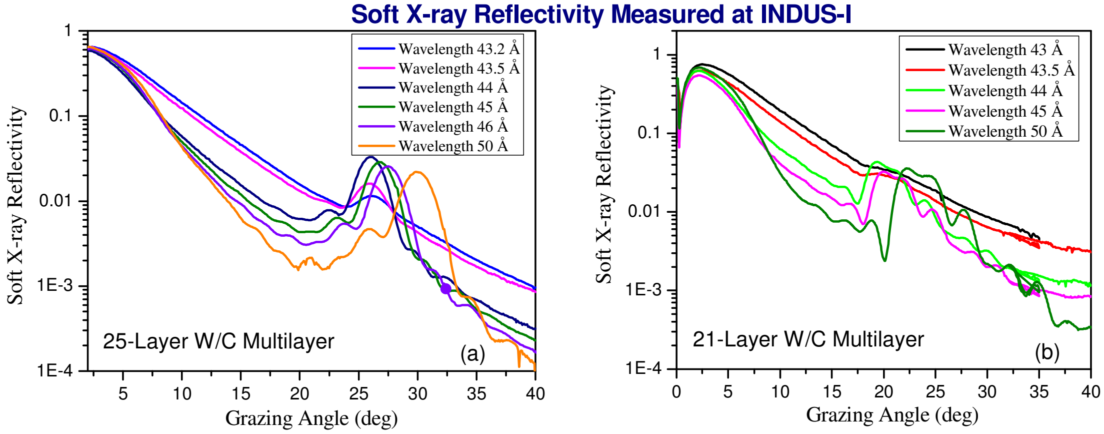

Fig 7.14: Soft x-ray reflectivity measurement spectra of (a) 25-layer W/C mirror (b) 21-layer W/C multilayer mirror

In case of W/C multilayer, it has also been observed that though the interface roughness and hence interface width for C-on-W interfaces are almost constant throughout the multilayer structure, these parameters are found to increase for W-on-C interface from the bottom to the top of the multilayers. This cumulative increase in interface roughness of W/C mutlilayers has been attributed to generation of high internal stress and increase in substrate temperature during deposition. So it is concluded that in case of W/Si multilayer there is a smoothening process which is due to deposition of energetic W atom [100], however in case of W/C multilayer high internal stress dominates over the smoothening process.

Subsequently, a 25-layer and a 21-layer W/Si multilayers has been designed and deposited which can give high reflectivity at soft X-ray wavelengths of 45 Å and 130 Å respectively at 30^o grazing angle of incidence. Similarly a 25-layer and a 21-layer W/C multilayer are designed and deposited to manifest peak reflectivities for 44Å soft X-ray at 25^o and 20^o grazing angle of incidence respectively. GIXR measurements with CuK_α radiation shows good quality of the multilayers and finally soft X-ray reflectivity measurement with INDUS-I synchrotron radiation source shows considerably high reflectivity of the multilayers at their designed wavelengths. Since the studies presented in this chapter show that roughness of the multilayers do not increase considerably with increase in the number of deposited layers, it suggests that the reflectivity of the mirrors can be increased further by depositing more number of layers.

CHAPTER 8

Summary & Future work plan

In this thesis, starting with the description of interaction of neutrons and X-ray with matter with their similarity and dissimilarity, optical indices of a material for both neutrons and X-rays have been established. The expressions for specular reflectivity of a bulk surface, of a single layer thin film on a substrate and of periodic as well as non-periodic multilayers i.e. supermirror have been formulated and the effect of realistic parameters such as surface roughness and interface roughness of the multilayer structure on the formulation of reflectivity have been discussed. Along with specular reflectivity, the non-specular reflectivity of a surface using Born Approximation (BA) and using Distorted Wave Born Approximation (DWBA) have been discussed and formulated in details. It has been established that with the specular and non-specular reflectivity analysis, the thickness of the film, density of the material, interface width, interface roughness, interface diffusion, in-plane and vertical correlation lengths, can be measured for single layer and multilayer films. In this thesis work all the thin films and multilayers deposited have been characterized by specular and non-specular grazing incidence X-ray reflectivity (GIXR) technique along with atomic force microscopy (AFM) and spectroscopic ellipsometry (SE) measurements in some cases.

In Chapter 3, different variants of sputtering techniques for thin film deposition have been discussed including the advantage of using sputtering over electron beam evaporation technique for deposition of multilayer devices in the application of neutron and X-rays, where stringent conditions on surface and interface roughness of the deposited layers are needed to be maintained. Since hard X-ray and neutron mirrors work in a very small grazing angle of incidence, large size thin film and multilayer coatings are required to cover the whole footprint of the X-ray or neutron beam. In order to meet this requirement of large area single layer and multilayer coatings, a 9 meter long inline DC/RF sputtering system has been developed in our laboratory in which thin films and multilayers can be deposited on upto 1500 mm x 150 mm area of substrates with thickness variation of less than 5%. The deposition process has been made fully computer controlled by an in-house developed LabVIEW based automation program so that a large number (~1000) layers can be deposited automatically without human intervention. In Chapter-3 the design and development of this system has been described thoroughly along with the optimization of process parameters. Neutron supermirror is a non-periodic multilayer of large number of layers where Bragg peaks obtained from different parts of the multilayer structure overlap with each other and a continuous brand of high reflectivity is achieved upto a high value of grazing angle of incidence. A GUI based program has been developed in-house under this thesis work, for designing neutron supermirror multilayer structure and for simulating neutron reflectivity spectrum from such a structure using the well-known Hayter and Mook formalism, which is discussed Chapter 4. During process error analysis using this program, it is seen that the thickness variation of more than 5% is not tolerable during the deposition of these supermirrors.

In the aim of depositing large area, high m-value Co/Ti supermirror polarizer, the process parameters of the in-house developed 9 m long d.c sputtering system have been optimized and calibrated by depositing several single layer and multilayer films and characterizing by GIXR technique. During this experiment it is observed that there is a ‘growth offset’ in the Co and Ti layer thickness which is due to asymmetric diffusion at Co-on-Ti and Ti-on-Co. Considering this, Co/Ti based thin film multilayer supermirrior polarizers of up to m=2.5, have been fabricated successfully using the design structure generated by in-house developed program. The Co/Ti supermirror shows high reflectivity (~80%) up to a reasonably large critical wavevector transfer (q_z) of ~0.06 Å^{-1} which is capable for use in the actual neutron experiment. It has been observed that use of a mixed ambience of argon and air while depositing Co layers or increasing the Co layer thickness from its nominal value by ~10 Å improves the reflectivity pattern of the supermirrors significantly. The TEM measurement of supermirror confirms the sharp interface when Co layer is deposited in the mixed ambience of argon and air.

In Chapter 5 the optimization of process parameter of in-house developed RF sputtering system for deposition of Ni/Ti supermirror has been described. Characterizing the single layer Ni and Ti films by GIXR and AFM techniques, it is found that the top surface roughness of the Ni and Ti films satisfies the power growth law with the thickness of the film. The values of growth exponent (β) for Ti and Ni films are found be 0.42±0.05 and 0.57±0.003, respectively and the roughness exponents related to the evolution of the correlation length have also been obtained, which are found to be ~0.73 for Ti films and ~0.90 for Ni films. These values are close to the theoretical predictions and previous reported values for other materials.

Ni/Ti periodic multilayers of 11-layer, 21-layer, 31-layer, and 51-layers having different bi-layer thicknesses have been deposited and characterized by both GIXR with X-rays of 1.54 Å wavelength and neutron reflectivity with cold neutron of 7.5 Å wavelength at ILL, Grenoble France. Analyzing these data it is seen that the top layer roughness of the multilayers does not depend on the total thickness of the multilayers like single layer film. By measuring the interface width it is seen that Ni-on-Ti interface width is higher compared to Ti-on-Ni interface, manifesting that Ni diffusion is more in Ti layers than Ti diffusion in Ni layers. It is also seen that the interface widths strongly depend on the bi-layer thickness of the multilayers which has been explained by the assumption of "restart of the growth at the interface" phenomenon. Similar power law for growth of roughness in single layers has been applied for multilayer interface width as a function of bi-layer thickness and the value of growth exponent of the interfaces has been obtained for both interfaces. Subsequently, Ni/Ti supermirror of m=1.75 and m=2.0 having 62 and 98 number of layers have been deposited following the design structure generated by the home-made computer program. These supermirrors are characterized by measuring neutron reflectivity at 2.5 Å wavelength at DHRUVA reactor at Bhabha Atomic Research Center, Mumbai. The m=1.75 and m=2.0 supermirror show 92% and 71% reflectivity at their respective cut off angles.

In the Chapter 6 the development of an Ion Beam Sputtering (IBS) system has been described, this system has been used for deposition of W/Si and W/C soft X-ray multilayer mirrors. The process parameters of the IBS system have been optimized by depositing single layer W film, tri-layer W/Si/W film and tri-layer W/C/W films at Ar^+ ion energies of 600, 800, 1000, 1200 eV during W layer deposition. These samples have been characterized by specular and non-specular X-ray reflectivity at 1.54 Å wavelength and AFM measurements. It is seen that the interface width and inter-diffusion at W-on-Si interface and W-on-C interfaces are much higher than that at Si-on-W and C-on-W interface respectively. The interface diffusion decreases as ion energy of W deposition increases for Si-on-W interface and C-on-W interface and is minimum when W-layer is deposited with 1000 eV Ar^+ ions, since the density of W layer is maximum at his energy which has been observed during the characterization of single layer W film. The competition between two processes viz., increase in adatoms energies on reaching the substrate vis-a-vis increase in sputtering yield and deposition rate is attributed for obtaining maximum density of W layers at an optimum Ar^+ ion energy of 1000 eV and hence subsequent depositions of W/Si and W/C multilayer structures have been carried out at this optimum energy of Ar^+ ions.

In Chapter 7, the development and characterization of W/Si and W/C soft X-ray multilayers are discussed in detail. W/Si multilayers having 5, 7, 9, 13 and 17 layers and W/C multilayer having 5, 7, 9 and 13 layers have been deposited on c-Si substrates. All these samples have been characterized by specular GIXR measurement and non-specular GIXR measurements in detector scan geometry at the 1st Bragg peak position with 1.54Å wavelength and all the interface parameters of W/Si and W/C multilayers have been measured. It has been observed that in case of W/Si multilayers there is a smoothening process at the W-on-Si interfaces, which is due to deposition of energetic W atoms and interface width does not increase across the depth of the multilayer cumilitatively from the bottom to the top, however in case of W/C multilayers high internal stress dominates over the smoothening process and interface roughness is found to increase from the bottom to the top of the multilayers.

Finally a 25-layer and a 21-layer W/Si multilayer have been designed and deposited to reflect soft X-rays of 45 Å and 130 Å wavelength respectively at 30^o grazing angle of incidence and a 21-layer and a 25-layer W/C multilayer have been designed and deposited to show reflect soft X-ray of 44 Å wavelength at 20^o and 25^o grazing angle of incidence respectively. All the soft X-ray mirrors are tested at the Reflectivity beamline at INDUS-1 synchrotron source at RRCAT, Indore and these mirrors are found to show reasonably high reflectivities at their design conditions.

In conclusion, during this thesis work some high ‘m-value’ neutron supermirrors, neutron supermirror polarizer and soft X-ray multilayer mirrors have been developed using various in-house built sputtering systems. It has been demonstrated that good quality multilayer devices could be realized in these home-built systems. By characterizing several single layer and multilayer thin film samples in specular and non-specular geometry, with X-ray and neutron, it has been observed that the interface width as well as interface diffusion in a multilayer thin film is always asymmetric. It is also seen that the top surface roughness of a multilayer does not generally depend on the total thickness of the multilayer, as at the each interface the growth process restarts without propagating the bottom layer roughness, except in some case like W/C multilayer where some other effect like inherent stress in the multilayer is found to be more dominating. So as a future work, it is proposed to control the interface roughness by applying proper buffer layers at the interfaces of the multilayer to prevent diffusion of one material in to the other. Also it is proposed to deposit the neutron and X-ray multilayers by the recently invented High Power Impulse Magnetron Sputtering (HiPIMS) technique which imparts higher energies to the adatoms of a growing film.

References

1. J. Chadwick, Possible Existence of a Neutron, Nature, 129 (1932) 312.
2. W.C. Röntgen, On a New Kind of Rays, The British Journal of Radiology, 4 (1931) 32-33.
3. G.L. Squires, Introduction to the Theory of Thermal Neutron Scattering, Dover Publications, 1997.
4. J. Als-Nielsen, D. McMorrow, Elements of Modern X-ray Physics, second Edition ed., Wiley: A John Wiley & Sons, Ltd Publication, West Sussex, PO19 8SQ, United Kingdom, 2011.
5. D.T. Attwood, Soft X-Rays and Extreme Ultraviolet Radiation Principles and Applications, Chambridge University Press, 2000.
6. Advanced Tomographic Methods in Materials Research and Engineering, Oxford University Press, 2008.
7. I.S. Anderson, R. McGreevy, H.Z. Bilheux, Neutron Imaging and Applications: A Reference for the Imaging Community, Springer, 2009.
8. J. Daillant, A. Gibaud, X-ray and Neutron Reflectivity Principles and Applications, Springer, Berlin Heidelberg, 2009.
9. F. Mezei, P.A. Dagleish, Corrigendum and first experimental evidence on neutron supermirrors, Commun. Phys, 2 (1977) 41-43.
10. F. Mezei, Novel polarized neutron devices: supermirror and spin component amplifier, Commun. Phys, 1 (1976) 81-85.
11. O. Schärpf, Recent advances with supermirror polarizers, AIP Conference Proceedings, 89 (1982) 182-189.
12. Neutron Data Booklet, Second ed., Institut Laue-Langevin, Grenoble, France.
13. D. Yamazaki, R. Maruyama, K. Soyama, H. Takai, M. Nagano, K. Yamamura, Neutron beam focusing using large-m supermirrors coated on precisely-gured aspheric surfaces, Journal of Physics: Conference Series, 251 (2010) 012076.
14. O. Schärpf, I.S. Anderson, The role of surfaces and interfaces in the behaviour of non-polarizing and polarizing supermirrors, Physica B: Condensed Matter, 198 (1994) 203-212.
15. P. Høghøj, I. Anderson, R. Siebrecht, W. Graf, K. Ben-Saidane, Neutron polarizing Fe/Si mirrors at ILL, Physica B: Condensed Matter, 267–268 (1999) 355-359.
16. M.S. Kumar, V.R. Shah, C. Schanzer, P. Böni, T. Krist, M. Horisberger, Polarized neutron reflectivity of FeCoV/Ti multilayers, Physica B: Condensed Matter, 350 (2004) E241-E244.
17. C.F. Majkrzak, J.W. Cable, J. Kwo, M. Hong, D.B. McWhan, Y. Yafet, J.V. Waszczak, C. Vettier, Observation of a Magnetic Antiphase Domain Structure with Long-Range Order in a Synthetic Gd-Y Superlattice, Physical Review Letters, 56 (1986) 2700-2703.
18. S.J. Blundell, J.A.C. Bland, Polarized neutron reflection as a probe of magnetic films and multilayers, Physical Review B, 46 (1992) 3391-3400.
19. O. Schärpf, H. Capellmann, The XYZ-Difference Method with Polarized Neutrons and the Separation of Coherent, Spin Incoherent, and Magnetic Scattering Cross Sections in a Multidetector, physica status solidi (a), 135 (1993) 359-379.
20. J.R. Stewart, P.P. Deen, K.H. Andersen, H. Schober, J.-F. Barthelemy, J.M. Hillier, A.P. Murani, T. Hayes, B. Lindenau, Disordered materials studied using neutron polarization analysis on the multi-detector spectrometer, D7, Journal of Applied Crystallography, 42 (2009) 69-84.
21. P. Fouquet, B. Farago, K.H. Andersen, P.M. Bentley, G. Pastrello, I. Sutton, E. Thaveron, F. Thomas, E.

Moskvin, C. Pappas, Design and experimental tests of a novel neutron spin analyzer for wide angle spin echo spectrometers, Review of Scientific Instruments, 80 (2009) 095105.

22. X-Ray Data Booklet Third Edition ed., Lawrence Berkeley National Laboratory, University of California, Berkely, CA 94720, 2009.
23. Berglund, Rymell, Peuker, Wilhein, Hertz, Compact water-window transmission X-ray microscopy, Journal of Microscopy, 197 (2000) 268-273.
24. H. Legall, G. Blobel, H. Stiel, W. Sandner, C. Seim, P. Takman, D.H. Martz, M. Selin, U. Vogt, H.M. Hertz, D. Esser, H. Sipma, J. Luttmann, M. Höfer, H.D. Hoffmann, S. Yulin, T. Feigl, S. Rehbein, P. Guttmann, G. Schneider, U. Wiesemann, M. Wirtz, W. Diete, Compact X-ray microscope for the water window based on a high brightness laser plasma source, Opt. Express, 20 (2012) 18362-18369.
25. Y. Uspenskii, D. Burenkov, T. Hatano, M. Yamamoto, Optimal Design of Multilayer Mirrors for Water-Window Microscope Optics, OPT REV, 14 (2007) 64-73.
26. J.-F. Adam, J.-P. Moy, J. Susini, Table-top water window transmission X-ray microscopy: Review of the key issues, and conceptual design of an instrument for biology, Review of Scientific Instruments, 76 (2005) 091301.
27. L. Artyukov, A.V. Vinogradov, Y.S. Kas'yanov, S.V. Savel'ev, X-ray microscopy in the carbon window region, Quantum Electronics, 34 (2004) 691-692.
28. D.G. Stearns, R.S. Rosen, S.P. Vernon, Multilayer mirror technology for soft-X-ray projection lithography, Appl. Opt., 32 (1993) 6952-6960.
29. F.E. Christensen, A. Hornstrup, N.J. Westergaard, H.W. Schnopper, J.L. Wood, K. Parker, Graded d-spacing multilayer telescope for high-energy X-ray astronomy, in, 1992, pp. 160-167.
30. N. Yamaguchi, J. Katoh, T. Cho, S. Miyoshi, S. Aoki, K. Nakajima, Simple soft x-ray spectrograph with a multilayer mirror for plasma diagnostics, Applied Physics Letters, 60 (1992) 821-823.
31. S. Eisebitt, J. Lüning, W. Schlotter, M. Lörgen, O. Hellwig, W. Eberhardt, J. Stöhr, Lensless imaging of magnetic nanostructures by X-ray spectro-holography, Nature 432(7019) (2004 Dec 16) 885-888.
32. T. Haga, M.C.K. Tinone, M. Shimada, O. T., O. A., Soft X-ray multilayer beam splitters, J. Synchrotron Rad., 5 (1998) 690-692.
33. F. Family, T. Vicsek, Dynamics of Fractal Surfaces, World Scientific, Singapore, 1991.
34. H.-N. Yang, T.-M. T.-M. Lu, G.-C. Wang, Diffraction from Rough Surfaces and Dynamic Growth Fronts, World Scientific, Singapore, 1993.
35. J.H. Jeffries, J.K. Zuo, M.M. Craig, Instability of Kinetic Roughening in Sputter-Deposition Growth of Pt on Glass, Physical Review Letters, 76 (1996) 4931-4934.
36. Y.L. He, H.N. Yang, T.M. Lu, G.C. Wang, Measurements of dynamic scaling from epitaxial growth front: Fe film on Fe(001), Physical Review Letters, 69 (1992) 3770-3773.
37. J. Wang, G. Li, P. Yang, M. Cui, X. Jiang, B. Dong, H. Liu, X-ray reflectivity and scanning-tunneling-microscopy study of surface roughness scaling of molybdenum films Europhys. Lett, 42 (1998).
38. H. You, R.P. Chiarello, H.K. Kim, K.G. Vandervoort, X-ray reflectivity and scanning-tunneling-microscope study of kinetic roughening of sputter-deposited gold films during growth, Physical Review Letters, 70 (1993) 2900-2903.
39. Z.-J. Liu, Y.G. Shen, Oscillating growth of surface roughness in multilayer films, Applied Physics Letters, 84 (2004) 5121-5123.
40. D.E. Savage, N. Schimke, Y.H. Phang, M.G. Lagally, Interfacial roughness correlation in multilayer films: Influence of total film and individual layer thicknesses, Journal of Applied Physics, 71 (1992) 3283-3293.

41. J.M. Freitag, B.M. Clemens, Nonspecular X-ray reflectivity study of roughness scaling in Si/Mo multilayers, Journal of Applied Physics, 89 (2001) 1101-1107.
42. A. Paul, G.S. Lodha, Interface roughness correlation due to changing layer period in Pt/C multilayers, Physical Review B, 65 (2002) 245416.
43. Y.-P. Wang, H. Zhou, L. Zhou, R.L. Headrick, A.T. Macrander, A.S. Özcan, Interface roughness evolution in sputtered WSi2⁄Si multilayers, Journal of Applied Physics, 101 (2007) 023503.
44. V. Holý, Diffuse X-ray scattering from non-ideal periodical crystalline multilayers, Appl. Phys. A, 58 (1994) 173-180.
45. V. Holý, T. Baumbach, Nonspecular X-ray reflection from rough multilayers, Physical Review B, 49 (1994) 10668-10676.
46. D.K.G. de Boer, Influence of the roughness profile on the specular reflectivity of x rays and neutrons, Physical Review B, 49 (1994) 5817-5820.
47. D.G. Stearns, D.P. Gaines, D.W. Sweeney, E.M. Gullikson, Nonspecular X-ray scattering in a multilayer-coated imaging system, Journal of Applied Physics, 84 (1998) 1003-1028.
48. M. Born, E. Wolf, Principles of Optics (4th.ed.), Pergamon Press 1970.
49. H. Kiessig, Interferenz von Röntgenstrahlen an dünnen Schichten [Interference of X-rays in thin layers], Annalen der Physik, 402 (1931) 715-725 &768-788
50. J.B. Hayter, H.A. Mook, Discrete thin-film multilayer design for X-ray and neutron supermirrors, J. Appl. Cryst., 22 (1989) 35-41.
51. L.G. Parratt, Surface Studies of Solids by Total Reflection of X-Rays, Physical Review, 95 (1954) 359-369.
52. O. Frédéric, Neutron scattering on magnetic nanostructures, IRAMIS - Laboratoire Léon Brillouin CEA/CNRS, 2008.
53. L. Névot, P. Croce, Characterization of surfaces by grazing X-ray reflection- application to study of polishing of some silicate glasses, Revue de Physique Appliquée (1980) 761-779, (1980) 761-779.
54. S.K. Sinha, E.B. Sirota, S. Garoff, H.B. Stanley, X-ray and neutron scattering from rough surfaces, Physical Review B, 38 (1988) 2297-2311.
55. D.K.G. de Boer, X-ray scattering and x-ray fluorescence from materials with rough interfaces, Physical Review B, 53 (1996) 6048-6064.
56. Y. Yoneda, Anomalous Surface Reflection of X Rays, Physical Review, 131 (1963) 2010-2013.
57. D.L. Windt, IMD Version 4.1.1, in: http://cletus.phys.co-lumbia.edu/windt/idl, 2000.
58. U. Pietsch, V. Holý, T. Baumbach, High-resolution X-ray scattering: from thin films to nanostructures, 2nd Edition ed., Springer, Berlin, 2004.
59. D.L. Windt, F.E. Christensen, W.W. Craig, C. Hailey, F.A. Harrison, M. Jimenez-Garate, R. Kalyanaraman, P.H. Mao, Growth, structure, and performance of depth-graded W/Si multilayers for hard X-ray optics, Journal of Applied Physics, 88 (2000) 460-470.
60. D.M. Mattox, Foundations of Vacuum Technology, Noyes/William Andrew Publishing, Norwich, NY, USA, 2003.
61. G.K. Wehner, G.S. Anderson, The nature of physical sputtering, in Handbook of Thin Film Technology,, McGraw-Hill Book Co., USA, 1970.
62. F. Simeon, Note on the production of mirrors by cathodic bombardment, in On the Making of Reflecting Surfaces,, Fleetway Press, Ltd., London, The Imperial Collegeof Science and Technology, 1920.
63. F.M. Penning, Coating by cathode disintegration, U.S. Patent, No: 2,146,025, in, 1939.

64. K. Wasa, W. Andrew, Handbook of Sputter Deposition Technology: Fundamentals and Applications for Functional Thin Films, Nano-materials and MEMS, Elsiver, 2012.

65. ASM Handbook, Volume 5 - Surface Engineering, ASM International, USA, 1995.

66. S. Rossnagel, Sputtering and sputter deposition, in Handbook of Thin-Film Deposition Processes And Techniques 2nd Edition, Noyes Publications, William Andrew Publishing, Norwich, New York, USA, 2002.

67. J.A. Thornton, J.E. Greene, Sputter deposition processes, in Handbook of Deposition Technologies for Films and Coatings, Noyes Publications, Park Ridge, New Jersey, USA, 1994.

68. J.A. Thornton, The microstructure of sputter-deposited coatings, Journal of Vacuum Science & Technology A, 4 (1986) 3059-3065.

69. J.E. Greene, Nucletion, film growth, and microstructural evolution, in Handbook Of Deposition Technologies For Films And Coatings,, Noyes Publications, Park Ridge, New Jersey, USA, 1994.

70. K.S.S. Harsha, Principles of Physical Vapor Deposition of Thin Films, Elsevier Ltd. USA, 2006.

71. E. Shidoji, M. Nemoto, T. Nomura, Y. Yoshikawa, Three-Dimensional Simulation of Target Erosion in DC Magnetron Sputtering, Japanese Journal of Applied Physics, 33 (1994) 4281.

72. B.J. T, Magnetron sputtering source with improved target utilization and deposition rate, in, Google Patents, 2001.

73. B. Chapman, Glow Discharge Process Sputtering and Plasma Etching, John Willy & Sons, New York, 1980.

74. D.T. Wei, A.W. Louderback, Method for fabricating multi-layer optical films US patent No. US4142958 A, in, Google Patents, 1979.

75. K. Seshan, Handbook of Thin-Film Deposition Processes and Techniques Principles, Methods, Equipment and Applications, William Andrew Publishing Norwich, New York, U.S.A., 2002.

76. R. Anton, T. Wiegner, W. Naumann, M. Liebmann, C. Klein, C. Bradley, Design and performance of a versatile, cost-effective microwave electron cyclotron resonance plasma source for surface and thin film processing, Review of Scientific Instruments, 71 (2000) 1177-1180.

77. V. Kouznetsova, K. Macáka, J.M. Schneidera, U. Helmerssona, I. Petrovb, A novel pulsed magnetron sputter technique utilizing very high target power densities, Surface and Coatings Technology 122 (1999) 290-293.

78. A. Biswas, R. Sampathkumar, A. Kumar, D. Bhattacharyya, N.K. Sahoo, K.D. Lagoo, R.D. Veerapur, M. Padmanabhan, R.K. Puri, D. Bhattacharya, S. Singh, S. Basu, Design and development of an in-line sputtering system and process development of thin film multilayer neutron supermirrors, Review of Scientific Instruments, 85 (2014) 123103.

79. A. Biswas, S.M. Haque, J. Misal, K.D. Lagoo, R.D. Veerapur, M. Padmanabhan, R.K. Puri, R. Sampathkumar, Ajaykumar, D. Bhattacharya, D. Bhattacharyya, N.K. Sahoo, Installation and commissioning of a large area coating system for neutron and X-ray optical devices, AIP Conference Proceedings, 1591 (2014) 985-987.

80. E. Fermi, W. Zinn, Phys. Rev., 70 (1946) 103.

81. G.P. Felcher, Magnetic depth profiling studies by polarized neutron reflection, Physica B: Condensed Matter, 192 (1993) 137-149.

82. S. Basu, S. Singh, A new polarized neutron reflectometer at Dhruva for specular and off-specular neutron reflectivity studies, Journal of Neutron Research, 14 (2006) 109-120.

83. Parratt Software, in: http://www.physics.brocku.ca/~tharroun/parratt/.

84. R.M.A. Azzam, N.M. Bashara, Ellipsometry and Polarized Light North Holland, 1999.

85. D. Bhattacharyya, A. Biswas, Spectroscopic ellipsometric study on dispersion of optical constants of Gd2O3 films, Journal of Applied Physics, 97 (2005) 053501.
86. A. Biswas, D. Bhattacharyya, N.K. Sahoo, B.S. Yadav, S.S. Major, R.S. Srinivasa, Spectroscopic ellipsometry studies of GaN films deposited by reactive rf sputtering of GaAs target, Journal of Applied Physics, 103 (2008) 083541.
87. Physics of Thin Films, Academic, San Diego, 1994.
88. N.K. Sahoo, M. Senthilkumar, S. Thakur, D. Bhattacharyya, Correlation of optical and microstructural properties of Gd2O3 thin films through phase-modulated ellipsometry and multi-mode atomic force microscopy, Applied Surface Science, 200 (2002) 219-230.
89. O. Schärpf, Properties of beam bender type neutron polarizers using supermirrors, Physica B: Condensed Matter, 156–157 (1989) 639-646.
90. M. Hino, H. Hayashida, M. Kitaguchi, Y. Kawabata, M. Takeda, R. Maruyama, T. Ebisawa, N. Torikai, T. Kume, S. Tasaki, Development of large-m polarizing neutron supermirror fabricated by using ion beam sputtering instrument at KURRI, Physica B: Condensed Matter, 385–386, Part 2 (2006) 1187-1189.
91. R. Maruyama, D. Yamazaki, T. Ebisawa, M. Hino, K. Soyama, Development of neutron supermirror with large-scale ion-beam sputtering instrument, Physica B: Condensed Matter, 385–386, Part 2 (2006) 1256-1258.
92. M. Senthil Kumar, P. Böni, M. Horisberger, Neutron reflectivity and interface roughness in Ni/Ti and FeCoV/TiNx supermirrors, Nuclear Instruments and Methods in Physics Research Section A: Accelerators, Spectrometers, Detectors and Associated Equipment, 529 (2004) 90-93.
93. D. Clemens, P. Böni, H.P. Friedli, R. Göttel, C. Fermon, H. Grimmer, H. van Swygenhoven, J. Archer, F. Klose, T. Krist, F. Mezei, P. Thomas, Polarizing Ti1−uXu/FexCoyVz supermirrors, Physica B: Condensed Matter, 213–214 (1995) 942-944.
94. V.G. Syromyatnikov, A. Menelle, Z.N. Soroko, A.F. Schebetov, Neutron double multilayer monochromator-polarizer Co/Ti, Physica B: Condensed Matter, 248 (1998) 355-357.
95. T. Ebisawa, N. Achiwa, S. Yamada, T. Akiyoshi, O. Sunao, Neutron Reflectivities of Ni-Mn and Ni-T i Multilayers for Monochromators and Supermirrors, Journal of Nuclear Science and Technology, 16[9
96. I. Carron, V. Ignatovich, Algorithm for preparation of multilayer systems with high critical angle of total reflection, Physical Review A, 67 (2003) 043610.
97. N.K. Pleshanov, Algorithm for the real-structure design of neutron supermirrors, Nuclear Instruments and Methods in Physics Research Section A: Accelerators, Spectrometers, Detectors and Associated Equipment, 524 (2004) 273-286.
98. A. Biswas, D. Bhattacharyya, N.K. Sahoo, D. Bhattacharya, S. Singh, S. Basu, Development of high 'm-value' neutron supermirror polarizer, in: 5th Conf. on Neutron Scattering, Mumbai, 2015, pp. 123.
99. P. Houdy, Kinetic ellipsometry applied to soft X-ray multilayer growth control, Revue Phys. Appl., 23 (1988) 1653-1659.
100. A. Biswas, D. Bhattacharyya, Correlation of interface roughness for ion beam sputter deposited W/Si multilayers, Journal of Applied Physics, 109 (2011) 084311.
101. S. Maidul Haque, A. Biswas, D. Bhattacharya, R.B. Tokas, D. Bhattacharyya, N.K. Sahoo, Surface roughness and interface width scaling of magnetron sputter deposited Ni/Ti multilayers, Journal of Applied Physics, 114 (2013) 103508.
102. B. Yang, L.J. Pilione, J.E. Yehoda, K. Vedam, R. Messier, Nonuniformity in void concentration between the initial and final growth stage of sputtered a-Ge films studied using spectroscopic

ellipsometry, Physical Review B, 36 (1987) 6206-6208.

103. K. Smardz, L. Smardz, A. Jezierski, Magnetisation of Co/Ti Multilayer, in: European Conference "Physics of Magnetism '99", Acta Physica Polonica, A, 1999, pp. 507.

104. O. Elsenhans, P. Böni, H.P. Friedli, H. Grimmer, P. Buffat, K. Leifer, J. Söchtig, I.S. Anderson, Development of Ni/Ti multilayer supermirrors for neutron optics, Thin Solid Films, 246 (1994) 110-119.

105. A.L. Barabasi, H.E. Stanley, Fractal Concepts in Surface Growth, Cambridge University Press, Cambridge, England, 1995.

106. P. Meakin, Fractals, Scaling and Growth Far From Equilibrium, Cambridge University Press, Cambridge, England, 1998.

107. S. Singh, S. Basu, P. Bhatt, A.K. Poswal, Kinetics of alloy formation at the interfaces in a Ni-Ti multilayer: X-ray and neutron reflectometry study, Physical Review B, 79 (2009) 195435.

108. M. Senthil Kumar, P. Böni, D. Clemens, Mechanical and structural properties of Ni/Ti multilayers and films: An application to neutron supermirrors, Journal of Applied Physics, 84 (1998) 6940-6942.

109. H.-C. Mertins, F. Schäfers, H. Grimmer, D. Clemens, P. Böni, M. Horisberger, W/C, W/Ti, Ni/Ti, and Ni/V multilayers for the soft-x-ray range: experimental investigation with synchrotron radiation, Appl. Opt., 37 (1998) 1873-1882.

110. S.M. Haque, A. Biswas, D. Bhattacharya, S. Singh, S. Basu, D. Bhattacharyya, N.K. Sahoo, Development of RF magnetron sputter deposited multilayer neutron supermirror, in: International Symposium on Neutron Scattering, Mumbai, 2013.

111. M. Kardar, G. Parisi, Y.-C. Zhang, Dynamic Scaling of Growing Interfaces, Physical Review Letters, 56 (1986) 889-892.

112. Z.W. Lai, S. Das Sarma, Kinetic growth with surface relaxation: Continuum versus atomistic models, Physical Review Letters, 66 (1991) 2348-2351.

113. J. Yu, J.G. Amar, Dynamical scaling behavior in two-dimensional ballistic deposition with shadowing, Physical Review E, 66 (2002) 021603.

114. A. Biswas, D. Bhattacharyya, Ion energy dependence of interface parameters of ion beam sputter deposited W/Si interfaces, Nuclear Instruments and Methods in Physics Research Section B: Beam Interactions with Materials and Atoms, 268 (2010) 1594-1600.

115. D.G. Stearns, R.S. Rosen, S.P. Vernon, Fabrication of high-reflectance Mo–Si multilayer mirrors by planar-magnetron sputtering, Journal of Vacuum Science & Technology A, 9 (1991) 2662-2669.

116. M.J.H. Kessels, F. Bijkerk, F.D. Tichelaar, J. Verhoeven, Determination of in-depth density profiles of multilayer structures, Journal of Applied Physics, 97 (2005) 093513.

117. M.J.H. Kessels, J. Verhoeven, A.E. Yakshin, F.D. Tichelaar, F. Bijkerk, Ion beam induced intermixing of interface structures in W/Si multilayers, Nuclear Instruments and Methods in Physics Research, Section B: Beam Interactions with Materials and Atoms, 222 (2004) 484-490.

118. M.J.H. Kessels, J. Verhoeven, F.D. Tichelaar, F. Bijkerk, Ion-induced interface layer formation in W/Si and WRe/Si multilayers, Surface Science, 582 (2005) 227-234.

119. M. Gupta, A. Gupta, D.M. Phase, S.M. Chaudhari, B.A. Dasannacharya, Development of an ion-beam sputtering system for depositing thin films and multilayers of alloys and compounds, Applied Surface Science, 205 (2003) 309-322.

120. A. Biswas, A.K. Poswal, R.B. Tokas, D. Bhattacharyya, Characterization of ion beam sputter deposited W and Si films and W/Si interfaces by grazing incidence X-ray reflectivity, atomic force microscopy and spectroscopic ellipsometry, Applied Surface Science, 254 (2008) 3347-3356.

121. S.M. Feng, G.L. Zhu, J.D. Shao, K. Yi, Z.X. Fan, X.M. Dou, Co/C and W/Si multilayers deposited by

ion-beam sputtering for the soft X-ray range, Appl. Phys. A, 74 (2002) 553-555.

122. E.D. Palik (Ed.), Handbook of Optical Constants of Solids, Academic Press, Orlando, FL 1985.

123. A.R. Forouhi, I. Bloomer, Optical dispersion relations for amorphous semiconductors and amorphous dielectrics, Physical Review B, 34 (1986) 7018-7026.

124. P. Petrik, M. Fried, T. Lohner, R. Berger, L.P. Bíró, C. Schneider, J. Gyulai, H. Ryssel, Comparative study of polysilicon-on-oxide using spectroscopic ellipsometry, atomic force microscopy, and transmission electron microscopy, Thin Solid Films, 313-314 (1998) 259-263.

125. T. Suzuki, S. Adachi, Chemical Treatment Effect of Si(111) Surfaces in NH4F Solution Studied by Spectroscopic Ellipsometry Jpn. J. Appl. Phys, 33 (1994) 5599.

126. J. Isidorsson, C.G. Granqvist, K. von Rottkay, M. Rubin, Ellipsometry on sputter-deposited tin oxide films: optical constants versus stoichiometry, hydrogen content, and amount of electrochemically intercalated lithium, Appl. Opt., 37 (1998) 7334-7341.

127. J. Koh, Y. Lu, C.R. Wronski, Y. Kuang, R.W. Collins, T.T. Tsong, Y.E. Strausser, Correlation of real time spectroellipsometry and atomic force microscopy measurements of surface roughness on amorphous semiconductor thin films, Applied Physics Letters, 69 (1996) 1297-1299.

128. A. Biswas, D. Bhattacharyya, Development of W/C soft X-ray multilayer mirror by ion beam sputtering (IBS) system for below 50Å wavelength, AIP Conference Proceedings, 1451 (2012) 79-81.

129. D. Bhattacharyya, A.K. Poswal, M. Senthilkumar, P.V. Satyam, A.K. Balamurugan, A.K. Tyagi, N.C. Das, Surface roughness and interface diffusion studies on thin Mo and W films and Mo/Si and W/Si interfaces, Applied Surface Science, 214 (2003) 259-271.

130. H.-J. Voorma, E. Louis, N.B. Koster, F. Bijkerk, Temperature induced diffusion in Mo/Si multilayer mirrors, Journal of Applied Physics, 83 (1998) 4700-4708.

131. M.B. Stearns, C.H. Chang, D.G. Stearns, Optimization of growth conditions of vapor deposited Mo/Si multilayers, Journal of Applied Physics, 71 (1992) 187-195.

132. X. Ji, H. Ju, D.E. McCready, K.M. Krishnan, Interface structure and perpendicular exchange bias in (Co⁄Pt)n⁄FeMn multilayers, Journal of Applied Physics, 98 (2005) 116101.

133. M. Cevro, G. Carter, Ion beam sputtering and dual ion beam sputtering of titanium oxide films J. Phys. D: Appl. Phys., 28 (1995) 1962.

134. R. Balu, A.R. Raju, V. Lakshminarayanan, S. Mohan, Investigations on the influence of process parameters on the structural evolution of ion beam sputter deposited chromium thin films, Materials Science and Engineering: B, 123 (2005) 7-12.

135. O.B. Duchemin, An Investigation of Ion Engine Erosion by Low Energy Sputtering, in, California Institute of Technology Pasadena, California, 2001.

136. E. Franke, H. Neumann, M. Zeuner, W. Frank, F. Bigl, Particle energy and angle distributions in ion beam sputtering, Surface and Coatings Technology, 97 (1997) 90-96.

137. SRIM-98, version 98.01, in. http://www.srim.org/SRIM/SRIMLEGL.htm

138. A. Ulyanenkov, R. Matsuo, K. Omote, K. Inaba, J. Harada, M. Ishino, M. Nishii, O. Yoda, X-ray scattering study of interfacial roughness correlation in Mo/Si multilayers fabricated by ion beam sputtering, Journal of Applied Physics, 87 (2000) 7255-7260.

139. C. Teyssier, E. Quesnel, V. Muffato, P. Schiavone, Stress characteristics in EUV mask Mo/Si multilayers deposited by ion beam sputtering, Microelectronic Engineering, 61–62 (2002) 241-250.

140. C. Largeron, E. Quesnel, J. Thibault, Interface growth mechanism in ion beam sputtering-deposited Mo/Si multilayers, Philosophical Magazine, 86 (2006) 2865-2879.

141. T. Salditt, D. Lott, T.H. Metzger, J. Peisl, G. Vignaud, P. Ho/gho/j, O. Schärpf, P. Hinze, R. Lauer,

Interfacial roughness and related growth mechanisms in sputtered W/Si multilayers, Physical Review B, 54 (1996) 5860-5872.

142. D.E. Savage, Y.H. Phang, J.J. Rownd, J.F. MacKay, M.G. Lagally, Determination of interfacial roughness correlation in W/C multilayer films: Comparison using soft and hard x-ray diffraction, Journal of Applied Physics, 74 (1993) 6158-6164.

143. D.E. Savage, J. Kleiner, N. Schimke, Y.H. Phang, T. Jankowski, J. Jacobs, R. Kariotis, M.G. Lagally, Determination of roughness correlations in multilayer films for x-ray mirrors, Journal of Applied Physics, 69 (1991) 1411-1424.

144. M.H. Modi, G.S. Lodha, S.R. Naik, A.K. Srivastava, R.V. Nandedkar, Smoothening of tungsten–carbon interfaces and change in interface asymmetry on heat treatment, Thin Solid Films, 503 (2006) 115-120.

145. A. Biswas, D. Bhattacharyya, N.K. Sahoo, Soft X-ray multilayer by ion beam sputtering process, Asian J. of Physics, 19 (2010) 109-124.

146. A. Paul, Effect of interface roughness on magnetic multilayers of Fe/Tb and Fe/Cr, Journal of Magnetism and Magnetic Material, 240 (2002) 497–500.

147. M. Chládek, V. Valvoda, C. Dorner, C. Holý, J. Grim, Quantitative study of interface roughness replication in multilayers using x-ray reflectivity and transmission electron microscopy, Applied Physics Letters, 69 (1996) 1318-1320.

148. M. Jergel, V. Holy, E. Majkova, S. Luby, R. Senderak, Interface Evolution in a W/Si Multilayer after Rapid Thermal Annealing Studied by X-ray Reflectivity and Diffuse Scattering, J. Appl. Cryst., 30 (1997) 642-646.

149. M. Jergel, V. Holy, E. Majkova, S. Luby, R. Senderak, Interface study of W-Si/Si and obliquely deposited W/Si multilayers by grazing-incidence high-resolution X-ray diffraction J. Phys. D: Appl. Phys. , 28 (1995) A241.

150. R.V. Nandedkar, K.J.S. Sawhney, G.S. Lodha, A. Verma, V.K. Raghuvanshi, A.K. Sinha, M.H. Modi and M. Nayak, First results on the reflectometry beamline on Indus, Current Science, 82 (2002) 298-304.

151. A.T. Macrander, Y.S. Chu, C. Liu, D.C. Mancini, Modeling of Interface Roughness Propagation in Sputtered Xray Multilayers Studied by Diffuse Xray Scattering, in: American Physical Society, Annual March Meeting, , AIP, Washington State Convention Center Seattle, Washington, 2001.

152. B.A. Vidal, J.C. Marfaing, X-ray reflectivity and transmission electron microscopy studies on thin and ultrathin W/C and W/Si multilayers structures, Journal of Applied Physics, 65 (1989) 3453-3458.

Appendix A

Other methods for calculating multilayer reflectivity

Other than the recursive method, using the following two methods also the neutron and X-ray reflectivity of the multilayer structure can be calculated.

A.1 Fourier method

The Fourier method [1] allows an analytical solution, based on the transformation of the depth dependent electron density $\rho(z)$ for X-ray and scattering length density for neutron, which is equivalent to the real refractive index, [1] combined with the Fresnel reflectivity $R_s(q_z)$ of a substrate, into a reflectivity of the total structure $R(q_z)$ using:

$$R(q_z) = R_s(q_z)\left|\frac{1}{\rho(\infty)}\int \frac{d\rho(z)}{dz} e^{iq_z z} dz\right|^2 \qquad (A.1)$$

the wave vector q_z is defined as:

$$q_z = \frac{4\pi \sin\theta_i}{\lambda} \qquad (A.2)$$

This method neglects the absorption and multiple scattering in the structure, and therefore cannot be used for quantitative analysis of the multilayer structure. Qualitatively this theory proves to be very useful to explain why the highest reflectivity is achieved for materials that have the largest difference in refractive index. A high contrast will lead to a higher value of the derivative of $\rho(z)$ and immediately results in a higher value of R.

Another trend easily explained using the Fourier method is the effect of the penetration depth, and thus absorption, on the selectivity of the multilayer mirror. In the Fourier analysis the stack

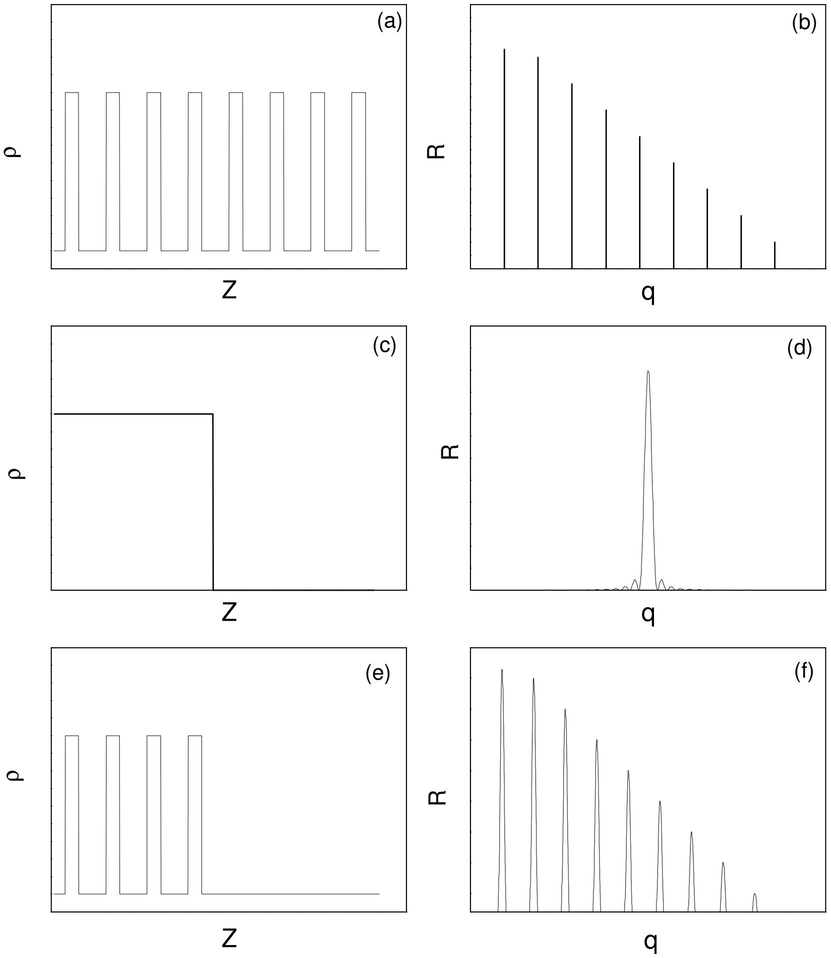

Fig. A.1: Explanation of influence of limited number of periods on selectivity. (a) Electron density profile of a semiinfinite stack (b) its reflectivity spectrum as calculated with the Fourier method (c) The envelope function used to limit the number of periods (d) Fourier transformation of above (e) The final density profile (f) and the resulting reflectivity spectrum

is considered to be semi-infinite, obviously neglecting absorption. The electron density ρ(*z*) of this stack, as plotted in Fig. A.1(a), can be described with a square wave function *S*(*z*). The result after applying the Fourier method is plotted in Fig. A.1(b). This spectrum contains delta peaks at the positions where the Bragg-condition is fulfilled. Due to absorption, the penetration depth of the radiation is not infinite and in a first approximation one could therefore assume that all layers below a certain critical depth do not contribute to the reflected signal while the layers above contribute completely. The effective electron density profile is shown in Fig. A.1(e). Basically, the derivative of the electron density function is multiplied with a rectangle function as shown in Fig. A.1(c). To determine the reflectivity of the resulting profile the reflectivity profile from the semiinfinite stack is thus convoluted with the Fourier transform of the rectangle function, which is a sinc function as shown in Fig. A.1(d). The resulting reflectivity profile is shown in Fig. A.1(f), where each delta peak is replaced with the square of a sinc function (*sin*(*x*)/*x*). This shows that indeed the width of the peaks is increased, and thus the selectivity is decreased, when one limits the number of participating periods. At the same time the reflectivity drops, since the height of the sinc function is proportional to the width of the rectangle function.

A.2 Matrix method

The exact solution of structures having diffused boundaries cannot be calculated, the structures have to be approximated by a series of small layers having sharp boundaries. A good approximation might require over one hundred layers per period, which make the calculation much more complex. In this case, the matrix method [2], a variant on the recursive method, has proven to be much easier to use since it takes the full advantage of the periodic structure of a multilayer mirror. Using this method one relates the forward $E^+(z)$ and backward $E^-(z)$ travelling plane waves on each side of the structure to each other using a 2x2 matrix *S*:

$$\begin{pmatrix} E^+(z) \\ E^-(z) \end{pmatrix} = \begin{pmatrix} S_{11} & S_{12} \\ S_{21} & S_{22} \end{pmatrix} \begin{pmatrix} E^+(z+d) \\ E^-(z+d) \end{pmatrix} \qquad (A.3)$$

or

$$E(z) = SE(z+d) \qquad (A.4)$$

where d equals the thickness of the structure. The scattering matrix S represents the overall reflection and transmission characteristics of the structure and can be composed of a product of the interface and layer matrices I and L:

$$S = \prod_{l=1}^{N} I_l L_l \qquad (A.5)$$

where N equals the number of layers, I_l equals the interface matrix between layer l and l-1

$$I_l = \frac{1}{t_{l-1,l}} \begin{pmatrix} 1 & r_{l-1,l} \\ r_{l-1,l} & 1 \end{pmatrix} \qquad (A.6)$$

and L_l equals the layer matrix of layer l

$$L_l = \begin{pmatrix} e^{i\phi_l} & 0 \\ 0 & e^{i\phi_l} \end{pmatrix} \qquad (A.7)$$

The reflectivity R of the structure can easily be calculated using:

$$R = \frac{E^-(z)}{E^+(z)} \qquad (A.8)$$

and by taking $E^-(z+d)=0$ yields:

$$R = \frac{S_{21}}{S_{11}} \qquad (A.9)$$

The main advantage of this calculation method is the ability to perform fast calculations of systems with many periods, since one can calculate a matrix describing one period, and then raise this matrix to the power of the number of periods to obtain the result for the full multilayer stack.

Appendix-B

Design program of neutron supermirror

B.1 Flow chart of supermirror design

The flow chart of the supermirror design program using Hayter and Mook model is following:

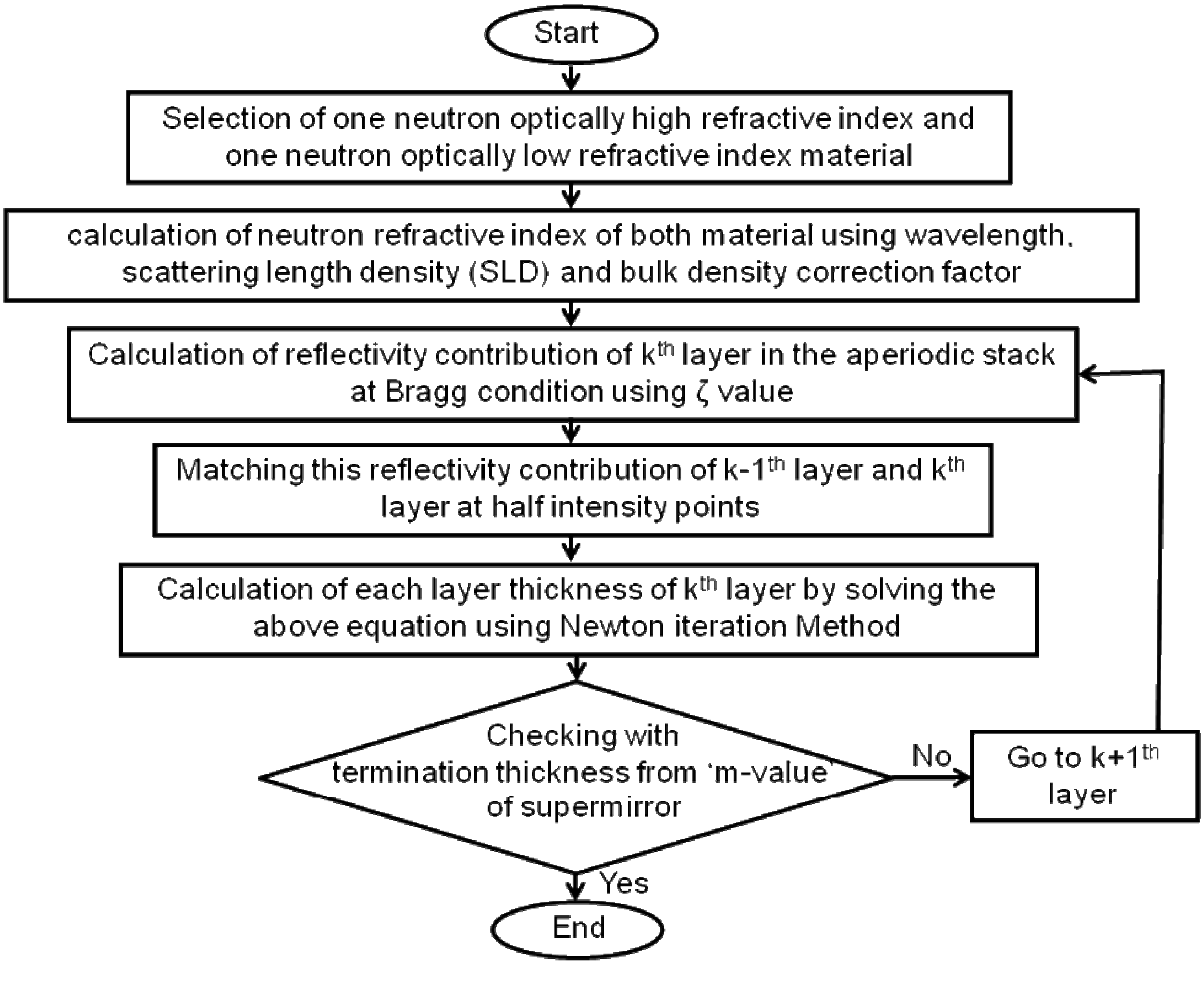

B.2 MATLAB code of the GUI program for supermirror design

Front end GUI program

```
function varargout = SupGui(varargin)
gui_Singleton = 1;
gui_State = struct('gui_Name',       mfilename, ...
                   'gui_Singleton', gui_Singleton, ...
                   'gui_OpeningFcn', @SupGui_OpeningFcn ...
                   'gui_OutputFcn', @SupGui_OutputFcn, ...
                   'gui_LayoutFcn', [] , ...
                   'gui_Callback',   []);
if nargin && ischar(varargin{1})
    gui_State.gui_Callback = str2func(varargin{1});
end

if nargout
    [varargout{1:nargout}] = gui_mainfcn(gui_State, varargin{:});
else
    gui_mainfcn(gui_State, varargin{:});
end

function SupGui_OpeningFcn(hObject, eventdata, handles, varargin)
handles.output = hObject;
guidata(hObject, handles);
function varargout = SupGui_OutputFcn(hObject, eventdata, handles)
varargout{1} = handles.output;
function Mat_1_Callback(hObject, eventdata, handles)
function Mat_1_CreateFcn(hObject, eventdata, handles)
if ispc && isequal(get(hObject,'BackgroundColor'), get(0,'defaultUicontrolBackgroundColor'))
    set(hObject,'BackgroundColor','white');
end

function Mat_2_Callback(hObject, eventdata, handles)
function Mat_2_CreateFcn(hObject, eventdata, handles)
if ispc && isequal(get(hObject,'BackgroundColor'), get(0,'defaultUicontrolBackgroundColor'))
    set(hObject,'BackgroundColor','white');
end

function Dens1_Callback(hObject, eventdata, handles)
density1 = str2double(get(hObject,'string'));
if isnan(density1)
    errordlg('You must enter a numeric value','Bad Input','modal')
end

function Dens1_CreateFcn(hObject, eventdata, handles)
if ispc && isequal(get(hObject,'BackgroundColor'), get(0,'defaultUicontrolBackgroundColor'))
    set(hObject,'BackgroundColor','white');
end

function rough1_Callback(hObject, eventdata, handles)
rough1 = str2double(get(hObject,'string'));
if isnan(rough1)
    errordlg('You must enter a numeric value','Bad Input','modal')
end

function rough1_CreateFcn(hObject, eventdata, handles)
if ispc && isequal(get(hObject,'BackgroundColor'), get(0,'defaultUicontrolBackgroundColor'))
    set(hObject,'BackgroundColor','white');
end

function rough2_Callback(hObject, eventdata, handles)
rough2 = str2double(get(hObject,'string'));
if isnan(rough2)
    errordlg('You must enter a numeric value of roughness','Bad Input','modal')
end

function rough2_CreateFcn(hObject, eventdata, handles)
```

```
if ispc && isequal(get(hObject,'BackgroundColor'), get(0,'defaultUicontrolBackgroundColor'))
    set(hObject,'BackgroundColor','white');
end

function dens2_Callback(hObject, eventdata, handles)
density2 = str2double(get(hObject,'string'));
if isnan(density2)
    errordlg('You must enter a numeric value','Bad Input','modal')
end

function dens2_CreateFcn(hObject, eventdata, handles)
if ispc && isequal(get(hObject,'BackgroundColor'), get(0,'defaultUicontrolBackgroundColor'))
    set(hObject,'BackgroundColor','white');
end

function Mat_subs_Callback(hObject, eventdata, handles)
function Mat_subs_CreateFcn(hObject, eventdata, handles)
if ispc && isequal(get(hObject,'BackgroundColor'), get(0,'defaultUicontrolBackgroundColor'))
    set(hObject,'BackgroundColor','white');
end

function Roughsub_Callback(hObject, eventdata, handles)
roughsub = str2double(get(hObject,'string'));
if isnan(roughsub)
    errordlg('You must enter a numeric value sub rough','Bad Input','modal')
end

function Roughsub_CreateFcn(hObject, eventdata, handles)
if ispc && isequal(get(hObject,'BackgroundColor'), get(0,'defaultUicontrolBackgroundColor'))
    set(hObject,'BackgroundColor','white');
end

function Wavelength_Callback(hObject, eventdata, handles)
function Wavelength_CreateFcn(hObject, eventdata, handles)
if ispc && isequal(get(hObject,'BackgroundColor'), get(0,'defaultUicontrolBackgroundColor'))
    set(hObject,'BackgroundColor','white');
end

function mvalue_Callback(hObject, eventdata, handles)
function mvalue_CreateFcn(hObject, eventdata, handles)
if ispc && isequal(get(hObject,'BackgroundColor'), get(0,'defaultUicontrolBackgroundColor'))
    set(hObject,'BackgroundColor','white');
end

function ZetaValue_Callback(hObject, eventdata, handles)
function ZetaValue_CreateFcn(hObject, eventdata, handles)
if ispc && isequal(get(hObject,'BackgroundColor'), get(0,'defaultUicontrolBackgroundColor'))
    set(hObject,'BackgroundColor','white');
end

function Type_Super_Callback(hObject, eventdata, handles)
function Type_Super_CreateFcn(hObject, eventdata, handles)
if ispc && isequal(get(hObject,'BackgroundColor'), get(0,'defaultUicontrolBackgroundColor'))
    set(hObject,'BackgroundColor','white');
end

function Parameter_Callback(hObject, eventdata, handles)
)
val = get(handles.Mat_1,'Value');
string_list = get(handles.Mat_1,'String');
material1 = string_list{val};
material1_neg = string_list{val+1};
val = get(handles.Mat_2,'Value');
string_list = get(handles.Mat_2,'String');
material2 = string_list{val};
material2_neg = string_list{val+1};
val = get(handles.Mat_subs,'Value');
string_list = get(handles.Mat_subs,'String');
materialsub = string_list{val};
density1_cor = str2double(get(handles.Dens1,'String'))/100;
density2_cor = str2double(get(handles.dens2,'String'))/100;
```

```
roughness1 = str2double(get(handles.rough1,'String'));
roughness2 = str2double(get(handles.rough2,'String'));
roughness_sub = str2double(get(handles.Roughsub,'String'));
wave_length = str2double(get(handles.Wavelength,'String'));
m_value = str2double(get(handles.mvalue,'String'));
zeta = str2double(get(handles.ZetaValue,'String'));
fid_input=fopen('Input.txt','wt');
fid_sub=fopen('Subs_Input.txt','wt');
fid_super=fopen('Super_Input.txt','wt');
fid_pol=fopen('Pol_down_Input.txt','wt');
 fprintf(fid_input, '%s %f %f\n',material1, density1_cor, roughness1);
 fprintf(fid_input, '%s %f %f\n',material2, density2_cor, roughness2);
 fprintf(fid_sub, '%s %f\n',materialsub,  roughness2);
 fprintf(fid_super, '%f %f %f\n',wave_length, m_value, zeta);
if (get(handles.Type_Super,'Value')>1)    % Selecting    fprintf(fid_pol, '%s %f
%f\n',material1_neg, density1_cor, roughness1);
    fprintf(fid_pol, '%s %f %f\n',material2, density2_cor, roughness2);
end


function layer_stuc_Callback(hObject, eventdata, handles)
    axes(handles.layer_graph)
if (get(handles.Type_Super,'Value')>1)    % Selecting    Ver3_both;
    msgbox('The output are saved in Output_layer.txt and Output_layer_down.txt!!');
else
    Ver3;
    msgbox('The output are saved in Output_layer.txt!!');
end

function Reflect_Callback(hObject, eventdata, handles)
axes(handles.ref_graph)
if (get(handles.Type_Super,'Value')>1)    % Selecting    Fifth_both;
    msgbox('The output are saved in Output.txt and Output_down.txt!!');
else
    Fifth;
    msgbox('The output are saved in Output.txt !!');
end

function Untitled_1_Callback(hObject, eventdata, handles)
function edit9_Callback(hObject, eventdata, handles)
function edit9_CreateFcn(hObject, eventdata, handles)
if ispc && isequal(get(hObject,'BackgroundColor'), get(0,'defaultUicontrolBackgroundColor'))
    set(hObject,'BackgroundColor','white');
end

function fv=fHM(wk, k, delta, beta, zeta);
global w
global del_w
h1=beta(1)/delta(1);
gama=sqrt(2*abs(delta));
psi1=wk*gama(1);
psi2=acos(((1-delta(1))/(1-delta(2)))*cos(psi1));
rho=(psi2-psi1)/(psi2+psi1);
kapa=-(1-rho)/(1+rho);
neu=log(1-zeta)/(2*log((1-rho)/(1+rho)));
rho_bar_k=(1-abs(kapa)^(1/neu))/(1+abs(kapa)^(1/neu));
w(k)=wk;
del_w(k)=(2*w(k)/pi)*asin(3*rho_bar_k/sqrt(8));
if(k<2)
    fv=sqrt((4*(w(k)+del_w(k))^2)*((w(k)+del_w(k))^2 + 1)-h1^2)/(2*(w(k)+del_w(k)))- 3/sqrt(8);
else
    fv=sqrt((4*(w(k)-del_w(k))^2)*((w(k)-del_w(k))^2 + 1)-h1^2)/(2*(w(k)-del_w(k))) -
sqrt((4*(w(k-1)+del_w(k-1))^2)*((w(k-1)+del_w(k-1))^2 + 1)-h1^2)/(2*(w(k-1)+del_w(k-1)));
end

function pardata = parratt(varargin)
qz = varargin{1};                   profile = varargin{2};
wavelength = varargin{3};
nLayer = size(profile,1);           z = profile(:,1);
delta = profile(:,2);
beta = profile(:,3);
```

```
sigma = profile(:,4);
k = 2*pi/wavelength;
if size(qz,2) == 1
    qz = qz';
   end

n = 1-delta+i*beta;
qzInVac = sqrt(qz.^2+4*k^2-4*k^2*n(1)^2);
QLayer = sqrt(4*(n*ones(1,size(qzInVac,2))).^2*k^2-4*k^2+(ones(size(n,1),1)*qzInVac).^2);
sigma_NM=(sigma.^2)*ones(1,size(qzInVac,2));
r = ((QLayer(1:end-1,:)-QLayer(2:end,:))./(QLayer(1:end-1,:) + QLayer(2:end,:)));
r=r.*exp(-0.5*(QLayer(1:end-1,:).*QLayer(2:end,:)).*((sigma_NM(2:end,:))));
R = r(end,:);
 if nLayer > 2
    thick = diff(z);        thick = thick(1:end-1);
    for iInterface = nLayer-2:-1:1
        R = (r(iInterface,:)+R.*exp(i*QLayer(iInterface+1,:)*thick(iInterface)))./...
(1+r(iInterface,:).*R.*exp(i*QLayer(iInterface+1,:)*thick(iInterface)));
    end
end

RR = abs(R).^2;
pardata = [qz' RR'];
```

Code for reflectivity simulation program

```
clear
format long;
fid=fopen('Profile.txt','wt');
fid_out=fopen('output.txt','wt');
[lamda, m_value, zeta]=textread('Super_Input.txt','%f %f %f' );
lamda=lamda*1E-10;
ang_start=0;    alpha_start=ang_start*(pi/180);
ang_end=3;      alpha_end=ang_end*(pi/180);
no_point=600;
angle_res=(alpha_end-alpha_start)/no_point;
for (j=0:no_point)
    QZ(j+1)=4*pi*sin(angle_res*j)/(lamda*1E10)
End

d_upto=0;
delta_vac=0.0;
beta_vac=0;
n=1;
    Prof(n,1)=d_upto*1E10;
    Prof(n,2)=delta_vac;
    Prof(n,3)=beta_vac;
    Prof(n,4)=0;
    fprintf(fid,'Vac=%f %f %f %f\n', Prof(n,1), Prof(n,2), Prof(n,3), Prof(n,4));
n=n+1;
[material, At_weight, dens, scat_cross, abs_coeff]=textread('Neutron_Material_Database.dat','%s
%f %f %f %f' );
[mat_str, thickness, density_corr, roughness]=textread('Output_layer.txt','%s %f %f %f' );
no_layer=size(mat_str, 1);
no_inter=no_layer+1;
for (m=no_layer:-1:1)
    k=strmatch(mat_str(m), material, 'exact');
    atomic_weight=At_weight(k);
    density=dens(k)*density_corr(m);
    b=scat_cross(k)*1E-15;
    sigma_abs=abs_coeff(k)*1E-28;
    avog_number=6.02214129E23;
    d_upto=d_upto+double(thickness(m)*1E-10);
    sigma=roughness(m)*1E-10;          rho=(density/atomic_weight)*avog_number*1E6;
delta=double(0.5*(lamda*lamda*rho*b)/pi);       b2=sigma_abs/(2*1.789E-10);
beta=double(0.5*(lamda*lamda*rho*b2)/pi);;
    n_layer=1-delta+j*beta;
    Prof(n,1)=d_upto*1E10;
    Prof(n,2)=delta;
```

```
    Prof(n,3)=beta;
    Prof(n,4)=sigma*1E10;        fprintf(fid,'Film=%f %f %f %f rhob=%f rhob2=%f\n', Prof(n,1),
Prof(n,2), Prof(n,3), Prof(n,3), rho*b, rho*b2);
    n=n+1;
end

[mat_sub,  rough_sub]=textread('Subs_Input.txt','%s %f' );
    k=strmatch(mat_sub, material, 'exact');
    atomic_weight=At_weight(k);
    density=dens(k);
    b=scat_cross(k)*1E-15;
    sigma_abs=abs_coeff(k)*1E-28;

rho=(density/atomic_weight)*avog_number*1E6;       delta=double(0.5*(lamda*lamda*rho*b)/pi);
b2=sigma_abs/(2*1.789E-10);                beta=double(0.5*(lamda*lamda*rho*b2)/pi);
    Prof(n,1)=d_upto*1E10;
    Prof(n,2)=delta;
    Prof(n,3)=beta;
    Prof(n,4)=rough_sub;                fprintf(fid,'Subs=%f %f %f %f\n', Prof(n,1), Prof(n,2),
Prof(n,3), Prof(n,4));
    lamda=lamda*1E10;
    pardata=parratt(QZ, Prof, lamda);
    for (j=1:no_point)
    fprintf(fid_out,'%d %d\n', (180/pi)*asin(pardata(j,1)*lamda/(4*pi)), pardata(j,2));
    end
plot((180/pi)*asin(pardata(:,1)*lamda/(4*pi)),pardata(:,2)), xlim([0 3]), xlabel('Angle
(degree)'), ylabel('Neutron Reflectivity'), title('Supermirror Reflectivity Spectrunm'), grid on;
```

Appendix C

Design criteria of soft X-ray multilayer mirror

The soft X-ray multilayer design has mainly two parts (a) choosing material combination and (b) design of the structure. As it has been discussed in Chapter 2, the refractive index of any material for X-ray depends on the electron density or atomic number, Z. So in order to provide the refractive index contrast between the layer materials the combination must be of high Z and low Z.

If normal incidence reflectivity of a single interface is calculated, approximately it can be written as follows:

$$R \approx \frac{(\Delta\delta)^2 + (\Delta\beta)^2}{4} \qquad (C.1)$$

where, $\Delta\delta$ and $\Delta\beta$ are the differences in dispersion and extinction coefficients between the two material, respectively, the details expression of these quantities are described in Chapter 2. Normally the low Z material in this combination is chosen such that there is no absorption edge in the designed wavelength to achieve the low β. An intention behind choosing this material is also the "anomalous dispersion" of the X-ray at the corresponding edges where the refractive index becomes slightly more than unity, which in turn, can be utilized to get the enhanced reflectance. However the condition, that $\Delta\beta$ has to be maximum does not entirely hold true when the combined reflections from a large number of interfaces are desired. In that case the large β will lead to significant absorption and the reflection from a few interfaces at the top will only contribute to the reflected intensity. Hence the maximum $\Delta\beta$ selection rule is generally compromised and the high Z material are also selected from the low β region and the probability of high reflectance was then increased by designing the mirror with a large number of interfaces. In addition to the optical contrast, the tendency of miscibility, chemical diffusion or reactions of the material combinations has also to be considered while choosing the material combination. Sometimes thesebecome so critical, that the optically suggested combination need to be sacrificed.

The design of multilayer implies the determination of the multilayer period, *d*, the high absorbing layer-to-bilayer thickness ratio, Γ, and the total number of bilayer, *N*.

As the absorption in the two materials is generally different, the optimum thickness combination of the two materials is usually unequal, so $\Gamma \neq 0.5$ for X-ray. Calculating the phase and absorption the optimum thickness combination can be found by the following formula [3]:

$$\tan(\pi\Gamma_{\mathrm{opt}}) = \pi\left[\Gamma_{\mathrm{opt}} + \frac{\mathrm{Im}(\varepsilon_2)}{\mathrm{Im}(\varepsilon_1 - \varepsilon_2)}\right] \tag{C.2}$$

where, ε_1, ε_2 are the complex dielectric constant of the two material in which ε_1 is more absorbing, Γ_{opt} is the optimum value of Γ . However in most of the cases this formula comes out with an unphysical thickness combination. The best way is to use some simulation software like IMD and generate the theoretical reflectivity spectrum using the standard optical constants or using the measured optical constants. The combination of *d* and Γ which gives the highest reflectivity at the designed wavelength and angle is selected. Once *d* and Γ are chosen, the next design step was the determination of the total number of periods needed to obtain the maximum theoretical reflectivity. Since the reflectivity of a single surface (eqn. C.1) is typically on the order of 10^{-4}-10^{-6} at normal incidence, in-phase reflection from 10^2-10^3 interfaces are required to reach the maximum reflectivity; thereafter, the absorption in the multilayer stack limits the reflectivity. The simulations are performed to obtain *N* corresponding to saturation reflectivity. The maximum reflectivity is the only criteria to determine *N* in the case of periodic multilayer structure which are also wavelength dispersive mirrors, act as narrow-band pass filters and need as high reflectivity as possible at desired wavelength.

References

1. M. Tolan, X-ray scattering from soft-matter thin films, Springer-Verlag, Berlin Heidelberg New York, 1999.
2. R.M.A. Azzam, N.M. Bashara, Ellipsometry and Polarized Light North Holland, 1999.
3. A.V. Vinogradov, B.Y. Zeldovich, X-ray and far uv multilayer mirrors: principles andpossibilities, Appl. Opt., 16 (1977) 89-93